Free-Flow Counterflow Gradient Focusing for Protein Fractionation

by

Matthew Courtney

A thesis
presented to the University of Waterloo
in fulfillment of the
thesis requirement for the degree of
Doctor of Philosophy
in
Mechanical and Mechatronics Engineering

Waterloo, Ontario, Canada, 2022

© Matthew Courtney 2022

Examining Committee Membership

The following served on the Examining Committee for this thesis. The decision of the Examining Committee is by majority vote.

External Examiner:	Dirk Janasek Senior Scientist Translational Analytics Leibniz Institute for Analytical Sciences
Supervisor:	Carolyn L. Ren Professor Dept. of Mechanical and Mechatronics Engineering University of Waterloo
Internal Members:	Dongqing Li Professor Zhao Pan Assistant Professor Dept. of Mechanical and Mechatronics Engineering University of Waterloo
Internal-External Member:	Brian Ingalls Professor Dept. of Applied Mathematics University of Waterloo

Author's Declaration

I hereby declare that I am the sole author of this thesis. This is a true copy of the thesis, including any required final revisions, as accepted by my examiners.

I understand that my thesis may be made electronically available to the public.

Abstract

In free-flow electrophoresis (FFE), a pressure-driven flow applied perpendicular to the electric field enables the continuous separation of charged solutes. Meanwhile, outlets located at the end of the separation region provide the opportunity for convenient sample collection. Consequently, FFE has drawn interest for many biological applications, including protein purification, real-time monitoring, and sample preparation prior to mass spectroscopy. However, the poor separation resolution associated with FFE has limited its potential. While advanced separation modes like free-flow isoelectric focusing (FF-IEF) offer improved performance, they often lead to further complications.

The objective of this work is to introduce an alternative separation mode in FFE that can address some of its most prevalent limitations. This technique was inspired by a counterflow gradient focusing mechanism that has been studied extensively in capillary electrophoresis. In its present form, free-flow counterflow gradient focusing (FF-CGF) relies on an additional pressure-driven flow through the sidewalls of an FFE separation chamber. The added flow will then move towards the outlets, and in the process, create a velocity gradient in the direction of the electric field. As a result, charged solutes migrating across the separation region will focus at a position where their electrophoretic velocity is counterbalanced by the fluid flow. This mechanism is similar in principle to FF-IEF, except it does not require a complex separation medium, and focused solutes are less prone to precipitation.

The first component of this work involves the physical modeling of the FF-CGF system. First, analytical equations describing the fluid velocity and the resulting focusing mechanism are derived. Then, a numerical model is provided for a detailed understanding of the solute dispersion that occurs during focusing. In particular, the interplay between molecular diffusion, the parabolic velocity profile of the counterflow, and the strength of the gradient is studied. An asymmetric solute distribution is demonstrated for a wide range of experimental conditions, and this knowledge can be used to predict separation resolution, throughput, and cross-contamination. Finally, the analytical and numerical models are updated to account for the presence of electroosmotic flow, which is shown to produce a pressure-driven backflow that can influence solute dispersion.

The second component of this work involves the practical implementation of the FF-CGF system, and there is an emphasis on strategies for generating the counterflow gradient. The initial prototype is made using soft lithography, and high resistance side channels are used to produce a uniform counterflow gradient along the length of the chamber. The second prototype is made from a more rigid material, and provides a design that is more reliable and scalable. Furthermore, a commercial porous membrane is used to supply the counterflow. During this design, detailed guidelines are provided for the factors influencing device performance, including the porous parameters, the separation chamber dimensions, the outlet channels, and the ion

exchange membranes needed to supply the electric field. Finally, a third prototype is constructed based on the aforementioned guidelines, and it is designed specifically for applications that require minute sample volumes. Moreover, this design can provide a better voltage efficiency, and operate at higher gradient strengths than the previous prototypes. Throughout this entire design process, the prototypes are used to demonstrate the separation of model proteins, and in general, the results are consistent with the analytical and numerical models. In the end, the design and implementation of FF-CGF highlights the versatility of this method, and may allow FFE to reach its full potential as a powerful protein fractionation tool.

Acknowledgements

First, I would like to thank my supervisor, Dr. Carolyn Ren, who has always supported me, and provided me with the opportunity to grow as a researcher and a leader. Her dedication is very inspiring, and her guidance and encouragement throughout my study is greatly appreciated. Next, I would like to thank Dr. Tom Glawdel, who came up with the idea for free-flow counter-flow gradient focusing, and provided helpful advice and expertise throughout my study. I feel incredibly fortunate to have had the opportunity to learn from Dr. Ren and Dr. Glawdel, and explore this truly novel concept further.

I would also like to thank my Ph.D. defense committee members: Dr. Brian Ingalls, Dr. Dongqing Li, Dr. Zhao Pan, and Dr. Dirk Janasek. Their valuable time and insights are greatly appreciated.

The members of the Waterloo Microfluidics Lab have also been instrumental to the completion of my study. When I was an undergraduate, Cody Chen, Ning Qin, and Gurkan Yesiloz all contributed significantly to my growth as a researcher. Then when I became Ph.D. student, I had the privilege of supervising Ethan Thompson, who was a first year undergraduate at the time, and always went above and beyond what was expected of him. In addition, I would like to thank the other members of the lab who made my time as a student more enjoyable: Marie Hébert, Runze Gao, Jeff Farnese, Tomasz Zablotny, Weijia Cui, Pei Zhao, Anson Lau, Wasim Kapadia, Will Baxter, and Lucas Pilozo-Hibbit.

The financial support from the National Sciences and Engineering Research Council as part of a three year scholarship is also greatly appreciated. I would also like to thank Dr. Carolyn Ren for her financial support.

Finally, I am deeply grateful for all the love and support from my family and friends. In particular, I would like to thank my parents, Anne and Scott, my siblings, Colin and Jillian, my wife, Sarah, and her parents, Cathy and Peter.

Dedication

First, I would like to dedicate this to my wife, Sarah, and my son, Benjamin. Second, I would like to dedicate this to my parents. This thesis would not have been possible without their hard work and support.

Table of Contents

List of Figures **xiii**

List of Tables **xviii**

1 Introduction **1**
1.1 Background 1
1.2 Thesis Outline 5

2 Literature Review **8**
2.1 Free-Flow Electrophoresis 8
2.1.1 Introduction 8
2.1.2 Modeling Free-Flow Electrophoresis 8
2.1.3 Separation Modes 16
2.1.4 Practical Considerations 20
2.1.5 Applications 23
2.2 Counterflow Gradient Focusing 26
2.2.1 Introduction 27
2.2.2 Modeling Counterflow Gradient Focusing 28
2.2.3 Separation Modes 29
2.2.4 Applications 33

3 Free-Flow Counterflow Gradient Focusing **35**
3.1 Introduction 35
3.2 Modeling Free-Flow Counterflow Gradient Focusing 36
3.2.1 Focusing Mechanism 36

3.2.2 Counterflow Gradient . . . 38
3.2.3 Position and Residence Time . . . 39
3.2.4 Focal Point . . . 41
3.2.5 Numerical Simulations . . . 42
3.3 Device Design . . . 43
3.4 Experimental Methods . . . 45
3.4.1 Materials . . . 45
3.4.2 Device Fabrication . . . 45
3.4.3 Membrane Fabrication . . . 45
3.4.4 Experimental Setup . . . 47
3.5 Results and Discussion . . . 47
3.5.1 Symmetric Gradient . . . 48
3.5.2 Asymmetric Gradient . . . 48
3.5.3 Protein Fractionation . . . 48
3.6 Future Considerations . . . 49
3.7 Concluding Remarks . . . 50

4 Investigating Peak Dispersion I: Hydrodynamics 52
4.1 Introduction . . . 52
4.2 Modeling Peak Dispersion . . . 53
4.2.1 Focal Position . . . 53
4.2.2 Convection-Diffusion Model . . . 55
4.2.3 Time Dependence . . . 56
4.3 Methodology . . . 57
4.3.1 Method of Moments Approach . . . 57
4.3.2 Numerical Simulation Approach . . . 61
4.3.3 Curve Fitting Approach . . . 61
4.4 Results and Discussion . . . 64
4.4.1 Small Gradient Regime ($G_x \leq 1$) . . . 64
4.4.2 Transition Gradient Regime ($1 \leq G_x \leq 20$) . . . 66
4.4.3 Large Gradient Regime ($G_x > 20$) . . . 66
4.4.4 Comparison to Free-Flow Zone Electrophoresis . . . 67

4.4.5 Future Considerations . . . 67
4.5 Concluding Remarks . . . 69

5 Investigating Peak Dispersion II: Electrodynamics 70
5.1 Introduction . . . 70
5.1.1 Motivation . . . 70
5.2 Modeling Electroosmotic Backflow . . . 71
5.2.1 Velocity Field . . . 72
5.2.2 Focusing Mechanism . . . 73
5.2.3 Centerline Position . . . 74
5.2.4 Solute Dispersion Model . . . 76
5.3 Experimental Section . . . 78
5.3.1 Materials . . . 78
5.3.2 Device Fabrication . . . 79
5.3.3 Electrode Device . . . 79
5.3.4 Experimental Setup . . . 79
5.3.5 Experimental Parameters . . . 80
5.3.6 Peak Measurements . . . 80
5.3.7 Peak Fitting . . . 81
5.3.8 Electric Field Measurement . . . 81
5.4 Results and Discussion . . . 82
5.4.1 Preliminary Experimental Observations . . . 82
5.4.2 Measured Parameters . . . 84
5.4.3 Comparison to Numerical Model . . . 85
5.5 Future Considerations . . . 87
5.5.1 Peak Measurements . . . 87
5.5.2 EOF Suppression . . . 88
5.5.3 Device Design . . . 88
5.5.4 Additional Modeling . . . 89
5.6 Concluding Remarks . . . 89

6 Improving Device Design I: Preparative Scale **90**
6.1 Introduction . . . 90
6.1.1 Motivation . . . 90
6.1.2 Design Overview . . . 92
6.2 Methodology . . . 94
6.2.1 Numerical Simulations . . . 94
6.2.2 Materials . . . 94
6.2.3 Experimental Setup . . . 94
6.2.4 Fabrication Protocols . . . 95
6.2.5 Peak Analysis . . . 95
6.3 Design Guidelines . . . 96
6.3.1 Resistance Criteria . . . 96
6.3.2 Porous Membranes . . . 98
6.3.3 Outlet Channels . . . 101
6.3.4 Side Chambers . . . 102
6.3.5 Electrode Integration . . . 102
6.3.6 Sample Injection . . . 104
6.4 Results and Discussion . . . 106
6.4.1 Device Design . . . 107
6.4.2 Experimental Setup . . . 107
6.4.3 Device Performance . . . 109
6.4.4 Peak Measurements . . . 110
6.5 Future Considerations . . . 112
6.5.1 Experimental Parameters . . . 113
6.5.2 Small Gradient Regime . . . 113
6.5.3 Large Gradient Regime . . . 114
6.6 Concluding Remarks . . . 115

7 Improving Device Design II: Analytical Scale **117**
7.1 Introduction . . . 117
7.1.1 Motivation . . . 117
7.2 Design Guidelines . . . 119

7.2.1 Design Overview . . . 119
7.2.2 Device Dimensions . . . 119
7.2.3 Numerical Simulations . . . 121
7.3 Experimental Section . . . 122
7.3.1 Materials . . . 122
7.3.2 Device Fabrication . . . 122
7.3.3 Experimental Setup . . . 122
7.3.4 Experimental Parameters . . . 123
7.4 Results and Discussion . . . 124
7.4.1 Device Performance . . . 125
7.4.2 Peak Dispersion . . . 125
7.5 Future Considerations . . . 126
7.5.1 Protein Purification at the Isoelectric Point . . . 126
7.6 Concluding Remarks . . . 127

8 Conclusions and Recommendations **129**
8.1 Contributions of this Thesis . . . 129
8.2 Recommendations for Extension of Work . . . 131

References **133**

APPENDICES **151**

A Supporting Information of Peak Dispersion Investigation **152**
A.1 Analytical Model . . . 152
A.2 Equilibrium Conditions . . . 153
A.3 Sample Dilution . . . 154
A.4 Trendlines for Fitting Parameters . . . 155

List of Figures

1.1 A schematic of an FFE separation chamber [19]. 2

1.2 a) Commercial preparative scale FFE device. [23]. b) Analytical scale μFFE device [24] 3

1.3 COMSOL v5.6 simulation of the FF-CGF principle. The fluid velocity in the z- and x-directions is shown to illustrate the counterflow gradient. The electric potential and the resulting electrophoretic velocity for a given solute are also shown. Finally, the concentration of different solutes focusing across the separation chamber is shown, and it is seen that the focal position occurs where the electrophoretic velocity is counterbalanced by the fluid velocity. 5

2.1 a) A schematic of an FFE device with an illustration of the relevant dispersion sources. Note that the coordinate system from the original image was altered to maintain consistency with this study. b) Electrohydrodynamic dispersion due to conductivity differences between the sample (κ_{sample}) and the background buffer (κ_0) [38]. 9

2.2 Common separation modes in FFE: a) FFZE, b) FF-IEF, c) FF-ITP, d) FF-FSE [19]. 17

2.3 Schematic of the preparative scale apparatus that is operated in FF-IEF mode [81]. 21

2.4 a) Standard sample injection. b) Wall-free sample injection [84]. 22

2.5 a) A μFFE device directly coupled to mass spectroscopy (MS) [32]. b) Nanoliquid chromatography (nLC) directly coupled to μFFE with laser induced fluorescence (LIF) detection for multidimensional analysis [109]. 25

2.6 A plot of the electrophoretic velocity gradient, the bulk flow velocity, and a combination of the two. The zero-velocity point occurs where the electrophoretic velocity and bulk flow velocity are counterbalanced [48]. 27

2.7 a) A free-flow CGF device divided into subcompartment using porous membranes [120]. b) A TGF device operated in a scanning mode [125]. c) A DFGF with an electrode array along the bottom of the chamber [126]. 31

3.1 a) An FFE chamber with a counterflow introduced through the sidewalls to produce a velocity gradient in the x-direction, with b) a close-up view of the two sample analytes, blue and red, focused in the velocity gradient according to their electrophoretic velocity. c) A cross-sectional view of the velocity gradient in the FFE chamber. 37

3.2 a) The gradient of across $\langle u \rangle$ the FF-CGF chamber. The total x-velocity $u_{\mathrm{T,i}}$ of two analytes with $u_{\mathrm{EP,b}} = 0.4u_0$ and $u_{\mathrm{EP,r}} = 0.8u_0$. Note the focal point as $u_{\mathrm{T,i}}$ crosses the x-axis. 40

3.3 Numerical simulation of 15 x 35 x 0.1 mm FF-CGF chamber with a 1 mm/s input velocity at sidewalls and -500 V applied across the chamber, distributed uniformly along the length of the chamber. a) Velocity field. b) Electric field (333.33 V/cm). c) z-Velocity field. d) x-Velocity field. 42

3.4 Numerical simulation for the FF-CGF separation of 3 analytes, each with a diffusion coefficient of 10^{-10} m^2/s. Their mobilities were 0, 1×10^{-13}, and 2×10^{-13} s·mol/kg. (a) No applied voltage. (b) A -500 V applied voltage across the chamber for an electric field of 333.33 V/cm. 44

3.5 a) An image of the FF-CGF PDMS chip b) An exploded drawing of the Nafion ion-exchange membrane device. An ionic current (I) and counterflow buffer (Q) go through this device and into the side chamber. c) A close-up drawing of the micro-channels that are used to supply I and Q through the sidewalls of the separation chamber. 46

3.6 From left to right, the separation of Xylene Cyanol FF (blue), BPB (purple), Orange G (orange), and Ponceau S (red) at different applied currents. a) A symmetric velocity gradient and b) its corresponding separation profile at the end of the chamber. c) An asymmetric velocity gradient and d) its corresponding separation profile at the end of the chamber. 47

3.7 a) From left to right, the separation of Hemoglobin (brown-orange), BSA-BPB (blue), and BPB (purple) at different applied currents. b) The corresponding separation profiles at the end of the chamber. 49

4.1 a) A schematic of an FF-CGF device with focal points at different y-positions. b) The focal position along the height direction due to the parabolic profile of the counterflow. 54

4.2 Skew and kurtosis for different G_x values as a function of Pe_{EP}/G_x. COMSOL simulations were used to evaluate $G_x < 10$, and the method of moments formulation was used to $G_x > 10$. 60

4.3 The simulated separation peaks at 95% focused for different Pe_{EP}/G_x values at a) $G_x = 0.1$, b) $G_x = 1$, c) $G_x = 10$, and d) $G_x = 100$. The simulated solute concentration distribution and x-velocity field at $Pe_{EP}/G_x = 20$ for e) $G_x = 0.1$, f) $G_x = 1$, g) $G_x = 10$, and h) $G_x = 100$. 62
4.4 Normalized simulated peaks fitted with the EMG and EV functions for a) $G_x = 0.1$ and b) $G_x = 100$. The cumulative distribution functions for the simulated and fitted peaks at c) $G_x = 0.1$ and d) $G_x = 100$. 63
4.5 Mixing parameter representing the fraction of solute that is in the EMG component for high G_x values. 64
4.6 The EMG fitting parameters for different dimensionless parameters for both a) small gradients ($G_x < 1$) and b) large gradients ($G_x > 20$). 65
4.7 Comparing the optimal peak width in FFZE ($L^* = 1000$) to the peak width of the EMG component at $G_x = 0.1$ and $G_x = 100$. The lateral migration distance is $S^* = Pe_{EP}/G_x$ for $G_x = 0.1$ and $S^* = 2Pe_{EP}/3G_x$ for $G_x = 100$. 68

5.1 a) The cross-section of an FF-CGF chamber along with the focal position of different particles along the height direction. b) The corresponding $x-y$ flow field of the fluid velocity and electrophoretic velocity. 74
5.2 a) The average focal position $\langle x \rangle_f$ and the centerline position x_c for charged particles moving through an FF-CGF chamber. The corresponding solute distributions when b) $G_x = 0.1$ and c) $G_x = 100$. 76
5.3 The separation of Cyt C, Hg, and BSA at various G_x values, and their corresponding peak measurements. 83
5.4 Comparison of the experimental peak measurements to the numerical simulations of the dispersion model assuming $\mu_{EOF} = 3.7 \times 10^{-4}$ cm^2/Vs. From left to right, the peaks represent Cyt C, Hg, and BSA. From bottom to top, the applied currents are a) 300 μA and 400 μA, b) 400 μA and 600 μA, c) 700 μA and 1200 μA, and d) 900 μA and 1900 μA. 86

6.1 An overview of a FF-CGF system for preparative scale applications. 93
6.2 a) Simulation of x-velocity magnitude for different ratios of R_{side} to R_{cham}. Streamlines of charged solutes are shown to illustrate the impact of the counterflow gradient uniformity. b) Simulation of the counterflow gradient uniformity represented as $\nabla\langle u \rangle$ at $z = 0.9L$ relative to $\nabla\langle u \rangle$ at $z = 0.5L$ for a wide range of device dimensions ($L \times W \times H$). 98

6.3 3D COMSOL simulations for an FF-CGF chamber with a symmetric boundary condition along the z-direction. The pressure contours are provided for the top and bottom view. The porous membrane is 30 mm x 5 mm x 3 mm, with an average pore size of 10 μm and a porosity of 35%. 100

6.4 The x-velocity in an FF-CGF chamber and the streamlines of various charged solutes. a) The influence of the hydrodynamic resistance (R_{out}) of the outlet channels on the counterflow gradient. b) The influence of the geometry of an outflow region on the counterflow gradient. 101

6.5 The separation of xylene cyanol FF (blue) and ponceau S (red). As the current increases in the right image, ion concentration polarization (ICP) appears to influence separation due to a stacking effect. Note the location of the porous chambers and electrode chambers. 103

6.6 Simulation of velocity magnitude in a proposed FF-CGF device with a portion of the counterflow from the side channels directed into a waste channel to help flush away the effects of ion concentration polarization (ICP) at the electrode via holes. The black arrows represent the flow into the separation chamber, while the blue arrows represent the flow into the waste channel. 105

6.7 Comparing a low sample slow rate (Q_s) in a), b), and c) to a high sample flow rate (Q_s) in d), e), f), where Q_c is the flow rate on each side of the chamber. An analytical solution for particle transit is presented in a) and d), with the corresponding simulation of solute concentration shown in b) and e). An alternative simulation with a reduced injection width is also shown in c) and f). 106

6.8 A layout of the three relevant layers used in the present FF-CGF device. A PMMA cover containing the side chamber and electrode reservoir is also shown on one side of the device. 108

6.9 An image of the present FF-CGF device mounted on a microscope. 109

6.10 a) The separation of xylene cyanol FF, orange G, and ponceau S with a side flow rate of $Q_c = 40$ μL/min, a top flow rate of $Q_t = 1$ μL/min, and a sample flow rate of $Q_s = 0.2$ μL/min. b) The separation of Cyt C, Hg, and BSA with a side flow rate of $Q_c = 10$ μL/min, a top flow rate of $Q_t = 0.5$ μL/min, and a sample flow rate of $Q_s = 0.1$ μL/min. 110

6.11 Peak measurements for the separation of rhodamine B (RhB) and fluorescein (FL) at different side flow rates (Q_c) and applied currents. In addition, the top flow rate and the sample flow rate for each experiment was a) $Q_t = 0.1$ μL/min and $Q_s = 0.025$ μL/min, b) $Q_t = 0.2$ μL/min and $Q_s = 0.05$ μL/min, c) $Q_t = 0.3$ μL/min and $Q_s = 0.075$ μL/min, and d) $Q_t = 0.4$ μL/min and $Q_s = 0.1$ μL/min. . 111

7.1 A schematic of a potential analytical scale device for FF-CGF. Numerical simulations show a surface plot for the x-velocity magnitude when the height is 50 μm, as well as the streamlines of several charged solutes with mobilities of 2, 2.5, and 3×10^{-4} cm^2/Vs. 120

7.2 Image of the analytical scale FF-CGF device mounted on a fluorescence microscope. 123

7.3 Fluorescent images of BSA-FITC at different applied currents and G_x numbers, and the corresponding peak measurements. 124

7.4 a) An alternative analytical FF-CGF device with the outlet channels replaced by a collection port and two waste ports. Numerical simulations show a surface plot of the x-velocity magnitude, as well as the streamlines of various charged solutes. The electric field is 800 V/cm, and $G_x = 50$ when the diffusion coefficient is $D = 5 \times 10^{-7}$ cm^2/s. A close-up view of two solutes that b) cannot be separated at the collection port and c) can be separated at the collection port when its hydrodynamic resistance (R_h) is increased. 127

List of Tables

2.1 Summary of dimensionless numbers relevant to FFE. 11

5.1 Experimental flow rates and the corresponding G_x values for each protein. 80
5.2 Fitted EMG parameters for the peaks at different G_x values. 85
5.3 Estimates of electric field and electrophoretic mobility. 85

6.1 Fitted EMG parameters and estimated separation conditions assuming $2h = 0.012$ cm, $\mu_{EP} = -3.6 \times 10^{-4}$ cm^2/Vs, and $D = 4.3 \times 10^{-6}$ cm^2/s. 112
6.2 Experimental parameters for an FF-CGF chamber with $G_x = 0.25$, $L = 50$ cm, $2b = 10$ cm, $D = 5 \times 10^{-7}$ cm^2/s, and $u_{EP} = 2.5 \times 10^{-4}$ cm^2/Vs. 114
6.3 Experimental parameters for an FF-CGF chamber with $G_x = 100$, $L = 50$ cm, $2b = 2$ cm, $D = 5 \times 10^{-7}$ cm^2/s, and $u_{EP} = 2.5 \times 10^{-4}$ cm^2/Vs. 115

7.1 Experimental parameters for an FF-CGF chamber with $G_x = 50$, $L = 1$ mm, $2b = 2$ mm, $D = 5 \times 10^{-7}$ cm^2/s, and $u_{EP} = 2.5 \times 10^{-4}$ cm^2/Vs. The 25 parallel side channels have a length of 250 μm and a width of 20 μm. 121

Chapter 1

Introduction

1.1 Background

Proteins are incredible molecules that are essential to the operation of living cells. Each protein is made from a unique amino acid sequence, and this allows them to form highly complex structures with a wide range of properties. For example, they can provide the cell with structural support, or form channels and pumps at the cell wall to enable the passage of different molecules. Additionally, they can serve as enzymes to initiate chemical reactions, or act as molecular machines that generate movement. Furthermore, they can interact with each other to transmit and store information, and generate intricate communication networks that drive cell function [1] [2].

Clearly, the study of proteins can provide a seemingly endless source of scientific exploration. More importantly, proteins are critical to identifying the underlying mechanisms that contribute to disease, and have the potential to play a significant role during diagnosis and treatment [3] [4] [5]. Therefore, life science research and the pharmaceutical industry have dedicated significant resources to the development of instruments that can advance our understanding of proteins [6]. For example, mass spectrometers are commonly used to sequence proteins, and this knowledge can then be related to their function, subcellular location, modifications, and interaction with other proteins [7]. In addition, x-ray crystallography and nuclear magnetic resonance are powerful tools for understanding the three-dimensional structure of proteins, and this information can be used to predict their bioactivity [8] [9]. Finally, surface plasmon resonance is often used to provide a detailed analysis of the binding affinity between two proteins of interest [10].

Before a protein sample is analyzed with the aforementioned techniques, it often needs to be isolated from a complex mixture of cell extract containing thousands of proteins and other contaminants [11]. Since the isolation relies on the unique properties of a protein, the separation process itself can also contribute important information to the analysis [12]. Consequently,

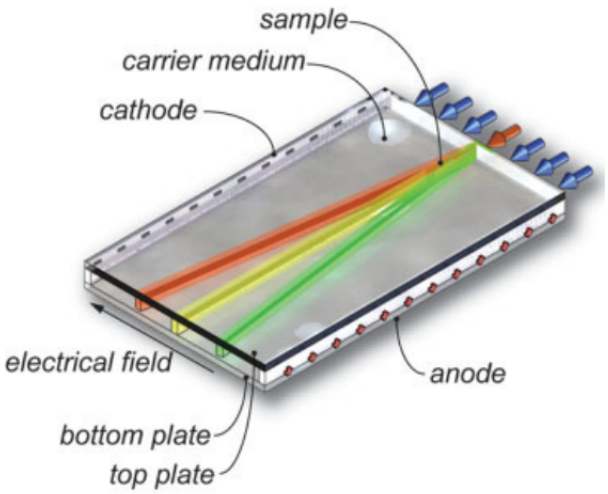


Figure 1.1: A schematic of an FFE separation chamber [19].

protein separation techniques are highly valuable, and this is not to mention the growing biopharmaceutical industry that desires purified protein samples during manufacturing [13]. There are many separation methods that exist, but chromatography and electrophoresis are the two most widely used [14]. In chromatography, a column is packed with media that interacts with proteins as they pass through. The strength of the interaction determines the apparent velocity of the protein, and can depend on a number of properties, including size, ionic charge, hydrophobicity, and binding affinity [15]. As a result, different proteins will elute from the column at different times for high resolution separations. In electrophoresis, proteins migrate through an electric field with a unique velocity that depends on their size, charge, isoelectric point, or some combination of the two [16]. Therefore, the proteins will form distinct bands across a separation medium which usually consists of a gel matrix or a capillary. Due to the diversity of protein structures and properties, the ideal separation mode will depend on the application [17]. Furthermore, it is common to combine several techniques, as this can increase the resolution, and provide an extra dimension of knowledge to the analysis [18].

Traditionally, chromatography and electrophoresis are operated in a batch mode, which means that the entire sample is loaded prior to separation [20]. However, it is also possible to perform electrophoretic separations in a continuous mode if a pressure-driven flow is applied perpendicular to the direction of the electric field [21]. This technique is known as free-flow electrophoresis (FFE), and an illustration of the separation process is shown in Fig. 1.1. In this example, a thin carrier solution flows between parallel plates while electrodes at the sidewalls produce an orthogonal electric field. When a narrow sample stream is injected with the carrier medium,

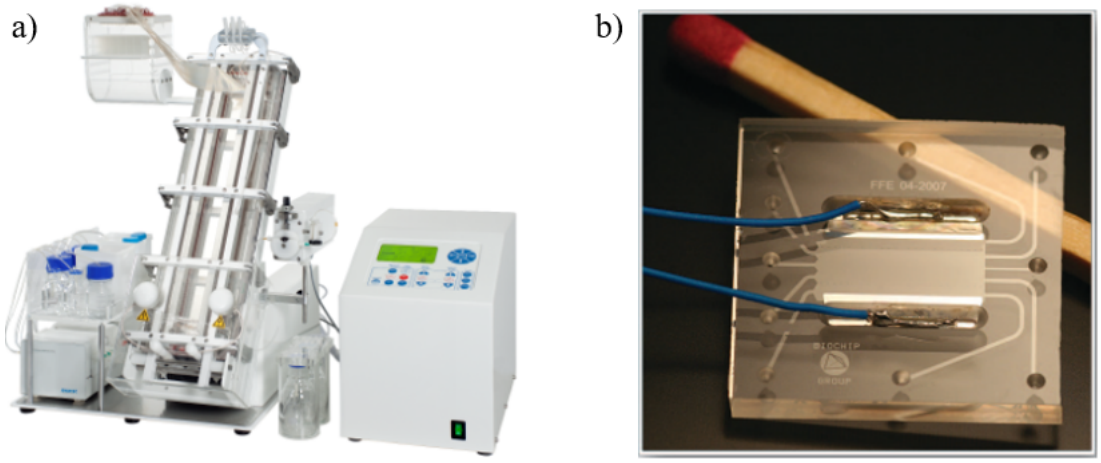


Figure 1.2: a) Commercial preparative scale FFE device. [23]. b) Analytical scale μFFE device [24]

charged solutes migrate laterally according to their electrophoretic velocity and form distinct bands across the separation chamber [19]. Outflow ports located at the end of the chamber then enable the collection of the separated solutes. In addition to proteins, FFE has also been used to separate small molecules, peptides, DNA, membranes, organelles, and cells [22].

FFE was initially developed by Barrollier *et al.* [25] and Hannig [26] around 1960, and since then it has seen significant interest, including several commercial devices (see Fig. 1.2a), and experiments in space to study gravitational effects [27]. Compared to the other separation techniques, FFE has generated excitement for the following reasons: i) several charged species can be separated and collected simultaneously; ii) the continuous operation allows for significantly higher quantities of purified sample when compared to capillary electrophoresis (mg/hr vs. μg/hr); iii) sample collection avoids the tedious extraction process associated with gel electrophoresis; iv) the sample remains in solution which simplifies the potential for further analysis; and v) its gentle separation conditions do not require harsh solvents or detergents, and this helps preserve the bioactivity of enzymes and other sensitive biological species [28] [22] [29].

More recently, the emergence of microfluidic technologies enabled the reduction in separation chamber height, as well as the integration of complex microchannel networks for advanced processing (see Fig. 1.2b). The initial microfluidic devices borrowed fabrication techniques from the microelectronics industry [30], and eventually started to leverage new soft lithography methods for polymer based devices [31]. This led to the classification of miniaturized FFE (μFFE), which has expanded the opportunities in FFE due to the following advantages: i) the microscale flows avoid the possibility of turbulence; ii) the effects of Joule heating are mitigated due to improved heat dissipation and negligible gravitational effects; iii) the smaller volumes enable

the precise handling of minute samples; iv) it can be directly interfaced with mass spectroscopy, and other separation modes for multidimensional analysis [32] [33]; v) integration with online detection systems enables real-time monitoring of dynamic protein interactions [34]; and vi) its portability provides additional versatility [35] [36].

Despite the potential of FFE, there are several technical challenges that have limited its widespread use. Most significantly, the parabolic profile of the pressure-driven flow will distort the separated bands and result in poor resolution [37]. On top of this hydrodynamic broadening effect, molecular diffusion, sample injection width, and electroosmotic flow also contribute to a reduced separation quality [38]. At larger scales, there is the added concern of natural convection, which arises due to Joule heating [39]. Significant efforts have been made to improve the resolution by introducing various focusing techniques. For example, isotachophoresis (ITP) [40] and field step electrophoresis (FSE) [41] rely on steep electric field gradients to concentrate proteins, but this leads to a stacking effect that is not ideal for sample collection. Isoelectric focusing (IEF) has also been introduced to FFE, and this separation mode has achieved the most success [42]. The free-flow isoelectric focusing (FF-IEF) method relies on a pH gradient across the separation chamber, which allows proteins to migrate to a pH where their net charge is zero. This is known as the isoelectric point (pI), and it produces self-sharpening bands that are significantly less impacted by hydrodynamic broadening, molecular diffusion, and sample injection width [43]. With that said, FF-IEF has many practical issues of its own. For example: i) the carrier ampholytes needed to generate the pH gradient are expensive and can contaminate the purified fractions; ii) many proteins approach the pI slowly, which is not ideal due to the continuous nature of FFE; ii) many proteins have poor solubility at the pI, which can harm the separation performance; and iv) the pI produces sharp gradients in conductivity and concentration, and this can also result in broadening effects [44] [45] [46] [22] [47].

The objective of the present work is to introduce an alternative focusing method that addresses some of the issues associated with IEF, and hopefully allows FFE to reach its potential as a powerful protein fractionation tool. The proposed technique relies on a counterflow gradient focusing (CGF) mode, which has been developed extensively in capillary electrophoresis [48], and belongs to a family of equilibrium gradient methods that includes IEF [49] [50]. In free-flow counterflow gradient focusing (FF-CGF), the idea is to generate a velocity gradient in fluid flow across the separation region that opposes electrophoretic migration. Consequently, proteins will focus at a unique position along the gradient where their electrophoretic velocity is counterbalanced by the fluid flow (see Fig. 1.3). Unlike FF-IEF, FF-CGF does not require complex buffer compositions, and it avoids many of the problems associated with the pI. Throughout this work, there will be an emphasis on developing strategies for producing the counterflow gradient, which can be achieved by introducing a pressure-driven flow through the sidewalls of the FFE chamber. Furthermore, the underlying physics of the focusing mechanism will be discussed in

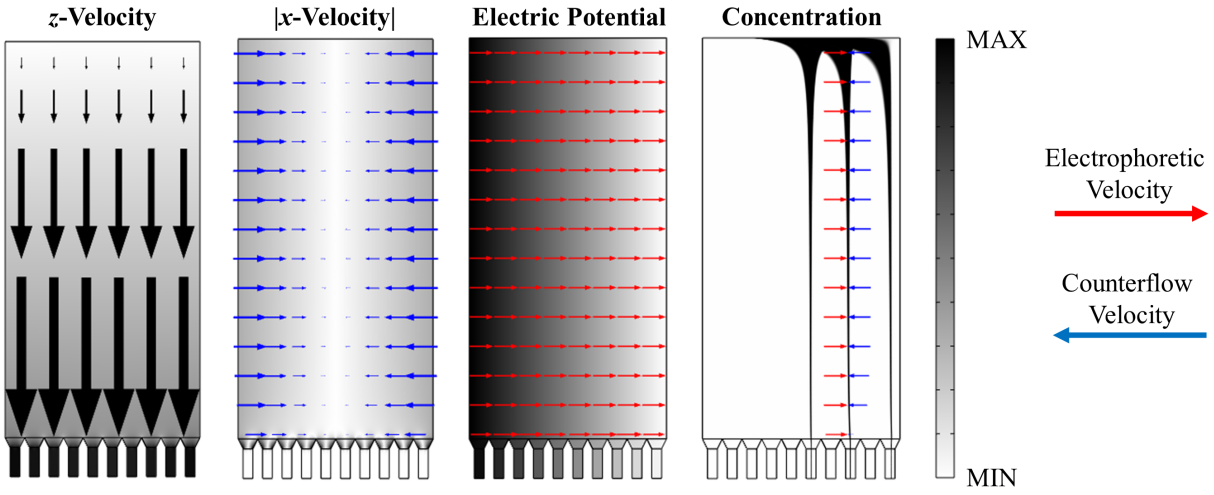


Figure 1.3: COMSOL v5.6 simulation of the FF-CGF principle. The fluid velocity in the z- and x-directions is shown to illustrate the counterflow gradient. The electric potential and the resulting electrophoretic velocity for a given solute are also shown. Finally, the concentration of different solutes focusing across the separation chamber is shown, and it is seen that the focal position occurs where the electrophoretic velocity is counterbalanced by the fluid velocity.

great detail, as this can be used to help predict separation performance, understand the relevant sources of band broadening, and guide the design of future FF-CGF devices. Finally, several FF-CGF devices will be presented to demonstrate the separation of proteins and small molecules in practice.

1.2 Thesis Outline

In Chapter 2, a detailed overview of both FFE and CGF will be provided. For FFE, advances in the area of physical modeling will be discussed, with an emphasis on the many sources of dispersion that persist in FFE systems. Then, a detailed survey of the available FFE separation modes will be provided, including FF-IEF, FF-ITP, and FF-FSE. After that, there will be a brief summary of the practical concerns that need to be carefully considered for successful device operation at the preparative and analytical scale. This will be followed by highlighting some of the most promising applications in FFE. For CGF, a description of the focusing mechanism will be provided, along with strategies for generating the gradient. In addition, a recent dispersion model will be outlined. Finally, examples of existing CGF methods will be demonstrated, before concluding with a discussion on the future directions of the field.

In Chapter 3, the concept of FF-CGF will be introduced and described in detail. First, analytical and numerical models will be derived for predicting the fluid dynamics and solute transport in the system. Then, preliminary guidelines for the practical implementation of FF-CGF will be provided, before an initial prototype is fabricated using standard soft lithography techniques. Experiments will demonstrate the successful separation of small molecules and proteins under different gradient modes, and the results are shown to be consistent with the modeling.

In Chapter 4, the solute dispersion that exists in FF-CGF will be investigated. The key physical parameters to be studied include molecular diffusion, the parabolic velocity profile of the counterflow, and the strength of the gradient. There is an interesting interplay between all of these factors which can be modeled using the convection-diffusion equation, and the results demonstrate a wide variety of solute distributions. When diffusive transport is dominant, the solute peaks resemble a skewed Gaussian curve. When convective transport is dominant, the curve becomes much more asymmetric due to the influence of the parabolic profile, and a highly concentrated region begins to emerge at the centerline position. Although the traditional methods of moments formulation could not be used to model this behaviour, an alternative peak fitting method provided helpful analysis. In the end, the ideal experimental parameters will depend on a number of factors, including throughput, cross-contamination, and Joule heating.

In Chapter 5, the solute dispersion model will be expanded to account for electroosmotic flow (EOF) across an FF-CGF chamber. When EOF is present, the pressure across the chamber will automatically adjust to maintain the fixed inflow rates at the sidewalls. This leads to a pressure-driven backflow, and although it does not influence the focal position, its parabolic velocity profile can influence solute dispersion. During this chapter, preliminary experimental results from the initial prototype will be analyzed and compared to the dispersion models. Interestingly, there is significantly less agreement at higher currents, and this may be due to the effects of Joule heating.

In Chapter 6, the design of the FF-CGF system will be described in great detail, including the influence of porous membranes, separation chamber dimensions, outlet channels, ion-exchange membranes, and sample injection. Furthermore, an alternative fabrication method is used to create a device that is more robust. Along the way, the potential for scaling up the device will be considered, as well as the design requirements for preparative applications. Overall, the device exhibits the potential to produce reliable separations and high quality peak measurements.

In Chapter 7, an alternative FF-CGF will be designed that is specific to analytical scale applications like real-time monitoring and direct interfacing with mass spectroscopy. During this process, the design guidelines from the previous chapter are used to build a device with a uniform counterflow gradient and a better voltage efficiency. Unlike previous designs, this device can be operated at high gradient strengths, and the resulting peaks observed in this regime appear to be consistent with the dispersion models.

In Chapter 8, the key contributions of this work will be summarized, and future directions will be recommended. More specifically, the new FF-CGF method, along with the new dispersion models, device designs, and experimental results will be described. Overall, FF-CGF displays great potential as a protein fractionation tool, but several key limitations need to be addressed, including the dispersion caused by the parabolic profile of the counterflow.

Chapter 2

Literature Review

The subject matter included in Chapter 2.2 is published: **M. Courtney**, C.L. Ren. Counterflow Gradient Electrophoresis for Focusing and Elution. Electrophoresis, 40 (2019), 643-658. [51]

2.1 Free-Flow Electrophoresis

2.1.1 Introduction

The purpose of this section is to provide an overview of the theoretical and technical developments in FFE and μFFE, and discuss some of the challenges that need to be addressed. First, a theoretical background will be provided with an emphasis on the factors that influence separation resolution. Second, the main separation modes will be introduced, including free-flow isoelectric focusing (FF-IEF), isotachophoresis (FF-ITP), and field step electrophoresis (FF-FSE). Third, some considerations for the practical implementation of preparative and analytical scale devices will be discussed. Finally, some of the main applications of FFE and μFFE will be highlighted.

2.1.2 Modeling Free-Flow Electrophoresis

The traditional free-flow zone electrophoresis (FFZE) mode as illustrated in Fig. 1.1 has been the subject of many theoretical studies that focus on predicting the lateral migration distance and the concentration distribution of the solute. While determining the migration distance is straightforward, understanding the solute distribution can be quite complicated as it depends on a number of factors which will be discussed in this section. It is important to understand these factors in order to predict the separation resolution and optimize the experimental parameters.

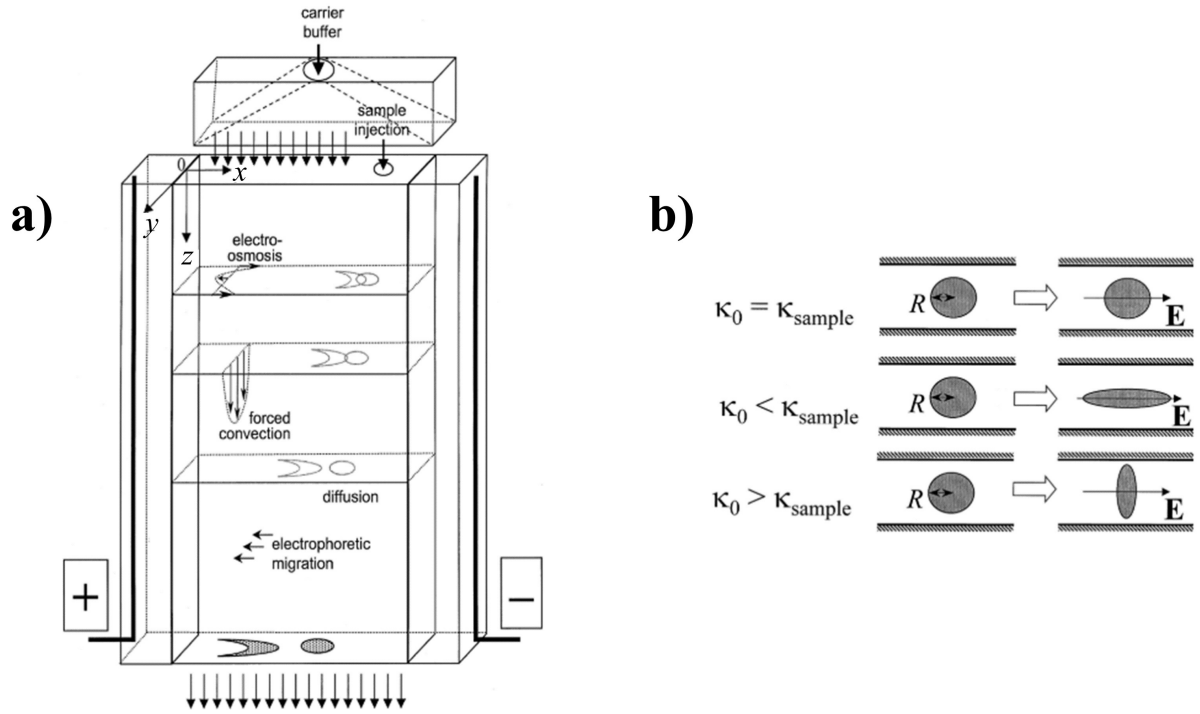


Figure 2.1: a) A schematic of an FFE device with an illustration of the relevant dispersion sources. Note that the coordinate system from the original image was altered to maintain consistency with this study. b) Electrohydrodynamic dispersion due to conductivity differences between the sample (κ_{sample}) and the background buffer (κ_0) [38].

Consider an FFE chamber where the pressure-driven flow moves in the z-direction and the electric field is applied in the x-direction (see Fig. 2.1). The lateral migration distance of a solute in an FFZE separation chamber is similar to a standard electrophoretic device and is given as [35]:

$$x = \mu_{EP} E t \tag{2.1}$$

where μ_{EP} is the electrophoretic velocity of the solute, E is the electric field, and t is the residence time in the separation chamber. The electrophoretic mobility is represented as [35]:

$$\mu_{EP} = \frac{q}{6\pi\eta r} \tag{2.2}$$

where q is the charge, η is viscosity, and r is the ionic radius. Realizing that the residence time can be related to the carrier buffer velocity (U_z) and the separation chamber length (L), the lateral

migration distance can be rewritten as [35]:

$$x = \mu_{\mathrm{EP}} E (L/U_z) \tag{2.3}$$

which allows the position of the solute to be determined based on the experimental parameters.

In general, the concentration distribution of a solute around this position is assumed to be Gaussian, and consequently the variance can be used to predict the width of the separated bands and their resulting resolution. The variance is given as [35]:

$$\sigma^2_{\mathrm{total}} = \sigma^2_{\mathrm{inj}} + \sigma^2_{\mathrm{D}} + \sigma^2_{\mathrm{HD}} + \sigma^2_{\mathrm{ED}} + \sigma^2_{\mathrm{JH}} + \sigma^2_{\mathrm{EHD}} \tag{2.4}$$

where the contributing factors include sample injection width (σ^2_{inj}), molecular diffusion (σ^2_{D}), hydrodynamic dispersion (σ^2_{HD}), electrodynamic dispersion (σ^2_{ED}), Joule heating effects (σ^2_{JH}), and electrohydrodynamic dispersion (σ^2_{EHD}). An illustration of some of these dispersion sources is shown in Fig. 2.1. Clearly, dispersion can have a major influence on the separation performance, and therefore the remainder of this section will focus on providing a theoretical background for the additive terms seen in Eq. 2.4.

Scaling and Dimensionless Numbers

Before describing the factors that influence dispersion in more detail, it is helpful to review some dimensionless numbers to understand the forces that influence mass transport and the resulting solute distribution [39] [52]. A summary of the dimensionless numbers relevant to FFE is provided in Table 2.1. The Reynolds number (Re) describes the competition between inertial and viscous forces, and it is typically low ($\mathrm{Re} < 1$) in FFE because the length scale is defined by the small gap between the parallel plates. This implies operation in the laminar flow regime, which indicates that the fluid flow velocity profile is parabolic, and the resulting solute streams are well-defined. The Péclet number (Pe) describes the competition between convective and diffusive transport, which has important implications in FFE. If convective transport is dominant, the solute distribution will resemble the parabolic shape of the fluid flow, but if diffusive transport is dominant, then there will be a more uniform solute distribution along the height direction. Finally, the Grashof number (Gr) describes the competition between buoyancy and viscous force. Buoyancy is typically negligible for the length scales in microfluidics, but it can become influential at the preparative scale as chambers approach 1 mm in height [28]. In fact, density gradients can be created due to local variations in temperature (σ^2_{JH}), conductivity (σ^2_{EHD}), and solute concentration [39] [38] [29]. It is important to consider these influences because the resulting natural convection will distort the peak shape and reduce the separation resolution. The

Table 2.1: Summary of dimensionless numbers relevant to FFE.

Dimensionless Number	Description	Equation
Reynolds (Re)	inertia/viscous	$\frac{\rho U d}{\eta}$
Péclet (Pe)	convective/diffusive	$\frac{U d}{D}$
Grashof (Gr)	buoyancy/viscous	$\frac{\rho g \Delta \rho d^3}{\eta^2}$

following equation has been used when predicting the significance of natural convection during FFE [46]:

$$\frac{\mathrm{Gr}}{\mathrm{Re}^2} = \frac{g \Delta \rho d}{\rho U^2} \tag{2.5}$$

where g is the gravitational acceleration, $\Delta\rho$ is the density gradient, d is the height of the chamber, ρ is the buffer density, and U is the buffer velocity. If Eq. 2.5 is much less than 1, then natural convection is negligible [46].

Method of Moments Formulation

There have been several theoretical models developed by Dutta using a method of moments approach to develop a closed-form expression for solute dispersion in FFZE under different experimental conditions [53] [54] [43]. Assuming laminar flow, the velocity profile of the pressure-driven flow between parallel plates can be written as [53]:

$$U_z = \frac{3}{2}\langle U_z \rangle \left(1 - \frac{4y^2}{d^2}\right) \tag{2.6}$$

where $\langle U_z \rangle$ is the area-averaged velocity of the carrier solution. This expression can then be used in the convection-diffusion equation to describe the mass transport of the solute in an FFZE chamber [53]:

$$\mu_{\mathrm{E}} E \frac{\partial C}{\partial x} + \frac{3}{2}\langle U_z \rangle \left(1 - \frac{4y^2}{d^2}\right) \frac{\partial C}{\partial z} = D\left(\frac{\partial^2 C}{\partial x^2} + \frac{\partial^2 C}{\partial y^2} + \frac{\partial^2 C}{\partial z^2}\right) \tag{2.7}$$

where C represents the concentration of the solute and D is the diffusion coefficient. Note the inclusion of the electrokinetic velocity term as well, which accounts for both the electrophoretic

and electroosmotic velocity ($\mu_E = \mu_{EP} + \mu_{EO}$). If C_0 represents the sample concentration at the inlet, then Eq. 2.7 can be written in dimensionless form as follows [53]:

$$Pe_x \frac{\partial C^*}{\partial x^*} + \frac{3}{2} Pe_z \left(1 - 4y^{*^2}\right) \frac{\partial C^*}{\partial z^*} = \frac{\partial^2 C^*}{\partial x^{*^2}} + \frac{\partial^2 C^*}{\partial y^{*^2}} + \frac{\partial^2 C^*}{\partial z^{*^2}} \tag{2.8}$$

where $x^* = x/d$, $y^* = y/d$, $z^* = z/d$, and $C* = C/C_0$. Also note that $Pe_x = \mu_E E d/D$ and $Pe_z = \langle U_z \rangle d/D$ represent the Péclet numbers in the x and z-directions. Next, the statistical moments of the solute distribution can be determined when the nth moment of C^* in the $x-y$ plane can be written as [53]:

$$m_n = \int_{-1/2}^{1/2} \int_{-\infty}^{\infty} x^{*^n} C^* \, dx^* \, dy^* \tag{2.9}$$

By multiplying Eq. 2.8 by x^{*^n} and then integrating along the x^* and y^*-coordinates, it can be written in terms of the nth moment. The differential equation is now simplified and can be solved by applying the appropriate boundary conditions. The average position of the solute can then be represented by m_1, while the normalized spatial variance of the solute can be represented by $\sigma^2 = m_2/m_0 - m_1^2/m_0^2$ [53]. As will be seen in the following discussion, this method of moments formulation has been useful for understanding solute variance for a number of factors seen in Eq. 2.4. Moreover, this theoretical work was in agreement with an experimental study on sample stream bandwidth conducted by Fonslow and Bowser [37] [53].

Sample Injection Width

The sample injection width is a factor that can influence the width of the sample stream in FFZE. This makes sense according to Eq. 2.3 because the lateral migration distance is relative to its starting position, which can vary significantly if the injection width is large. Theoretically, the variance for the sample injection width has been derived as [53]:

$$\sigma_{inj}^2 = \frac{\delta^2}{12} \tag{2.10}$$

where δ represents the sample injection width. In general, sample injection width should be as narrow as possible to minimize its contribution to dispersion, although this will reduce sample throughput and is limited by the device fabrication constraints.

Molecular Diffusion

Molecular diffusion occurring in the direction orthogonal to the buffer flow can be a major contributor to solute dispersion in FFZE. Theoretically, the peak variance due to molecular diffusion

is written as [53]:

$$\sigma_{\mathrm{D}}^2 = \frac{2DL}{\langle U_z \rangle} \tag{2.11}$$

Note that this term is related to the residence time $t = L/\langle U_z \rangle$, indicating that the solute distribution will continue to disperse as it migrates through the separation chamber.

Hydrodynamic Dispersion

Hydrodynamic dispersion is often the most influential source of peak broadening in FFZE. It is related to the parabolic profile of the buffer velocity, as solute molecules located closer to the top and bottom walls of the separation chamber will have a slower velocity than a solute molecule located at the centerline (see Eq. 2.6) [53]. Therefore, the residence time of the solute molecules will depend upon their position along the height direction, and this will affect their lateral migration distance (Eq. 2.1) and the resulting peak width (see Fig. 2.1a). Theoretically, this variance can be written as [53]:

$$\sigma_{\mathrm{HD}}^2 = \frac{S^2 d^2 \langle U_z \rangle}{105DL} \tag{2.12}$$

where $S = \mu_{\mathrm{E}} EL/\langle U_z \rangle$ represents the lateral migration distance. Note the presence of the diffusion coefficient, which is related to the interplay between the parabolic velocity profile and the molecular diffusion along the height direction. The derivation of Eq. 2.12 assumes that the residence time is much greater than the characteristic diffusion time across the gap between parallel plates, and therefore is only valid when the solute distribution resembles a Gaussian distribution [53]. This is not necessarily the case at the preparative scale due to the larger Péclet numbers, as solute distributions in the $x-y$ plane have been noted as having a crescent shape that matches the parabolic velocity profile. The method of moments formulation becomes more complicated in this scenario, although there have been some alternative approaches to modeling this behaviour [55].

Electrodynamic Dispersion

Electrodynamic dispersion is another influential source of peak broadening in FFZE that can produce the aforementioned crescent shape. It is related to the electroosmotic flow (EOF) across the chamber, which is generated due to the electric double layer at the chamber walls [56]. Although EOF has a relatively flat velocity profile, it gets blocked or partially blocked at the sidewalls, and produces a pressure-driven backflow (see Fig. 2.1a) [39] [38]. The resulting velocity profile is

also parabolic in nature, and it alters the lateral velocity in Eq. 2.7 to [54]:

$$U_x = \mu_{\mathrm{E}} E \left(1 - \frac{3\alpha}{2}\left(1 - \frac{4y^2}{d^2}\right)\right) \tag{2.13}$$

where α represents the fraction of electrokinetic flow that is blocked at the sidewalls. Note that α also alters the lateral migration distance to $S = \mu_{\mathrm{E}} E(1-\alpha)L/\langle U_z \rangle$. Interestingly, when updating the method of moments formulation with Eq. 2.13, it simply alters the hydrodynamic dispersion term as follows [54]:

$$\sigma^2_{\mathrm{HD}} = \frac{S^2 d^2 \langle U_z \rangle}{105(1-\alpha)^2 DL} \tag{2.14}$$

and there is no additional term for σ^2_{ED} in Eq. 2.4. This result suggests that there is an interplay between the parabolic velocity in both the x and z-directions which can alter the residence time and the resulting dispersion. If the competing parabolic profiles produce a counteracting crescent distortion, then the σ^2_{HD} term is reduced, but if the crescent distortions are in the same direction, then σ^2_{HD} term is increased. Consequently, measuring EOF and the resulting backflow becomes important for estimating the solute distribution in FFZE [54].

Joule Heating Induced Dispersion

Joule heating induced dispersion is a common issue in FFE that is difficult to model because it can have an influence on a number of experimental parameters including electrophoretic mobility, molecular diffusion, ionic current, buffer viscosity, and local density gradients. Fortunately, Dutta has modeled most of the relevant factors at the analytical scale using a method of moments formulation. The temperature difference along the height direction from the centre of the chamber to the wall can be written as [57]:

$$\Delta T = \frac{\lambda_0 I_0 E^2 d^2}{k} \tag{2.15}$$

where I_0 is the ion concentration in the buffer, and λ_0 and k are the ionic and thermal conductivity of the buffer at $T_0 = 25^{\circ}\mathrm{C}$ (wall temperature), respectively. The temperature, T, along the height of the chamber is then approximated as a parabolic profile [57]:

$$\frac{T - T_0}{\Delta T} = \frac{1 - 4{y^*}^2}{8\cos(\sqrt{\alpha_T \Delta T}/2)} + O(\Delta T^2) \tag{2.16}$$

where $\alpha_T = 0.025\ \mathrm{K}^{-1}$ is the thermal expansion coefficient (for water). The convection-diffusion equation seen in Eq. 2.7 can then be rewritten as [57]:

$$\mu^0_{\mathrm{EP}} \frac{\eta_0}{\eta} E \frac{\partial C}{\partial x} + \mu^0_{\mathrm{EO}} E \frac{\partial C}{\partial x} + U_z \frac{\partial C}{\partial z} = D \frac{\partial^2 C}{\partial x^2} + \frac{\partial}{\partial y}\left(D \frac{\partial C}{\partial y}\right) + D \frac{\partial^2 C}{\partial z^2} \tag{2.17}$$

where η_0 is the viscosity of water at $T_0 = 25^{\circ}\mathrm{C}$ and η is the temperature dependent viscosity that varies along the height direction. Note that D is temperature dependent along the y direction in this formulation, as is U_z due to its dependence on viscosity. Also note how the electrophoretic velocity is dependent on viscosity, whereas the electroosmotic velocity remains constant when the Debye layer is much smaller than the chamber height [57]. Solving Eq. 2.17 provides a closed-form expression for σ^2_{JH} that is related to the temperature dependence of molecular diffusion and hydrodynamic dispersion. While there is an increase in molecular diffusion in the x-direction, interestingly, Joule heating reduces hydrodynamic dispersion because the increased diffusion along the height direction lessens the impact of the parabolic flow profile [57]. Although this implies that Joule heating can reduce dispersion when σ^2_{HD} is the dominant term, it should be interpreted with caution as Eq. 2.17 does not account for natural convection which may arise due to Joule heating at the preparative scale. In this scenario, the Grashof number can be written in terms of temperature as [52]:

$$\mathrm{Gr} = \frac{g\rho^2\alpha_T\Delta T d^3}{\eta^2} \tag{2.18}$$

where α_T is the thermal expansion coefficient, and this equation can be used in Eq. 2.5 to predict the influence of natural convection. It should be noted that there have been additional models for studying temperature effects in FFE [58] [59] [60] .

Electrohydrodynamic Dispersion

Electrohydrodynamic dispersion is another factor in FFE that was originally modeled by Rhodes *et al.* [61]. It is related to conductivity gradients that may exist between the sample stream and the background electrolyte, as this distorts the local electric field and produces a shear stress on the liquid (see Fig. 2.1b). If the sample conductivity is greater than that of the buffer, then the solute distribution will spread in the direction parallel to the electric field [38]. On the other hand, if the buffer conductivity is greater, then the solute distribution spreads perpendicular to the electric field [38]. In general, this form of broadening is avoided in FFZE provided that the sample is prepared with a conductivity that is similar to the separation buffer [39]. However, it may occur in other separation modes such as FF-IEF, where the sample stream is concentrated by the focusing mechanism [41].

Other Dispersion Sources

Another form of dispersion that was frequently addressed in the older preparative scale devices is sedimentation due to high concentrations of solute [38]. Once again, a modified Grashof

number can be used to estimate the influence of the density gradient due to local variations in concentration [52]:

$$\mathrm{Gr} = \frac{g\rho^2 \alpha_C \Delta C d^3}{\eta^2} \tag{2.19}$$

where α_C is the density coefficient for species C. Typically, sedimentation becomes an issue when the chamber height is in the millimeter range and the solute concentration is greater than 7 g/L [38]. In addition, high protein concentrations can lead to interactions with other proteins, and this can also reduce the separation resolution [62]. More recently, the method of moments formulation by Dutta has provided additional sources of dispersion for consideration. For one, there is an orientation factor that accounts for the fact that the sample stream is deflected at an angle in to the x-axis in FFZE [53]. Another interesting study investigated the dispersion due to gradients in buffer velocity across the width of the chamber due to unwanted variations in channel geometry [63].

Optimizing Resolution and Bandwidth

As mentioned previously, having the ability to estimate the location (x_i) and width (σ_i) of the ith solute distribution is helpful for predicting the separation resolution, which can be written as follows for Gaussian peaks [37]:

$$R_s = \frac{x_1 - x_2}{(\sigma_1 + \sigma_2)/2} \tag{2.20}$$

At the analytical scale, the peak width is mostly influenced by molecular diffusion and hydrodynamic dispersion [53]. Typically, one term is more dominant than the other, and there exists an ideal buffer velocity where the sum of these two terms is minimized [54]:

$$U_{opt} = \sqrt{105\left(2DL + \frac{2S^2D}{L}\right)\frac{DL(1-\alpha)^2}{S^2d^2}} \tag{2.21}$$

2.1.3 Separation Modes

Until this point the discussion on FFE has been mainly focused on FFZE (see Fig. 2.2a), and it was seen that this technique has many sources of dispersion that can significantly hinder the separation resolution. Therefore, advanced separation modes are often employed in FFE to improve the performance, and these methods often leverage some kind of focusing mechanism to counteract dispersion.

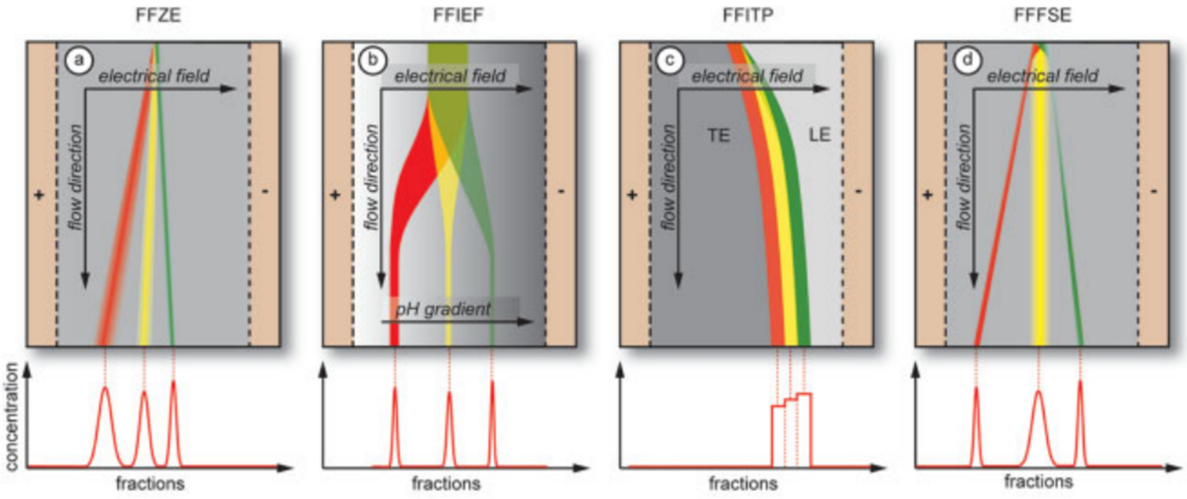


Figure 2.2: Common separation modes in FFE: a) FFZE, b) FF-IEF, c) FF-ITP, d) FF-FSE [19].

Free-Flow Isoelectric Focusing

Free-flow isoelectric focusing (FF-IEF) is a separation mode that relies on a pH gradient across the separation region (see Fig. 2.2b). In general, proteins will migrate across this gradient until they reach a position where their net charge is zero, and this is known as the isoelectric point (pI) [46]. In terms of solute dispersion, FF-IEF has several advantages over FFZE. Most notably, diffusing molecules will return to their pI for a self-sharpening mechanism that improves resolution and sensitivity [50]. Furthermore, analytes will migrate to their pI regardless of their initial starting position, and this provides more flexibility with the sample injection width [50]. Finally, the focal position is unaffected by the parabolic velocity profile of the carrier medium, and therefore FF-IEF will not suffer from hydrodynamic broadening as long as the solute has sufficient time to focus [42]. With that said, electrodynamic dispersion is still an issue if EOF is not suppressed, and this phenomenon has also been modeled by Dutta [43].

Despite the promise of FF-IEF, there are many practical concerns that limit its applicability. First, the carrier ampholytes needed to generate the pH gradient are expensive, and they can contaminate the purified samples [47]. The latter issue is especially problematic when using UV detection or coupling FFE to mass spectroscopy, as the carrier ampholytes can interfere with the signal [64]. Furthermore, carrier ampholytes can bind to proteins in a manner that is difficult to reverse, and likely alters its properties [47]. Second, some proteins experience long focusing times because their net charge around the pI is low, and this is not ideal for the continuous nature of FFE [44]. Compounding this problem is the fact that carrier ampholytes also take time to

generate the pH gradient [41]. Third, the benefits of the focusing mechanism can be negated by the high concentrations that it generates, as this can lead to sedimentation in free solution [45]. Moreover, the neutral charge at the pI can create local gradients in conductivity and temperature, and this causes eletrohydrodyanamic dispersion and natural convection [45] [65]. Fourth, many proteins have poor solubility at the pI due to their neutral charge at that point, and this can also result in unwanted dispersion [42]. Finally, FF-IEF is often limited to the separation of proteins and peptides, as other potential solutes will not necessarily have a well-defined pI [48].

In recent decades, there have been efforts to mitigate the drawbacks of FF-IEF, and it has become the most popular FFE mode due to its high resolution. For example, the separation medium has been optimized to generate a gradient over a wide pH range, speed up the focusing, improve the solubility of proteins, and limit their interactions with harmful carrier ampholytes [42] [47]. With that said, the focusing times still require several minutes, and the initial sample concentration must be low to avoid precipitation and steep local gradients [42] [41] [22]. Combined, both of these factors limit the throughput. In another example, Bier developed an apparatus that continuously recycled the sample through the separation chamber, and this was designed to address the slow focusing and Joule heating issues in FF-IEF [45]. Interestingly, the residence time was significantly reduced due to the high flow velocities and a short chamber length, and this helped prevent eletrohydrodyanamic dispersion and natural convection at high electric fields (see Eq. 2.5) [65]. Although this technique was operated in batch mode, it could achieve preparative scale quantities, and had some commercial success.

Finally, FF-IEF has also been employed at the analytical scale, and the reduced length scales enabled faster separations and eliminated the concern of natural convection. For example, the initial microfluidic devices by Xu *et al.* [66] and Kohlheyer *et al.* [67] focused samples within seconds and provided high resolution separations. After that, there were some interesting new chamber geometries proposed, including a cascaded design with steep and shallow gradient regions to improve resolution [68], as well as a triangular design that aimed to increase throughput [69]. In addition, there have been some alternative techniques proposed for generating a pH gradient, including the immobilization of carrier ampholytes to a supporting media [70], as well as a bipolar membrane strategy that offered speed and versatility [71].

Free-Flow Isotachophoresis

Free-flow Isotachophoresis (FF-ITP) is another powerful focusing technique that has been used in FFE (see Fig. 2.2c). For this mode, the separation region consists of a leading electrolyte (LE) zone with a high mobility, and a trailing electrolyte (TE) zone with a low mobility. This generates an electric field gradient, and forces solutes with an intermediate mobility to stack at the interface [40]. Like FF-IEF, this produces a self-sharpening mechanism that can reach high

concentrations, but it requires long focusing times to separate solutes with a similar mobility. One solution to reach a faster steady state involved introducing a counterflow across the chamber [44], and this was improved further by operation in a recycling mode [65]. However, it remains challenging to isolate solutes that are stacked side-by-side, and it is often difficult to find a spacer that can help increase the separation distance [72]. Nonetheless, FF-ITP has been used for some preparative scale applications [22]. More recently, this mode has also been employed at the analytical scale, and the microfluidic device was able to focus the target analyte within seconds [73]. Interestingly, the concentrated zone did not contain any additional buffer additives, and this enables direct coupling with mass spectroscopy [72].

Free-Flow Field Step Electrophoresis

Free-flow field step electrophoresis (FF-FSE) is a practical method for increasing the concentration of solutes in FFE (see Fig. 2.2d) [22]. In this technique, the separation region consists of multiple buffers with different conductivities. The sample stream begins in the low conductivity buffer, and it will migrate with a high electrophoretic velocity until it reaches the high conductivity buffer and decelerates [31]. As a result, the solute will focus at this electric field step, and this has been used in some preparative scale applications to increase the concentration of a target analyte [62]. However, there does not appear to be many examples where FF-FSE is used to isolate multiple solutes from complex mixtures because there tends to be a stacking effect at the buffer interface. That said, there have been a few FF-FSE devices reported at the analytical scale [19], and one technique implemented a linear conductivity gradient across the separation region in an effort to focus multiple analytes at different locations [74].

Interval Free-Flow Zone Electrophoresis

Interval FFZE is another operation mode that has been used at the preparative scale, and its main purpose is to eliminate the hydrodynamic dispersion that is prominent in FFZE [75]. In this technique, the first step is to load the sample stream along the length of the chamber. Then, the pressure-driven flow is stopped, and an electric field is applied to allow the charged solutes to migrate across the separation region with a velocity that is determined by their mobility. Finally, the electric field is removed, and the pressure-driven flow is reintroduced to collect the separation fractions at the outlet. Altogether, interval FFZE provides a higher separation resolution than traditional FFZE because the parabolic flow profile no longer influences later migration [76]. Although this method is not operated continuously, the commercial device has demonstrated protein fractionation in large quantities, and serves as a versatile alternative to the popular FF-IEF [77].

Other Modes

There have also been some new FFE modes proposed in recent years that deserve mentioning. First, there is a technique that relies on a temperature gradient to alter the conductivity across the separation region. Consequently, the electrophoretic velocity will vary along the gradient, and this allows analytes to focus at a position where it is counterbalanced by EOF [78]. This mode is known as free-flow temperature gradient focusing (FF-TGF), and more information on the mechanism can be found in Section 2.2. Second, there is a technique that leverages the ion concentration polarization (ICP) effect that emerges when a cation selective membrane (Nafion) is used to isolate an electrode compartment from the separation region [79]. In ICP, there are enriched and depleted ion zones due to the selectivity of the membrane, and this generates a conductivity gradient across the separation region. As a result, this free-flow ion concentration polarization focusing (FF-ICPF) mode is similar to FF-TGF, although the gradient tends to be steeper and localized at the edge of the depletion region. Finally, a technique known as free-flow affinity electrophoresis has been demonstrated, and it consists of high mobility ligands that bind to target peptides and increases the separation distance relative to other solutes for improved resolution [80].

2.1.4 Practical Considerations

At this point, it is clear that FFE is a complicated system that depends on a number of factors, and it is easy for the separation resolution to deteriorate during operation. For example, it can be difficult to mitigate the effects of electrolysis, stabilize the flow, control temperature, collect the sample fractions, and optimize the contents of the buffer solution. Consequently, FFE has seen significant development in recent decades in order to reduce the technology to practice. This is true at both the preparative scale and the analytical scale, and therefore this section will provide a brief overview of the practical challenges that deserve consideration when designing and operating an FFE system.

Preparative Scale

The development of preparative scale FFE began in 1960 [26], and by the late 1990s robust experimental protocols had been established for commercial purposes [42]. A schematic of the entire apparatus can be seen in Fig. 2.3, and it can be used for a number of different operation modes [29]. The dimensions of this device are typically 50 cm $\times$ 10 cm $\times$ 0.4 mm [81], and this is achieved by clamping a spacer between two plastic plates [28]. Note that the chamber height defined by the spacer can vary between 0.05 and 1 mm, and is chosen by considering

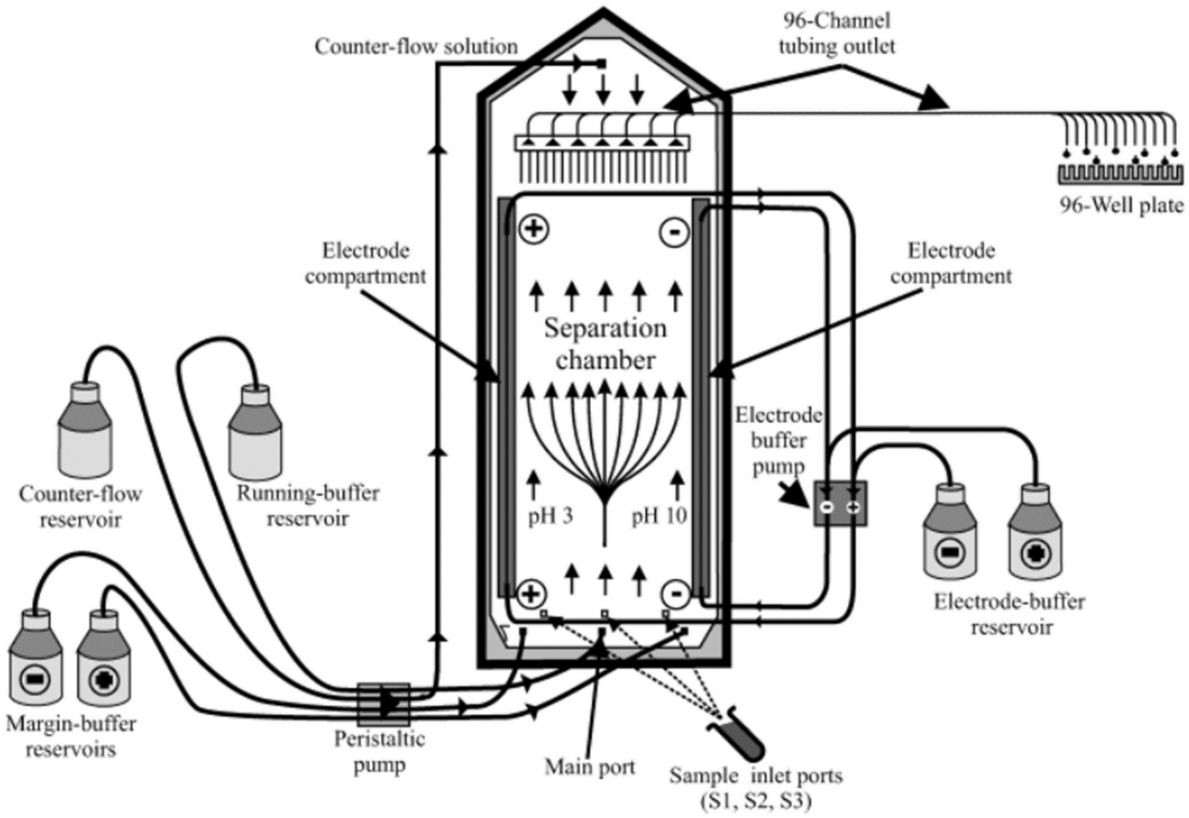


Figure 2.3: Schematic of the preparative scale apparatus that is operated in FF-IEF mode [81].

factors like sample throughput and dispersion [39]. At this scale, peristaltic pumps are used for the sample and separation buffer because they can process large volumes. For the electric field, electrode compartments are located on each side of the chamber, and they are isolated from the separation region using membranes that are ion conductive but impermeable to fluid flow. These membranes are critical to the design because they help prevent electrolysis products such as bubbles and pH changes from entering the separation region. For additional measure, the electrode compartments are constantly replenished with fresh buffer solution, and margin buffers with high ionic concentrations flow along the sides of the separation region to suppress pH changes at the membrane [29]. Note that these margin buffers can also reduce the effects of ion concentration polarization (ICP) [82], which is inherent to most ion exchange membranes because of their charge selectivity [59].

There are many additional strategies that can improve device performance. For example, pulsations from the peristaltic pump often affect the flow stability, and these can be reduced with a

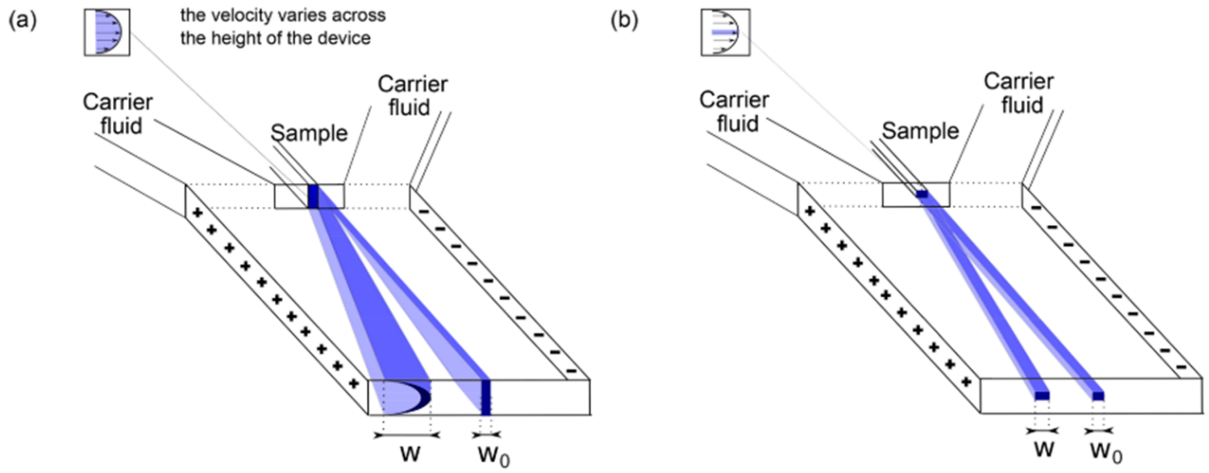


Figure 2.4: a) Standard sample injection. b) Wall-free sample injection [84].

gas cushion injector [83]. Second, the device should be mounted on cooling plates to limit the effects of Joule heating, as this has been shown to reduce the temperature within the separation region to 11.5℃ [29]. Furthermore, the entire device can be tilted for an upward flow that limits the effects of potential density gradients [82]. Third, it is possible to restrict the sample input along the height direction for a wall-free injection, and this helps prevent dispersion caused by the parabolic flow profile and the temperature gradient (see Fig. 2.4) [29] [84]. Fourth, various additives can be included in the buffer solution to limit protein interactions, improve solubility, or alter the viscosity [85]. Most importantly, dynamic wall coatings such as hydroxypropylmethylcellulose (HPMC) are used to suppress EOF and minimize electrodynamic dispersion [29]. Finally, sample collection through different outlet tubings can be challenging due to variations in viscosity, bubble formation, and undesired pressure fluctuations, and this can affect the fluid flow upstream [29] [86]. This problem can be solved with a multichannel peristaltic pump that sets a fixed outflow rate through each tubing [87] [88], and more recently a negative pressure collector has also been explored [86]. In the commercial instruments, a counterflow at the end of the separation region is used to make the outflow more uniform (see Fig. 2.3), and this strategy provides better long-term stability than the peristaltic pumps [89]. Note that this counterflow method also provides the option of altering the outflow media to help prepare the separated fractions for further processing [29].

Analytical Scale

Analytical scale μFFE devices use much smaller dimensions because throughput is less important, and the chamber height typically ranges from 10 to 100 μm. At these length scales, the current is reduced, there is better heat dissipation, and issues related to density gradients and flow stability become much less significant (see Table 2.1) [36]. Moreover, the smaller volumes enable the use of syringe pumps which tend to experience less pulsations. With that said, working at this scale introduces new challenges that are mostly related to device fabrication and electrode integration. In terms of fabrication, devices made from glass offer robust performance due to their rigidity and stable surface properties, but etching the channels and bonding the substrates can be complicated and expensive [90] [36]. As an alternative, polydimethylsiloxane (PDMS) devices made from standard soft lithography techniques are commonly used for prototyping, but they have poor structural integrity and inconsistent EOF behaviour [91] [21]. More recently, strategies involving the lamination of a double-sided spacer tape between two polymethylmethacyrlate (PMMA) substrates have been employed, as this material combines the benefits of glass with the convenience of PDMS [92] [36] [88]. Similarly, devices made from injection molding [93] and 3D printed materials [94] have also been explored. However, one drawback of these hard plastic substrates is a reduction in fabrication quality at the microscale [95].

In μFFE devices, the need to integrate electrodes and isolate their electrolysis products from the separation region becomes much more challenging (see Fig. 1.2b). The initial strategy was to use microchannels to connect electrode chambers to the separation chamber, but their high resistance limited the electric field across the separation region [30]. Since then, numerous alternatives have been proposed to improve voltage efficiency, and they have been reviewed extensively [19] [35] [21] [36]. Briefly, one successful technique involved the polymerization of ion permeable gel membranes along the sides of the separation region, although there were some concerns related to their long-term mechanical stability [96]. Another method removed the membrane, and used deep electrode channels adjacent to the separation region to purge the electrolysis products without disrupting the separation [90]. Since then, a similar technique involving partition bars has been proposed to reduce the need for precise flow control [91]. More recently, commercial track-etched porous membranes have been used to isolate the electrode compartments, and this is a practical option that resembles the preparative scale FFE devices [31].

2.1.5 Applications

Although this work focuses mainly on developments in FFE related to physical modeling and technical design, it is important to review some of the promising applications in this area. In general, FFE is often used for proteomics research, and is especially useful for sample prepara-

tion prior to mass spectroscopy. Therefore, it is helpful to briefly define proteomics and mass spectroscopy before this section begins. Proteomics involves the pursuit of understanding complex biological networks at the molecular level, and it includes the study of protein-protein interactions, protein modifications, protein function, and protein location within cells [7]. Mass spectroscopy (MS) is a tool that is critical to proteomics research due to its ability to identify and quantify proteins [97]. In general, MS works by ionizing the peptide fragments that make up a protein, and then separating them in an electric field according to their charge to mass ratio. After that, the resulting spectral information can be related to the amino acid sequence of a protein [98].

Protein Purification

FFE has always exhibited the potential for high throughput protein purification due to its continuous nature, but the prominent dispersion sources significantly hindered its separation resolution. This is especially true for FFZE, and by the 1970s other techniques like chromatography became the separation method of choice [99]. However, FFE remained useful for samples that were prone to irreversible adsorption, sedimentation, or denaturation [99]. In the last few decades, the commercial devices have been used for two noteworthy applications that are related to sample preparation prior to MS [100]. First, FFE is used to isolate organelles such as mitochondria and Golgi membranes, and then MS analyzes their proteins [101]. The FFE step is helpful because it gives information about the location of the proteins within the cell. FFZE is often used for this application due to its gentle separation conditions, and dispersion is likely limited due to the low diffusion coefficients of the organelles. Second, FF-IEF is used for the high resolution separation of complex samples prior to MS, as this step can help remove abundant proteins for improved sensitivity, and provide information about the pI of the protein [102] [103]. More recently, an interesting FF-IEF application has been proposed to help isolate and characterize the charge variants of monoclonal antibodies [104] [105]. This information is of interest to the pharmaceutical industry during manufacturing, and FF-IEF is the preferred method because the traditional capillary isoelectric focusing (cIEF) has difficulty collecting sufficient quantities of the separated protein prior to MS.

Direct Coupling to Mass Spectroscopy

Since FFE is frequently used for sample preparation prior to MS, there have been efforts to improve this process by directly coupling these instruments at the analytical scale (see Fig. 2.5a). In an early example, FFE was used as an intermediate step between cIEF and MS, and its purpose was to remove the carrier ampholytes following cIEF because they are harmful to the MS signal

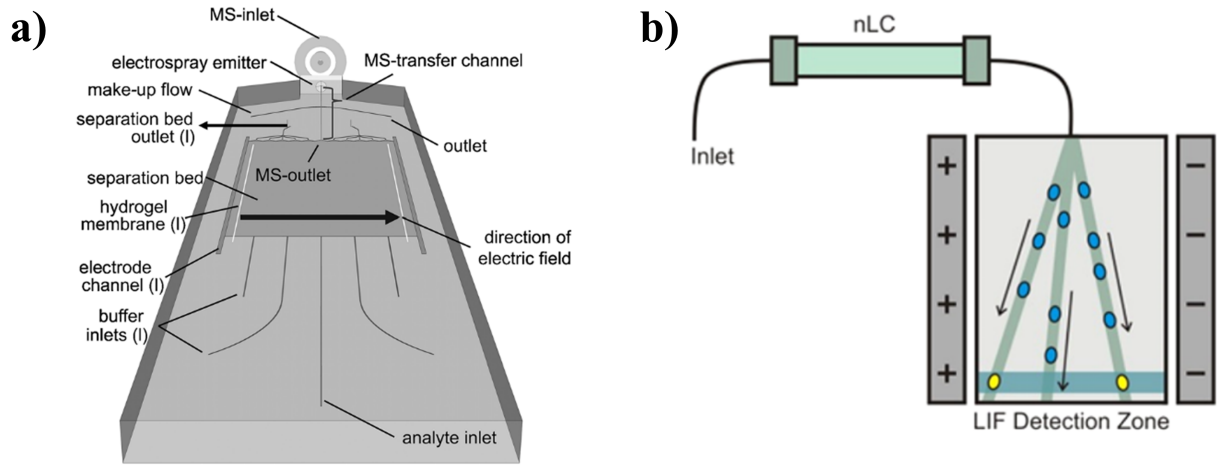


Figure 2.5: a) A µFFE device directly coupled to mass spectroscopy (MS) [32]. b) Nanoliquid chromatography (nLC) directly coupled to µFFE with laser induced fluorescence (LIF) detection for multidimensional analysis [109].

[106]. The analysis of model proteins was achieved, although the direct coupling of cIEF and FFE can lead to unwanted backflow. Similarly, FFE was used to remove sodium dodecyl sulfate (SDS) from a sample, as this additive is commonly used in separation buffers and can also damage the MS signal [107]. In another example, a µFFE device was coupled with a nanospray MS emitter for the detection of trace analytes, and downstream microchannel networks were helpful for preparing the sample for MS [32]. Note that multiple analytes sequentially ran through the emitter by manipulating the flow rates in the µFFE chamber. This process was also achieved using FF-ITP, and the focusing mechanism was able to concentrate and purify the sample streams prior to MS [72]. For an additional improvement, a switching valve can be added between the µFFE and the MS device to avoid manipulating the flow upstream [88]. Finally, a µFFE device has demonstrated the transfer of a peptide from a complex sample to a solvent that enhances the MS signal [108].

Real-Time Monitoring

The continuous nature of FFE offers the potential for real-time monitoring, and this is especially true at the analytical scale because of the reduced sample volumes and online detection systems that can view the entire separation region [36]. For example, µFFE has been used to study bioassays that dynamically change their experimental conditions. In one study, the concentration of cyclodextrin in the separation buffer was varied over time to monitor its impact on the separa-

tion of different amino acids [110]. In another study, ligand-aptamer complexes were separated from unbound aptamers, and the concentration of ligand was increased over time to measure the binding affinity [34]. Combined, these experiments provided convenience and high throughput analysis, and demonstrated that μFFE can be a powerful tool for studying protein interactions in dynamic systems. Moreover, Dutta has recently extended the method of moments formulation to model these free-flow affinity assays and gain additional information about the binding kinetics [111]. Moving forward, a real-time monitoring μFFE device could also be used for analyzing samples in a clinical setting, or for quality control during industrial processes, but this is an area that is yet to be explored [35].

Multidimensional Analysis

One of the main challenges in proteomics is the fact that proteins have an incredibly wide range of properties and abundances [81]. As a result, complex mixtures often require several rounds of processing to isolate and analyze proteins of interest. Traditionally, FFE has been well-suited for this application because separated fractions remain in solution and can be easily transferred to other separation methods. For example, FF-IEF has been used in combination with reversed-phase high-performance liquid chromatography (RP-HPLC), and this provides information about the pI and relative hydrophobicity of the proteins [81]. Recently, this multidimensional analysis has been explored at the analytical scale due to its reduced sample volumes and ability for direct coupling with different separation techniques. Usually, μFFE is used as the second dimension because of its high sampling rates, as this helps maximize peak capacity and reduce the overall analysis time [36]. So far, μFFE has managed to successfully perform two dimensional separations with nanoliquid chromatography for the analysis of bovine serum albumin tryptic peptides (see Fig. 2.5b) [33] [109]. Likewise, capillary electrophoresis has been coupled to the sample injection of μFFE, and although the only source of orthogonality between the two separation modes was a change in pH and cyclodextrin concentration, it helped demonstrate the potential of μFFE as a powerful tool for multidimensional analysis [112].

2.2 Counterflow Gradient Focusing

The purpose of this section is to review a technique known as counterflow gradient focusing, which was originally proposed for preparative scale applications, but eventually gained traction as a promising separation mode in capillary electrophoresis [51].

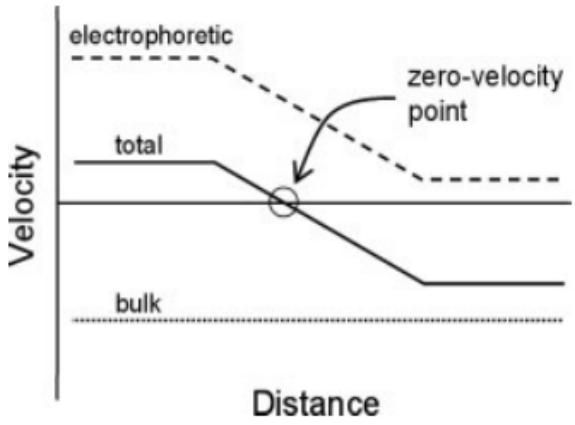


Figure 2.6: A plot of the electrophoretic velocity gradient, the bulk flow velocity, and a combination of the two. The zero-velocity point occurs where the electrophoretic velocity and bulk flow velocity are counterbalanced [48].

2.2.1 Introduction

Capillary electrophoresis (CE) is a powerful analytical technique that is often recognized for its contribution to the human genome project [113]. In the traditional capillary zone electrophoresis (CZE), analytes migrate through the capillary with a velocity that is determined by their electrophoretic mobility [114]. Similar to FFZE, this technique has a number of shortcomings that limit its resolution and sensitivity. For one, the width of the separation bands depends on the initial sample injection pulse, and significant efforts have been made to concentrate this initial zone [114]. Second, molecular diffusion causes the width of analyte zones to continuously disperse as they migrate through the capillary [50]. Third, analytes with similar mobilities can require long capillaries to fully resolve, and this is not ideal for the many analytical applications that demand miniaturization and portability [50].

The aforementioned issues have been addressed by introducing equilibrium gradient methods (EGMs) to CE. Originally termed by Giddings, EGMs introduce a gradient along the separation region to focus analytes at equilibrium positions where their net velocity is zero [49]. In essence, this gradient acts as a restoring force, which allows analytes to concentrate rather than disperse. Furthermore, analytes will reach their equilibrium position regardless of their initial starting point, and this eliminates the concern for narrow injection widths and long capillaries [50]. The most popular EGM in CE is capillary isoelectric focusing (cIEF), which can achieve high resolution separations with a low detection limit [115]. In cIEF, the gradient is defined by the pH, and electric forces cause analytes to separate and focus at the pH where their net charge is zero.

However, this equilibrium position, which is commonly referred to as the isoelectric point (pI), is not always well-defined, and some analytes have poor solubility in this state [116]. Moreover, the carrier ampholytes required to generate the pH gradient are expensive, and their pH range is often limited to values between 3 and 10 [48].

The limitations of cIEF motivated researchers to explore alternative EGMs that can be applied to CE. This led to the emergence of counterflow gradient focusing, which introduces a bulk solution flow to oppose electrophoretic migration [48]. If one or both of these transport mechanisms vary across the separation region, then analytes will focus at a position where the electrophoresis is counterbalanced by the fluid flow. An example of this mechanism is provided in Fig. 2.6, where it is seen that an electrophoretic gradient produces the zero-velocity point [48]. This position depends on electrophoretic mobility, and therefore different analytes can be separated and focused along the gradient. Many strategies have been proposed to generate this velocity gradient, and they will be discussed during the remainder of this section. Interestingly, the first apparatus that employed this counterflow gradient focusing (CGF) method was intended for preparative scale applications [117], and in the early 1990s there was a brief overlap between CGF and FFE [118] [119] [120].

2.2.2 Modeling Counterflow Gradient Focusing

The focusing mechanism for electrophoretic EGMs is best understood with the help of the linear flux equation [116]:

$$N_x = -D\frac{dc}{dx} + (u_x + \mu_{\mathrm{EP}} E_x)\, c = 0 \tag{2.22}$$

where N_x is the molar flux in the x-direction, D is the diffusion coefficient, c is the solute concentration, u_x is the average fluid velocity in the x-direction, μ_{EP} is the electrophoretic mobility, and E_x is the electric field in the x-direction. Note that the term in brackets represents the total velocity of the solute, and at least one of the terms within should vary along the x-direction to generate the gradient. Then, the focal point is represented by the x-position where the two velocity terms are equal in magnitude but opposite in direction. At this point, an equilibrium exists between diffusion and the gradient restoring force, and this will determine the peak width. A closer look at the flux equation helps guide the design of the gradient [116]:

$$N_x = -D\frac{dc}{dx} + \left(u_x + z\omega\frac{I_x}{\sigma_c}\right) c = 0 \tag{2.23}$$

where z is the solute charge, ω is the absolute solute mobility, I_x is the current density, and σ_c is the conductivity. As a result, there are several parameters that can be tuned to generate a velocity gradient. In the early preparative scale designs, u_x was usually the variable term [118] [119]

[120], but more recently it has been either I_x or σ_c [48]. Specific strategies for varying these terms in practice will be provided in Section 2.2.3.

In many cases, the u_x is generated by pressure-driven flow in a capillary, and the resulting parabolic flow profile will have an impact on solute dispersion. This phenomenon has been modeled by Ivory when there is an electric field gradient, and the steady-state convection-diffusion equation can be written as [121]:

$$\frac{\partial}{\partial x}\left[\left(u_{x,max}\left(\frac{1}{2}-r^2\right)\right)c\right]-\frac{\partial}{\partial x}\left[(\mu_{\mathrm{EP}}Fx)c\right]=\frac{D}{r}\frac{\partial}{\partial r}r\frac{\partial c}{\partial r}+D\frac{\partial^2 c}{\partial x^2} \tag{2.24}$$

where r is the radial coordinate of the capillary, $u_{x,max}$ is the maximum velocity in the capillary, and F represents the counteracting force generated by the electric field gradient. Note that this is assumed to be a linear gradient that is not influenced by focused solutes. Also, note that Eq. 2.24 is in a shifted coordinate system that focuses the solute at $x = 0$, and accounts for electroosmotic velocity [121]. The dimensionless form can be written as:

$$Pe\left(\frac{1}{2}-r^{*2}\right)\frac{\partial}{\partial x^*}c^*-G_f\frac{\partial}{\partial x^*}(x^*c^*)=\frac{1}{r^*}\frac{\partial}{\partial r^*}r^*\frac{\partial c^*}{\partial r^*}+\frac{\partial^2 c^*}{\partial x^{*2}} \tag{2.25}$$

where x^* and r^* scale with the capillary radius (a), and c^* is relative to the initial concentration. Also, $Pe = u_{x,max}a/D$ is the Péclet number for the counterflow, $G_f = \mu_{\mathrm{EP}}Fa^2/D$ is the dimensionless number representing the counteracting gradient force. Like the FFE models seen in Section 2.1.2, Eq. 2.25 can then be solved using a method of moments formulation to estimate the dispersion, and this derivation was also applied to the dimensions of a microchannel [121]. The result is similar to the well-known Taylor-Aris dispersion, which describes the evolution of a solute pulse that is subject to the parabolic velocity profile of flow through a tube [122] [123]. However, Ivory highlights a subtle difference in EGMs due to their ability to reach a steady-state [121].

2.2.3 Separation Modes

Now that the underlying mechanism for CGF has been established, this section will look at some of the many strategies that has been used in practice to generate the gradient.

Fluid Velocity Gradients

As mentioned previously, many of the early CGF designs managed to generate a gradient in the counterflow velocity. The first instance by O'Farrell in 1985 consisted of a column packed with

two layers of resins that differed in terms of size exclusion [117]. This created a steep gradient in apparent solute velocity at the interface when a buffer flow was introduced, and charged proteins could stack here if electrophoretic migration occurred in the opposite direction. In a second example, Giddings proposed crossflow gradients along the height direction of a thin channel, which would allow charged solutes to form hyperlayers in the presence of electrophoresis [124]. However, in practice there were difficulties finding a permeable wall material that could generate a uniform crossflow throughout the channel. For an example that is related to FFE, Ivory implemented a recycling FFZE mode that altered the outflow conditions to create a crossflow at the recycle-feed port. This allowed a protein with an opposing electrophoretic velocity to focus in this region while other proteins from the mixture were removed [118]. In another example, Culkin [119] and Egen *et al.* [120] patented similar strategies that used porous membranes to divide the separation chamber into subcompartments. Then, by withdrawing a fraction of fluid flow from the outlet of each subcompartment, a velocity gradient can be created across the chamber (see Fig. 2.7a). As a result, charged solutes can focus in the subcompartment where their electrophoretic velocity is counterbalanced by the crossflow gradient.

Electric Field Gradient Focusing

Electric field gradient focusing (EFGF) by Koegler and Ivory was one of the first methods to generate a gradient in electrophoretic velocity [127]. In this method, a current density gradient was created by varying the inner cross-sectional area of a Plexiglas cylinder. Within the cylinder was a dialysis tubing, and this contained the counterflow and the sample. For miniaturization, this form of EFGF was also implemented with a microchannel that was enclosed by an ion conductive polymer whose cross-sectional area varied along the length of the separation region [128] [129]. Although this device could achieve high concentration factors, resolution was restricted by a number of factors, including unreliable ionic transport through the conductive membrane, local variations in EOF, and Taylor dispersion [130] [131]. To improve upon these issues, a microchannel packed with a poly(ethylene glycol)-fictionalized monolith was able to suppress both EOF and Taylor dispersion [132]. In addition, the ionic transport was improved by removing impurities from the polymer matrix and shifting to smaller ions that could migrate more freely [133]. Finally, this device operated in a scanning mode by adjusting the voltage over time, and this allowed the focused peaks to sequentially elute from the microchannel [134].

Dynamic Field Gradient Focusing

In an alternative installment by Huang and Ivory, an electric field gradient was created by interfacing the separation region with an array of electrodes [135]. For this dynamic field gradient

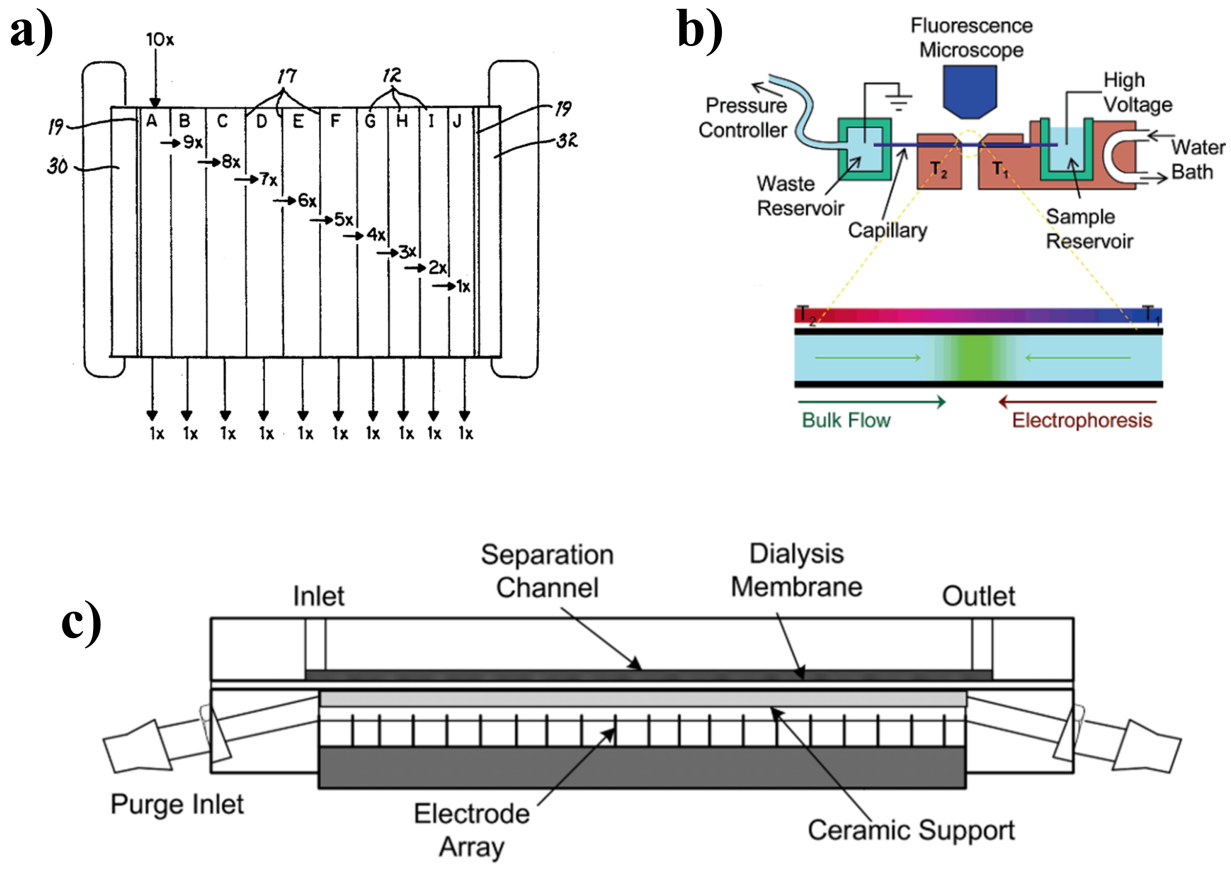


Figure 2.7: a) A free-flow CGF device divided into subcompartment using porous membranes [120]. b) A TGF device operated in a scanning mode [125]. c) A DFGF with an electrode array along the bottom of the chamber [126].

focusing (DFGF) apparatus, the voltage at each electrode can be adjusted throughout the separation for added versatility. For example, the device can be operated in a scanning mode to sequentially elute analytes, or it can be tuned at specific regions for improved resolution. A schematic of the device is shown in Fig. 2.7c, where it can be seen that a membrane is used to isolate the separation channel from the electrode arrays, and this acts as a barrier for analytes that are drawn to the electrode. In addition, it facilitates the removal of Joule heating and electrolysis effects. Extensive work has been done to optimize the electrode regions, with an emphasis on improving voltage efficiency, and reducing the steric and ionic exclusion around the membranes [136] [137] [138]. In one scenario, the membrane was removed altogether, and a vacuum was used to remove electrolysis bubbles [139]. There have also been studies devoted to performing

DFGF at the microscale [140], as well as the preparative scale. For the latter, a rotor was used to reduce axial dispersion, and mg quantities of proteins could be isolated [141] [142].

Conductivity Gradient Focusing

Greenlee and Ivory introduced a technique that generated the gradient by varying the conductivity [143]. In the original apparatus, two parallel channels were separated by a dialysis membrane, and ions migrated from the high conductivity channel to the low conductivity channel to setup the gradient. Although this device received some additional interest [144] [145], it was limited by the fact that the gradient was exponential, and therefore difficult to separate analytes. With that said, some microfluidic devices have managed to leverage the ion concentration polarization (ICP) effect to generate steep conductivity gradients and extremely high concentration factors [146] [147]. In this format, ICP is typically achieved with an ion selective membrane [148] or a nanochannel [149], and EOF is used to supply the counterflow.

Temperature Gradient Focusing

Temperature gradient focusing (TGF) was proposed by Ross and Locasio as a more effective means of generating the conductivity gradient [150]. In this format, cooling and heating blocks were located beneath a microchannel to create a temperature gradient from 10 to 80℃ across the separation region (see Fig. 2.7b). Meanwhile, the ionic strength of the buffer was temperature dependent, and this is what helps create the conductivity gradient [151]. Interestingly, TGF managed successful operation without the need to isolate the electrodes with a membrane, and this helped avoid some of the issues that limited EFGF and DFGF. Furthermore, there have been additional fabrication techniques proposed to miniaturize the temperature sources [152] [153] [154]. Typically, EOF was used to supply the counterflow and limit Taylor dispersion, although a pressure controller could be used to vary the flow with time and operate in a scanning mode for increased peak capacity [125]. However, several models have been dedicated to understanding the separation resolution in TGF, and found that the thermal effects can influence dispersion in a number of ways [155] [156]. Additionally, concentrated peaks may lead to nonlinear interactions in the system when the buffer concentration is low, and this can reduce resolution further [157].

Micellar Affinity Gradient Focusing

As an extension of TGF, micellar affinity gradient focusing (MAGF) has been proposed as an alternative method. In this system, surfactants are added to the separation buffer to generate micelles, and their affinity with different analytes is temperature dependent [158] [159]. As a

result, the focal point of an analyte must now consider its retention factor with the micelle as well as the electrophoretic velocity of the micelle itself. An important benefit of MAGF is that it can be applied to neutral and hydrophobic analytes in addition to charged species. Furthermore, unlike TGF, the ionic strength of the buffer does not have to depend on temperature.

Bilinear Gradient Focusing

Finally, bilinear gradients have been used for several of the aforementioned techniques, and this helps address a fundamental issue with gradient focusing methods [133]. Because the peak width and resolution are both inversely proportional to the square root of the field gradient, the resolution and peak capacity cannot be improved simultaneously. In other words, a steeper gradient will create more focused peaks, but it will also bring them closer together. Sun *et al.* was the first to implement a bilinear gradient in the EFGF mode, and it was done so by carefully designing the cross-sectional area of the conductive polymer surrounding the microchannel [133]. In this setup, the steep portion of the gradient was used to stack the analytes into narrow bands. Then, by adjusting either the counterflow or the applied voltage, the analytes were sequentially introduced to the shallow gradient for high resolution separations. Since then, bilinear gradients in TGF [160] and MAGF [161] have also been demonstrated. Furthermore, a methods of moments formulation has been used to derive a model for dispersion in bilinear gradients [162].

2.2.4 Applications

Many of the CGF techniques have demonstrated the separation of various analytes, including proteins, DNA, and small molecules. With that said, there does not appear to be many noteworthy applications [48]. One possible explanation for its limited use may be due to the difficulty of collecting analytes in their concentrated form, and then scaling this up to larger quantities. Another reason may be the fact that CGF systems are much more complicated to design than the traditional CE platforms. For example, the EFGF and DFGF devices required carefully designed membranes to isolate the electrodes, and packed columns to limit Taylor dispersion. Although TGF seemed to address these issues, the available buffers are limited by the need for a temperature-dependent ionic strength, and the analytes must have good thermal stability. Furthermore, the focused analytes may cause the electric field gradient to behave in a nonlinear manner that affects the resolution.

Finally, an in depth analysis by Shackman and Ross in 2007 pointed out that other areas of CE have seen significant developments that rival the resolving power and concentration enrichment of CGF [48]. However, when scaling down to lab-on-a-chip systems capable of multidimensional analysis, many of these advanced CE techniques add layers of complexity to the design.

Therefore, CGF is favoured in this situation due to its unique ability to separate and concentrate analytes in one step. This is especially true for multidimensional analysis, because CGF can focus peaks, and then allow them to sequentially transition to the second dimension for maximum peak capacity. The potential for multidimensional analysis was also suggested by Ivory in a similar 2007 review [50]. Unfortunately, since then there has been limited progress made in this area [163], and perhaps this highlights the practical limitations of fully integrated lab-on-a-chip systems in general.

Chapter 3

Free-Flow Counterflow Gradient Focusing

The work included in this chapter is published: **M. Courtney**, E. Thompson, T. Glawdel, C.L. Ren. Counterflow Gradient Focusing in Free-Flow Electrophoresis for Protein Fractionation. Analytical Chemistry, 92 (2019), 7317-7324. [164]

Tomasz Glawdel (Adjunct Professor in the Department of Mechanical Engineering, University of Waterloo) came up with the idea of free-flow counterflow gradient focusing, and assisted in the development of the physical modeling and device design. Ethan Thompson (Undergraduate Student, Department of Nanotechnology Engineering, University of Waterloo) assisted in the initial prototyping phase of the device design, and helped with the experimental setup.

3.1 Introduction

The purpose of this chapter is to introduce the concept of counterflow gradient focusing (CGF) to free-flow electrophoresis (FFE). At this point, the FFE principle, and its potential as a powerful tool for protein fractionation, should be clear (see Chapter 1). In addition, the limitations of FFE in terms of dispersion and practical implementation have been described in detail (see Chapter 2.1.2 and 2.1.4). Furthermore, the advanced focusing mechanisms that can be applied to FFE should be well understood, with an emphasis on free-flow isoelectric focusing (FF-IEF) and its practical challenges (see Chapter 2.1.3). Finally, the concept of CGF, and its advantages over FF-IEF should be noted (see Chapter 1 and 2.2).

In summary, this work presents a new free-flow counterflow gradient focusing (FF-CGF) technique that introduces a counterflow at both sides of the chamber to produce a velocity gradient that opposes electrophoretic migration. This FF-CGF method is similar in principle to the focusing method in FF-IEF, but analytes focus based on electrophoretic mobility instead. Unlike FF-IEF, FF-CGF provides versatility due to its simple buffer conditions, and it avoids many of

the concerns associated with focusing solutes at their isoelectric point. This work will provide a theoretical foundation FF-CGF as well as design guidelines, and then experimental validation will follow. Next, recommendations for future technical and fundamental work will be proposed for new opportunities in the field.

Before beginning, it should be acknowledged that there are several previous methods that resemble the implementation of CGF in FFE. For example, Culkin [119] and Egen *et al.* [120] proposed comparable strategies consisting of an FFE chamber divided into subcompartments using porous membranes, and by withdrawing a fraction of fluid flow from each subcompartment outlet, a counterflow was created across the membranes. Using a similar withdrawal technique, Ivory altered a recycle zone FFE device to produce a counterflow by the recycle-feed port that allowed a single analyte band to focus at the centre of the chamber while other analytes were removed [118]. A single-band focusing chamber was also suggested by Rhodes and Snyder using porous sidewalls that introduced a uniform counterflow through the chamber to counter electrophoretic migration [165]. Finally, inspired by a technique previously developed in CE [150], Becker *et al.* used a temperature gradient and an electroosmotic counterflow across an FFE chamber to focus analytes [78]. Despite the potential of the aforementioned techniques, most are limited due to either a complicated setup, membrane fouling, long focusing times, or low peak capacities. Therefore, in this work, the proposed FF-CGF method is unique because the FFE chamber can maintain its standard form without the need for subcompartments, and several analytes can separate and focus across the chamber simultaneously.

3.2 Modeling Free-Flow Counterflow Gradient Focusing

The goal of this section is to describe the concept of focusing in FF-CGF, derive analytical equations for the fluid flow and solute transit, provide a strategy for numerical simulations, and offer design guidelines for generating a uniform gradient along the length of the chamber.

3.2.1 Focusing Mechanism

For a general FF-CGF mechanism, consider an FFE chamber with the electric field (E) applied in the x-direction (see Fig. 3.1a). The analytes will migrate across the chamber with an electrophoretic velocity (u_{EP}) that depends on its electrophoretic mobility (μ_{EP}):

$$u_{\mathrm{EP}} = \mu_{\mathrm{EP}} E \tag{3.1}$$

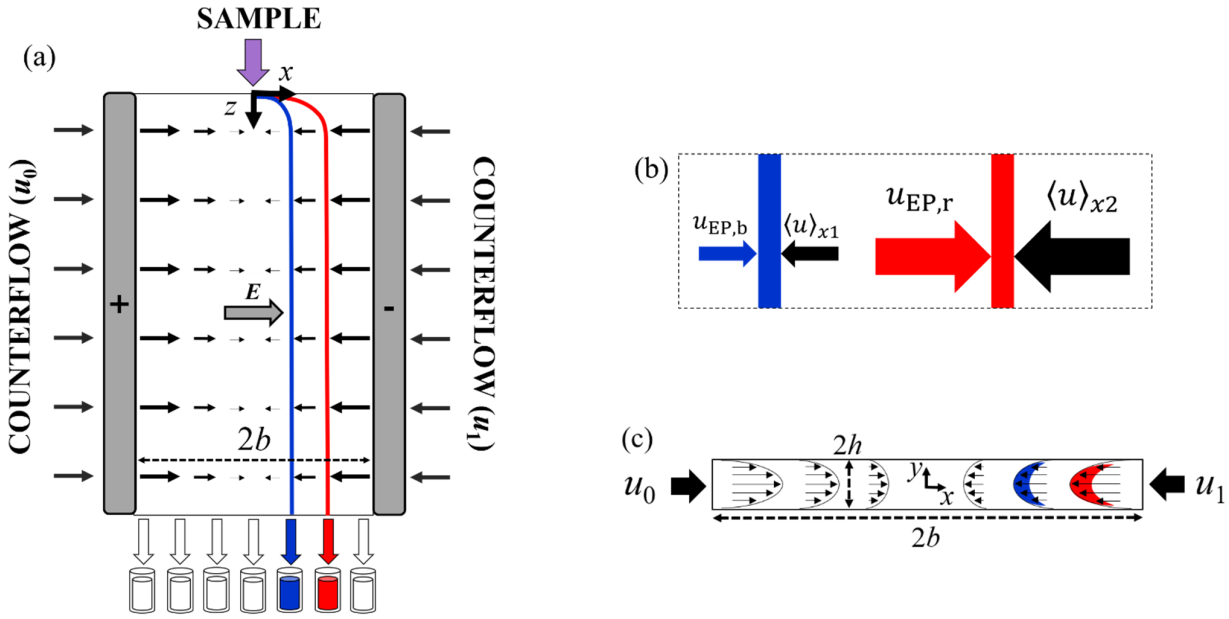


Figure 3.1: a) An FFE chamber with a counterflow introduced through the sidewalls to produce a velocity gradient in the x-direction, with b) a close-up view of the two sample analytes, blue and red, focused in the velocity gradient according to their electrophoretic velocity. c) A cross-sectional view of the velocity gradient in the FFE chamber.

If a liquid counterflow is introduced to oppose electrophoretic migration, the total velocity of the analyte in the x-direction (u_T) can be written as:

$$u_{\mathrm{T}} = u_{\mathrm{EP}} + \langle u \rangle \tag{3.2}$$

where $\langle u \rangle$ is the area-averaged velocity of the counterflow in the x-direction, and can be due to pressure-driven flow, electroosmotic flow (EOF), or a combination of the two [150]. When one or both velocity terms in Eq. 3.2 are made to vary along the x-direction, there will be a unique x-position where they are equal in magnitude but opposite in direction (see Fig. 3.1b) resulting in a zero u_{T}. This equilibrium point depends on μ_{EP} and is therefore unique to different analytes. As these analytes are focused, they will simultaneously be transported towards the outlets due to the z-velocity component of the sample flow, which is perpendicular to E.

3.2.2 Counterflow Gradient

The proposed FF-CGF mechanism has a gradient in $\langle u \rangle$ across the chamber while u_{EP} is constant. The gradient in $\langle u \rangle$ will be produced by introducing a pressure-driven counterflow from both sidewalls of the FFE separation chamber (see Fig. 3.1a). As the counterflow moves incrementally towards the center of the chamber with a given x-velocity, a fraction will be converted into z-velocity and move towards the outlets. Consequently, the x-velocity of the counterflow will decrease until it reaches the center of the chamber. This counterflow gradient will allow different analytes to separate and focus across the chamber according to Eq. 3.2, before exiting through the outlets. It is assumed that the counterflow at both sidewalls is equal in magnitude along the z-direction. It should also be noted that the continuous addition of flow from the sidewalls will create an increasing velocity in the z-direction.

A simplified 2D mathematical model of the velocity field within the FF-CGF chamber can be derived using a method similar to Ref. [124]. This model will solve for the area-averaged x-velocity $\langle u \rangle$ and area-averaged z-velocity $\langle w \rangle$. For this model, consider a chamber where the length L and breadth $2b$ are much greater than the height $2h$. By assuming incompressible flow, the net volumetric flow rate $\dot{V}$ through an arbitrary segment of the chamber with a width of Δx and a length of Δz is equal to zero:

$$\dot{V} = 2h\Delta z \left(\langle u \rangle_x - \langle u \rangle_{x+\Delta x} \right) + 2h\Delta x \left(\langle w \rangle_z - \langle w \rangle_{z+\Delta z} \right) = 0 \tag{3.3}$$

If the segment being analyzed is much smaller than the length and the breadth of the chamber, then the following expressions can be written:

$$\langle u \rangle_{x+\Delta x} - \langle u \rangle_x = \frac{d \langle u \rangle}{dx} \Delta x \tag{3.4}$$

$$\langle w \rangle_{z+\Delta z} - \langle w \rangle_z = \frac{d \langle w \rangle}{dz} \Delta z \tag{3.5}$$

By substituting these equations back into Eq. 3.3, the following differential equation can be obtained:

$$\frac{d \langle u \rangle}{dx} + \frac{d \langle w \rangle}{dz} = 0 \tag{3.6}$$

If the inflow through the sidewalls is assumed to be constant along the z-direction and described by the boundary conditions of $\langle u \rangle = u_0$ at $x = -b$ and $\langle u \rangle = u_1$ at $x = b$ (see Fig. 3.1), then Eq. 3.6 can be simplified by setting Δx of the segment equal to breadth of the chamber $2b$:

$$\frac{d \langle w \rangle}{dz} = \frac{u_0 - u_1}{2b} \tag{3.7}$$

Solving for $\langle w \rangle$ in Eq. 3.7 gives the following expression for velocity in the z-direction of the chamber:

$$\langle w \rangle = \left(\frac{u_0 - u_1}{2b} \right) z + \langle w \rangle_0 \tag{3.8}$$

where $\langle w \rangle_0$ represents the initial z-direction at $z = 0$. Additionally, substituting Eq. 3.7 back into Eq. 3.6 gives the following expression:

$$\frac{d \langle u \rangle}{dx} = - \left(\frac{u_0 - u_1}{2b} \right) \tag{3.9}$$

Solving for $\langle u \rangle$ in Eq. 3.9 gives the following expression for velocity in the x-direction of the chamber:

$$\langle u \rangle = - \left(\frac{u_0 - u_1}{2b} \right) x + \langle u \rangle_0 \tag{3.10}$$

By applying the boundary conditions of $\langle u \rangle = u_0$ at $x = -b$ and $\langle u \rangle = u_1$ at $x = b$, the final expression for $\langle u \rangle$ is:

$$\langle u \rangle = \left(\frac{u_0 + u_1}{2} \right) - \left(\frac{u_0 - u_1}{2b} \right) x \tag{3.11}$$

For the scenario where $u_0 = -u_1$, the expressions for $\langle u \rangle$ and $\langle w \rangle$ can be simplified to the standard form:

$$\langle u \rangle = -\frac{u_0}{b} x = - \bigtriangledown \langle u \rangle x \tag{3.12}$$

$$\langle w \rangle = \frac{u_0}{b} z + \langle w \rangle_0 = \bigtriangledown \langle u \rangle z + \langle w \rangle_0 \tag{3.13}$$

where $\bigtriangledown \langle u \rangle = u_0 / b$ is the gradient of x-velocity and $\langle w \rangle_0$ is the initial z-velocity at $z = 0$.

3.2.3 Position and Residence Time

The area-averaged velocity field within the chamber can be used to track the position of the analyte at time t. Substituting Eq. 3.12 into Eq. 3.2, the x-velocity of a mass particle with a constant u_{EP} can be determined from the following expression:

$$\frac{\partial \langle x \rangle}{\partial t} = u_{\mathrm{EP}} - \bigtriangledown \langle u \rangle x \tag{3.14}$$

Assuming $x = 0$ at $t = 0$, this differential equation can be used to find the mean x-position of the analytes as a function of t:

$$x = \frac{u_{\mathrm{EP}}}{\bigtriangledown \langle u \rangle} \left(1 - e^{-\bigtriangledown \langle u \rangle t} \right) \tag{3.15}$$

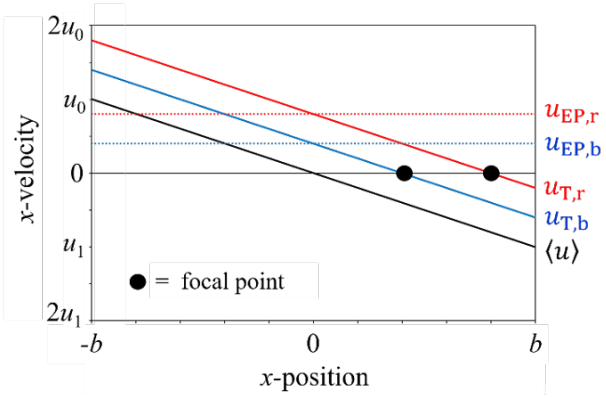


Figure 3.2: a) The gradient of across $\langle u \rangle$ the FF-CGF chamber. The total x-velocity $u_{\mathrm{T,i}}$ of two analytes with $u_{\mathrm{EP,b}} = 0.4u_0$ and $u_{\mathrm{EP,r}} = 0.8u_0$. Note the focal point as $u_{\mathrm{T,i}}$ crosses the x-axis.

Now, rewriting Eq. 3.12 as a differential equation to consider the z-velocity of a mass particle during transit:

$$\frac{\partial \langle z \rangle}{\partial t} = \nabla \langle u \rangle z + \langle w \rangle_0 \tag{3.16}$$

Assuming $z = 0$ at $t = 0$, this differential equation can be used to find the mean z-position of the analytes as a function of t:

$$z = \frac{\langle w \rangle_0}{\nabla \langle u \rangle} \left(e^{\nabla \langle u \rangle t} - 1 \right) \tag{3.17}$$

Rearranging this equation to solve for t gives the transit time through the chamber as a function of z-position:

$$t = \frac{1}{\nabla \langle u \rangle} \ln \left(1 + \frac{\nabla \langle u \rangle}{\langle w \rangle_0} z \right) \tag{3.18}$$

Setting $z = L$ into this equation will give the residence time of the analyte in the separation chamber. Substituting this expression back into Eq. 4.13 gives the mean x-position of an analyte with a constant u_{EP} as a function of z:

$$x = \frac{u_{\mathrm{EP}}}{\nabla \langle u \rangle} \left(1 - \left(1 + \frac{\nabla \langle u \rangle}{\langle w \rangle_0} z \right)^{-1} \right) \tag{3.19}$$

3.2.4 Focal Point

The mean focal point for an analyte with a constant u_{EP} can also be found using the area-averaged velocity field in the chamber. Substituting Eq.3.12 into Eq. 3.2 gives the following expression:

$$u_T = u_{\mathrm{EP}} - \nabla \langle u \rangle x \tag{3.20}$$

A graphical representation of this expression is shown in Fig. 3.2 for different analytes. Note that analytes will migrate towards its focal point (where u_T crosses the x-axis), regardless of its initial x-position. Therefore, at $u_T = 0$, the mean focal point is:

$$\langle x \rangle_f = \frac{u_{\mathrm{EP}}}{\nabla \langle u \rangle} \tag{3.21}$$

When considering the overall focal point x_f of an analyte, it is also important to consider velocity profile of the fluid flow in the height direction of the chamber (y-direction). If it is assumed that the x-velocity (u) and the z-velocity (w) of the fluid within the chamber are constrained to a parabolic profile in the y-direction:

$$u(y) = \frac{3}{2} \langle u \rangle \left(1 - \frac{y^2}{h^2}\right) \tag{3.22}$$

$$w(y) = \frac{3}{2} \langle w \rangle \left(1 - \frac{y^2}{h^2}\right) \tag{3.23}$$

Substituting Eq. 3.12 and Eq. 3.13 into Eq. 3.22 and Eq. 3.23, respectively, then the overall velocity profiles are given as:

$$u(x,y) = -\frac{3}{2} \nabla \langle u \rangle x \left(1 - \frac{y^2}{h^2}\right) \tag{3.24}$$

$$w(y,z) = \frac{3}{2} \left(\nabla \langle u \rangle z + \langle w \rangle_0\right) \left(1 - \frac{y^2}{h^2}\right) \tag{3.25}$$

From Eq. 3.24, if $u_{\mathrm{EP}} = -u(x,y)$ at the focal point, and a shifted co-ordinate of $x = \langle x \rangle_f + x_f$ is applied, then the focal point is given by:

$$x_f = \frac{u_{\mathrm{EP}}}{\nabla \langle u \rangle} \left(\frac{2}{3} \left(1 - \frac{y^2}{h^2}\right)^{-1} - 1\right) \tag{3.26}$$

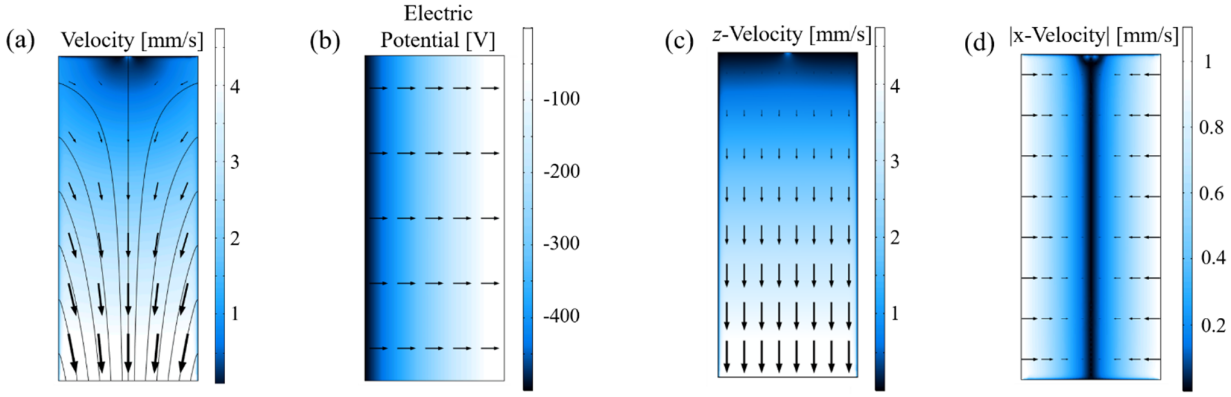


Figure 3.3: Numerical simulation of 15 x 35 x 0.1 mm FF-CGF chamber with a 1 mm/s input velocity at sidewalls and -500 V applied across the chamber, distributed uniformly along the length of the chamber. a) Velocity field. b) Electric field (333.33 V/cm). c) z-Velocity field. d) x-Velocity field.

Eq. 3.26 can provide some insight towards the band-broadening and resulting resolution at x_f. While deriving a mathematical model that also considers molecular diffusion and the overall dispersion is beyond the scope of this work, Eq. 3.26 indicates that Taylor dispersion will be a factor due to the parabolic term [121]. The electrodynamic dispersion caused by EOF should also be considered in future models [54]. For example, the pressure-driven backflow caused by EOF could minimize Taylor dispersion when it opposes the counterflow, as the subtraction of their parabolic profiles will flatten the overall profile [166].

3.2.5 Numerical Simulations

The FF-CGF principle has also been validated using a simplified 2D numerical simulation (COMSOL v5.3). The fluid dynamics were calculated using the continuity equation and a simplified Navier-Stokes equation that neglected the inertial terms and the electrokinetic body forces:

$$\nabla \cdot \vec{\mathbf{u}} = 0 \tag{3.27}$$

$$-\nabla p + \mu \nabla^2 \vec{\mathbf{u}} - 12\frac{\mu \vec{\mathbf{u}}}{d_y^2} = 0 \tag{3.28}$$

where $\vec{\mathbf{u}}$ is the velocity of the fluid, p is the pressure, and μ is the dynamic viscosity. Also note that the final term is due to the shallow channel height approximation, with d_y being the chamber height. The electrostatics were computed simultaneously using the following equation:

$$\vec{E} = -\nabla V \tag{3.29}$$

where V is the electric potential. Note that this assumes that the electric field is constant across the separation region, and is unaffected by the local conductivity gradients that may arise due to the focused solute. The steady-state analyte transport through the chamber was then calculated using the convection-diffusion equation and the molar flux (N_i) equation:

$$\nabla \cdot \left(-D_i \nabla c_i + \mu_{\mathrm{EP}} c_i \overrightarrow{E} \right) + \overrightarrow{\mathbf{u}} \cdot \nabla c_i = 0 \tag{3.30}$$

where D_i is the diffusion coefficient of the i^{th} analyte and c_i is the molar concentration of that analyte. The diffusive term that helps determine the width of the focused band only accounts for molecular diffusion in this model.

The velocity field and electric field within the FFE chamber are shown in Fig. 3.3. Most notably, the x-velocity of the fluid from the sidewalls is uniform along the z-direction and decreases linearly in the x-direction towards the center of the chamber. The steady-state analyte transport through the chamber due to the velocity gradient and electric field is shown in Fig. 3.4. Note that this is a 2D model, and therefore does not consider Taylor dispersion in y-direction. In Fig. 3.4a, when there is no applied electric field, all three analytes will focus down the center of the chamber due to hydrodynamic focusing. The terminal width of the peak is determined by the focusing gradient and the diffusion coefficient. In addition, due to the side flow there is a continuous dilution of the analytes as they traverse the chamber. The FF-CGF principle is demonstrated when an electric field is applied in Fig. 3.4b, as the analytes focus into different streams according to their unique electrophoretic mobility before exiting the chamber. Note that parameters such as side flows and electric field need to be tuned to keep the analytes within the chamber in the x-direction.

3.3 Device Design

To make a practical FF-CGF device, the design of the FFE chamber was critical to replicate the hydrodynamic and electric field distribution in the simplified simulation. In the current approach, there are parallel microchannels that connect to the sidewalls and span the entire length of the separation chamber (see Fig. 3.5a). At the other end of the microchannels, there are additional side chambers that include access holes for buffer inflow and ionic current (see Fig. 3.5b). There were also outlet channels placed between the end of the separation chamber and the outlets to ensure that the outlets did not affect the sample streamlines.

For a uniform velocity gradient and electric field across the separation chamber, there must be an equal buffer flow rate (Q) and ionic current (I) through all of the microchannels (see Fig. 3.5c). Therefore, the hydrodynamic resistance and electrical resistance of the microchannels

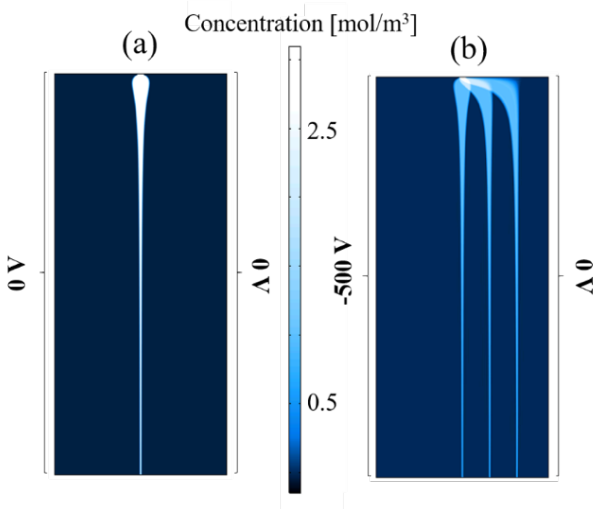


Figure 3.4: Numerical simulation for the FF-CGF separation of 3 analytes, each with a diffusion coefficient of 10^{-10} m^2/s. Their mobilities were 0, 1×10^{-13}, and 2×10^{-13} s·mol/kg. (a) No applied voltage. (b) A -500 V applied voltage across the chamber for an electric field of 333.33 V/cm.

must be significantly greater than that of the side chambers and the separation chamber. When considering that the hydrodynamic resistance is given as [167]:

$$R_{hyd} = \frac{12\mu L}{W d_y^3}\left[1 - \frac{d_y}{W}\left(\frac{192}{\pi^5}\sum_{n=1,3,5}^{\infty}\frac{1}{n^5}\tanh\frac{n\pi W}{2d_y}\right)\right]^{-1} \tag{3.31}$$

where d_y is the chamber height and W is the width of the separation chamber. Therefore, this critical design requirement can be satisfied by making the height of the microchannels small relative to the adjacent chambers. Of course, the relative height of the microchannels must not be too small, as this would limit the voltage drop across the separation chamber. Therefore, the height ratio between the adjacent chambers and the microchannels was limited to 10:1 (see Fig. 3.5c). A more detailed understanding of the criteria for achieving a uniform counterflow gradient along the length of the chamber can be found in Chapter 6.3.

3.4 Experimental Methods

3.4.1 Materials

All chemicals were purchased from Sigma Aldrich. The electrode buffer consisted of 445 mM of Tris and 445 mM of boric acid, with the pH adjusted to 8.2 using an HCl solution. The buffer counterflow pumped into the separation chamber was 89 mM of Tris and 89 mM of boric acid. The dye molecules separated in the FF-CGF experiments were prepared in a 20% glycerol solution: Ponceau S (0.1% w/v), Orange G (0.2% w/v), Bromophenol Blue (0.05% w/v), and Xylene Cyanol FF (0.1% w/v). These dye molecules are commonly used in gel electrophoresis as reference DNA markers.[66] The glycerol was found to help dissolve the dyes. The proteins separated in the FF-CGF were prepared in a solution of DI water: Hemoglobin (50 mg/mL) and Bovine Serum Albumin (BSA) (50 mg/mL). The BSA was labeled with Bromophenol Blue (BPB) at a 4:1 molar ratio [168].

3.4.2 Device Fabrication

A schematic of the device is shown in Fig. 3.5. Standard soft lithography techniques were used to fabricate this device. Briefly, SU-8 (2005, Microchem) was deposited and patterned on a silicon wafer to produce microchannels with a target height of 10 μm. Then, SU-8 (2075, Microchem) was deposited on the same wafer to pattern the remaining features with a target height of 100 μm. Markers were used to ensure proper alignment between the two SU-8 layers. Polydimethylsiloxane (PDMS) with a 10:1 ratio of base to curing agent was poured onto the silicon master and cured for 3 h at 95ºC. A 1.5 mm biopsy punch was then used to create access holes for the cured PDMS mold. Finally, two 50 mm x 75 mm glass slides were bonded to the top and bottom of the PDMS as shown in Fig. 3.5a using oxygen plasma with a power of 29.6 W at 500 mTorr for 1 min. The top glass slide is bonded first to prevent the PDMS chamber from sagging, while the bottom glass slide seals the chamber.

3.4.3 Membrane Fabrication

Membranes are often used in FFE at the chamber sidewalls for electrode isolation, as this ensures electrolysis bubbles do not affect the separation process [31]. This can be challenging in FF-CGF due to the additional requirement of having uniform fluid flow through the sidewalls. For a simplified approach, reusable membrane devices were fabricated and easily plugged into the PDMS chip. As shown in Fig. 3.5b, these devices allowed buffer counterflow (Q) and ionic current (I) to enter the side chambers. To fabricate this device, two layers of PDMS were bonded

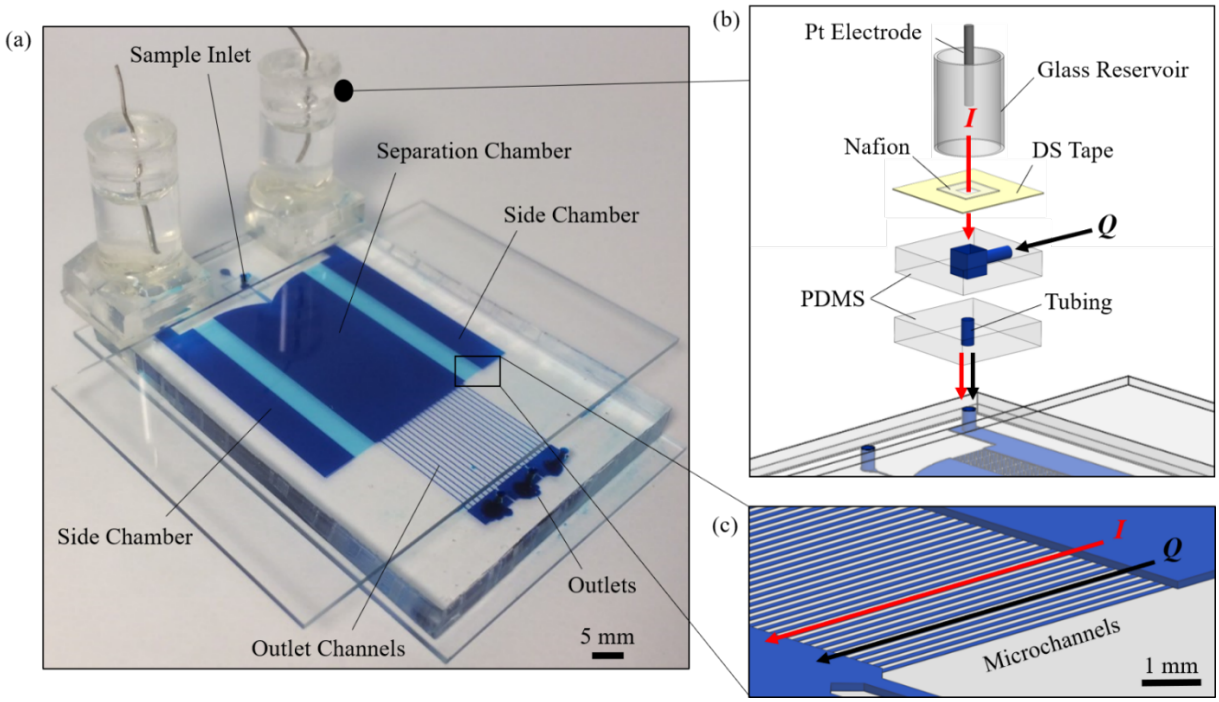


Figure 3.5: a) An image of the FF-CGF PDMS chip b) An exploded drawing of the Nafion ion-exchange membrane device. An ionic current (I) and counterflow buffer (Q) go through this device and into the side chamber. c) A close-up drawing of the micro-channels that are used to supply I and Q through the sidewalls of the separation chamber.

using oxygen plasma. The top PDMS layer had a Q-port and an I-port as shown in Fig. 3.5b. Both ports were connected to a piece of tubing in the bottom PDMS layer that could plug into the inlet of an FFE side chamber. A glass reservoir that contained electrode buffer and a platinum (Pt) electrode was bonded to the top PDMS layer using silicone glue. An ion-exchange membrane (Nafion 117, FuelCellStore) was bonded to the top of the I-port using double-sided tape (DS tape) (ARcare 90106, Adhesives Research) to isolate the electrode while allowing ionic current to pass through. There was a hole in the centre of DS tape to ensure the membrane was in contact with the buffer from the Q-port. Note that the bottom of the DS tape was spin-coated with a thin layer of PDMS and bonded to the top PDMS layer using oxygen plasma. Also note that using porous membranes as an alternative to the ion-exchange membrane would be less effective, as buffer from the Q-port would flow into the reservoir instead of the channel.

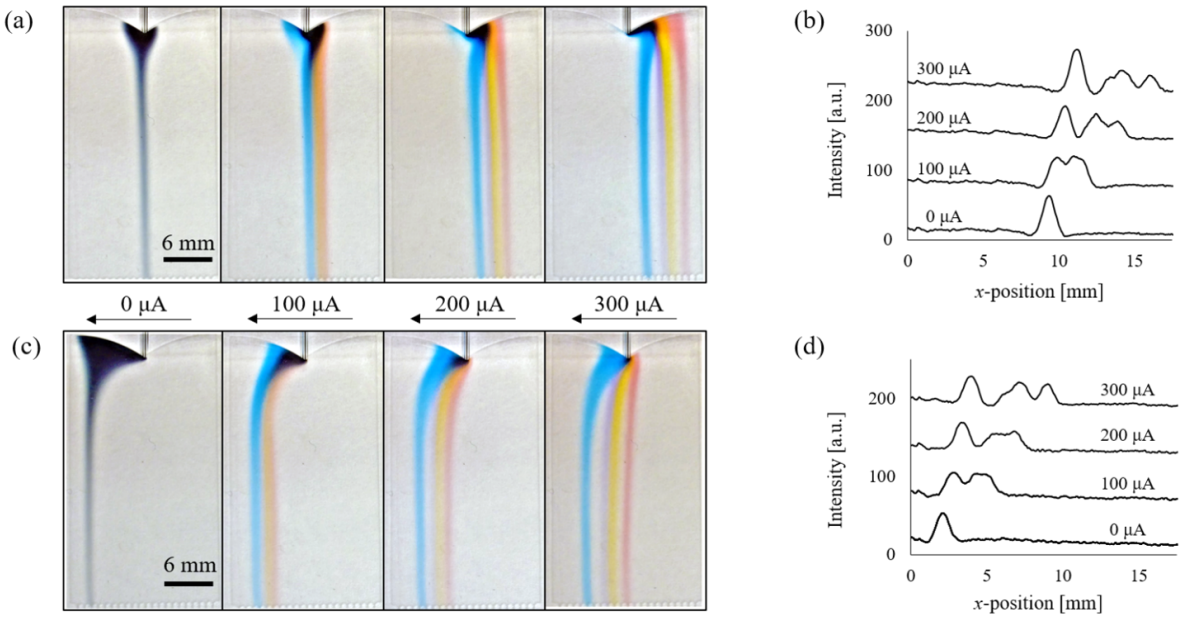


Figure 3.6: From left to right, the separation of Xylene Cyanol FF (blue), BPB (purple), Orange G (orange), and Ponceau S (red) at different applied currents. a) A symmetric velocity gradient and b) its corresponding separation profile at the end of the chamber. c) An asymmetric velocity gradient and d) its corresponding separation profile at the end of the chamber.

3.4.4 Experimental Setup

Syringe pumps were used to pump the buffer (Pump33, Harvard Apparatus) and sample (Pump11, Harvard Apparatus) into the FFE device. A high voltage supply (HVS448−3000, LabSmith) was used to apply the electric field at the electrodes using a constant current mode. Images of the separation peaks were analyzed using ImageJ software.

3.5 Results and Discussion

Compared to traditional FFE techniques, this FF-CGF technique presents several advantages including: i) its ability to focus analytes across the chamber; ii) its applicability for a wide range of analytes, from small molecules to proteins; iii) the use of simple buffer solutions; and iv) easily adjustable counterflow gradients. This section experimentally demonstrates these potentials.

3.5.1 Symmetric Gradient

To demonstrate the FF-CGF principle, a sample mixture containing Xylene Cyanol FF, BPB, Orange G, and Ponceau S was separated. The results are shown in Fig. 3.6, with the separation distance between the two analytes increasing as the current increases. As seen in Fig. 3.6a and 6b, each analyte migrates to the right side of the chamber until it reaches its equilibrium point. Overall, the streamlines of the separation peaks are similar to what was predicted in the mathematical model and numerical simulations seen in Fig. 3.2 and Fig. 3.4, respectively, therefore validating the CGF principle and the device design. Unlike FFZE, the separation peaks do not appear to widen significantly as they move across the chamber. This is due to the counterflow restoring force, which serves to return diffusing analytes to their focal point. Additionally, the lack of lateral migration in the FFE chamber could be reducing hydrodynamic broadening [37]. Finally, at 300 μA, the Ponceau S stream remains relatively narrow near the edge of the chamber (see Fig. 3.6a and 6b), despite being where the counterflow velocity is strongest, suggesting that the parabolic profile of the counterflow is being flattened by that of the opposing EOF backflow, as discussed following Eq. 3.26.

3.5.2 Asymmetric Gradient

In this format, the buffer flow rate through the right side of the chamber is greater than the left, such that the sample will focus on the left side of the chamber when no current is applied (see Fig. 3.6c). This form of gradient is particularly useful when all analytes have the same charge, as it effectively doubles the size of the FFE chamber, and therefore increases the number of outlets available for collection. As shown in Fig. 3.6c and 6d, the negative analytes will migrate from left to right when the velocity gradient is skewed to the left and a positive electric potential is applied on the right side of the chamber. This asymmetric technique could operate in a scanning mode, where a detector is placed in-line with the outlet in the center of the chamber. Then, the applied current could be gradually increased over time to allow analytes to sequentially pass through this center outlet channel for further processing.

3.5.3 Protein Fractionation

To demonstrate this device's potential for protein separation, Hemoglobin and BSA-BPB were separated (see Fig. 3.7). The BPB dye was prepared at an excess molar ratio to confirm it was indeed bound to the BSA. From Fig. 3.7, it can be seen that BSA-BPB is dark blue while the free BPB dye is purple. These results also appear to be consistent with the mathematical model and numerical simulations seen in Fig. 3.2 and Fig. 3.4, respectively. Due to the large size of

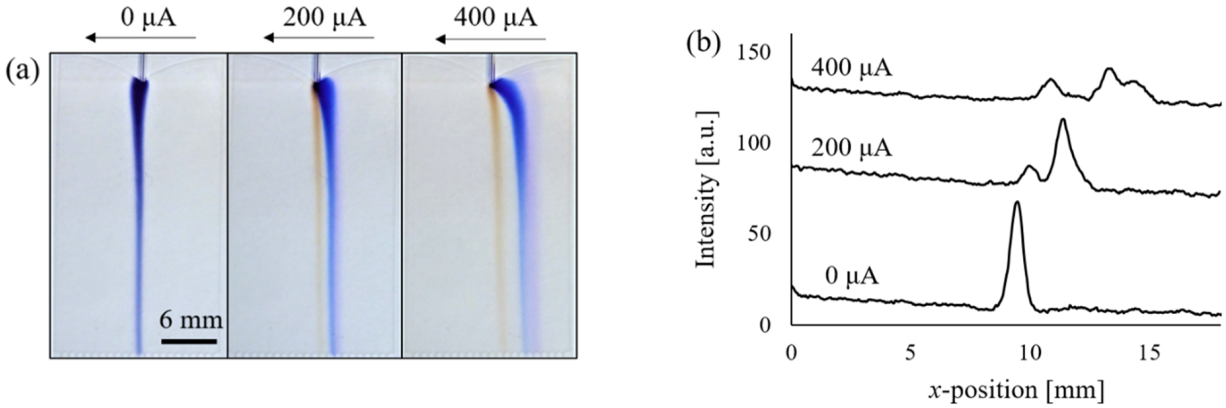


Figure 3.7: a) From left to right, the separation of Hemoglobin (brown-orange), BSA-BPB (blue), and BPB (purple) at different applied currents. b) The corresponding separation profiles at the end of the chamber.

the proteins, it could be assumed that their small diffusion coefficients would cause increased band-broadening due to the parabolic profile of the counterflow from Eq. 3.26. However, this does not appear to be the case as their peak widths are comparable to the dye molecules. As discussed earlier, one likely scenario is that Taylor dispersion is being suppressed due to the pressure-driven backflow caused by EOF.

3.6 Future Considerations

One potential drawback of FF-CGF is that the sample is being diluted by the side flow as it moves towards the outlets. This is opposite to most EGMs, which partially serve to concentrate the separated analytes. With that said, concentrated peaks can be seen as a disadvantage in some situations, as it can lead to undesired local conductivity gradients that can distort peaks or cause the analyte to precipitate [157]. It should also be noted that the analytes reach their equilibrium point almost immediately after injection (within the first 1/4 of the chamber), as seen in Fig. 3.6. Therefore, future designs could consider decreasing the length of the chamber significantly, as this would reduce sample dilution and device footprint.

Another technical challenge was related to voltage efficiency and electrode integration. Due to the small microchannels, the voltage drop across them was large limiting the electric field in the separation region. Higher currents required to improve separation in some cases could therefore lead to excessive Joule heating. Clearly, there is a need for better electrode integration in this system, and many of the current solutions for miniaturized FFE are challenging due to

the additional need for uniform flow through the sidewalls. For future designs, decoupling the fluid and ionic transport through the sidewalls should be considered, such that the ionic current is not subject to the same high-resistance criteria required for hydrodynamic flow. A conductive membrane integration within the separation chamber and near the sidewalls would be ideal, but it should not be permeable to fluid flow or increase the height of the chamber, as this could influence the velocity gradient.

The final technical hurdle is band-broadening. As with most CGF devices, Taylor dispersion is a common issue due the parabolic profile of the counterflow [121]. Therefore, future work in FF-CGF should consider the impact of Taylor dispersion. In terms of theoretical work, it would be beneficial to develop dispersion models to identify optimal conditions for separation. As discussed previously, these models should also consider EOF and the resulting pressure-driven backflow [54]. Fortunately there are several excellent dispersion studies developed for FFE to use as a starting point, including hydrodynamics [53], pressure-driven crossflow, [43] and fluid shear. [63] In terms of experimental work, further studies are required to compare the resolving power of FF-CGF to existing techniques, while innovative designs should be considered to minimize Taylor dispersion.

3.7 Concluding Remarks

The goal of this work was to introduce and validate FF-CGF. First, a mathematical model was presented to describe the focusing mechanism, followed by numerical simulations. Then, design guidelines were provided for the successful operation and fabrication of a FF-CGF device. Upon completing experiments, it was found that the separation profile of the analytes agreed with the simulations, therefore validating the FF-CGF principle and device design. The counterflow gradient was easily adjusted, and unlike capillary-based CGF methods, several analytes could be continuously separated and collected at once.

The results show that the focusing mechanism of FF-CGF offers several advantages over existing FFE methods. Compared to FFZE, the resolution will be less dependent on factors such as the sample injection width and the size of the separation region. As a result, the device footprint can be reduced for simple integration and lower power requirements. Compared to FF-IEF, it is similar in principle, except the focal point is determined by the electrophoretic mobility of the analyte rather than its pI. This offers versatility, as many analytes either do not have a well-defined pI, or have poor solubility at that point. Furthermore, no expensive carrier ampholytes are required, therefore reducing cost. Similarly, when compared to FF-ITP or field-step electrophoresis, no complex buffer compositions or spacers are required. With FFE being used increasingly with mass-spectroscopy [108], the relaxed buffer constraints of FF-CGF are

desirable.

Finally, this initial investigation demonstrates that FF-CGF has the potential for high resolution separations. Unlike FFZE, the separation peaks do not appear to widen significantly as they migrate through the chamber, and there are several possible explanations. For one, the counterflow focusing mechanism is acting as a restoring force that minimizes diffusion. Second, the lack of lateral migration is likely reducing hydrodynamic broadening. Third, there is evidence to suggest that the counterflow combined with the backflow from EOF is suppressing the band-broadening caused by the parabolic flow-profile. Interestingly, this result would imply that Taylor dispersion and electrodynamic dispersion are canceling each other out. Overall, preliminary results appear promising, and should be explored further, both theoretically and experimentally. In doing so, it is recommended that technical issues such as voltage efficiency are also addressed.

Chapter 4

Investigating Peak Dispersion I: Hydrodynamics

The work included in this chapter is published: **M. Courtney**, T. Glawdel, C.L. Ren. Investigation Peak Dispersion in Free-Flow Counterflow Gradient Focusing. Electrophoresis, 43 (2022), 776-784. [169]

Tomasz Glawdel (Adjunct Professor in the Department of Mechanical Engineering, University of Waterloo) assisted in the development of the method of moments formulation and the numerical model.

4.1 Introduction

The purpose of this chapter is to develop a model for understanding dispersion in free-flow counterflow gradient focusing (FF-CGF). Although the preliminary results of FF-CGF have shown promise, peak dispersion must be thoroughly understood to make it a practically useful separation tool. Importantly, an investigation is needed to understand how molecular diffusion and the parabolic profile of the counterflow affect the solute distribution. In doing so, the potential of FF-CGF can be evaluated in terms of separation resolution. Such a study would also enable analytical chemists to predict peak behaviour and optimize the operating conditions for a particular application. Finally, a theoretical framework for peak dispersion will provide engineers with the tools to improve FF-CGF performance further.

At this point, the common sources of dispersion in FFE should be well understood, and their models can be used as a starting point for this chapter (see Chapter 2.1.2). For example, solute peaks in free-flow zone electrophoresis tend to suffer from hydrodynamic dispersion, which is related to the parabolic profile of the pressure-driven flow and its impact on lateral migration distance [53]. Furthermore, there is an additional electrodynamic dispersion source which created due to pressure-driven flow across the chamber that is caused by electroosmotic backflow [54].

Finally, dispersion has also been modeled in free-flow isoelectric focusing (FF-IEF), and there is no hydrodynamic dispersion because the isoelectric point is not influenced by the parabolic profile of the carrier medium. However, electrodynamic dispersion can still be a factor if the electroosmotic backflow is not suppressed [43].

The dispersion of a solute pulse subjected to parabolic flow was originally studied by Taylor [122]. Shortly thereafter, Aris [123] described this mechanism analytically with a method of moments formulation that has recently been employed by Ivory [121] for EGMs and Dutta [53] [54] [43] for several different FFE models. The resulting statistical moments can then be used to estimate the resolution of Gaussian peaks [162]. While this method is a useful starting point for FF-CGF, the following study indicates that the corresponding differential equation is more complicated and may not have an analytical solution. Additionally, numerical simulations show that the focusing mechanism produces an asymmetric peak, and therefore statistical moments are less useful for predicting resolution. As an alternative approach, the simulated concentration profiles can be described with a curve fitting algorithm commonly used to deconvolute skewed chromatographic peaks [170] [171]. In the end, a useful method for analyzing and predicting peak behaviour in FF-CGF is provided, followed by a discussion on the practical implications and future work.

4.2 Modeling Peak Dispersion

The purpose of this section is to understand how the gradient strength and the parabolic counter-flow profile influences the focal position and solute dispersion.

4.2.1 Focal Position

An analytical model for the fluid flow in FF-CGF has been previously derived for a chamber of length L, breadth $2b$, and height $2h$ (see Chapter 3.2). For the scenario presented in Fig. 4.1a, where u_0 is the magnitude of the x-velocity input at the chamber sidewalls ($x = \pm b$ along the z-direction), the resulting solute velocities in the x- and z-direction are defined as:

$$u_{\mathrm{T}}(x,y) = u_{\mathrm{EP}} - \frac{3}{2}\nabla\langle u\rangle x\left(1-\frac{y^2}{h^2}\right) \tag{4.1}$$

$$w(y,z) = \frac{3}{2}\left(\nabla\langle u\rangle z + w_0\right)\left(1-\frac{y^2}{h^2}\right) \tag{4.2}$$

respectively, where u_{EP} is the electrophoretic velocity of the solute for a given electric field $\overrightarrow{E}$, and w_0 is the inflow z-velocity at $z = 0$. The term $\nabla\langle u\rangle = u_0/b$ represents the x-velocity gradient

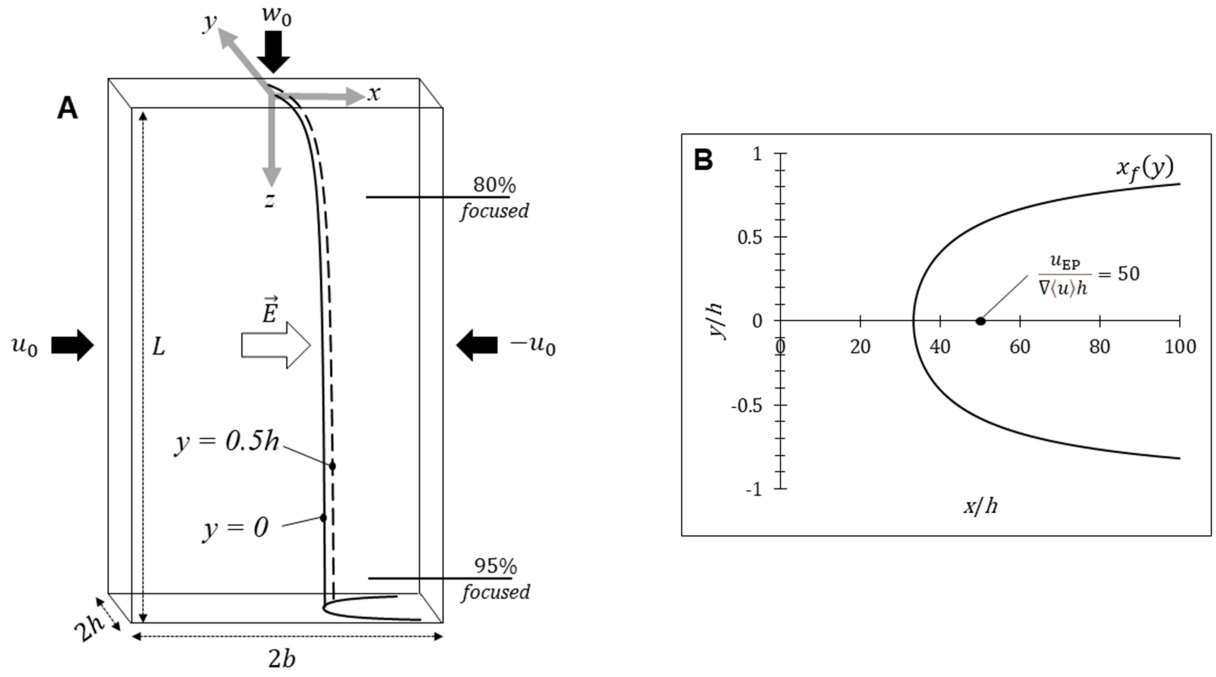


Figure 4.1: a) A schematic of an FF-CGF device with focal points at different y-positions. b) The focal position along the height direction due to the parabolic profile of the counterflow.

on each side of the chamber, and while it is scalar, the ∇ notation enables a more compact form. By setting $u_{\mathrm{T}}(x,y) = 0$, the focal point of a solute along the height direction is given as:

$$x_f(y) = \frac{2}{3}\frac{u_{EP}}{\nabla\langle u\rangle}\left(1 - \frac{y^2}{h^2}\right)^{-1} \tag{4.3}$$

Fig. 4.1b shows that the resulting focal point reflects the parabolic nature of the counterflow. Consequently, the smearing seen near the top and bottom of the chamber will increase peak dispersion. It is helpful to visualize this effect as the solute travels along the z-direction (see Appendix A.1 for derivation):

$$x(y,z) = x_f(y)\left[1 - \left(1 + \frac{\nabla\langle u\rangle}{w_0}z\right)^{-1}\right] \tag{4.4}$$

Eq. 4.4 with $x_f(y)$ evaluated at different y-positions is shown in Fig. 4.1a, and the separation distance between the curves can help predict the peak width. Eq. 4.4 also shows that a solute

will approach its focal point asymptotically. Therefore, it is helpful to redefine Eq. 4.4 relative to $x_f(y)$ to understand the level of focusing within the chamber (see Fig. 4.1a):

$$\frac{\%focused}{100} = 1 - \left(1 + \frac{\nabla \langle u \rangle}{w_0} z\right)^{-1} \tag{4.5}$$

Note how w_0 and the chamber length ($z = L$) can play a role in the level of focusing.

4.2.2 Convection-Diffusion Model

The concentration profile of the solute distribution can be modeled using the convection-diffusion equation [121]:

$$\frac{\partial c}{\partial t} + \nabla \cdot (\mathbf{u}c) = \nabla \cdot (D \nabla c) \tag{4.6}$$

where c is the concentration of the solute, $\mathbf{u}$ is the vector velocity, D is the diffusion coefficient, and ∇ is the gradient operator. Then, substituting the Eq. 4.1 into Eq. 4.6, the focusing mechanism in the x-y cross-section is represented as:

$$\frac{\partial c}{\partial t} - \frac{3}{2} \nabla \langle u \rangle x \left(1 - \frac{y^2}{h^2}\right) \frac{\partial c}{\partial x} + u_{\mathrm{EP}} \frac{\partial c}{\partial x} = D \frac{\partial^2 c}{\partial x^2} + D \frac{\partial^2 c}{\partial y^2} + \left[\frac{3}{2} \nabla \langle u \rangle \left(1 - \frac{y^2}{h^2}\right) c\right] \tag{4.7}$$

Note that Eq. 4.6 presents a simplified 2D dispersion model because a solute will migrate towards its focal point independent of the z-velocity. Consequently, this model is more appropriate for situations where the solute distribution approaches equilibrium ($\sim 95\%$ focused). Now, Eq. 4.6 can be written in dimensionless form as:

$$\frac{\partial c^*}{\partial t^*} - \frac{3}{2} G_x x^* \left(1 - y^{*^2}\right) \frac{\partial c^*}{\partial x^*} + Pe_{\mathrm{EP}} \frac{\partial c^*}{\partial x^*} = \frac{\partial^2 c^*}{\partial x^{*^2}} + \frac{\partial^2 c^*}{\partial y^{*^2}} + \left[\frac{3}{2} G_x \left(1 - y^{*^2}\right) c^*\right] \tag{4.8}$$

where $t^* = Dt/h^2$, $x^* = x^*/h$, $y^* = y/h$, $Pe_{\mathrm{EP}} = u_{\mathrm{EP}} h/D$, $G_x = \nabla \langle u \rangle h^2/D$, $c^* = c/c_0$, and c_0 is the initial solute concentration. Note that Pe_{EP} is the Peclet number for the electrophoretic velocity and G_x is the gradient number for the counterflow [121]. These dimensionless quantities are useful for describing the convective transport relative to the diffusive transport. Finally, note that the electrophoretic term assumes that there are no variations in the local electric field due to the focused solute. Interestingly, the solute stream is being simultaneously concentrated and diluted, so the concentration is not expected to increase relative to the initial concentration.

Shifted Coordinate for $G_x < 1$

When using numerical simulations to solve Eq. 4.8, it is helpful to apply a shifted coordinate system to reduce computation efforts. As will be seen in the following sections, most of the solute is concentrated around the average focal position when $G_x < 1$. Therefore, applying a shifted coordinate of $x = x_f + u_{\mathrm{EP}}/\nabla \langle u \rangle$ to Eq. 4.7, the dimensionless form can be written as:

$$\begin{aligned} \frac{\partial c^*}{\partial t^*} - \frac{3}{2} G_x x_f^* \left(1 - y^{*^2}\right) \frac{\partial c^*}{\partial x_f^*} + Pe_{\mathrm{EP}} \left(1 - \frac{3}{2}\left(1 - y^{*^2}\right)\right) \frac{\partial c^*}{\partial x_f^*} \\ = \frac{\partial^2 c^*}{\partial x_f^{*^2}} + \frac{\partial^2 c^*}{\partial y^{*^2}} + \left[\frac{3}{2} G_x \left(1 - y^{*^2}\right) c^*\right] \end{aligned} \tag{4.9}$$

Shifted Coordinate for $G_x > 1$

For $G_x > 1$, it will be seen in the following sections that the solute becomes increasingly focused at the centerline position along the parabolic profile, and therefore a shifted coordinate of $x = x_f + 2u_{\mathrm{EP}}/3\nabla \langle u \rangle$ is more appropriate for these situations. Applying this alternative shifted coordinate to Eq. 4.7, and the dimensionless form can be written as:

$$\frac{\partial c^*}{\partial t^*} - \frac{3}{2} G_x x_f^* \left(1 - y^{*^2}\right) \frac{\partial c^*}{\partial x_f^*} + Pe_{\mathrm{EP}} y^{*^2} \frac{\partial c^*}{\partial x_f^*} = \frac{\partial^2 c^*}{\partial x_f^{*^2}} + \frac{\partial^2 c^*}{\partial y^{*^2}} + \left[\frac{3}{2} G_x \left(1 - y^{*^2}\right) c^*\right] \tag{4.10}$$

4.2.3 Time Dependence

Given that the dispersion model shown in Eq. 4.7 has a time dependence, it is helpful to know the exact time scale during numerical simulations. Recall from Chapter 3.2.3 was derived as:

$$t = \frac{1}{\nabla \langle u \rangle} \ln\left(1 + \frac{\nabla \langle u \rangle}{\langle w \rangle_0} z\right) \tag{4.11}$$

Therefore, the dimensionless from of time can be related to the z-position in the chamber as follows:

$$t^* = \frac{1}{G_x} \ln\left(1 + \frac{G_x}{Pe_Z} z^*\right) \tag{4.12}$$

where $Pe_z = w_0 h/D$, and this will help determine the length of the chamber required for high levels of focusing. Alternatively, the time can be related to the x-position in that chamber to

approximate a peak dispersion as the solute approaches equilibrium conditions ($\sim 95\%$ focused). Recall the derivation from Chapter 3.2.3:

$$x = \frac{u_{\mathrm{EP}}}{\nabla \langle u \rangle} \left(1 - e^{-\nabla \langle u \rangle t}\right) \tag{4.13}$$

When rearranged to be relative to the average focal point, the above equation can be written in terms of the level of focusing:

$$\frac{\%focused}{100} = \left(1 - e^{-\nabla \langle u \rangle t}\right) \tag{4.14}$$

Finally, the above equation can be written in its dimensionless form, and this can be helpful for determining the time steps during numerical simulations:

$$t^* = -\frac{1}{G_x} \ln\left(1 - \frac{\%focused}{100}\right) \tag{4.15}$$

It should be noted that the above equations are valid when the sample is injected at $x = 0$, and larger sample injection widths will require longer focusing times that are beyond the scope of this work. The Appendix contains additional information on the level of focusing required to reach steady-state (see Appendix A.2), as well as a method for approximating sample dilution due to the addition of pressure-driven flow from the sidewalls (see Appendix A.3).

4.3 Methodology

First, this section will outline the method of moments formulation. Unlike other FFE modes, it will be seen that it does not yield an analytical solution, and the approximate solutions are not useful due to the non-Gaussian behaviour of the focused peaks. Therefore, an alternate approach to understanding peak dispersion will be provided by combining numerical simulations with an asymmetric curve fitting method.

4.3.1 Method of Moments Approach

An analytical solution to Eq. 4.8 would be ideal to reduce the computation efforts needed to understand peak dispersion. A method of moments approach is commonly used to solve the convection-diffusion equation in FFE [53] [54] [43]. According to Dutta, the *n*th moment of a solute distribution is:

$$M_n = \int_{-1}^{1} \int_{-\infty}^{\infty} {x^*}^n c^*(x^*, y^*)\, dx^* dy^* \tag{4.16}$$

Note that this is presented in dimensionless form for both the x- and y-direction, and it is assumed that the x-direction is infinitely long.

Moment Statistics

The moments can then be used to calculate the key parameters of a solute distribution, such as mean position μ, variance σ^2, skewness κ_1, and kurtosis κ_2 [172]:

$$\mu = \frac{M_1}{M_0} \tag{4.17}$$

$$\sigma^2 = \frac{M_2}{M_0} - \left(\frac{M_1}{M_0}\right)^2 \tag{4.18}$$

$$\kappa_1 = \frac{M_3/M_0 - 3(M_1/M_0)(M_2/M_0) + 2\left(M_1/M_0\right)^3}{\left(\sqrt{M_2/M_0 - \left(M_1/M_0\right)^2}\right)^3} \tag{4.19}$$

$$\kappa_2 = \frac{M_4/M_0 - 4(M_1/M_0)(M_3/M_0) + 6\left(M_1/M_0\right)^2(M_2/M_0) - 3\left(M_1/M_0\right)^4}{\left(M_2/M_0 - \left(M_1/M_0\right)^2\right)^2} \tag{4.20}$$

Formulation

For this formulation, it is assumed that Eq. 4.8 is solved under steady-state conditions for simplification, and this means that the time-dependence it removed. Furthermore, the boundary conditions can be written as [53]:

$$\text{BC 1:} \quad c^*, \frac{\partial c^*}{\partial x^*} = 0 \text{ as } x^* \to \pm\infty$$

$$\text{BC 2:} \quad \frac{\partial c^*}{\partial y^*} = 0 \text{ at } y^* = \pm 1$$

The first step in achieving a method-of-moments formulation is multiplying Eq. 4.8 by x^{*^n}:

$$Pe_{\text{EP}} x^{*^n} \frac{\partial c^*}{\partial x^*} - \frac{3}{2} G_x \left(1 - y^{*^2}\right) x^{*^{n+1}} \frac{\partial c^*}{\partial x^*} = x^{*^n} \frac{\partial^2 c^*}{\partial x^{*^2}} + x^{*^n} \frac{\partial^2 c^*}{\partial y^{*^2}} + \frac{3}{2} G_x \left(1 - y^{*^2}\right) x^{*^n} c^* \tag{4.21}$$

Then, integrating along the x^*-coordinate from $-\infty$ to ∞, the following integrals must be solved as follows:

$$\int_{-\infty}^{\infty} x^{*^n} \frac{\partial c^*}{\partial x^*} \partial x^* = x^{*^n} c^* |_{-\infty}^{\infty} - n \int_{-\infty}^{\infty} x^{*^{n-1}} c^* \partial x^* = -n\phi_{n-1} \tag{4.22}$$

$$\int_{-\infty}^{\infty} x^{*^{n+1}} \frac{\partial c^*}{\partial x^*} \partial x^* = x^{*^{n+1}} c^* |_{-\infty}^{\infty} - (n+1) \int_{-\infty}^{\infty} x^{*^n} c^* \partial x^* = -(n+1)\,\phi_n \tag{4.23}$$

$$\int_{-\infty}^{\infty} x^{*^n} \frac{\partial^2 c^*}{\partial x^{*^2}} \partial x^* = x^{*^n} \left. \frac{\partial c^*}{\partial x^*} \right|_{-\infty}^{\infty} - n \int_{-\infty}^{\infty} x^{*^{n-1}} \frac{\partial c^*}{\partial x^*} \partial x^* = -n(n-1)\phi_{n-2} \tag{4.24}$$

where $\phi_n = \int_{-\infty}^{\infty} x^{*^n} c^* dx^*$. Note that BC 1 was applied to solve the above integrals, and this results in the following equation:

$$\frac{\partial^2 \phi_n}{\partial y^{*^2}} - n\frac{3}{2} G_x \left(1 - y^{*^2}\right) \phi_n = -nPe_{\mathrm{EP}} \phi_{n-1} + n\,(n-1)\,\phi_{n-2} \tag{4.25}$$

Note that the above differential equation can be solved for ϕ, and this can be related to the nth moment as $m_n = \int_{-1}^{1} \phi_n dy^*$. When $n = 0$, and by applying the appropriate boundary conditions it can be shown that $\phi_0 = \delta$, where δ is a constant which represents the total mass of solute in the system [53]. When $n = 1$, Eq. 4.25 can therefore be written as:

$$\frac{\partial^2 \phi_1}{\partial y^{*^2}} - \frac{3}{2} G_x \left(1 - y^{*^2}\right) \phi_1 = -Pe_{\mathrm{EP}} \delta \tag{4.26}$$

Note that the homogeneous component of this equation is similar to the form of an equation known as the Weber parabolic cylinder function [173]. In fact, by making the substitution $y^* = \eta / \left((3G_x/2)^{1/4}\sqrt{2}\right)$ and letting $a = \sqrt{3G_x/2}/2$:

$$\frac{\partial^2 \phi_1}{\partial \eta^2} + \left(\frac{1}{4}\eta^2 - a\right) \phi_1 = -\frac{Pe_{\mathrm{EP}} \delta}{2\sqrt{3G_x/2}} \tag{4.27}$$

where the homogeneous component is the Weber parabolic cylinder function. For increasing values of n, the equation will maintain this form. Unfortunately, there is no clean analytical equation for this function [173], and approximations become increasingly complicated in its inhomogeneous form [174]. Preliminary attempts to approximate a solution were unsuccessful, so a built-in MATLAB solver of ordinary differential equations was used instead.

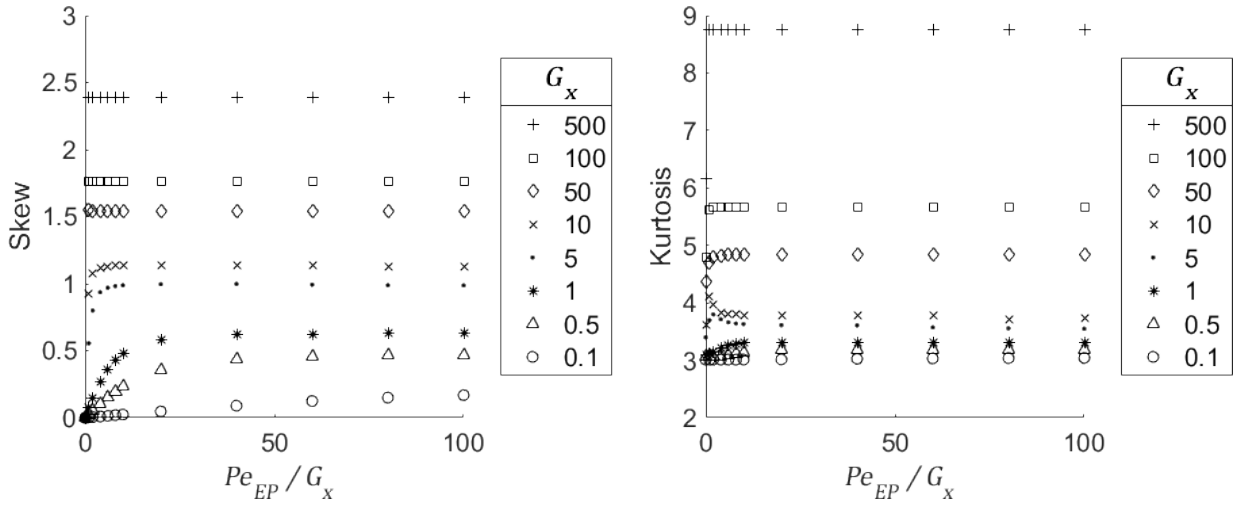


Figure 4.2: Skew and kurtosis for different G_x values as a function of Pe_{EP}/G_x. COMSOL simulations were used to evaluate $G_x < 10$, and the method of moments formulation was used to $G_x > 10$.

Evaluation

Moment analysis has also been used in chromatography for the last several decades, and it can be helpful for understanding the shape of a solute distribution [175] [176]. For example, the skew is related to the symmetry of the peak, where positive values indicate a right-tailed curve and negative values indicate a left-tailed curve. The kurtosis, or excess, is less intuitive, but can be related to the flatness of a peak. In chromatography, a kurtosis greater than 3 suggests that the fraction of solute in the tails of the peak is greater than that of Gaussian, while values less than 3 suggest that there is less solute in the tails. Fig. 4.2 shows the skew and kurtosis of solute peaks at their equilibrium position. They are plotted for different G_x values as a function of Pe_{EP}/G_x. For $G_x \leq 10$, the method-of-moments formulation was inaccurate for reasons that have yet to be determined. Therefore, COMSOL simulations of the 2D solute distribution were used for this range (see Section 4.3.2 for more details). At $G_x = 0.1$, the skew remains small enough to be considered similar to that of a Gaussian distribution, but note that it gradually increases with increasing Pe_{EP}. As G_x approaches 1, the skew rises to the point where a Gaussian is no longer appropriate. However, the kurtosis remains close to 3. As G_x increases beyond 1, both the skew and the kurtosis indicate that a Gaussian distribution is no longer applicable. In fact, as G_x continues to increase, it can be seen that both the skew and the tailing become quite significant. Therefore, because the distribution is non-Gaussian and there is no analytical solution to Eq. 4.25, the moment analysis is not useful for predicting separation performance in FF-CGF, and other methods need to be employed.

4.3.2 Numerical Simulation Approach

A commercial software package (COMSOL, v5.3) was used to solve Eq. 4.9 and Eq. 4.10 using the Transport of Diluted Species module, and the resulting separation peaks are shown in Fig. 4.3 for different dimensionless parameters. Note that the term in square brackets for Eq. 4.9 and Eq. 4.10 must be added as a reaction rate in COMSOL to account for the continuous counter-flow input and avoid a concentration sink. To improve the computation efficiency, a symmetric boundary condition was used at $y^* = 0$, and a shifted coordinate system was applied around the focal point. The simulation assumes a relatively small sample injection width of $3h$ centered around $x = 0$, though the model can be readily applied to larger widths if needed. Finally, the solute peaks were measured by taking the linear projection of the concentration onto $y^* = 0$, as this represents the average concentration along the height direction.

4.3.3 Curve Fitting Approach

Non-Gaussian solute distributions are frequent in chromatography due to extra-column effects [170] [176] [175]. These peaks are often fitted with asymmetric curves to resolve overlapping distributions [170]. A common function used during this process is the exponentially modified Gaussian (EMG), which represents the convolution of a Gaussian and exponential distribution, and can be written as [177] [178]:

$$f_{\mathrm{EMG}}(x) = \frac{1}{2\tau} \exp\left(\frac{1}{2\tau}\left(2\mu_G + \frac{\sigma_G^2}{\tau} - 2x\right)\right) \times \mathrm{erfc}\left(\frac{\mu_G + \frac{\sigma_G^2}{\tau} - x}{\sqrt{2}\sigma_G}\right) \tag{4.28}$$

where μ_G is the mean position of the Gaussian component, σ_G is the standard deviation of the Gaussian component, τ represents the decay rate of the exponential component, and erfc is the complementary error function. The EMG function is popular because it can fit to a wide range of curves, and its parameters have physical relevance [171]. In particular, its statistical moments are readily available, including a mean position of $M_1 = \mu_G + \tau$, and a standard deviation of $M_2 = \sigma_G^2 + \tau^2$ [179].

In FF-CGF, the asymmetric behaviour of the solute distributions makes the EMG a good candidate for modeling. Therefore, the simulated COMSOL peaks can be normalized to an area of 1 and then fit using a nonlinear least-squares method in MATLAB (see Fig. 4.4). The peaks were fitted at 95% focused according to Eq. 4.15, as this provides a useful estimate for steady-state conditions (Appendix A.2). For $G_x \leq 5$, the EMG can be fitted to the simulated peaks with reasonable accuracy. For $G_x > 5$, a concentrated solute region begins to emerge near the centerline, followed by a long peak tail that is difficult to model with the EMG or any other

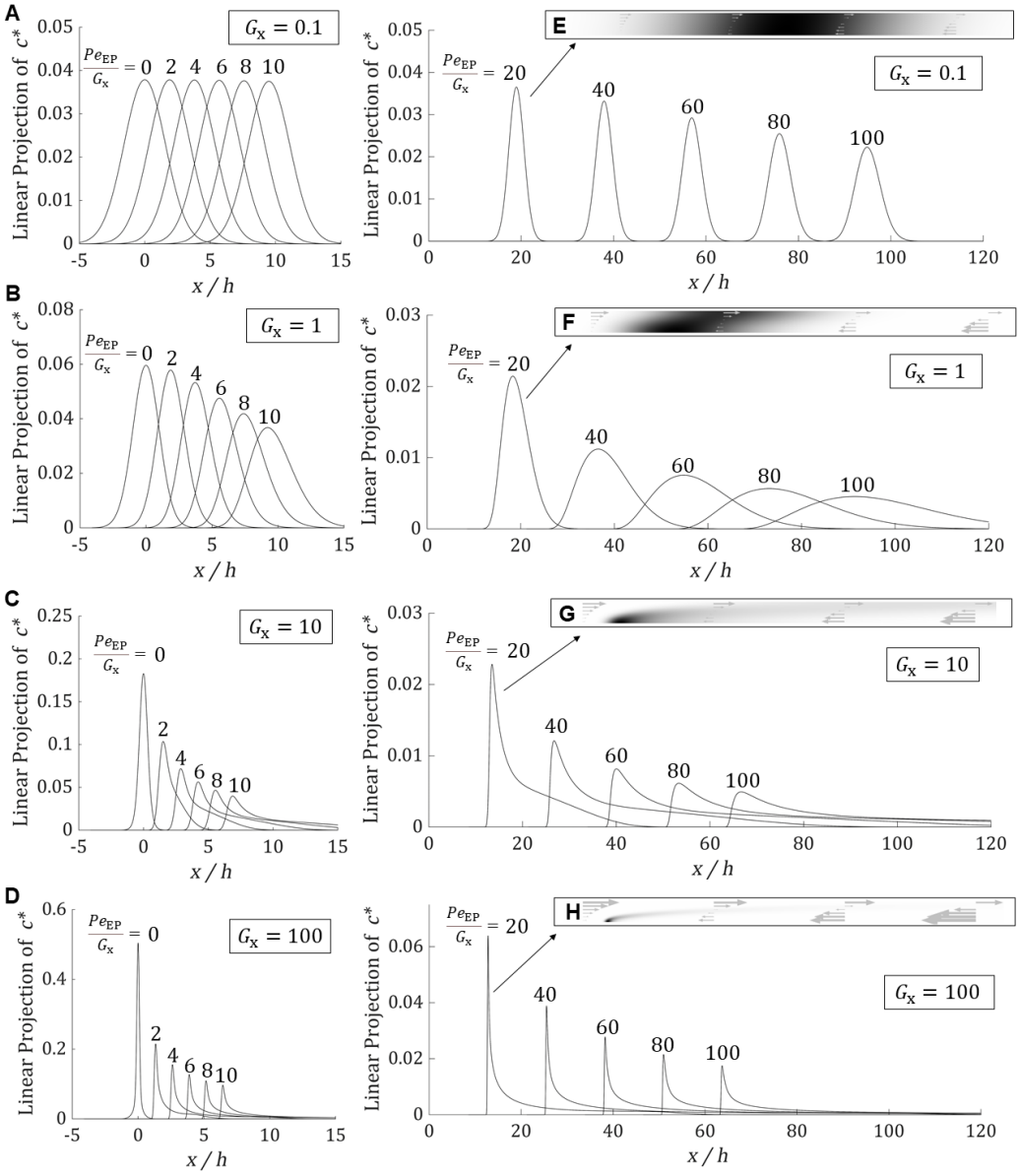


Figure 4.3: The simulated separation peaks at 95% focused for different Pe_{EP}/G_x values at a) $G_x = 0.1$, b) $G_x = 1$, c) $G_x = 10$, and d) $G_x = 100$. The simulated solute concentration distribution and x-velocity field at $Pe_{EP}/G_x = 20$ for e) $G_x = 0.1$, f) $G_x = 1$, g) $G_x = 10$, and h) $G_x = 100$.

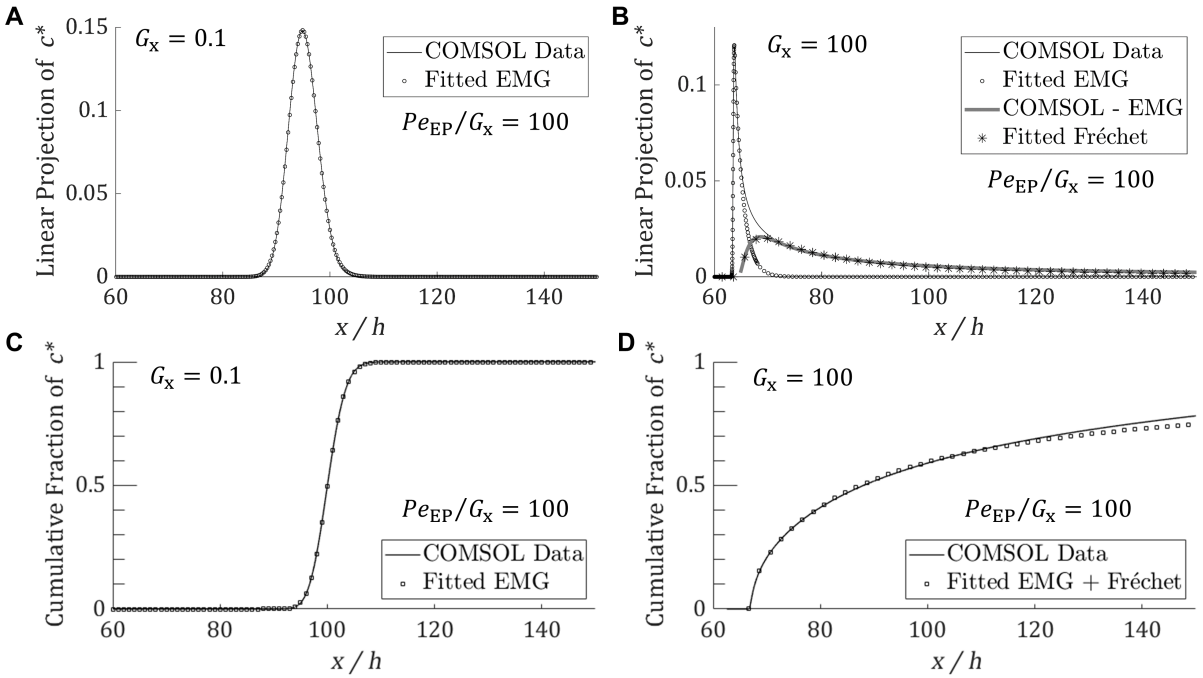


Figure 4.4: Normalized simulated peaks fitted with the EMG and EV functions for a) $G_x = 0.1$ and b) $G_x = 100$. The cumulative distribution functions for the simulated and fitted peaks at c) $G_x = 0.1$ and d) $G_x = 100$.

asymmetric function (see Fig. 4.4b). With that said, the concentrated region resembles an EMG, and is easily distinguishable from the tail region. As a result, this region can be cut-off at the location of the half maximum and fitted with an EMG. An advantage of this approach is that it maintains consistency with lower G_x values, and the EMG parameters of the concentrated region have a physical relevance that can be used when evaluating the resolution of these heavily skewed peaks.

After fitting the concentrated region with the EMG and then subtracting this function from the original simulated peak, the resulting peak was found to resemble an extreme value (EV) distribution, which is written as [180].

$$f_{\mathrm{EV}}(x) = \frac{|\alpha|}{\sigma_{EV}} \left(\frac{x - \mu_{EV}}{\sigma_{EV}} \right)^{-(1+\alpha)} \exp\left[- \left(\frac{x - \mu_{EV}}{\sigma_{EV}} \right) \right]^{-\alpha} \tag{4.29}$$

for $x \geq \mu_{EV}$, and $f_{\mathrm{EV}}(x) = 0$ for $x < \mu_{EV}$. It should be noted that μ_{EV} is a location parameter, σ_{EV} is a scale parameter, and α is a shape parameter that is negative for the Weibull distribution

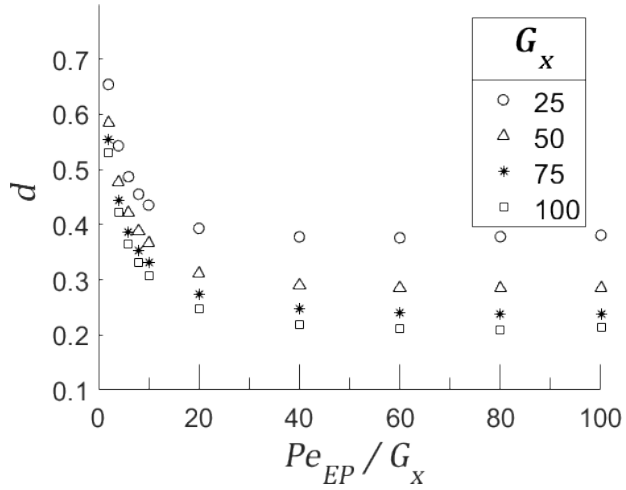


Figure 4.5: Mixing parameter representing the fraction of solute that is in the EMG component for high G_x values.

and positive for the Fréchet distribution. For $5 < G_x \leq 20$, it was seen that a Weibull fit works well, while the Fréchet fit is more appropriate for higher G_x values (see Fig. 4.4b). In the end, the simulated COMSOL peak can be written as a linear combination of the EMG and EV functions [180]:

$$f(x) = d\, f_{\mathrm{EMG}}(x) + (1-d)\, f_{\mathrm{EV}}(x) \tag{4.30}$$

where d is a mixing parameter that can range from 0 to 1. An advantage of Eq. 4.30 is that d can provide information about the fraction of solute that is found within the highly concentrated region (see Fig. 4.5). More generally, the cumulative distribution function for Eq. 4.30 is particularly useful for FFE applications (see Fig. 4.4c and 4.4d), as it can be used to predict the amount of solute collected at each outlet, and the overlap of neighboring peaks.

4.4 Results and Discussion

The goal of this section is to analyze the simulated peaks for different G_x regimes to understand their physical behaviour and evaluate the potential of FF-CGF as a separation tool.

4.4.1 Small Gradient Regime ($G_x \leq 1$)

For $G_x = 0.1$, Fig. 4.3a shows that the solute peaks resemble a symmetric curve for a wide range of Pe_{EP} values. As Pe_{EP}/G_x approaches 100, a subtle skew emerges due to the increasing

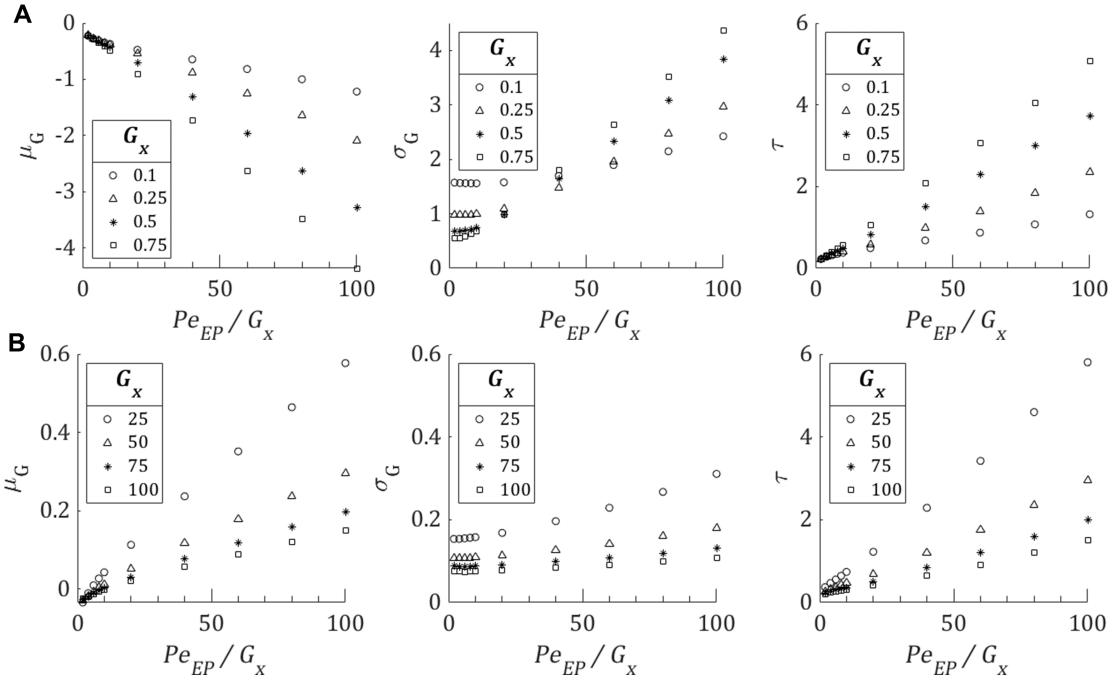


Figure 4.6: The EMG fitting parameters for different dimensionless parameters for both a) small gradients ($G_x < 1$) and b) large gradients ($G_x > 20$).

influence of convection and the parabolic nature of the focusing mechanism. As the value of G_x approaches 1, Fig. 4.3b shows that the presence of this skew becomes more prominent for smaller Pe_{EP}/G_x values.

Fig. 4.4a provides an example of the EMG fit at $G_x = 0.1$ and $Pe_{\mathrm{EP}}/G_x = 100$, while the corresponding cumulative distribution is shown in Fig. 4.4c. Fig. 4.6a shows that the fitting parameters can provide useful information about the peak behaviour. First, μ_G, which defines the x-position relative to the area-averaged focal point, becomes more negative as G_x and Pe_{EP}/G_x increase, and this means that the focal position is shifting closer to the centreline. Second, σ_G and τ show that the peak width and asymmetry are low for $G_x = 0.1$, and begin to increase as G_x and Pe_{EP} increase due to the influence of the parabolic velocity profile. Finally, there are evident trends for the fitting parameters that can be used to estimate peak behavior, and these can be found in Appendix A.4.

For practical use, working in this regime can be effective, especially around $G_x = 0.1$, as the peak dispersion is relatively stable for a wide range of Pe_{EP} values. Furthermore, there is no peak tailing, which means that the contamination of neighboring peaks can be well-controlled.

Moreover, Pe_{EP} values required for focusing in this range are relatively low, so Joule heating will be minimal. One drawback of working in this regime is that the fluid velocity is slow, and therefore the throughput will be limited. While increasing the initial z-velocity can increase throughput without increasing dispersion, Eq. 4.5 suggests that this will require long chamber lengths to achieve a high focusing percentage.

4.4.2 Transition Gradient Regime ($1 \leq G_x \leq 20$)

The solute peaks in this regime experience a significant change in shape. Fig. 4.3b shows that the peaks at $G_x = 1$ continue to resemble a skewed Gaussian, while Fig. 4.3c shows that the peaks at $G_x = 10$ become much more asymmetric due to the increasing influence of the parabolic counterflow and the diminishing diffusive transport. In general, the peaks in this regime are quite dispersed and it is not recommended to work in this range. Consequently, further information on the curve fitting process and the resulting fitting parameters was moved to Appendix A.4.

4.4.3 Large Gradient Regime ($G_x > 20$)

Although the asymmetric trend continues in this regime, some interesting properties emerge that may be useful for FFE applications. For example, Fig. 4.3d shows solute peaks for $G_x = 100$ over a wide range of Pe_{EP}/G_x values, and the concentrated region is very narrow, while the tail region is less prominent. Fig. 4.4b shows an example of how a peak in this regime can be fit with an EMG and a Fréchet function. The corresponding cumulative distribution shown in Fig. 4.4d shows that the quality of fit is initially strong, but then beings to diverge at the far end of the tail. With that said, the fraction of solute in this region is so small that the difference between the curves is negligible in practice.

The fitting parameters for this regime are shown in Fig. 4.6b for a wide range of dimensionless numbers and they provide some useful information about the peak behaviour. First, μ_G, which is defined as the centre of mass relative to the centreline position and can be seen to decrease with increasing G_x due to the increasing strength of the focusing mechanism. Both σ_G and τ also decrease with increasing G_x, and this represents the decreasing width of the EMG component. As Pe_{EP}/G_x increases, all three parameters increase due to the influence of the parabolic profile. Once again, there are evident trends that can be used to predict peak behavior, and they are provided in Appendix A.4. The fitting parameters for the Fréchet distribution have less physical relevance, though they remain useful for predicting tail behaviour, and the trendlines are provided in Appendix A.4.

In terms of practical use, working in this regime can be effective when peak identification is a priority. Fig. 4.3d shows that the concentrated region is very narrow and easily distinguishable

from the tail region. As a result, this can enable separations with a high resolution and a large peak capacity. When purification is the priority, one drawback of this regime is that the significant peak tailing will lead to contamination between neighboring peaks and loss of sample. For example, at $G_x = 100$ and $Pe_{\mathrm{EP}}/G_x = 100$, Fig. 4.4d shows that only about 20% of the solute is contained within the concentrated region. Another disadvantage is that the large Pe_{EP} values in this regime require high electric fields, which may lead to excessive Joule heating. With that said, looking again at Fig. 4.3d, it is possible to imagine a scenario where a neutral solute is focused at $Pe_{\mathrm{EP}}/G_x = 0$, while four additional solutes are focused at $Pe_{\mathrm{EP}}/G_x = \pm 2$ and $Pe_{\mathrm{EP}}/G_x = \pm 10$. The overlap between these peaks is low, and may be particularly useful for separating protein isoforms [104]. Moreover, Eq. 4.5 indicates that a high initial z-velocity is reasonable for high G_x values, and this will enable a high throughput for preparative-scale applications.

4.4.4 Comparison to Free-Flow Zone Electrophoresis

The second moment of the EMG, $M_2 = \sigma_G^2 + \tau^2$, becomes useful for predicting the peak width in FF-CGF, and enables a comparison to FFZE. The optimal peak width in FFZE has been previously derived, and its dimensionless form can be written as [54]:

$$\frac{\sigma_{\min}}{h} = \sqrt{\frac{\delta^{*2}}{12} + \left[\frac{8}{150}\left(S^{*2} + \frac{1}{L^{*2}}S^{*4}\right)\right]^{\frac{1}{2}}} \tag{4.31}$$

where $L^* = L/h$ represents the length of the chamber, S^* represents the lateral migration distance, and $\delta^* = \delta/h$ represents the sample injection width. If δ^* is neglected, the ideal standard deviation is plotted in Fig. 4.7 as a function of S^*. In comparison, the fitting parameters are used to plot the second moment in FF-CGF for $G_x = 0.1$ and $G_x = 100$. While $G_x = 100$ neglects the tail component, it is reasonable to assume that the EMG component is sufficient for peak identification applications. As a result, Fig. 4.7 shows that the theoretical resolution for FF-CGF is better than FFZE for a wide range of lateral migration distances. Furthermore, the resolution of FF-CGF is not limited by a narrow sample injection width, and this becomes advantageous for high throughput applications. Moreover, $\sigma_{\min}$ in FFZE depends strongly on the z-velocity, which may also restrict sample throughput [53]. Finally, the focusing mechanism in FF-CGF will provide additional forgiveness when there are pressure fluctuations caused by the pump [86].

4.4.5 Future Considerations

Sample injection is a factor that deserves further attention in FF-CGF. For one, increasing sample injection width can increase sample throughput significantly. Additionally, to combat sample

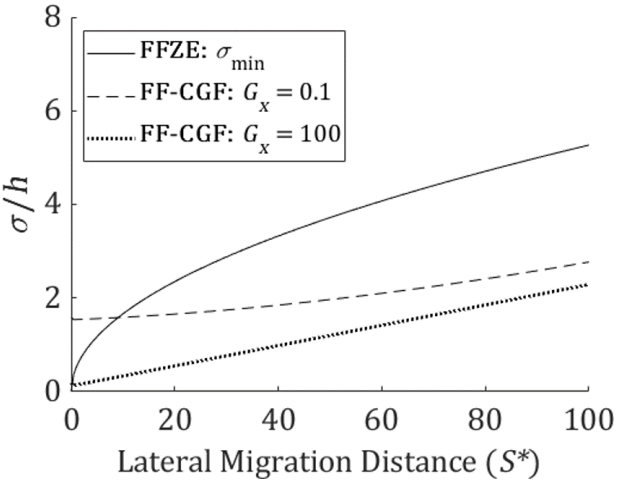


Figure 4.7: Comparing the optimal peak width in FFZE ($L^* = 1000$) to the peak width of the EMG component at $G_x = 0.1$ and $G_x = 100$. The lateral migration distance is $S^* = Pe_{\mathrm{EP}}/G_x$ for $G_x = 0.1$ and $S^* = 2Pe_{\mathrm{EP}}/3G_x$ for $G_x = 100$.

dilution, increasing the sample injection width can be a useful strategy for increasing sensitivity in peak identification applications. While the peak dispersion model presented in this study is valid for solute peaks that have reached their equilibrium width, there may be situations where it is acceptable to collect separated fractions before reaching this point. This is especially true for larger sample injection widths, as they will require longer focusing times that may not be feasible for a given chamber length. On another note, it would also be helpful to consider situations where the sample injection is focused in the height direction [181], as this could limit peak tailing at large G_x values. Interestingly, the mixing parameter d can provide a useful reference for the level of focusing that is required in the height direction to mitigate the peak tail.

There are additional peak broadening sources that should be considered in future studies. First, understanding the pressure-driven backflow caused by EOF is important, as this will have an influence on the parabolic profile of the counterflow [54]. Second, the interplay between the concentrated peaks and the sample dilution will have an interesting influence on electrohydrodynamic broadening [38].Third, it is important to study Joule heating, as the resulting density gradients at the preparative scale will contribute to broadening. It is interesting to refer to recycling IEF [45] [182], which is closely related to FFE. While this system addresses the slow focusing in FF-IEF, its short buffer residence times minimized Joule heating, and the high flow velocities minimized the natural convection caused by density gradients. For the high G_x values in FF-CGF, the flow velocities will also be high, and this may help counteract the Joule heating caused by the high Pe_{EP} values. Furthermore, the continuous addition of flow from the sidewalls

may provide additional cooling that should be considered.

Finally, there are some practical considerations for FF-CGF devices that deserve further attention. In particular, the inflow from the sidewalls must be uniform along the length of the chamber while maintaining a reasonable voltage drop across the chamber [164]. Maximizing the voltage efficiency and minimizing Joule heating is especially important for high Pe_{EP} values.

4.5 Concluding Remarks

In this work, a 2D model was presented to understand peak dispersion in FF-CGF. Through numerical simulation, the gradient number for the counterflow, G_x, was found to be particularly useful for understanding how molecular diffusion and the counterflow gradient influence peak shape. At small G_x numbers ($G_x < 1$), the solute distribution could be fitted with a skewed Gaussian distribution. Working around $G_x = 0.1$ will provide a high resolution with low peak contamination and applied voltages, though the throughput will be limited. At large G_x numbers ($G_x > 20$), the peak shape changes dramatically, as there is a concentrated region that can be fitted with a skewed Gaussian, followed by a long tail region. Working around $G_x = 100$ will provide a high resolution and throughput, though the peak contamination and applied voltages will be large. Overall, driven by the promise offered by FF-CGF as compared to the existing FFE techniques, the findings presented in this study are very useful for understanding and developing the technology further. Furthermore, the fitting parameters provided in this study can provide a practical method for estimating peak behaviour and can be used during experiments to deconvolute skewed peaks.

Chapter 5

Investigating Peak Dispersion II: Electrodynamics

Tomasz Glawdel (Adjunct Professor in the Department of Mechanical Engineering, University of Waterloo) assisted in the development of the analytical model for electroosmotic flow.

5.1 Introduction

The purpose of this chapter is to continue the investigation on peak dispersion in FF-CGF by accounting for the electroosmotic flow (EOF) in the system. First, various models will be presented to demonstrate how EOF impacts the counterflow velocity profile and the resulting solute dispersion. Then, experimental results will be presented to observe the influence of EOF in practice.

5.1.1 Motivation

EOF is a well-known phenomenon that arises in electrophoresis due to the formation of a nonuniform ion distribution near the charged wall of a capillary or microchannel [183]. This thin layer is often referred to as the electric double layer because it consists of an immobile and mobile phase, and it has net charge that is opposite to that of the solid surface. In the presence of an electric field, a force is exerted on the mobile layer which generates a viscous drag on the bulk solution, and this produces the EOF. The resulting velocity profile is relatively flat, and it is used in combination with electrophoretic velocity to determine the migration of different solutes. Consequently, EOF is an important parameter for predicting separation performance in electrophoretic devices, and it depends on a number of factors including pH, ion concentration, viscosity, and surface composition [56] [184].

In free-flow electrophoresis (FFE), understanding EOF is particularly important because it can also influence peak dispersion [39]. In a traditional FFE device, EOF moves in the direction of the electric field, and it is blocked at the sidewalls due to the presence of the ion-exchange membranes [38]. As a result, a pressure-driven backflow is created to counterbalance the EOF, and it has a parabolic velocity profile that can impact lateral migration distance [22]. This leads to electrodynamic dispersion, and the resulting solute distortion is similar to the hydrodynamic dispersion caused by the parabolic velocity profile of the carrier medium. Moreover, in FFZE there is an interplay between these two broadening sources, and electrodynamic dispersion can either increase or decrease the impact of hydrodynamic dispersion depending on the direction and magnitude of EOF [54]. Therefore, EOF should be carefully considered when optimizing the separation resolution in FFE. In practice, it is also possible to alter or suppress EOF with wall coatings and buffer additives that manipulate the surface charge and local viscosity [37] [185]. Furthermore, some FFE designs have managed to implement an open sidewall design in an effort to avoid EOF blockage [90].

In free-flow counterflow gradient focusing (FF-CGF), the impact of EOF on peak dispersion deserves further investigation. Contrary to traditional FFE, the pressure-driven backflow is not created due to EOF blockage at the sidewalls. Instead, it is generated in the presence of EOF to maintain the fixed inflow rates at the sidewalls. In this study, EOF and its pressure-driven backflow will be considered in combination with the counterflow to predict the overall velocity profile in the lateral direction. Then, this updated velocity profile will be included in the previously derived FF-CGF dispersion model to understand the impact of EOF. Interestingly, its presence does not influence the average focal point of a solute, but it can significantly alter the shape of the parabolic profile and the resulting solute dispersion. Finally, preliminary experimental results will be discussed in the context of EOF, and then a framework for future validation of the FF-CGF dispersion model will be provided.

5.2 Modeling Electroosmotic Backflow

The purpose of this section is to reconsider the derivation of the velocity field and focusing mechanism in the FF-CGF separation chamber when accounting for EOF and its pressure-driven backflow. Then, the convection-diffusion model will be updated to predict solute dispersion under these conditions. For this exercise, recall that L is the chamber length, $2b$ is the chamber width, and $2h$ is the chamber height. In addition, schematics of the FF-CGF chamber are presented in Fig. 5.1 and Fig. 5.2.

5.2.1 Velocity Field

For an FFE chamber with an electric field (E) applied in the x-direction, the corresponding EOF velocity can be written as [186]:

$$u_{\text{EOF}} = \mu_{\text{EOF}} E \tag{5.1}$$

where μ_{EOF} is the electroosmotic mobility. Note that the electroosmotic mobility can be written as [186]:

$$\mu_{\text{EOF}} = -\frac{\varepsilon_r \varepsilon_0 \zeta}{\eta} \tag{5.2}$$

where ε is the permittivity, η is the viscosity, and ζ is the zeta potential, which is related to the ion distribution at the microchannel surface. When considering the addition of the counterflow velocity in an FF-CGF chamber, the average fluid velocity in the x-direction can be represented as:

$$\langle u \rangle = \langle u_P \rangle + \langle u_{\text{EOF}} \rangle \tag{5.3}$$

where $\langle u_P \rangle$ is the pressure-driven flow component and $\langle u_{\text{EOF}} \rangle$ EOF component. Now, recall from Chapter 3.2 that the x-velocity was derived to be:

$$\langle u \rangle = \frac{1}{2}\left(-\frac{(u_0 - u_1)}{b}x + u_0 + u_1\right) \tag{5.4}$$

Note that u_0 and u_1 are the x-velocity inputs along the length of the chamber at $x = -b$ and $x = b$, respectively. In practice, u_0 and u_1 represent the fixed inflow rates at the sidewalls, and they are controlled by positive displacement pumps (i.e. syringe pumps). In the presence of EOF, the pressure is inherently adjusted to maintain these inflow boundary conditions, and this leads to the pressure-driven backflow. Mathematically, this is demonstrated by substituting Eq. 5.4 into Eq. 5.3 and rearranging for $\langle u_P \rangle$:

$$\langle u_P \rangle = \frac{1}{2}\left(-\frac{(u_0 - u_1)}{b}x + u_0 + u_1\right) - \langle u_{\text{EOF}} \rangle \tag{5.5}$$

where the first term represents the pressure-driven flow from the pump and the second term represents the pressure-driven backflow due to EOF. Note that this can then be simplified to the more familiar form when the gradient is symmetric ($u_0 = -u_1$):

$$\langle u_P \rangle = -\nabla\langle u \rangle x - \langle u_{\text{EOF}} \rangle \tag{5.6}$$

where $\nabla\langle u \rangle = u_0/b$ represents the x-velocity gradient. Finally, substituting Eq. 5.6 back into Eq. 5.3, and assuming the pressure-driven flow is constrained to a parabolic profile in the y-direction, the x-velocity of the fluid flow can be written as:

$$u(x,y) = -\frac{3}{2}\nabla\langle u \rangle x\left(1 - \frac{y^2}{h^2}\right) - \frac{3}{2}u_{\text{EOF}}\left(1 - \frac{y^2}{h^2}\right) + u_{\text{EOF}} \tag{5.7}$$

where the first term represents the counterflow, the second term represents the pressure-driven electroosmotic backflow, and the third term represents the EOF. Note that EOF and its pressure-driven backflow are in opposite directions. Also, the parabolic profile of the electroosmotic backflow can either increase or decrease the parabolic shape of the counterflow velocity depending on the direction and magnitude. This is demonstrated in Fig. 5.1, which shows a vector field of each individual term seen in Eq. 5.7, as well as a combination of the three.

5.2.2 Focusing Mechanism

When a mass particle is injected at the top of the chamber at $x = 0$ and $z = 0$, the electrophoretic velocity is given as:

$$u_{\mathrm{EP}} = \mu_{\mathrm{EP}} E \tag{5.8}$$

where μ_{EP} is the electrophoretic mobility. Now, by combining Eq. 5.7 and Eq. 5.8, the total x-velocity of the mass particle can be written as:

$$u_{\mathrm{T}}(x,y) = -\frac{3}{2}\nabla\langle u\rangle x\left(1-\frac{y^2}{h^2}\right) - \frac{3}{2}u_{\mathrm{EOF}}\left(1-\frac{y^2}{h^2}\right) + u_{\mathrm{EOF}} + u_{\mathrm{EP}} \tag{5.9}$$

Interestingly, by calculating the area-averaged velocity of Eq. 5.9, it can be seen that the EOF terms will cancel each other out:

$$\langle u_{\mathrm{T}}\rangle = -\nabla\langle u\rangle x - \langle u_{\mathrm{EOF}}\rangle + \langle u_{\mathrm{EOF}}\rangle + \langle u_{\mathrm{EP}}\rangle \tag{5.10}$$

Therefore, when setting $\langle u_{\mathrm{T}}\rangle = 0$ and solving for x, it can be seen that the average focal position in FF-CGF remains unchanged despite the presence of EOF:

$$\langle x\rangle_f = \frac{u_{\mathrm{EP}}}{\nabla\langle u\rangle} \tag{5.11}$$

This result also implies that the average x-position during transit through the FF-CGF chamber stays the same, and recall that it has been previously derived in Chapter 3.2 as a function of z:

$$\langle x\rangle = \frac{u_{\mathrm{EP}}}{\nabla\langle u\rangle}\left(1-\left(1+\frac{\nabla\langle u\rangle}{\langle w\rangle_0}z\right)^{-1}\right) \tag{5.12}$$

where $\langle w\rangle_0$ is the initial z-velocity at $z = 0$. However, when solving for the focal position along the height direction, EOF does have an influence due to the parabolic profile of the electroosmotic

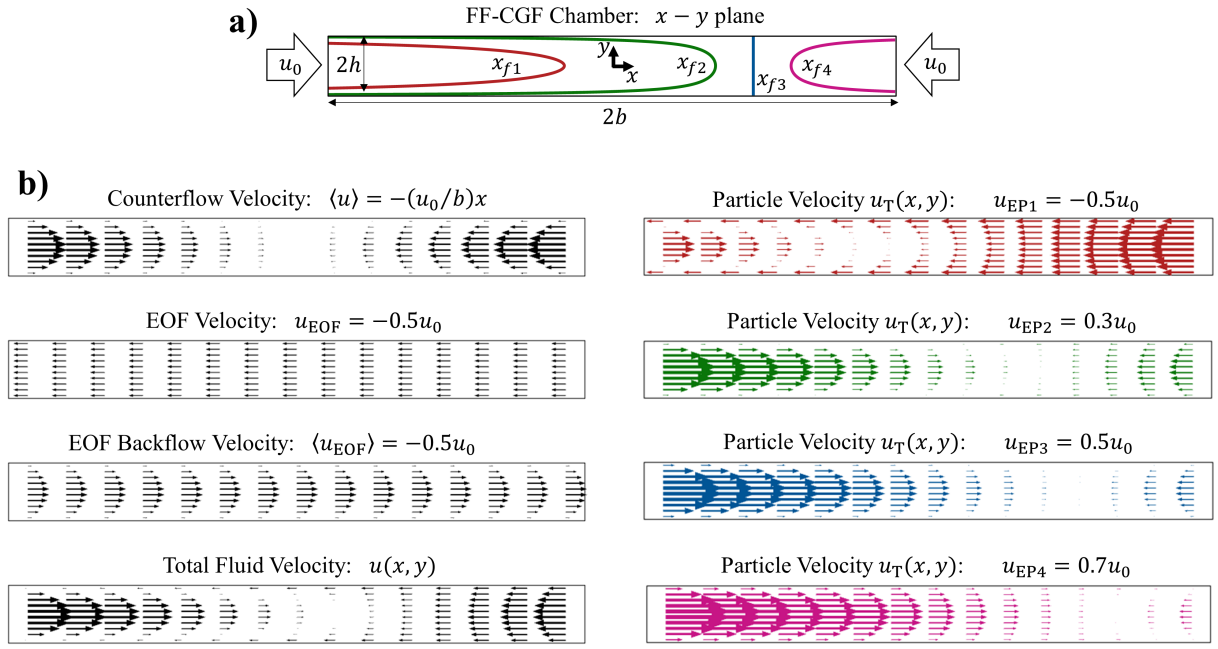


Figure 5.1: a) The cross-section of an FF-CGF chamber along with the focal position of different particles along the height direction. b) The corresponding $x-y$ flow field of the fluid velocity and electrophoretic velocity.

backflow. By shifting the coordinate system of Eq. 5.9 to $x = \langle x\rangle_f + x_f$ and then setting $u_T(x,y) = 0$, the overall focal position can be written as:

$$x_f = \frac{u_{EOF} + u_{EP}}{\nabla\langle u\rangle}\left(\frac{2}{3}\left(1-\frac{y^2}{h^2}\right)^{-1} - 1\right) \tag{5.13}$$

The above equation is an important result that illustrates how the direction and magnitude of EOF can impact the curvature of the focal position, and various examples are shown in Fig. 5.1a. For example, there will be no curvature when $u_{EP} = -u_{EOF}$, and this represents the position where the parabolic terms nullify each other.

5.2.3 Centerline Position

Eq. 5.13 also demonstrates how EOF can shift the centerline position ($y = 0$) of a particle, and this can influence the skew of the solute distribution. Furthermore, it will shift the position of the

peak when operating at higher gradient strengths ($G_x > 5$). Therefore, it is worth exploring the centerline position further by evaluating Eq. 5.9 at $y = 0$:

$$u_{\mathrm{T}}(x,0) = -\frac{3}{2}\nabla\langle u\rangle x - \frac{1}{2}u_{\mathrm{EOF}} + u_{\mathrm{EP}} \tag{5.14}$$

Now, by setting $u_{\mathrm{T}}(x,0) = 0$ and then solving for x, the focal position at the centerline is given as:

$$x_{fc} = \frac{2u_{\mathrm{EP}} - u_{\mathrm{EOF}}}{3\nabla\langle u\rangle} \tag{5.15}$$

In order to determine the centerline x-position during transit through the FF-CGF chamber, recall that Eq. 5.14 can be written as a differential equation by setting $u_{\mathrm{T}}(x,0) = \partial x/\partial t$, and the solution is:

$$x_c = \frac{2u_{\mathrm{EP}} - u_{\mathrm{EOF}}}{3\nabla\langle u\rangle}\left(1 - e^{-\frac{3}{2}\nabla\langle u\rangle t}\right) \tag{5.16}$$

The residence time has been derived in a previous study as a function of y and z, and remains unchanged in the presence of EOF because the z-velocity is independent of u_{EOF}. Therefore, at the centerline ($y = 0$) the residence time can be written as:

$$t_c = \frac{2}{3\nabla\langle u\rangle}\ln\left(1 + \frac{\nabla\langle u\rangle}{\langle w\rangle_0}z\right) \tag{5.17}$$

The above equation can then be substituted into Eq. 5.16 to solve for the x-position at the centerline as a function of z, and the result is:

$$x_c = \frac{2u_{\mathrm{EP}} - u_{\mathrm{EOF}}}{3\nabla\langle u\rangle}\left(1 - \left(1 + \frac{\nabla\langle u\rangle}{\langle w\rangle_0}z\right)^{-1}\right) \tag{5.18}$$

Note how Eq. 5.18 compares to Eq. 5.12. Both equations are plotted in Fig. 5.2 for different u_{EP} values, and they provide some useful information. First, these lines can help predict the location of the solute peak depending on the strength of the gradient. Second, the distance between the two lines is representative of the solute dispersion, and it is smaller for u_{EP} values closer to $u_{\mathrm{EP}} = -u_{\mathrm{EOF}}$. Third, the position of the centerline relative to the average focal position helps illustrate the direction of the skew. Finally, Eq. 5.12 and Eq. 5.18 are equivalent when $u_{\mathrm{EP}} = -u_{\mathrm{EOF}}$, and this is the location of the most concentrated peak.

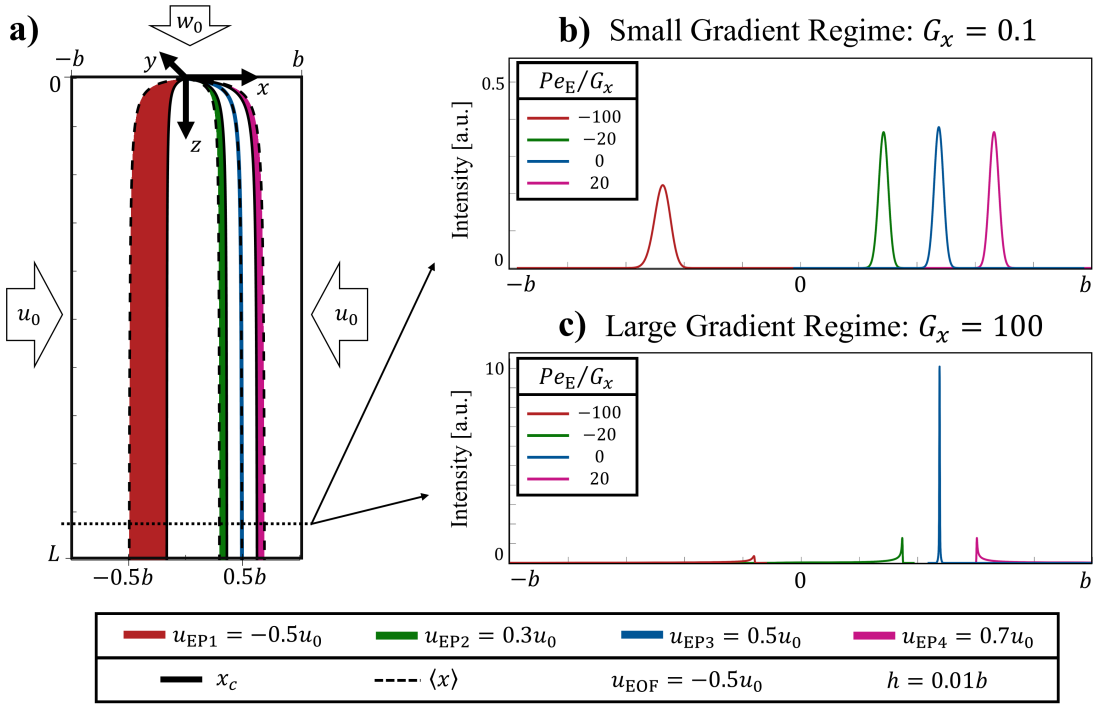


Figure 5.2: a) The average focal position $\langle x \rangle_f$ and the centerline position x_c for charged particles moving through an FF-CGF chamber. The corresponding solute distributions when b) $G_x = 0.1$ and c) $G_x = 100$.

5.2.4 Solute Dispersion Model

The influence of EOF on the actual solute distribution in the $x-y$ plane can be determined by using Eq. 5.9 in the convection-diffusion equation [54]:

$$\begin{aligned} &\frac{\partial c}{\partial t} - \frac{3}{2}\nabla\langle u\rangle x\left(1-\frac{y^2}{h^2}\right)\frac{\partial c}{\partial x} - \frac{3}{2}u_{\mathrm{EOF}}\left(1-\frac{y^2}{h^2}\right)\frac{\partial c}{\partial x} + u_{\mathrm{EOF}}\frac{\partial c}{\partial x} + u_{\mathrm{EP}}\frac{\partial c}{\partial x} \\ &\qquad = D\frac{\partial^2 c}{\partial x^2} + D\frac{\partial^2 c}{\partial y^2} + \left[\frac{3}{2}\nabla\langle u\rangle\left(1-\frac{y^2}{h^2}\right)c\right] \end{aligned} \tag{5.19}$$

where c is the solute concentration and D is the diffusion coefficient. Once again, note that the square bracket term appears because the counterflow velocity depends on x, and it is included as a reaction rate term in numerical simulations to avoid a concentration sink. Also, the time dependence is included to monitor the evolution of the focusing mechanism. Finally, it is helpful to apply a shifted coordinate during numerical simulations depending on the gradient strength.

Small Gradient Regime

In this regime ($G_x < 1$), the majority of the solute is concentrated at the average focal position, and therefore the shifted coordinate of $x = \langle x \rangle_f + x_f$ is applied:

$$\begin{aligned} \frac{\partial c}{\partial t} - \frac{3}{2}\nabla\langle u\rangle x_f \left(1 - \frac{y^2}{h^2}\right)\frac{\partial c}{\partial x_f} + (u_{\mathrm{EOF}} + u_{\mathrm{EP}})\left(1 - \frac{3}{2}\left(1 - \frac{y^2}{h^2}\right)\right)\frac{\partial c}{\partial x_f} \\ = D\frac{\partial^2 c}{\partial x_f^2} + D\frac{\partial^2 c}{\partial y^2} + \left[\frac{3}{2}\nabla\langle u\rangle\left(1 - \frac{y^2}{h^2}\right)c\right]. \end{aligned} \tag{5.20}$$

Then, the above equation can be written in its dimensionless form when $t^* = Dt/h^2$, $x_f^* = x_f/h$, $y^* = y/h$, $G_x = \nabla\langle u\rangle h^2/D$, $Pe_{\mathrm{E}} = (u_{\mathrm{EOF}} + u_{\mathrm{EP}})h/D$, $c^* = c/c_0$, and c_0 is the initial solute concentration:

$$\begin{aligned} \frac{\partial c^*}{\partial t^*} - \frac{3}{2}G_x x_f^*\left(1 - y^{*^2}\right)\frac{\partial c^*}{\partial x_f^*} + Pe_{\mathrm{E}}\left(1 - \frac{3}{2}\left(1 - y^{*^2}\right)\right)\frac{\partial c^*}{\partial x_f^*} \\ = \frac{\partial^2 c^*}{\partial x_f^{*^2}} + \frac{\partial^2 c^*}{\partial y^{*^2}} + \left[\frac{3}{2}G_x\left(1 - y^{*^2}\right)c^*\right]. \end{aligned} \tag{5.21}$$

Note that this is the same result as the previously derived FF-CGF model in Chapter 4.2.2, except the Péclet number is no longer $Pe_{\mathrm{EP}} = u_{\mathrm{EP}}h/D$, and now includes u_{EOF} as well. Therefore, the above equation now accounts for the total electrokinetic velocity, and it is an important difference because EOF can have a significant influence on solute dispersion. For example, Fig. 5.2b shows the solute distributions corresponding to the trajectories in Fig. 5.2a when $G_x = 0.1$. On the right side of the chamber, the solute dispersion is reduced in the presence of EOF because $Pe_{\mathrm{E}} < Pe_{\mathrm{EP}}$, and this represents the electroosmotic backflow suppressing the dispersion caused by the counterflow. Meanwhile, the solute dispersion is increased on the left side of the chamber because $Pe_{\mathrm{E}} > Pe_{\mathrm{EP}}$, and this signals that the electroosmotic backflow and the counterflow are in the same direction.

Large Gradient Regime

In this regime ($G_x > 20$), the solute becomes highly concentrated at the centerline, and therefore the shifted coordinate of $x = x_{fc} + x_f$ is more appropriate:

$$\begin{aligned} \frac{\partial c}{\partial t} - \frac{3}{2}\nabla\langle u\rangle x_f \left(1 - \frac{y^2}{h^2}\right)\frac{\partial c}{\partial x_f} + (u_{\mathrm{EOF}} + u_{\mathrm{EP}})\frac{y^2}{h^2}\frac{\partial c}{\partial x_f} \\ = D\frac{\partial^2 c}{\partial x_f^2} + D\frac{\partial^2 c}{\partial y^2} + \left[\frac{3}{2}\nabla\langle u\rangle\left(1 - \frac{y^2}{h^2}\right)c\right]. \end{aligned} \tag{5.22}$$

Note the importance of including the EOF term with the shifted centerline position due to the parabolic profile of the backflow. Then, the above equation can be written in its dimensionless form as:

$$\begin{aligned}\frac{\partial c^*}{\partial t^*} - \frac{3}{2}G_x x_f^* \left(1 - y^{*^2}\right) \frac{\partial c^*}{\partial x_f^*} + Pe_{\mathrm{E}} y^{*^2} \frac{\partial c^*}{\partial x_f^*} \\ = \frac{\partial^2 c^*}{\partial x_f^{*^2}} + \frac{\partial^2 c^*}{\partial y^{*^2}} + \left[\frac{3}{2}G_x \left(1 - y^{*^2}\right) c^*\right].\end{aligned} \tag{5.23}$$

Once again, this is the same result as the previously derived FF-CGF model in Chapter 4.2.2, except the Péclet number now encompasses the total electrokinetic velocity. Furthermore, Fig. 5.2c shows the solute distributions corresponding to the trajectories seen in Fig. 5.2a when $G_x = 100$, and the impact of EOF on dispersion is similar to what was discussed in the small gradient regime. Note that the influence that EOF has on the skew of the distribution is more noticeable at higher G_x numbers because convection is the dominant transport mechanism. Also, with EOF present the sharpest peak will be at $Pe_{\mathrm{E}} = 0$ rather than $Pe_{\mathrm{EP}} = 0$, and this indicates that charged solutes can be focused here. Consequently, the experimental parameters for EOF can potentially be tuned to maximize the resolution and purity of a given solute.

5.3 Experimental Section

The goal of the experimental portion of this study is to observe the dispersion of common proteins in a G_x range between 0.1 and 1. Therefore, this section will provide an overview of the protocols used to achieve this task with the original FF-CGF prototype in Chapter 3.4.2.

5.3.1 Materials

All chemicals were purchased from Sigma-Aldrich. The electrode buffer consisted of 445 mM of Tris and 445 mM of boric acid, with the pH adjusted to 8.4 using an HCl solution. This was then diluted to 89 mM of Tris and 89 mM of boric acid for the buffer counterflow pumped through the sides of the separation chamber. The protein solution was prepared in the separation buffer, and it consisted of bovine serum albumin (BSA), hemoglobin (Hg), and cytochrome c (Cyt C). The concentration of each protein was 50 mg/mL, and the BSA was labeled with bromophenol blue at a 1:1 molar ratio.

5.3.2 Device Fabrication

The FF-CGF device was fabricated using a multilayer soft lithography technique outlined in Chapter 3.4.2. Briefly, the silicon master mold had a 40 mm x 18 mm separation chamber with a target height of 100 μm, while the microchannels supplying the counterflow from the side chambers had a target height of 10 μm. The PDMS was prepared with a 10:1 ratio of base to curing agent and then baked for 3 h at 95℃. Finally, two 75 mm × 50 mm glass slides were bonded to the top and bottom of the PDMS using oxygen plasma with a power of 29.6 W at 500 mTorr for 1 min. The top layer was bonded first, and its purpose was to prevent the wide chamber from sagging.

5.3.3 Electrode Device

The device connecting the electrodes to the side chambers was upgraded since Chapter 3.4.3. While the ion exchange membrane remains the same (Nafion 117, FuelCellStore), the housing was changed from PDMS to PMMA because this material allows the device to be more durable. The layout of the device remains the same, and the different PMMA layers were prepared with a laser cutter (VLS2.30, Universal Laser Systems) before being bonded together with double-sided tape (ARcare 90106, Adhesives Research). Furthermore, a barbed plastic fitting (McMaster Carr) was used to connect the electrode device to the PDMS chip, and this facilitated a simpler and more reliable setup. Finally, the buffer and current inlets were decoupled in order to separate the buffer inflow from the effects of ion concentration polarization (ICP) at the membrane, and this enabled the use of significantly higher currents (from 400 μA to 1900 μA).

5.3.4 Experimental Setup

Syringe pumps (Pump 11 and Pump33, Harvard Apparatus) were used for the sample and buffer flow, while a high voltage supply (HVS448-3000, LabSmith) was used to supply the electric field. A constant current mode was used to adjust for voltage changes that may arise in the electrode device due to ICP, Joule heating, and bubble formation. Another improvement from the previous setup involved device preparation, which can be challenging due to bubbles that get trapped in the separation chamber. It was found that bubbles could be avoided by slowly loading the buffer from the sample inlet, and blocking all ports except the outlet. After slowly filling the separation chamber and outlet channels, the remaining inlets were unblocked to allow the microchannels and side chambers to fill. Then, the syringe pumps and electrode devices were properly fastened without introducing bubbles during connection.

Table 5.1: Experimental flow rates and the corresponding G_x values for each protein.

Side Flow Rate [µL/min]	Sample Flow Rate [µL/min]	**Cyt C** G_x	**Hg** G_x	**BSA** G_x
6.5	0.05	0.05	0.11	0.12
16.0	0.10	0.11	0.27	0.30
32.5	0.15	0.23	0.54	0.61
48.5	0.20	0.34	0.81	0.91

5.3.5 Experimental Parameters

The flow rates were chosen based on the goal of operating in the G_x range between 0.1 and 1. Recall that $G_x = \nabla\langle u\rangle h^2/D$, so both the diffusion coefficient and the velocity from the sidewalls are needed to approximate this value. The diffusion coefficients have been obtained from previous studies at similar pH values, and they are 6.15×10^{-7} cm^2/s for BSA [187], 6.9×10^{-7} cm^2/s for Hg [187], and 1.65×10^{-6} cm^2/s for Cyt C [188]. The velocity from the sidewalls (u_0) can be calculated from the buffer flow rate (Q) by assuming that $u_0 = Q/(2hL)$, with $2hL$ representing the cross-sectional area of the inflow. Therefore, the buffer flow rates and the corresponding G_x values are shown in Table 5.1. The sample flow rate is also shown for each G_x value, and these values were chosen to maintain protein visibility while allowing for sufficient focusing.

5.3.6 Peak Measurements

Images of the separation were analyzed using ImageJ software. First, the image is inverted to measure the gray scale intensity, and the smooth feature is used to remove the noise. Then, a region in the lower half of the chamber is highlighted to acquire the intensity profile across the chamber. The exact size and location of this region depends on the image, and it must ensure that there is no significant deviation in focal position due to nonidealities in the counterflow gradient. Finally, a custom MATLAB script is used to adjust the baseline and identify the peaks. Note that the edges of the separation chamber are also identified, and their locations help calibrate the width of the chamber.

5.3.7 Peak Fitting

Once the peaks have been identified, it is helpful to fit them with an exponentially modified Gaussian (EMG) function [177] [178]:

$$f_{EMG} = \frac{1}{2\tau} \exp\left(\frac{1}{2\tau}\left(2\mu_G + \frac{\sigma_G^2}{\tau} - 2x\right)\right) \times \text{erfc}\left(\frac{\mu_G + \frac{\sigma_G^2}{\tau} - x}{\sqrt{2}\sigma_G}\right) \tag{5.24}$$

where μ_G is the mean position of the Gaussian component, σ_G is the standard deviation of the Gaussian component, τ represents the decay rate of the exponential component, and erfc is the complementary error function. The first moment of $M_1 = \mu_G + \tau$ represents the mean position of the peak, while the second moment of $M_2 = \sigma_G^2 + \tau^2$ represents the variance of the peak, and both of these parameters are helpful for understanding peak dispersion [179]. For example, the first moment is used to determine $\langle x \rangle_f$, which is measured relative to the focused peak when no electric field is present.

5.3.8 Electric Field Measurement

The electric field is an important property that is difficult to measure in the current version of FF-CGF. For one, the effective voltage across the separation region will be different from the applied voltage at the electrodes, and most of the loss is due to the large resistance of the microchannels. In addition, the ion exchange membranes will polarize and create enriched and depleted ion regions that can alter the voltage in a way that is difficult to measure. This can also cause Joule heating and bubble formation which may influence the voltage loss in an unpredictable manner. Therefore, it is helpful to measure the electric field with a reference solute that has a known electrophoretic mobility. Then, recognizing that $\langle x \rangle_f = u_{\text{EP}} / \nabla \langle u \rangle$, with $\nabla \langle u \rangle$ determined by the flow rates and $\langle x \rangle_f$ measured from the fitted EMG curve, u_{EP} can be approximated. This value can then be used along with the reference mobility to estimate the electric field (see Eq. 5.8). Note that $\langle x \rangle_f$ is independent of EOF, so knowledge of its properties are not needed for the calculation. For this study, BSA was chosen as the reference protein because a previous FFE study with a similar separation buffer measured its electrophoretic mobility to be -1.7×10^{-4} cm^2/Vs [39]. As a final consideration, it is assumed that the conductivity of the focused solutes does not alter the electric field across the chamber.

5.4 Results and Discussion

This section will present preliminary results from the original FF-CGF device, and discuss its protein separation in the context of EOF and the dispersion model. While the current experimental setup only allows for coarse peak measurements, it provides a helpful qualitative understanding of dispersion. Furthermore, this study can be used as a guide for designing improved FF-CGF devices, and serves as a framework for future experimental validation.

5.4.1 Preliminary Experimental Observations

Fig. 5.3 shows the separation of BSA, Hg, and Cyt C at different G_x numbers, and it is helpful to observe electrodynamic dispersion over the entire separation region. In general, the corresponding peak measurements illustrate a trend for G_x and Pe_{E} that appears to agree with the previous investigation on FF-CGF peak dispersion. For G_x, the peak width remains relatively stable around 0.1, but as G_x goes beyond 0.5 and approaches 1, the peaks begin to disperse rapidly. This is especially true for BSA, which exhibits significant smearing in Fig. 5.3c and 5.3d. On the other hand, the G_x value for Cyt C remains below 0.5 due to its higher diffusion coefficient, and therefore its peaks appear to maintain their Gaussian shape. For Pe_{E}, as this value increases with current, there is clearly an increase in peak dispersion as well, and this is consistent with the previous numerical investigation.

In terms of electrodynamics, it is interesting to speculate the strength of EOF based on the results presented in Fig. 5.3. For BSA, a peak tail begins to emerge on the right side of the curve for higher G_x values. Referring back to Fig. 5.2, this implies that counterflow is opposing the EOF backflow, and indicates that the magnitude of EOF mobility is less than the electrophoretic mobility of BSA. For Hg, it does not experience significant peak tailing even at higher G_x values, and this implies a Pe_E value closer to 0 because the counterflow and EOF backflow are negating each other. Therefore, since the electrophoretic mobility has been reported to be -1.7×10^{-4} $\mathrm{cm}^2/\mathrm{Vs}$ and -3.9×10^{-5} $\mathrm{cm}^2/\mathrm{Vs}$ for BSA and Hg [39], respectively, the qualitative observations suggest that the EOF mobility is closer to 3.9×10^{-5} $\mathrm{cm}^2/\mathrm{Vs}$, which is quite low. For Cyt C, the dispersion appears to be relatively stable despite the counterflow and EOF backflow being in the same direction on that side of the chamber, and this also suggests a low EOF mobility.

In reality, the EOF mobility of PDMS/glass chips tends to be unpredictable because the surface properties of PDMS can vary depending on the fabrication procedure. With that said, the zeta potential of a glass/PDMS microchannel with an 89 mM Tris-borate solution has been reported to be -52.4 mV [186]. Referring back to Eq. 5.2, and assuming a relative permittivity of 80 and a viscosity of 0.001 Pa s, the EOF mobility is estimated to be 3.7×10^{-4} $\mathrm{cm}^2/\mathrm{Vs}$. This magnitude is greater than the electrophoretic mobility of BSA, which potentially invalidates

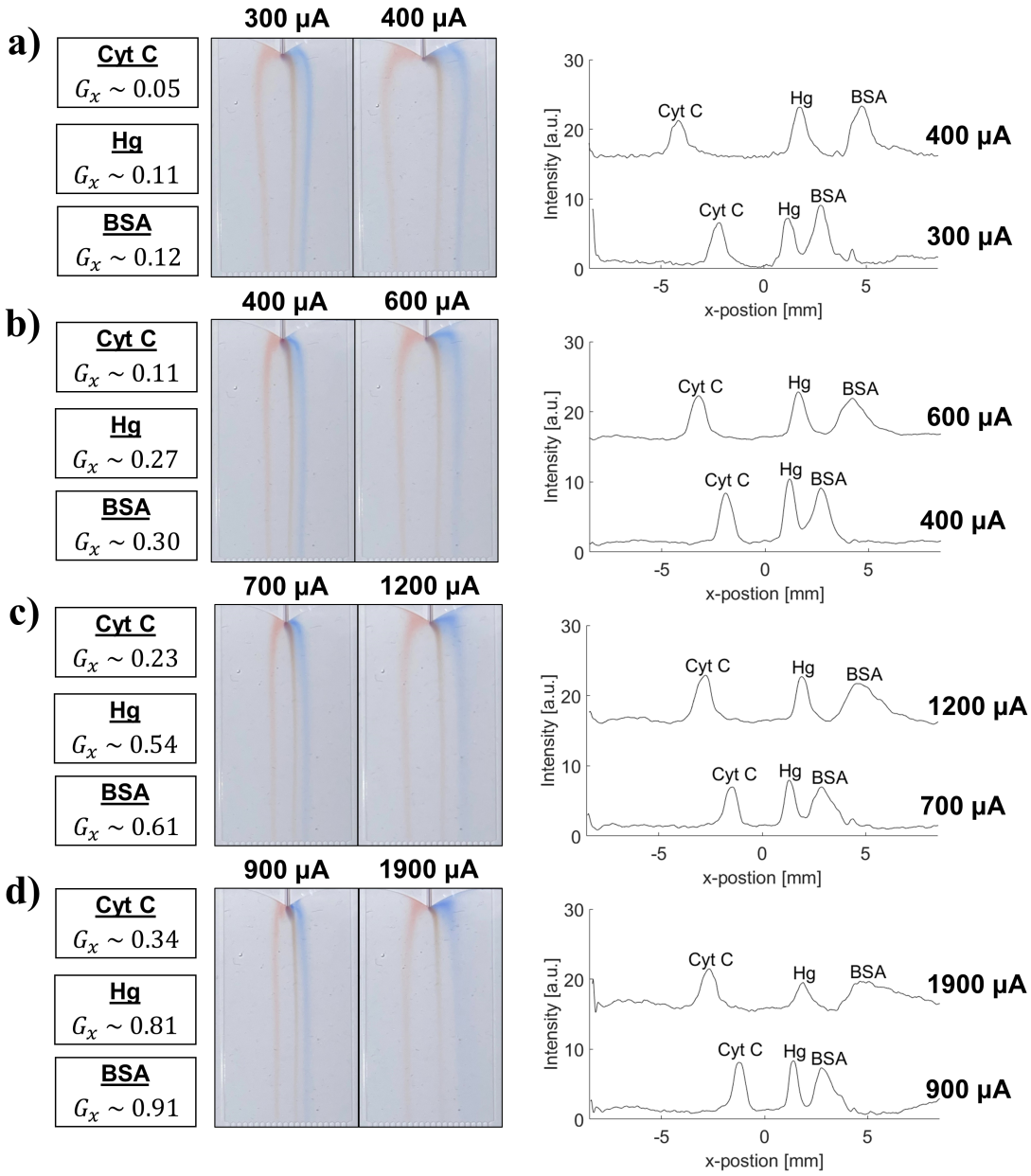


Figure 5.3: The separation of Cyt C, Hg, and BSA at various G_x values, and their corresponding peak measurements.

some of the previous qualitative observations. One possible explanation for the discrepancy may be due to the coarse peak measurement, which makes the baseline adjustment difficult, and may

exaggerate the presence of a peak tail. Alternatively, the peak tail may be caused by the blue dye disassociating from BSA at higher currents due to the increase in Joule heating. Or, it may be simply due to the inconsistencies of the PDMS surface chemistry, and the EOF mobility is lower than anticipated. Overall, this demonstrates the difficulty of comparing the current experimental setup to the numerical model.

5.4.2 Measured Parameters

To quantify dispersion, the peaks can be fitted with the EMG function from Eq. 6.1, and the resulting parameters along with the moment equations can then be used to determine the average focal position $\langle x \rangle_f$ and the standard deviation σ of the peak (see Section 5.3.7). The values are shown in Table 5.2, and they can be used to estimate the electric field E assuming a reference mobility of $\mu_{\text{EP, BSA}} = -1.7 \times 10^{-4}$ cm^2/Vs is used for BSA (see Section 5.3.8) [39]. Then, the electric field and $\langle x \rangle_f = u_{\text{EP}} / \nabla \langle u \rangle$ can be used to estimate the electrophoretic mobility of the remaining proteins (see Eq. 5.8). Compared to a previous study which measured the mobilities of Hg and Cyt C to be $\mu_{\text{EP, Hg}} = -3.9 \times 10^{-5}$ cm^2/Vs and $\mu_{\text{EP, Cyt C}} = 1.64 \times 10^{-4}$ cm^2/Vs [39], the results presented in Table 5.3 appear to be reasonable. There is some variation in $\mu_{\text{EP, Hg}}$, and one possible explanation may be due to Joule heating and electrolysis, as the reference mobility does not account for changes in temperature or pH. The effects of Joule heating are particularly evident due to the nonlinear behaviour of the current and electric field seen in Table 5.3 as G_x increases.

Note that the applied voltage and electric field shown in Table 5.3 can be used to help estimate the voltage efficiency across the chamber. For example, at an applied voltage of 463 V and an electric field of -4.7 V/cm, this corresponds to a voltage efficiency of 1.8% across the 1.8 cm separation region, which is reasonable given the large voltage drop across the microchannels. As the applied voltage and electric field increase to 650 V and -8.3 V/cm, respectively, the voltage efficiency reduces to 1.3%, and this is potentially caused by the increased resistance at the ion exchange membranes due to ICP [59]. Finally, note that under ideal conditions the measured values for σ in Table 5.2 could be compared to the previous numerical investigation to approximate a value for Pe_{E}, and this could then be used along with μ_{EP} and E to estimate the electroosmotic mobility. However, this is difficult in practice because the model does not account for the inevitable rise in temperature, and the quality of the peak measurements leads to Pe_{E} estimates that are inconsistent.

Table 5.2: Fitted EMG parameters for the peaks at different G_x values.

Cyt C			Hg			BSA		
G_x	$\langle x \rangle_f$ [mm]	σ [mm]	G_x	$\langle x \rangle_f$ [mm]	σ [mm]	G_x	$\langle x \rangle_f$ [mm]	σ [mm]
0.05	-2.3	0.30	0.11	1.1	0.28	0.12	2.6	0.36
	-4.2	0.41		1.7	0.38		4.7	0.48
0.11	-2.0	0.32	0.27	1.1	0.29	0.30	2.6	0.40
	-3.4	0.36		1.5	0.34		4.2	0.71
0.23	-2.2	0.31	0.54	0.7	0.29	0.61	2.2	0.53
	-3.5	0.40		1.3	0.32		4.2	0.84
0.34	-2.3	0.28	0.81	0.4	0.23	0.91	1.9	0.44
	-3.8	0.35		0.9	0.34		4.3	0.95

Table 5.3: Estimates of electric field and electrophoretic mobility.

			Cyt C	Hg	BSA
Current [μA]	Voltage [V]	E [V/cm]	μ_{EP} [cm^2/Vs]	μ_{EP} [cm^2/Vs]	μ_{EP} [cm^2/Vs]
300	463	-4.7	1.5×10^{-4}	-7.2×10^{-5}	-1.7×10^{-4}
400	650	-8.3	1.5×10^{-4}	-6.1×10^{-5}	-1.7×10^{-4}
400	572	-11.1	1.3×10^{-4}	-7.2×10^{-5}	-1.7×10^{-4}
600	862	-18.3	1.4×10^{-4}	-6.2×10^{-5}	-1.7×10^{-4}
700	854	-19.8	1.7×10^{-4}	-5.1×10^{-5}	-1.7×10^{-4}
1200	1284	-37.5	1.4×10^{-4}	-5.1×10^{-5}	-1.7×10^{-4}
900	946	-24.9	2.0×10^{-4}	-3.5×10^{-5}	-1.7×10^{-4}
1900	1780	-56.2	1.5×10^{-4}	-3.4×10^{-5}	-1.7×10^{-4}

5.4.3 Comparison to Numerical Model

To gain further insight into the validity of the EOF dispersion model, it is helpful to compare the numerical simulations to the experimental peak measurements. For this exercise, the G_x conditions presented in Fig. 5.3 can be simulated in COMSOL v5.6 using Eq. 5.21 (See Chapter 4.3.2). Recall that $Pe_E = (u_{EOF} + u_{EP})h/D$, where u_{EP} is determined from Table 5.3. Also, note that the EOF mobility of the glass/PDMS chip is assumed to be $\mu_{EOF} = 3.7 \times 10^{-4}$ cm^2/Vs.

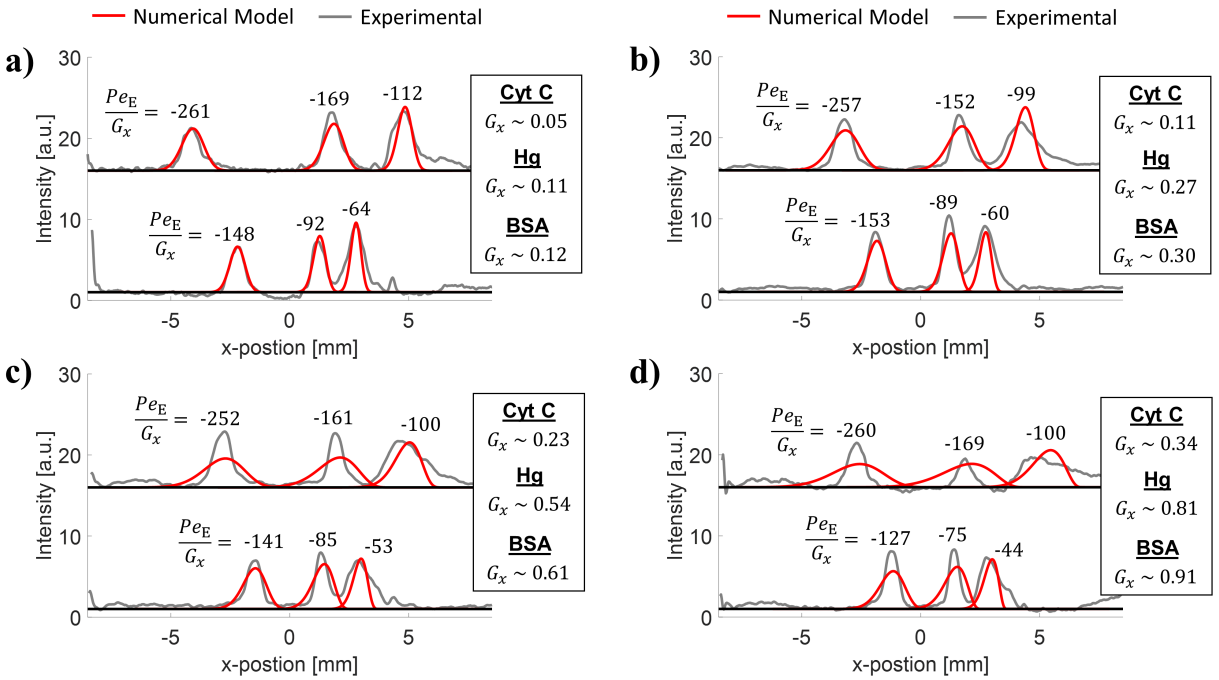


Figure 5.4: Comparison of the experimental peak measurements to the numerical simulations of the dispersion model assuming $\mu_{\mathrm{EOF}} = 3.7 \times 10^{-4}$ cm^2/Vs. From left to right, the peaks represent Cyt C, Hg, and BSA. From bottom to top, the applied currents are a) 300 µA and 400 µA, b) 400 µA and 600 µA, c) 700 µA and 1200 µA, and d) 900 µA and 1900 µA.

Finally, the shifted coordinates are applied using the $\langle x \rangle_f$ values seen in Table 5.3. Altogether, the results are presented in Fig. 5.4, and their comparison to the experimental peaks are reasonable.

According to Fig. 5.4a, the simulated peaks appear to be in agreement with the experimental data, and this outcome suggests that the dispersion model is a useful tool for predicting separation performance. Furthermore, the importance of accounting for EOF is evident, and this is especially true when EOF is significant. For example, the success of the model indicates that the EOF mobility is indeed around $\mu_{\mathrm{EOF}} = 3.7 \times 10^{-4}$ cm^2/Vs, and this is greater than the electrophoretic mobility of each protein in terms of magnitude. Consequently, the Pe_{E} values for Hg and BSA are negative even though they are focused on the right side of the chamber. Moreover, their Pe_{E} values are relatively large, and this implies that a strong EOF backflow is opposing the counterflow in this region. Importantly, this results in dispersion that is larger than expected when compared to the situation where no EOF is present. Likewise, the Pe_{E} value for Cyt C is much larger than expected in the presence of EOF, and this also leads to unnecessary dispersion. Therefore, EOF should be carefully considered in FF-CGF, and in this situation, it should be

suppressed to improve resolution.

According to the rest of Fig. 5.4, there appears to be less agreement between the numerical model and the experimental data. In Fig. 5.4d, the difference becomes clear as the simulated peak widths for Cyt C and Hg are significantly greater than the experimental peaks. The reason for this inconsistency is unknown, but one plausible explanation would be due to the effects of Joule heating, which are likely present in Fig. 5.4d because of the increased currents. In traditional FFE, Joule heating induced dispersion has been modeled previously [57], and there is an increase in diffusion along the height direction at higher temperatures that reduces the dispersion caused by the parabolic flow profile. In FF-CGF, there is likely a similar outcome occurring as the current increases in Fig. 5.4. Essentially, this lowers the actual G_x value to a range that is less impacted by the dispersion from the counterflow, and perhaps this is why the experimental peak widths are smaller than expected. In addition, due to the continuous inflow from the sidewalls, the middle of an FF-CGF chamber is likely to have a higher temperature, and this could explain why Hg experiences less dispersion than BSA despite them having similar G_x values. It should be noted that the increased temperatures will also have an impact on factors like viscosity, electrophoretic velocity, and EOF, but this becomes more complicated to model in terms of the expected Pe_{E} value [57] [56]. Altogether, it is interesting to speculate that Joule heating will improve resolution in FF-CGF, but this should be treated with caution as increased temperatures can also have detrimental effects such as natural convection, current instability, and protein denaturation.

5.5 Future Considerations

In the end, the experimental results provide a useful qualitative understanding of EOF and the resulting solute dispersion, but several improvements are needed to validate the numerical models.

5.5.1 Peak Measurements

One potential improvement involves the quality of the peak measurements. Although it is helpful to view the separation over the entire chamber, a fluorescence microscope that can focus on specific regions is better suited for high quality peak measurements. Preliminary experiments have explored the separation of common dye molecules such as fluorescein and rhodamine B [189], but this has created other challenges such as adsorption to the PDMS surface. In addition, the dye molecules have a lower diffusion coefficient, so it is difficult to achieve higher G_x numbers without excessive Joule heating. Therefore, future experiments should consider separating proteins that are labeled with a fluorescent dye. Moreover, it would be interesting to test analytes

with lower diffusion coefficients, as this would be a convenient way to study higher G_x values without pushing the limitations of the electric field.

5.5.2 EOF Suppression

Another parameter that would be interesting to study during the investigation on electrodynamic dispersion would be the strength of the EOF. For example, the EOF can be suppressed in order to observe the impact on peak dispersion, as this may offer some benefit in terms of separation resolution. Alternatively, the EOF could be tuned with dynamic coatings to achieve a Pe_{E} value close to 0 for a specific protein, as this will maximize the resolution around that point (see Fig. 5.2). Preliminary efforts to suppress EOF with 0.1% (w/v) 2-hydroxyethyl cellulose (HEC) have been unsuccessful [31], as there was no noticeable reduction in peak dispersion. The use of a 1% (w/v) polyvinylpyrrolidone (PVP) solution was also explored [189], but it appeared to interact with the bromophenol blue used to label BSA, and this created an large peak tail. Therefore, it is important to identify a coating that can suppress EOF while avoiding interactions with the proteins. Note that dynamic coatings may also have an influence on the separation parameters such as viscosity, diffusion, and electrophoretic mobility [190]. These changes must be considered in the dispersion model, and it will make a direct comparison between the results with and without EOF difficult.

5.5.3 Device Design

The most pressing concern for improving the experimental results is related to the FF-CGF device. For one, the surface properties of PDMS lead to inconsistencies with EOF, and it is prone to unwanted surface absorption of some dye molecules. Second, the success rate for building a device with a uniform counterflow gradient is low, and this is assumed to be caused by a combination of blockage in the microchannels and nonuniform chamber heights due to PDMS sagging. Third, a better strategy for voltage efficiency and heat dissipation is needed to increase the electric field range and minimize the effects of Joule heating induced dispersion. A logical next step for improving upon most of these issues would be to change from a PDMS device to one that is made of PMMA, as this material is commonly used in FFE due to its consistent surface properties and structural integrity [88]. However, it is difficult to fabricate microchannels in PMMA with a height of 10 μm, so another method is needed to generate the uniform counterflow gradient.

5.5.4 Additional Modeling

Finally, there are several other interesting areas of physical modeling that deserve further exploration in FF-CGF. The most significant is Joule heating, which is different than traditional FFE devices because of the continuous addition of counterflow from the sidewalls. This is likely to create a temperature gradient in the x-direction, which makes Joule heating induced dispersion dependent on the focal position. Going a step further, the interplay between Joule heating and solute dispersion should be studied, as this will influence molecular diffusion, viscosity, electrophoretic mobility, and EOF [57]. Altogether, this would require a more complicated experimental setup for validation, but it would provide a better understanding of the separation method.

5.6 Concluding Remarks

In this study, an analytical model was provided to account for the presence of EOF in FF-CGF. Notably, EOF induces a pressure-driven backflow across the separation chamber to maintain the fixed counterflow inputs at the sidewalls. As a result, this can alter the parabolic velocity profile in the lateral direction, and although it does not affect the average focal point, it can impact the centerline position and dispersion of a solute. With that said, EOF does not alter the FF-CGF dispersion model significantly, and it simply requires the *Pe* number to consider the electroosmotic velocity in addition to the electrophoretic velocity. Interestingly, this suggests that the EOF properties can be tuned to optimize the separation resolution for a given solute. Finally, preliminary experimental observations were provided based on the separation of common proteins, and there appears to be agreement with the numerical model at lower G_x values. However, as G_x increases there are likely some Joule heating effects that need to be considered in the future.

Chapter 6

Improving Device Design I: Preparative Scale

6.1 Introduction

The purpose of this section is to provide an improved understanding of how to design an FF-CGF device, and explore alternative fabrication protocols to improve device performance. Along the way, there will be an emphasis on strategies for scaling up the device for preparative protein purification.

6.1.1 Motivation

Protein purification is a challenging process for life science research and the pharmaceutical industry [18]. For several decades, FFE has been used to separate and collect large quantities of proteins from complex biological mixtures. In preparative scale FFE, the sample flow rate is usually around 5 mL/hr for a throughput of about 1 mg/hr, and it is particularly useful for proteins that are prone to irreversible absorption, sedimentation, or denaturation [99] [81] [191]. Unfortunately, several technical challenges persist which have limited the widespread use of FFE at this scale [22]. Previous chapters have shown that FF-CGF can improve upon some of the issues associated with traditional FFE techniques, and therefore it is worth exploring its potential for preparative purposes.

In FFZE, many of the strategies for increasing sample flow rate also lead to a reduction in separation resolution [22] [53]. For example, one option is to increase the buffer velocity, but this will also increase hydrodynamic dispersion, and solute bands may not have sufficient time to fully resolve before exiting the chamber. A second option is to increase the sample injection width, but this will have a direct influence on solute bandwidth. A third option is to increase the chamber height, but this will reduce heat dissipation while also increasing hydrodynamic

dispersion and the influence of buoyancy effects [39]. Finally, peristaltic pumps are often needed when handling large volumetric flow rates, and their inherent pulsations can disrupt the trajectory of the solute band [83].

As an alternative method, FF-IEF is frequently used because it can alleviate some of the technical limitations associated with FFZE [22]. For example, in addition to counteracting molecular diffusion, its focusing mechanism eliminates hydrodynamic dispersion caused by the parabolic profile of the buffer velocity, and enables larger sample injection widths [43] [50]. Moreover, it can help restore unwanted displacements due to pulsations. With that said, FF-IEF introduces new technical challenges at the preparative scale that limit sample throughput. For one, the large volumetric flow rates require large quantities of carrier ampholytes to generate stable pH gradients, and this can increase costs and require further processing to remove them from the purified sample [47]. Another issue is that the electrophoretic velocity approaching the pI is often slow because many proteins have a small net charge around this point, and this can result in long focusing times that restrict buffer velocity [44]. Likewise, carrier ampholytes lose their charge as they establish a pH gradient, and this can also contribute to long focusing times and reduce the current in the system [44] [41]. A final concern is that there may be unwanted band distortion at this scale because the pI can lead to poor solubility, and cause buoyancy issues due to local gradients in concentration, conductivity, and temperature [41] [45] [46].

With the development of FF-CGF, preliminary work has shown that there is potential to address some of the shortcomings associated with FFE at the preparative scale. In principle, the mechanism is similar to FF-IEF, except solutes focus according to their electrophoretic mobility rather than pI. Consequently, many of the benefits of FF-IEF are also true for FF-CGF. Furthermore, no expensive carrier ampholytes or complex buffer compositions are required to establish the gradient. Additionally, a constant charge is maintained across the chamber to help prevent the long focusing times and solubility concerns that plague some proteins in FF-IEF. Lastly, the continuous addition of counterflow from the sidewalls will increase the buffer velocity and dilute the focused solute streams, and both of these factors will help suppress any buoyancy issues that arise due to local density gradients.

Clearly, there are several reasons to pursue FF-CGF for high throughput protein purification, but the design of the initial prototype has several challenges that make it less than ideal for scaling up. In general, soft lithography techniques face manufacturing limitations due to the cost of PDMS as well as the size constraints associated with plasma bonding. For FFE, PDMS raises additional concerns including unwanted surface absorption, inconsistent EOF properties, poor heat dissipation, and weak structural integrity for wide chambers [192]. As a result, the alternative fabrication method for preparative scale FFE is often a thin spacer sandwiched between two PMMA plates, as this acrylic material is easy to machine and improves upon many of the issues related to PDMS [28] [88]. However, for FF-CGF this simple assembly becomes complicated

because the inner sidewalls of the spacer must now provide a uniform counterflow velocity along the length of the chamber in addition to the electric field. Therefore, the goal of this chapter is to establish design guidelines for an FF-CGF device that can address this challenge while providing the possibility to scale up to a higher sample throughput.

6.1.2 Design Overview

The initial FF-CGF prototype used a multilayer soft lithography technique to create side channels that were capable of supplying the separation chamber with the counterflow. The height of the side channels were small relative to the separation chamber to give them a high hydrodynamic resistance, and this ensured a uniform flow rate along the length of the chamber. Although experimental results demonstrated the success of this strategy, it becomes difficult to achieve when transitioning from soft lithography to a more scalable fabrication technique like the aforementioned PMMA assembly. Moreover, the high resistance side channels limit the effective voltage drop across the separation chamber, and this can be a major issue for high throughput separations that require high electric fields.

The original plan for a preparative scale FF-CGF device was to simply replace the side channels with a commercial porous membrane that can be easily integrated into the PMMA assembly. At the same time, the ionic current would be decoupled from the porous membrane to avoid subjecting it to the high resistance requirement and maximize the voltage drop across the separation chamber. After several rounds of prototyping, it was determined that the design of the FF-CGF system was more complicated than anticipated because a number of design factors can influence the fluid dynamics and electrokinetics. Consequently, a thorough investigation is needed to understand these key parameters and then construct a practical device for high throughput protein purification.

One portion of this study will use numerical simulations to understand the key FF-CGF design parameters presented in Fig. 6.1. For example, it is important to know the minimum resistance needed for the porous membrane to provide a uniform velocity gradient along the length of the chamber. During this process, the resistance of the separation chamber, outlet channels, side channels, and side chambers also deserve consideration. Furthermore, it is critical to position the electrodes and ion exchange membranes such that the impact of ion concentration polarization does not affect the separation process. Finally, when injecting the sample, it is helpful to predict the maximum throughput while also ensuring that different proteins can be resolved.

Another portion of this study will establish fabrication protocols for an FF-CGF device based on the information gained from the numerical simulations. This device consists of double-sided tape with PMMA sheets laminated on each side. A laser cutter is used to engrave side channels into the PMMA, provide access holes for the fluid flow, and remove regions of the double-sided

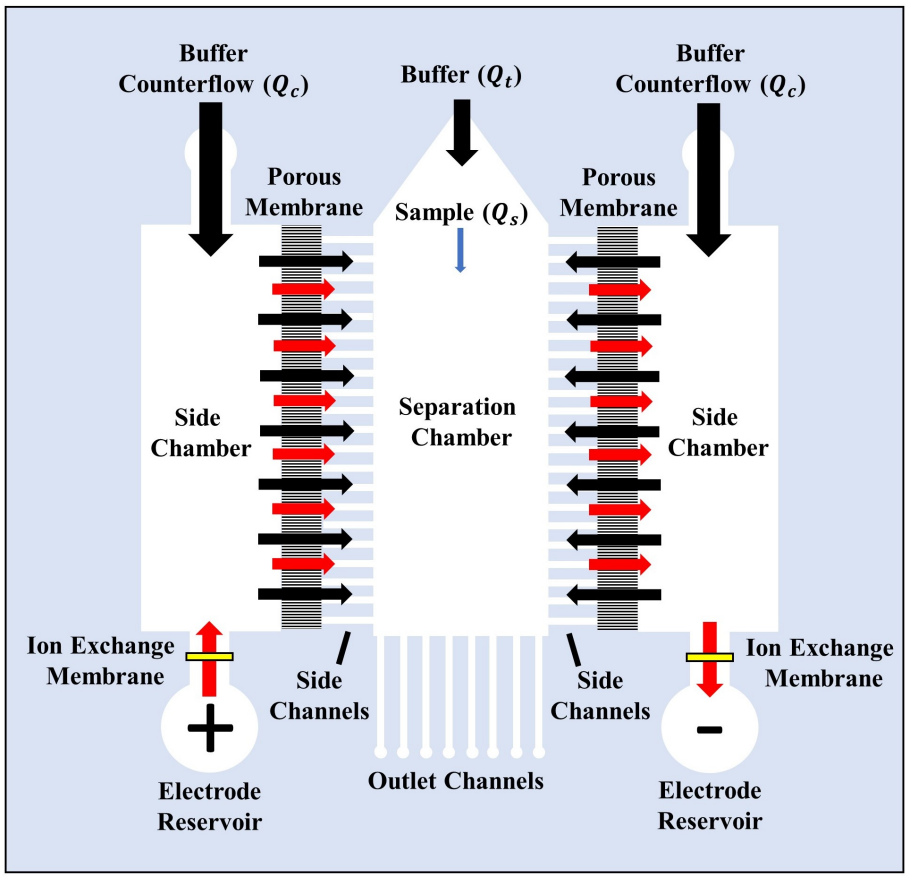


Figure 6.1: An overview of a FF-CGF system for preparative scale applications.

tape that make up the separation chamber. Meanwhile, porous substrates and ion exchange membranes are integrated into the PMMA sheets to supply the counterflow and current, respectively. After the fabrication is completed, the device will demonstrate the separation of small molecules and proteins to validate the design guidelines. It should be noted that building a preparative scale device that can rival the throughput of a commercial FFE instrument is beyond the scope of this work, as this would require a significant investment in multichannel peristaltic pumps, high voltage equipment, and cooling plates. With that said, this device was designed to be scalable, and the preliminary results should inspire confidence for investing in this area moving forward.

6.2 Methodology

The purpose of this section is to outline the techniques used during the development of the FF-CGF prototypes. This includes numerical simulations, device fabrication, and experimental setup.

6.2.1 Numerical Simulations

Numerical simulations in COMSOL v5.6 were used throughout this chapter to help guide the design of the preparative scale device. The protocols and relevant equations for 2D fluid flow, electrostatics, and chemical species transport have been outlined in previous chapters. In this chapter, there is the addition of flow in porous media that needs to be considered. According to COMSOL documentation, Darcy's law can be used to model the fluid flow for a low Reynolds number ($Re < 10$), and the Kozeny-Carmen equation can be used to model a porous membrane that resembles a packed bed of particles. Both of these equations will be described further in a later section of this chapter (see Section 6.3.2).

6.2.2 Materials

All chemicals were purchased from Sigma-Aldrich. The electrode buffer consisted of 445 mM of Tris and 445 mM of boric acid, with the pH adjusted to 8.4 using an HCl solution. This was then diluted to 89 mM of Tris and 89 mM of boric acid for the buffer counterflow pumped through the sides of the separation chamber. Various sample solutions were prepared in the separation buffer using xylene cyanol FF, orange G, ponceau S, rhodamine B, and fluorescein, and each dye had a concentration of 5 mg/mL. Another sample solution was prepared in the separation buffer, and it consisted of bovine serum albumin (BSA), hemoglobin (Hg), and cytochrome c (Cyt C). The concentration of each protein was 50 mg/mL, and the BSA was labeled with bromophenol blue at a 1:1 molar ratio.

6.2.3 Experimental Setup

Syringe pumps (Pump 11 and Pump33, Harvard Apparatus) were used for the sample and buffer flow, while a high voltage supply (HVS448-3000, LabSmith) was used to supply the electric field. A constant current mode was used to adjust for voltage changes that may arise due to ion concentration polarization (ICP), Joule heating, and bubble formation.

6.2.4 Fabrication Protocols

As previously mentioned, the devices discussed in this chapter (see Fig. 6.1) were made using a fabrication protocol that involved laser cutting and lamination. Briefly, PMMA sheets (McMaster-Carr) were cut to shape using a laser cutter (VLS2.30, Universal Laser Systems). A vector mode was used to create the chambers and access holes, while a raster mode was used to engrave microchannels on the PMMA surface. The PMMA sheets were joined together using double-sided tape (ARcare 90106, Adhesives Research) and a cold laminator (14Inch, INTBUYING). Furthermore, design features such as a separation chamber or via holes can be created from the double-sided tape layer using either a laser cutter or cutting plotter (Cricut Maker). Porous membranes (9619 and 9948, Porex) were used to generate a uniform counterflow gradient along the length of the separation chamber, and they could be easily cut to shape with a knife and bonded to the double-sided tape. Likewise, the ion-exchange membranes (Nafion 117, FuelCellStore) were bonded to the double-sided tape to connect the side chamber to the electrode reservoirs, and they were soaked in deionized water for 24 h prior to bonding to ensure that they did not expand upon contact with the buffer solution. The electrode reservoirs containing platinum electrodes (A-PT-Electrode, LabSmith) were made from an acrylic tubing (McMaster-Carr), and they were bonded to the PMMA layers using epoxy. Stainless steel tubing from dispensing needles (McMaster-Carr) was connected to the access holes, and they were also bonded to the PMMA using epoxy. Silicone rubber tubing (McMaster-Carr) was then attached to the stainless steel tubing in order to form a connection with the tubing from the syringe pumps. Note that a thin metal wire can be used to create a better seal around the rubber tubing. In addition, dowel pins (McMaster-Carr) can be used to plug the rubber tubing during experimentation.

6.2.5 Peak Analysis

A portion of the experimental validation of this FF-CGF device will consist of fluorescent peak measurements. First, the device was mounted on an inverted epifluorescence microscope (ECLIPSE Ti, Nikon) and a high sensitivity CCD Camera (Retiga 2000R, QImaging) was used to view the separation region. Illumination was supplied by a 100 W mercury halide lamp (Intensilight C-HGFIE, Nikon), and filter cubes (TRITC and FITC, Nikon) were used to acquire the desired fluorescence signals. ImageJ was then used to measure the intensity of the fluorescent images, and then MATLAB was used to fit the resulting peaks with an exponentially modified Gaussian (EMG) function [177] [178]:

$$f_{EMG} = \frac{1}{2\tau} \exp\left(\frac{1}{2\tau}\left(2\mu_G + \frac{\sigma_G^2}{\tau} - 2x\right)\right) \times \operatorname{erfc}\left(\frac{\mu_G + \frac{\sigma_G^2}{\tau} - x}{\sqrt{2}\sigma_G}\right) \tag{6.1}$$

where μ_G is the mean position of the Gaussian component, σ_G is the standard deviation of the Gaussian component, τ represents the decay rate of the exponential component, and erfc is the complementary error function. The first moment $M_1 = \mu_G + \tau$ represents the mean position of the peak, while the second moment $M_2 = \sigma_G^2 + \tau^2$ represents the variance of the peak [179]. These values can then be used to approximate the electric field across the separation region (see Section 5.3.8). Furthermore, recall that the G_x number of a peak can be related to the side flow rates (Q_c), where $G_x = \nabla\langle u\rangle h^2/D$, $\nabla\langle u\rangle = u_0/b$, $u_0 = Q_c/(2hL)$, $2b$ is the chamber width, L is the chamber length, $2h$ is the chamber height, and D is the diffusion coefficient.

6.3 Design Guidelines

The purpose of this section is to provide design guidelines for a FF-CGF device that is more scalable than the initial prototype. The discussion will mainly focus on strategies for generating a uniform counterflow gradient and electric field along the length of the chamber. This section will also include strategies for maximizing sample throughput.

6.3.1 Resistance Criteria

For an FF-CGF system with parallel side channels (see Fig. 6.1), each one should have the same ionic current and flow rate, as this will produce a uniform electric field and counterflow gradient along the length of the chamber, respectively. The current I through a microchannel can be determined from Ohm's law as [167]:

$$-\Delta V = IR_e \tag{6.2}$$

where ΔV is the voltage drop and R_e is the electrical resistance. The electrical resistance of a microchannel is written as [167]:

$$R_e = \frac{L}{\sigma_b HW} \tag{6.3}$$

where σ_b is the bulk conductivity of the solution, L is the channel length, W is the channel width, and H is the channel height. Meanwhile, the flow rate Q through a microfluidic channel can be determined by applying the electrical circuit analogy [167]:

$$\Delta p = QR_{hyd} \tag{6.4}$$

where Δp is the pressure drop and R_{hyd} is the hydrodynamic resistance. The hydrodynamic resistance of a microchannel can be written as [167]:

$$R_{hyd} = \frac{12\eta L}{WH^3}\left[1 - \frac{H}{W}\left(\frac{192}{\pi^5}\sum_{n=1,3,5}^{\infty}\frac{1}{n^5}\tanh\frac{n\pi W}{2H}\right)\right]^{-1} \tag{6.5}$$

where η is the viscosity. For both electrical and hydrodynamic resistance, when there are N side channels in parallel, the total resistance can be written as [167]:

$$R_{tot} = \frac{R_n}{N} \tag{6.6}$$

where R_n is the resistance of each side channel. While predicting the ionic current through the side channels is relatively straightforward, the flow rate is more complex. Referring back to Fig. 6.1, the flow rate through the side channels must also consider the resistance of the side chamber, separation chamber, and outlet channels in series. Furthermore, it is complicated by the fact that the series resistance of the separation chamber is different for each side channel. For example, a side channel near the top experiences a higher hydrodynamic resistance from the separation chamber than a side channel near the bottom. Consequently, according to Eq. 6.4, the hydrodynamic resistance of the separation chamber should be negligible relative to the side channels, as this will ensure that the flow rate through the side channels is approximately the same.

Therefore, when designing an FF-CGF device with a uniform counterflow gradient, it is helpful to compare the hydrodynamic resistance of the parallel side channels (R_{side}) to the separation chamber (R_{cham}). For example, Fig. 6.2a shows numerical simulations of the x-velocity in the system for different ratios of R_{side} to R_{cham}. Here, it can be seen that $R_{\text{side}}/R_{\text{cham}} = 1$ leads to a higher x-velocity at the bottom of the chamber, and this pushes the streamlines of charged solutes towards the middle of the chamber. However, the x-velocity becomes much more uniform along the length of the chamber when $R_{\text{side}}/R_{\text{cham}} = 5$, and the focal positions of the solute streamlines remain fixed. For a more quantitative understanding, the uniformity of the counterflow gradient can be approximated by comparing the x-velocity gradient $\nabla\langle u\rangle$ at the bottom of the chamber ($z = 0.9L$) relative to the middle of the chamber ($z = 0.5L$), and the results are shown in Fig. 6.2b for a variety device dimensions over a wide range of $R_{\text{side}}/R_{\text{cham}}$ values. In general, it appears that $R_{\text{side}}/R_{\text{cham}}$ should be at least 5 to achieve a uniform counterflow gradient, but this value can go higher for better results. Finally, it should be noted that R_{side} was increased in the numerical simulations by artificially varying the viscosity in the side channels (see Eq. 6.5), as other strategies are too computationally expensive. In reality, decreasing the height of the side channel is the most effective strategy for increasing the hydrodynamic resistance while minimizing the voltage drop. This is true because the electrical resistance is inversely proportional to H, while the hydrodynamic resistance is inversely proportional to H^3 (see Eq. 6.3 and Eq. 6.5).

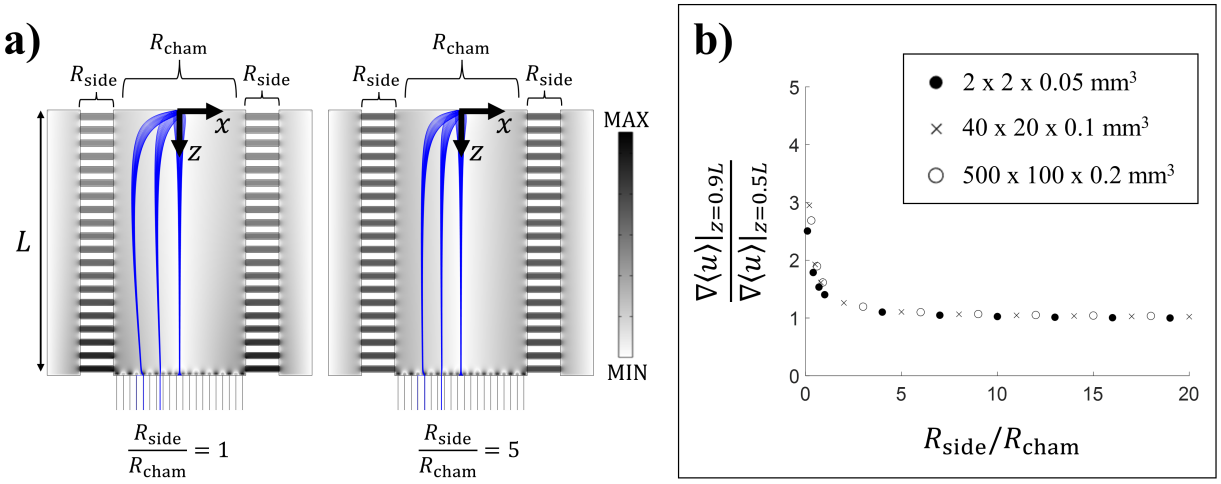


Figure 6.2: a) Simulation of x-velocity magnitude for different ratios of R_{side} to R_{cham}. Streamlines of charged solutes are shown to illustrate the impact of the counterflow gradient uniformity. b) Simulation of the counterflow gradient uniformity represented as $\nabla\langle u\rangle$ at $z = 0.9L$ relative to $\nabla\langle u\rangle$ at $z = 0.5L$ for a wide range of device dimensions ($L \times W \times H$).

6.3.2 Porous Membranes

When scaling up and transitioning away from soft lithography, incorporating side channels with a high resistance becomes difficult. For example, when using a laser cutter to engrave microchannels into the PMMA, it is difficult to achieve a depth of less than 50 μm, and the surface roughness is high. Moreover, when sealing these microchannels with double-sided tape, the adhesive can block the flow. Although these issues can be overcome with better fabrication protocols, a much more practical approach is to use commercial porous membranes that act as microchannels. These porous membranes can be easily integrated into the PMMA assembly, and placed in series with side channels to connect to the separation chamber (see Fig. 6.1).

In general, the pressure drop across a porous membrane is calculated according to Darcy's law, which is written as follows [193]:

$$\Delta p = Q\frac{\eta L}{kA} \tag{6.7}$$

where L is the membrane thickness, A is the cross-sectional area, and k is the permeability of the porous medium. Therefore, the hydrodynamic resistance of a porous membrane can be written as:

$$R_{hyd} = \frac{\eta L}{kA} \tag{6.8}$$

If the porous membrane resembles a packed bed of particles, then the permeability can be approximated using the Kozeny-Carman equation as follows [193]:

$$k = \frac{\varphi^3 d_p^2}{180(1-\varphi)^2} \tag{6.9}$$

where φ is the porosity of the membrane and d_p is the average diameter of the particles. Note that the porosity represents the fraction of empty volume in the porous membrane.

There were two different porous membranes that were considered during the construction of this FF-CGF device. The first option was a porous ceramic sheet from Innovacera that was made with aluminum oxide. This company offers sheets with custom thicknesses and pore sizes between 1 and 100 µm, while the porosity ranges from 40-50%. The second option was a porous sheet from Porex Filtration Group made from sintered ultra-high-molecular-weight polyethylene (UHMWPE). For the Porex sheets, there was less flexibility with the porous parameters, but it was ideal for prototyping because it was much less expensive and easier to cut to custom sizes. The sheet used most frequently during prototyping had a pore size between 7 and 12 µm, was available at a thickness of 1.5 mm and 3 mm (Porex 9619 and 9948, respectively), and had a minimum porosity of 35% according to the manufacturer. Note that there were several other Porex options available, but the pore sizes were larger and have more variability.

For the initial PMMA prototypes, the Porex 9948 membrane appeared to provide a sufficient hydrodynamic resistance for generating a uniform counterflow gradient. For confirmation, 3D numerical simulations were used to investigate the porous membrane assuming the Kozeny-Carman approximation with an average pore size of 10 µm and a porosity of 35%. Fig. 6.3 shows the porous membrane with a cross-sectional area of 5 mm by 30 mm, and it is connected to the side chamber and 15 parallel side channels. Note how the porous membrane is blocked at both ends to ensure that the first and last side channels do not receive additional inflow from these regions. The pressure drop across the membrane was calculated to be around 800 Pa when the input flow rate is 1×10^{-9} m/s^3, and this corresponds to a resistance of 8×10^{-11} Pa s/m^3. This is greater than the expected resistance of 3.55×10^{-11} Pa s/m^3 according to Eq. 6.8 because the geometry is more complex than what is assumed for Darcy's law. For example, the outflow is restricted to the geometry defined by the side channels, and this is much smaller than the cross-sectional area of the porous membrane. In the end, assuming the separation chamber has a length of 30 mm, a width of 10 mm, and a height of 0.12 mm, the resistance ratio between the simulated porous membrane and the separation chamber is about 38, which is more than enough for a uniform gradient based on Fig. 6.2b.

While the porous membrane design presented in Fig. 6.3 is acceptable for generating a uniform x-velocity gradient, and it may not be sufficient when scaling up to larger separation chamber lengths. However, several improvements can be made to increase the hydrodynamic resis-

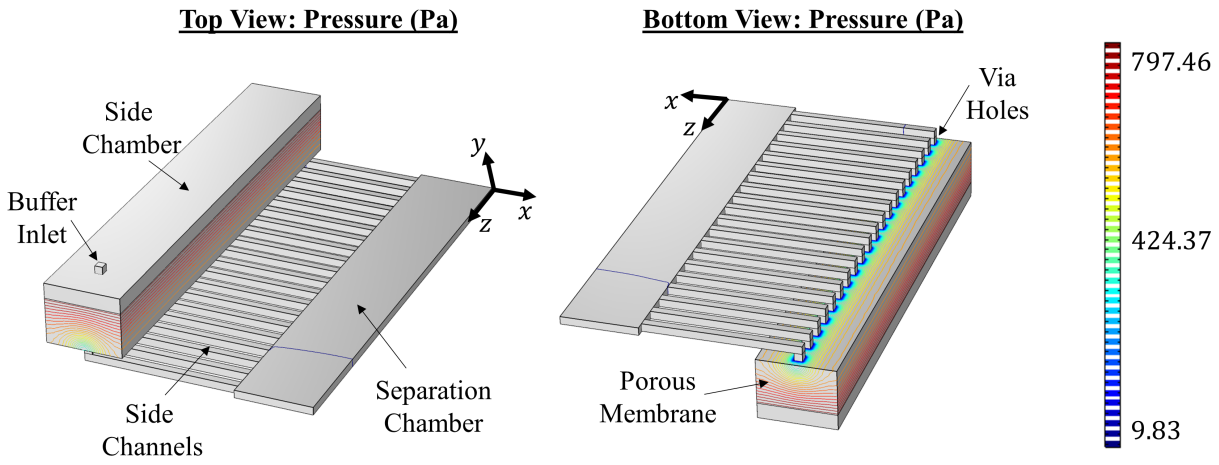


Figure 6.3: 3D COMSOL simulations for an FF-CGF chamber with a symmetric boundary condition along the z-direction. The pressure contours are provided for the top and bottom view. The porous membrane is 30 mm x 5 mm x 3 mm, with an average pore size of 10 μm and a porosity of 35%.

tance of the porous membrane. For example, its width can be reduced, and the sides can be blocked to restrict the flow. Note that this may complicate fabrication in terms of cutting the Porex and sealing the sides, but there will be an increase in resistance according to Eq. 6.8. Alternatively, the thickness of the porous sheet can be reduced, and the top can be covered to only allow inflow through the sides. In this case, the width of the sheet would act as L in Eq. 6.8, and can be easily increased for a higher resistance. Finally, another option would be to reduce the pore size to 1 μm by switching to the porous ceramic made by Innovacera, and this is also a more rigid material that may alleviate some of the fabrication concerns.

Due to the wide variety of options available for integrating porous membranes into the FF-CGF device, it is difficult to provide general design guidelines with clear analytical equations. Furthermore, the Kozeny-Carman equation may not provide an accurate approximation for some porous materials. With that said, this section justifies replacing microchannels with a porous membrane, and serves as a useful starting point when designing such a system. For example, Eq. 6.8 highlights the key parameters that influence hydrodynamic resistance, and the 3D numerical simulations can provide a more complete understanding. In addition, the Porex sheets are inexpensive and simple to cut, and this makes it easy to measure its performance experimentally.

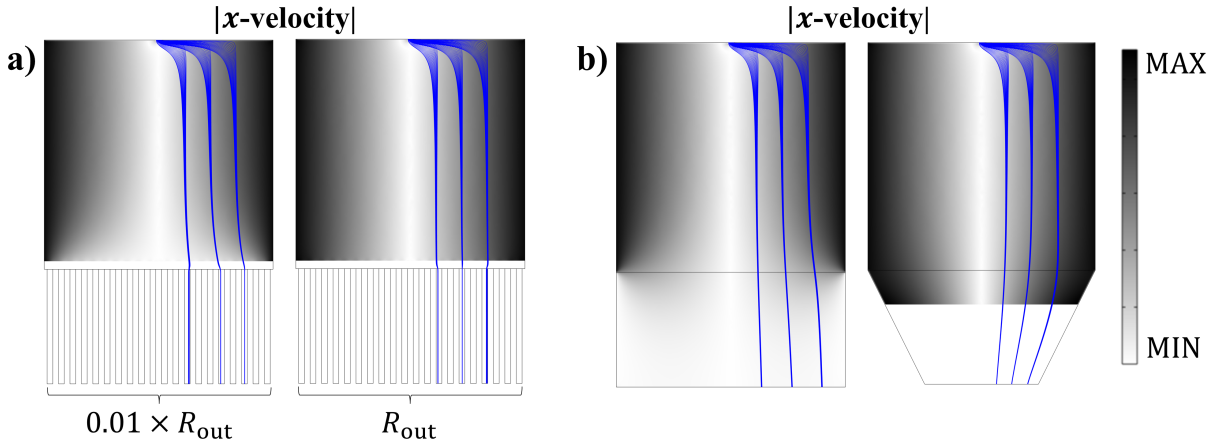


Figure 6.4: The x-velocity in an FF-CGF chamber and the streamlines of various charged solutes. a) The influence of the hydrodynamic resistance (R_{out}) of the outlet channels on the counterflow gradient. b) The influence of the geometry of an outflow region on the counterflow gradient.

6.3.3 Outlet Channels

Outlet channels are needed in FFE to collect the separated solutes (see Fig. 6.1). During the prototyping phase of the FF-CGF design, the outlet channels were found to have an impact on counterflow gradient uniformity. This was especially true when they were engraved into the PMMA with the laser cutter, as this resulted in an outlet channel height that was greater than that of the separation chamber. In this case, the relatively low hydrodynamic resistance made the majority of the counterflow exit through the outlet channels near the sidewalls (see in Fig. 6.4a). Consequently, the x-velocity component is lower than expected at the bottom of the chamber, and this pushes the charged solute streams towards the sidewalls. In general, it is important to be aware of the resistance of the outflow, but it is usually not an issue as long as the height of the outlet channel matches that of the separation chamber (see in Fig. 6.4a). On another note, all outlet channels should have an equal spacing on each side in order to receive an equal portion of the flow. For example, if there is excess space between the sidewalls and the first outlet on the left (see in Fig. 6.4a), this will alter the x-velocity by pushing this excess flow towards the middle of the chamber.

In practice, the outlet channels were difficult to include as part of the double-sided tape layer because they were long and unsupported at the end connected to the separation chamber. This caused them to bend during lamination and led to nonuniform channel widths that altered the resistance. To avoid this issue while keeping the height consistent, only a small portion of the outlet channels were connected to the separation chamber, and laser engraving was used to join

them with a longer portion that was supported on both ends. Another problem with the outlet channels is that they can contain air bubbles that can significantly increase the hydrodynamic resistance, and this leads to a nonuniform outflow through the channels that can disrupt the separation upstream. Since fluid flow will take the path of least resistance, it can also be difficult to remove these bubbles. In fact, bubbles appeared so frequently that outlet channels were discontinued during the prototyping phase in order to focus on other aspects of the design. The simpler alternative was to implement an outflow region that converged toward one outlet, and this geometry was ideal for maintaining a uniform x-velocity gradient near the bottom of the chamber (see in Fig. 6.4b). Note that this design could be useful for real-time monitoring applications where sample collection is not needed, or when a few outflow ports at the bottom of the separation region while allowing the rest of the flow to exit through the final outlet as waste. With that said, outlet channels will be required for preparative scale applications, and moving forward valves and multichannel peristaltic pumps should be considered to purge the bubbles and ensure a uniform flow through each outlet [88] [89] [86].

6.3.4 Side Chambers

The side chamber is another subtle design feature that can influence the uniformity of the counterflow gradient. Like the separation chamber, the resistance should be negligible compared to the side channels. If not, there will be a large pressure drop along the length that will contribute to an uneven flow rate through the side channels. For the example presented in Fig. 6.1, this would contribute to a higher x-velocity at the top of the chamber due to the location of the inlet. Similarly, a relatively high side chamber resistance will lead to a nonuniform electric field, and the design presented in Fig. 6.1 would see a higher current near the bottom of the chamber due to the position of the electrodes. In general, it is straightforward to control the resistance of the side chamber, although it may be inefficient to use volumes that are too large.

6.3.5 Electrode Integration

Generating the orthogonal electric field in FFE is a difficult task that has been the subject of many studies in recent years [19] [21]. The main challenge is connecting the electrodes to the sidewalls of the chamber while ensuring the effects of electrolysis such as pH changes and bubbles do not influence the electrokinetics and the fluid flow. In general, there is an electrode compartment that is isolated from the separation chamber using an ion exchange membrane that is impermeable to fluid flow but allows ionic current to pass through. Moreover, the buffer in the electrode compartment is constantly replenished to mitigate the effects of electrolysis bubbles, Joule heating, and ion concentration polarization (ICP) [29]. There have been many strategies for integrating

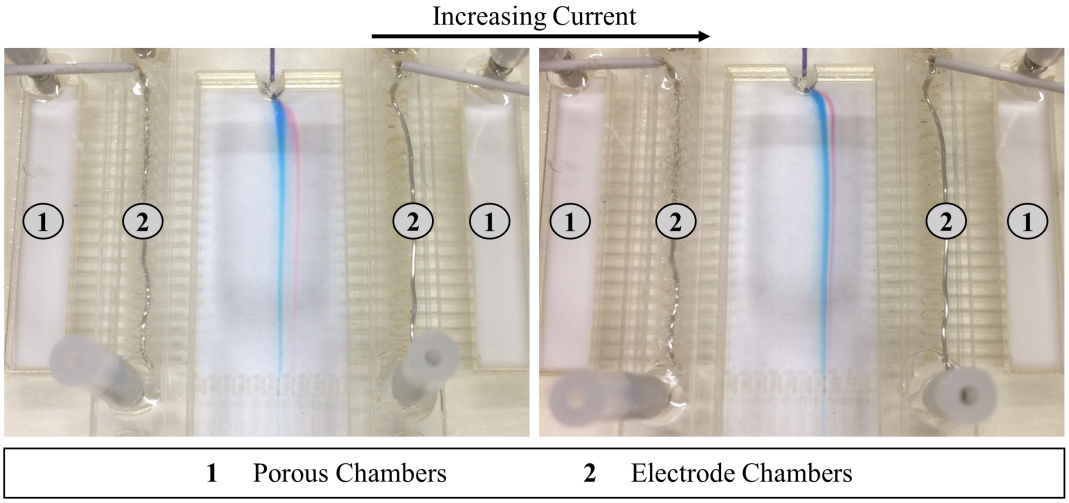


Figure 6.5: The separation of xylene cyanol FF (blue) and ponceau S (red). As the current increases in the right image, ion concentration polarization (ICP) appears to influence separation due to a stacking effect. Note the location of the porous chambers and electrode chambers.

the electrode compartment in FFE, and some techniques have managed successful operation by removing the membrane altogether [90]. However, in FF-CGF this difficult task becomes much more complicated by the need to introduce a uniform counterflow through the sidewalls as well.

The initial FF-CGF prototype made from PDMS placed the electrode compartment inline with the counterflow input, and the high resistance side channels were able to generate a uniform electric field and velocity gradient along the length of the chamber. This strategy resembles the electrode integration method used for the original μFFE system, and like this device there was a large voltage drop across the channels that limited the electric field. Therefore, one of the goals of the second prototype made from PMMA was to decouple the current input from the counterflow input in order to avoid subjecting the ionic transport to the same high resistance criteria. The logical approach was to have separate side compartments for the porous membrane and the ion exchange membrane, with via holes used to connect each one to the side channels. This device is shown in Fig. 6.5 with the electrode compartment located closer to the separation chamber to maximize the voltage efficiency. Unfortunately, having the ion exchange membrane positioned this close to the chamber created an ICP effect that impacted the separation significantly.

For the device seen in Fig. 6.5, a cation exchange membrane (Nafion) is used for both electrode compartments, and there is clearly an increased concentration of anions on the right side of the chamber that cannot pass through the membrane and into the positive electrode compartment. Similar to FF-FSE, this causes the red solute stream to sharpen at the interface where

the conductivity appears to increase. Furthermore, there is clearly a stacking effect, as the blue solute stream gets closer to the red stream as the current increases. Consequently, this approach to electrode integration is not ideal for FF-CGF because the ICP can significantly alter the focusing dynamics. Interestingly, this problem was easy to diagnose because a recent FFE study leveraged this ICP effect with a Nafion membrane in order to concentrate separated solutes [79]. Therefore, perhaps there is some future version of FF-CGF that takes advantage of ICP to create highly concentrated solute streams.

In the end, decoupling the transport of ionic current and counterflow through the sidewalls proved too difficult to achieve with the current prototype. Instead, the Nafion membrane was connected to the same side chamber as the porous membrane (see Fig. 6.1), and the following experimental section shows that the Porex material provided a uniform electric field along the length of the chamber. Moving forward, one solution to the ICP problem would be to replace the Nafion membrane with a porous membrane that is not ion selective, but it should also be impermeable to fluid flow to simplify the design of the system. For example, perhaps there is a hydrophobic porous membrane available that could ensure that a portion of the side flow does not leak into the electrode compartment. However, a more feasible alternative for the device presented in Fig. 6.5 would be to switch the position of the porous compartment and the electrode compartment, and redirect a portion of the counterflow away from the separation chamber and into a waste chamber. As seen in Fig. 6.6, this would help flush excess ions at the membrane surface, or replenish the region if it becomes depleted. Such a system would require a uniform outlet channel resistance, or else some of the waste may recirculate back into side channels towards the bottom of the separation chamber and alter the counterflow gradient. Similar to the outlet channels, this issue could not be overcome with the initial PMMA prototype, but it is likely solvable with better outflow control, and may be necessary for future FF-CGF devices that require high voltages and long-term operation.

6.3.6 Sample Injection

Sample injection is another important design parameter to consider in preparative scale FF-CGF because it can influence the throughput and separation resolution. To understand this process, it is helpful to return to the equation that describes the x-position during transit through the chamber. While the initial derivation assumed a mass particle entrance at $x = 0$, the boundary conditions can be altered to the more general form as (see Chapter 3.2):

$$x = \frac{u_{\mathrm{EP}}}{\nabla\langle u\rangle}\left(1 - \left(1 + \frac{\nabla\langle u\rangle}{\langle w\rangle_0} z\right)^{-1}\left(1 - \frac{\nabla\langle u\rangle}{u_{\mathrm{EP}}} x_0\right)\right) \tag{6.10}$$

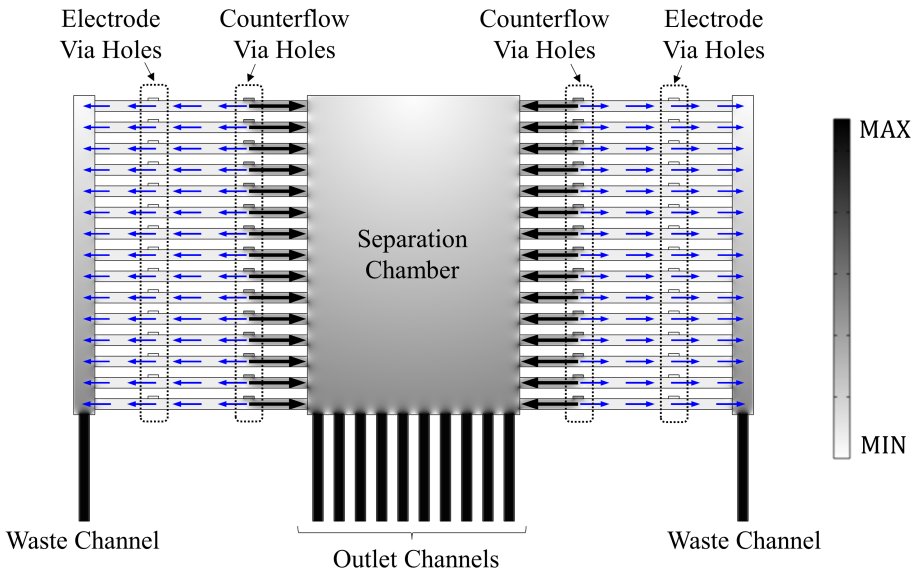


Figure 6.6: Simulation of velocity magnitude in a proposed FF-CGF device with a portion of the counterflow from the side channels directed into a waste channel to help flush away the effects of ion concentration polarization (ICP) at the electrode via holes. The black arrows represent the flow into the separation chamber, while the blue arrows represent the flow into the waste channel.

where x_0 is the starting x-position at $z = 0$. Therefore, if the sample injection width is 2δ, then Eq. 6.10 can be evaluated at $x_0 = \pm\delta$ to approximate the edges of the solute stream. Note that each streamline can be compared relative to the average focal position, $x_f = u_{\text{EP}}/\nabla\langle u\rangle$, to estimate the focusing percentage. Also note that the cross-sectional area of the sample injection is needed to relate the initial z-velocity, $\langle w\rangle_0$, to the sample flow rate, Q_s. For example, if the sample injection width is equivalent to the width of the separation chamber, then the sample flow rate can be written as $Q_s = (2b)(2h)\langle w\rangle_0$. This scenario is presented in Fig. 6.7 for different sample flow rates, and the analytical streamlines determined by Eq. 6.10 (see Fig. 6.7a and 6.7d) are in agreement with the corresponding COMSOL simulations (see Fig. 6.7b and 6.7e). Note that the area in between the edges of the solute stream is shaded black in Fig. 6.7a and 6.7d.

Furthermore, Fig. 6.7 shows how the sample injection can influence the separation resolution. In the case of Fig. 6.7a and 6.7b, the sample flow rate appears to provide the solute stream with enough time to reach its equilibrium width. However, when the throughput is increased by a factor of 5 (see Fig. 6.7d and 6.7e), the solute stream edges do not have sufficient time to focus, and the final distribution width is much larger. In practice, this scenario may be an acceptable means of increasing throughput depending on the mobility difference between the solutes of interest. During experiments, it is also possible to deviate from Eq. 6.10 to provide

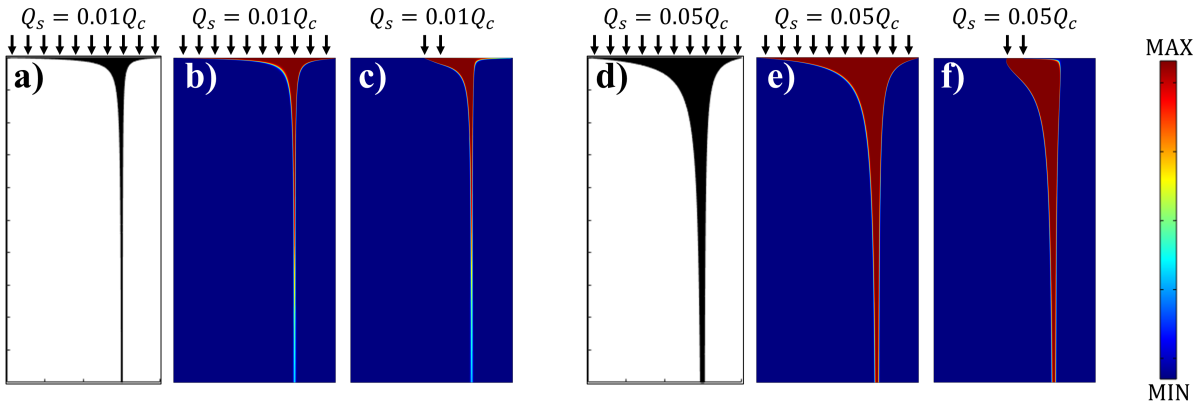


Figure 6.7: Comparing a low sample slow rate (Q_s) in a), b), and c) to a high sample flow rate (Q_s) in d), e), f), where Q_c is the flow rate on each side of the chamber. An analytical solution for particle transit is presented in a) and d), with the corresponding simulation of solute concentration shown in b) and e). An alternative simulation with a reduced injection width is also shown in c) and f).

more flexibility with $\langle w \rangle_0$. For example, Fig. 6.7c and 6.7f presents a practical design with a narrower injection width, but the sample flow rate is equivalent to Fig. 6.7b and 6.7e, respectively. At the same time, it is possible to add an initial buffer flow on each side of the sample injection to provide a cleaner sample entrance, and offer flexibility with the residence time. In the future, it could also help control the initial Péclet and Grashof numbers.

As an aside, the COMSOL simulations in Fig. 6.7 also demonstrate how the sample dilution is impacted by the sample injection. In the case of sufficient focusing (see Fig. 6.7b), the solute stream reaches its equilibrium width relatively early, and from there it becomes increasingly diluted. In the case of insufficient focusing (see Fig. 6.7e), the solute stream is being concentrated and diluted simultaneously, and as a result the overall concentration remains relatively constant throughout the chamber. Therefore, Eq. 6.10 can serve as a useful estimate of the sample dilution depending on the focusing percentage. However, at higher G_x numbers the concentration profile will likely be complicated by the influence of the parabolic profile.

6.4 Results and Discussion

The purpose of this section is to present the performance of an FF-CGF device that was designed based on the guidelines discussed in the previous section.

6.4.1 Device Design

The device was fabricated according to the laser cutting and lamination method outlined in a previous section (see Section 6.2.4). A layout of the three relevant layers are shown in Fig. 6.8, and this includes the top and bottom PMMA layers, as well as the double-sided tape layer in between. The separation chamber has a length of 30 mm and a width of 10 mm, and the height is defined by the thickness of the double-sided tape (0.14 mm). In reality, the height is likely smaller due to the compression of the adhesive during bonding. In Fig. 6.8, the side channels are engraved to approximately half the depth of the bottom PMMA layer, and this allows the porous membrane to connect to the separation chamber. Meanwhile, the via holes are present to ensure that the counterflow remains evenly distributed through the side channels after exiting the porous membrane. Furthermore, the ends of the porous sheets should be cut to maintain a consistent volume above each via hole, and the ends should be blocked with double-sided tape to prevent excess flow from these regions. During this process, the porous membranes formed a strong bond with the double-sided tape, and no leakage was observed during experiments. The same is true for attaching the Nafion membrane to the side chambers, except extra care is needed to ensure that its surface is fully in contact with the double-sided tape, or else it may expand upon hydration and create leaks. Finally, note the location of the sample inlet, which allows the sample to flow through the top PMMA layer and into the separation chamber.

6.4.2 Experimental Setup

An image of the actual FF-CGF is shown in Fig. 6.9 along with all of the relevant design features. During the experimental setup, the most difficult step was filling the device with the buffer solution while preventing bubbles from being trapped. Therefore, the current protocol will be described in this section. First, all access ports were plugged except the top flow inlet, the sample inlet, and the outlet. A syringe pump is then connected to the top flow inlet to slowly fill the separation chamber with buffer solution. The sample inlet and outlet should be plugged when they begin to overflow, and then the counterflow inlets and electrode waste ports should be unplugged. As a result, the side channels, porous membranes, and side chambers begin to fill with solution. It is likely that bubbles will become trapped in the side chamber, but because of its large volume it is easy to tilt the device and use gravity to direct them towards an access port. Importantly, the channel connecting the side chamber to the electrode reservoir should be free of bubbles to ensure an electrical connection, and then the electrode waste ports can be blocked (see Fig. 6.9). Moreover, it can be difficult to ensure the bubbles are fully removed from all of the side channels and porous membranes, so one option is to re-plug all ports except the top flow inlet, and then use the syringe pump to build up the pressure in the device. Then, by unplugging the electrode waste ports to release the pressure, bubbles from the porous membrane will

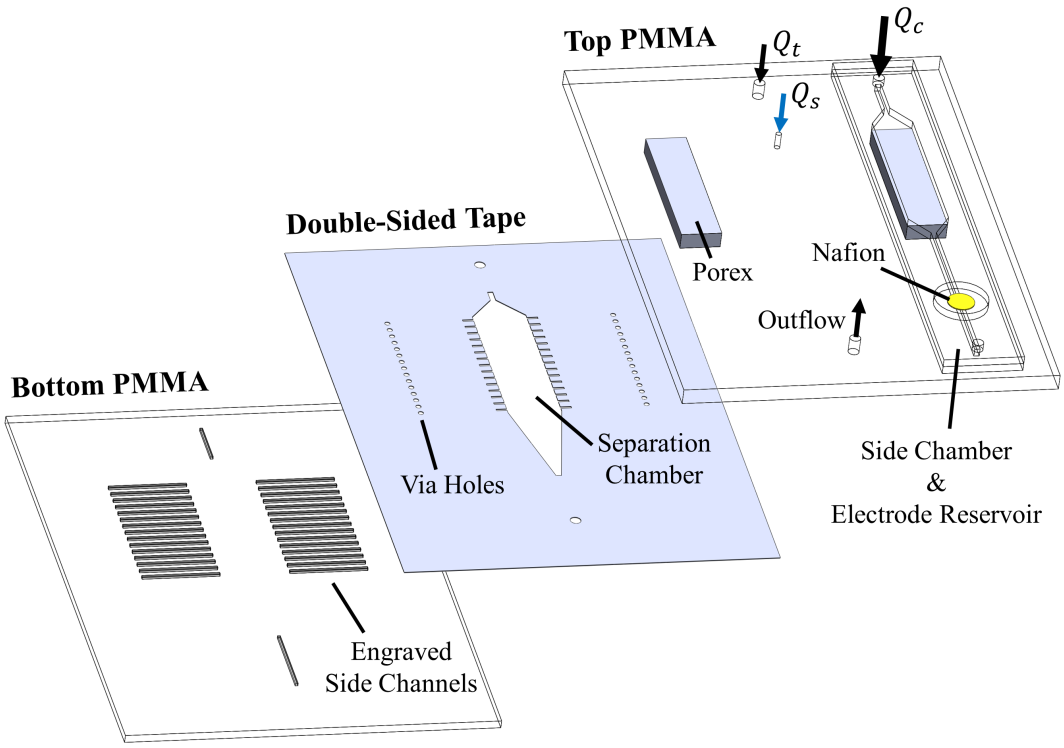
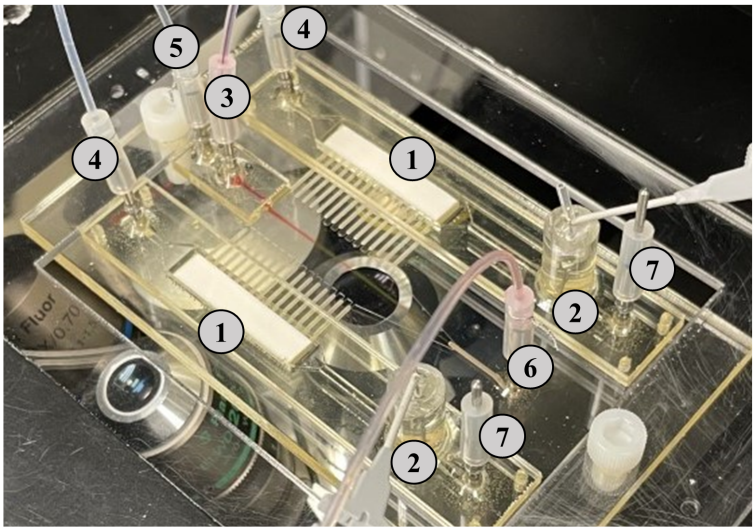


Figure 6.8: A layout of the three relevant layers used in the present FF-CGF device. A PMMA cover containing the side chamber and electrode reservoir is also shown on one side of the device.

enter the side chamber where they can be easily removed. This process must often be repeated several times, and it highlights one drawback of using the porous membranes. Another protocol for removing bubbles was to submerge the device in a water bath, and then place it in a vacuum chamber. However, this is a time-consuming and messy process, and there is no guarantee that all bubbles will be removed from the separation chamber.

After all bubbles are removed from the device, the syringe pumps can be connected to the counterflow inlets and sample inlet. During this process, it is helpful to allow these ports to overflow with solution from the top flow inlet, as this will prevent bubbles from reentering the system while connecting the tubing. After that, the outlet can also be unplugged and connected to a waste beaker to complete the setup of the fluid system. Then, the electrode reservoir can be filled with buffer solution, and its platinum electrodes can be connected to the high voltage supply. For long-term operation, the reservoirs can be connected to a peristaltic pump to continuously replenish the electrolyte solution. Finally, the device is ready for operation, and it can



1	Porous/Side Chamber
2	Electrode Reservoir
3	Sample Inlet
4	Counterflow Inlet
5	Top Flow Inlet
6	Outlet
7	Electrode Waste

Figure 6.9: An image of the present FF-CGF device mounted on a microscope.

be mounted on a microscope using a custom PMMA manifold (see Fig. 6.9). Note that further details on the equipment involved in the experimental setup, as well as preparation of the buffer and sample solutions, can be found in Section 6.2.

6.4.3 Device Performance

The uniformity of the counterflow gradient and electric field along the length of the chamber is demonstrated in Fig. 6.10. The separation of the dye molecules in Fig. 6.10a show an excellent agreement with the analytical and numerical models, and this helps validate the new design strategy which is heavily reliant on the high resistance of the porous membrane. The separation of various proteins is shown in Fig. 6.10b, and although focusing is achieved, there appears to be some nonidealities in the gradient that are important to point out. On the left side of the chamber, the Cyt C stream does not appear to reach its focal point as quickly as the Hg and BSA on the right. This is likely due to bubbles in either the side channels or porous membrane that are disrupting the counterflow gradient and electric field. While this is a minor issue, it highlights the importance of developing a robust protocol for removing all of the bubbles from the system. Moving forward, a better fabrication strategy for the side channels should also be considered, as the laser engraving strategy results in a high surface roughness that makes it easy for bubbles to become trapped.

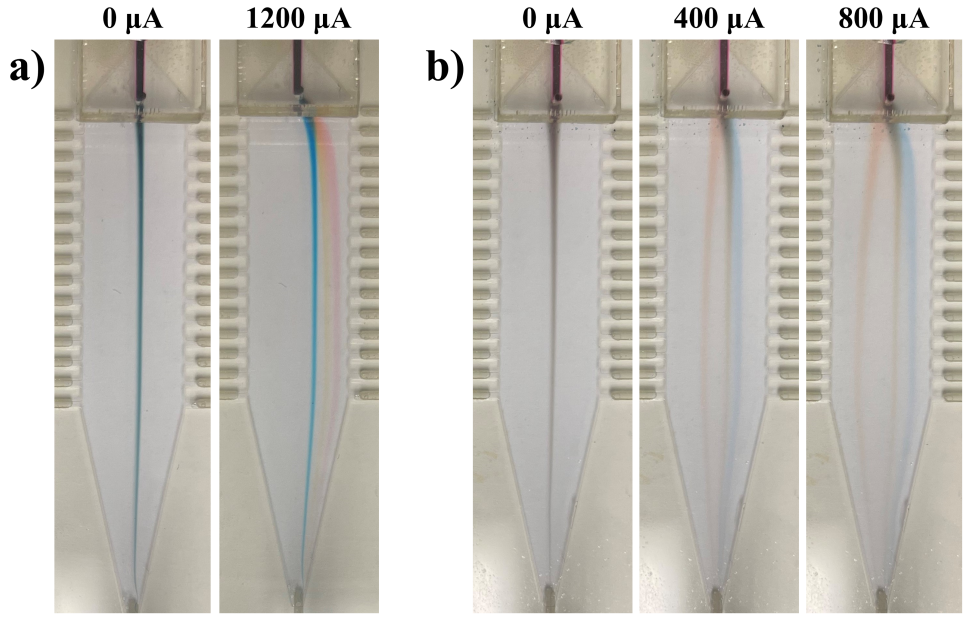


Figure 6.10: a) The separation of xylene cyanol FF, orange G, and ponceau S with a side flow rate of $Q_c = 40$ µL/min, a top flow rate of $Q_t = 1$ µL/min, and a sample flow rate of $Q_s = 0.2$ µL/min. b) The separation of Cyt C, Hg, and BSA with a side flow rate of $Q_c = 10$ µL/min, a top flow rate of $Q_t = 0.5$ µL/min, and a sample flow rate of $Q_s = 0.1$ µL/min.

6.4.4 Peak Measurements

The ability of this device to measure focused peaks experimentally is shown in Fig. 6.11. These peaks are then fitted with an EMG function, and the corresponding values for the average focal position $\langle x \rangle_f$ and the standard deviation σ are shown in Table 6.1. While it is difficult to calculate other relevant parameters without knowing the chamber height, they can be estimated by assuming it is around 0.012 cm. Therefore, the electric field E can be approximated with $\langle x \rangle_f$, the side flow rates shown in Fig. 6.11, and the assumption that fluorescein has an electrophoretic mobility of $\mu_{\text{EP}} = -3.6 \times 10^{-4}$ cm^2/Vs [189]. In addition, G_x can be approximated by assuming a diffusion coefficient of $D = 4.3 \times 10^{-6}$ cm^2/s [194]. Note that further details on obtaining these measurements can be found in Section 5.3. In general, the peaks seen in Fig. 6.11 appear to resemble a Gaussian shape, which is consistent with what is expected for the estimated G_x values shown in Table 6.1. Interestingly, as G_x increases, the peaks widths are noticeably reduced and their intensity is increased. Furthermore, a subtle peak tail emerges at higher G_x numbers, and this is particularly evident for fluorescein in Fig. 6.11d. This peak tail is on the right side, which

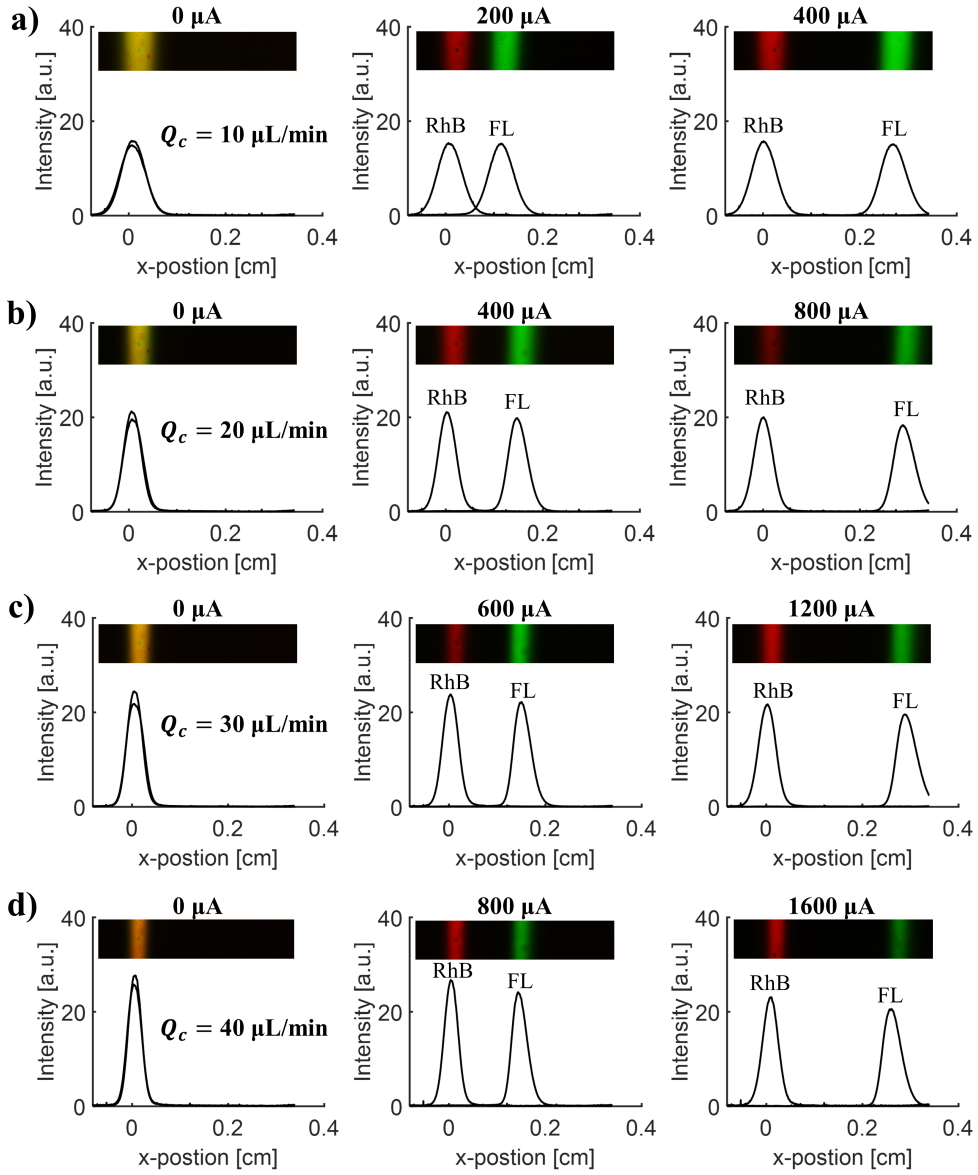


Figure 6.11: Peak measurements for the separation of rhodamine B (RhB) and fluorescein (FL) at different side flow rates (Q_c) and applied currents. In addition, the top flow rate and the sample flow rate for each experiment was a) $Q_t = 0.1$ µL/min and $Q_s = 0.025$ µL/min, b) $Q_t = 0.2$ µL/min and $Q_s = 0.05$ µL/min, c) $Q_t = 0.3$ µL/min and $Q_s = 0.075$ µL/min, and d) $Q_t = 0.4$ µL/min and $Q_s = 0.1$ µL/min.

Table 6.1: Fitted EMG parameters and estimated separation conditions assuming $2h = 0.012$ cm, $\mu_{EP} = -3.6 \times 10^{-4}$ cm^2/Vs, and $D = 4.3 \times 10^{-6}$ cm^2/s.

G_x	Q_c [µL/min]	Current [µA]	Voltage [V]	$\langle x \rangle_f$ [cm]	σ [cm]	E [V/cm]
0.08	10	200	89	0.12	0.0265	-2.96
		400	177	0.27	0.0270	-6.97
0.16	20	400	168	0.15	0.0210	-7.72
		800	298	0.29	0.0236	-15.13
0.23	30	600	262	0.15	0.0193	-11.90
		1200	550	0.30	0.0228	-22.80
0.31	40	800	404	0.15	0.0182	-15.34
		1600	498	0.26	0.0211	-27.22

indicates that the electroosmotic mobility for PMMA is less than the electrophoretic mobility for fluorescein ($Pe_E > 0$). According to literature, the electroosmotic mobility of PMMA has been measured to be around $\mu_{EOF} = 2.6 \times 10^{-4}$ cm^2/Vs [195], so this result makes sense. As a final note, the voltage and electric field values shown in Table 6.1 can be used to approximate the voltage efficiency when the chamber width is 1 cm. For example, at a voltage of 89 V and an electric field of -2.96 V/cm, this corresponds to a voltage efficiency of 3.3%. Consequently, the voltage drop across the porous membranes is significant, and there is certainly room for improvement in future iterations. Table 6.1 also reveals the nonlinear behaviour of the current and voltage due to Joule heating and ICP, and this is another area that deserves consideration in the future. Altogether, Fig. 6.11 has demonstrated the ability to analyze focused peaks with the current apparatus, which is not only useful for designing a preparative scale device, but also for studying the FF-CGF technique.

6.5 Future Considerations

Now that guidelines have been established for designing an FF-CGF device that is scalable, it is worth investigating the future steps required to approach mg/hr quantities in protein purification.

6.5.1 Experimental Parameters

For this exercise, it is helpful to use the dimensions of the commercial FFE instrument as a reference. The length is typically 50 cm, the width is either 5 cm or 10 cm, and the height ranges from 0.05 to 1.5 mm [28]. In most studies, the electric field typically does not exceed 200 V/cm [29], although some microfluidic devices have reported values approaching 600 V/cm due to the faster heat dissipation [37]. Meanwhile, the sample flow rate often ranges from 0.2 to 5 mL/hr [81] [191], and the total flow rate usually corresponds to a minimum residence time of around 5 min [196]. For the sample itself, the diffusion coefficient of a large protein is around 5×10^{-7} cm^2/s [197], while the maximum electrophoretic mobility is about 2.5×10^{-4} cm^2/Vs [198] [199], and these values can represent the upper limits of the G_x and Pe_{EP} values during FF-CGF protein purification.

6.5.2 Small Gradient Regime

In this regime ($G_x < 1$), Table 6.2 shows the relevant FF-CGF parameters for different chamber heights assuming a width of 10 cm and a length of 50 cm. Note that the experimental conditions presented in Table 6.2 correspond to a solute transit that is identical to the scenario presented in Fig. 6.7a. Additionally, the upper limit of G_x is 0.25, and many smaller proteins involved in the separation would have a G_x value closer 0.1. In general, operating in this range is ideal for maximizing the throughput while minimizing the effects of hydrodynamic dispersion.

Table 6.2 shows an interesting relationship between the chamber height and the other experimental parameters, and this is due to the fact that G_x is proportional to h^2, whereas Pe_{EP} is proportional to h. As a result, the smaller height enables higher flow rates for the given G_x, and this creates higher sample throughput. Moreover, Pe_{EP} is increased, and this allows for a higher peak capacity within the separation region. However, there are some disadvantages when using a height as low as 25 μm that deserve consideration. For one, $Pe_{\mathrm{EP}}/G_x = 2000$ will lead to significant dispersion and cause the resolution in the outer limits of the separation region to deteriorate. Second, an electric field of 800 V/cm will likely cause excessive Joule heating, although the small chamber height and the short residence time may provide some forgiveness. Third, the advantage of a high peak capacity in the middle of the separation region may be offset by the practical challenges associated with placing several outlet ports in close proximity. Finally, a height of 25 μm will make it difficult to generate a uniform counterflow gradient because the hydrodynamic resistance of the separation region will be high.

Therefore, a chamber height between 50 and 100 μm is likely more practical even though the throughput is lower. Nonetheless, the sample throughput will be around 1 mg/hr if the initial protein concentrations range from 1 to 2 mg/mL, and the flow rate can be increased further

Table 6.2: Experimental parameters for an FF-CGF chamber with $G_x = 0.25$, $L = 50$ cm, $2b = 10$ cm, $D = 5 \times 10^{-7}$ cm^2/s, and $u_{EP} = 2.5 \times 10^{-4}$ cm^2/Vs.

Height ($2h$)	25 μm	50 μm	100 μm
Side Flow (Q_c)	180 mL/hr	90 mL/hr	45 mL/hr
Sample Flow (Q_s)	1.8 mL/hr	0.9 mL/hr	0.45 mL/hr
Electric Field (E)	800 V/cm	200 V/cm	50 V/cm
Residence Time	1.10 min	4.42 min	17.68 min
Pe_{EP}/G_x	2000	1000	500

depending on the mobility difference between the proteins of interest (see Fig. 6.7d). Note that this throughput is comparable to preparative scale FFZE and FF-IEF, so FF-CGF is worth considering as an alternative FFE mode. Consequently, a reasonable next step would be to construct a device with a height around 100 μm, and the key challenges would be to mitigate the effects of ICP and ensure a uniform flow through the outlet channels. Finally, it is recommended to reduce the length to simplify the initial prototype, and test it with a relevant protein mixture to demonstrate the benefits of preparative scale FF-CGF in practice.

6.5.3 Large Gradient Regime

In this regime ($G_x > 25$), Table 6.3 shows the relevant FF-CGF parameters for different chamber heights assuming a width of 2 cm and a length of 50 cm. Note that the width is reduced to accommodate for the higher electric fields needed for this G_x range. Also, the sample flow rate is calculated assuming injection is limited to the middle 25% along the height direction because anything beyond this would be lost in the peak tails. Once again, the solute transit corresponds to the path seen in Fig. 6.7a, although for this G_x regime most of the sample will be focused closer to the centerline. Finally, the upper G_x limit is set to 100 because this should permit most protein sizes to have a G_x greater than 25. Ideally, the G_x could go even higher for sharper peaks, but this would challenge the limits of the electric field and the peristaltic pumps.

Compared to Table 6.2, Table 6.3 shows a similar relationship between the chamber height and the experimental parameters such as flow rate and electric field. The height of 500 μm offers

Table 6.3: Experimental parameters for an FF-CGF chamber with $G_x = 100$, $L = 50$ cm, $2b = 2$ cm, $D = 5 \times 10^{-7}$ cm^2/s, and $u_{\text{EP}} = 2.5 \times 10^{-4}$ cm^2/Vs.

Height ($2h$)	125 μm	250 μm	500 μm
Side Flow (Q_c)	2880 mL/hr	1440 mL/hr	720 mL/hr
Sample Flow (Q_s)	7.2 mL/hr	3.6 mL/hr	1.8 mL/hr
Electric Field (E)	2560 V/cm	640 V/cm	160 V/cm
Residence Time	4.14 s	16.57 s	66.29 s
$\boldsymbol{Pe_{\text{EP}}/G_x}$	80	40	20

the most manageable electric field, but with $Pe_{\text{EP}}/G_x = 20$ this implies a small peak capacity, and the sample throughput is not much greater than the small gradient regime (see Table 6.2). These factors can be improved by moving closer to a height of 250 μm, but this would begin to test the limits of the electric field. With that said, the residence time is very low, and perhaps this would help counteract some of the effects of Joule heating. As the height approaches 125 μm, it is interesting to note that the device is no longer practical due to the high electric field. However, perhaps there is some application where lower electric fields can be used to separate a few proteins in the middle of the separation region (near $x = 0$), as this would yield a significant throughput with highly concentrated peaks. Moreover, if the chamber width is increased to 10 cm, this would increase the throughput further. In the end, it is intriguing to consider a separation in the large G_x regime due to the potential benefits, but the system becomes much more complicated to build, and further development is needed to focus the sample injection and handle the large flow rates and voltages seen in Table 6.3.

6.6 Concluding Remarks

In the first portion of this chapter, a new design for an FF-CGF device was presented in order to make it more scalable for protein purification. First, a new fabrication method involving the lamination of PMMA and double-sided tape was proposed, and this offered better performance than the traditional soft lithography technique. Then, the challenge of generating a uniform counterflow gradient along the length of the separation chamber was discussed in depth, and it

was determined that adding porous membranes to the PMMA assembly is a practical solution. At the same time, the hydrodynamic resistance of the separation chamber, outlet channels, and side chamber also deserve consideration. During this investigation, design guidelines for maximizing the sample throughput and minimizing the effects of ion concentration polarization were also provided.

In the second portion of this chapter, a functioning prototype was constructed, and the successful separation of small molecules and proteins highlighted the potential of this device. Moreover, the device provided some useful peak measurements that helped further the understanding of this separation method. Finally, the presence of a uniform counterflow gradient and electric field along the length of the separation chamber was confirmed, and this helps validate the design guidelines provided for this fabrication method. With that said, there are several areas of improvement that should be considered moving forward, including precise flow control through the outlet channels, increased voltage efficiency, the mitigation of ion concentration polarization and Joule heating, and the removal of trapped bubbles during the experimental setup. In addition, the strategies for scaling up should be examined in more detail, as FF-CGF can likely rival the throughput of traditional FFE devices while offering the potential of improved resolution and versatility.

Chapter 7

Improving Device Design II: Analytical Scale

7.1 Introduction

The purpose of this chapter is to design an analytical scale FF-CGF device, and it was initiated for exploratory purposes. For one, there was an interest in applying the FF-CGF design guidelines to build a microfluidic device with a better voltage efficiency. Second, there was an interest in creating an FF-CGF device capable of observing protein separations at high gradient numbers ($G_x > 25$). Along the way, it was determined that this device is useful for handling minute sample volumes, and therefore this chapter will also discuss the potential applications and design requirements at this scale.

7.1.1 Motivation

In recent decades there have been several technological innovations for implementing FFE in microfluidics, and this has expanded the potential applications for FFE. While the preparative scale FF-CGF design discussed in a previous chapter is useful for the isolation of large quantities of proteins, it is not necessarily ideal for analytical scale applications. Therefore, the primary goal of this chapter is to address these limitations, and provide a framework for designing an FF-CGF device at this scale.

First, in FFE the continuous extraction process enables interfacing with analytical methods such as mass spectroscopy, chromatography, and other lab-on-a-chip technologies for the multidimensional analysis of important protein properties [33] [112] [21]. However, proper implementation would require microfabrication techniques that are not possible with the laser cutting and lamination method proposed for the preparative scale FF-CGF device. For example, complex microchannel networks downstream from the separation can be useful when a μFFE device

is coupled with a mass spectrometer, as this can help prepare the sample prior to the electrospray process [32]. In another possible scenario, microstructures can be used in microfluidics to continuously separate proteins and cells based on size [200] [201], and employing this method in tandem with FF-CGF would provide an additional dimension of separation and analysis. Finally, the high resolution separation and transfer of minute samples for further processing often benefits from outlet channels that are small and closely spaced, and this is difficult to achieve with the laser cutting method.

Second, the continuous nature of FFE offers the potential to monitor the concentration of analytes from complex mixtures in real-time, and this could be used in a clinical setting, or in an industrial bioreactor for quality control [35]. For these applications, it would be ideal to make the apparatus much smaller than the existing FF-CGF devices. For one, this would enable portability and simple integration with most work spaces. Furthermore, the smaller volumes would reduce the consumption of precious samples, and promote fast separations that are desirable for real-time detection [73]. Additionally, a small device would facilitate the use of a compact detection system that can view the entire separation region. Finally, if the voltage efficiency can be improved, this would allow for a more portable power supply.

Third, the continuous operation of FFE provides the ability to conduct high throughput biological assays where the experimental conditions can be changed dynamically. For example, the buffer conditions or the sample concentration can be varied with time, and this format has been used to measure the binding affinity between DNA aptamers and a target protein [110] [34] [202]. This illustrated the potential to conveniently measure protein interactions under different conditions, and should be exploited in FF-CGF for various pharmaceutical applications. Once again, a smaller device would be ideal to reduce the amount of expensive proteins that are needed for such a study. Moreover, the current FF-CGF devices consist of side chambers with very large volumes, and this would cause a long delay when attempting to vary the buffer conditions within the separation chamber itself. Consequently, an FF-CGF device that can quickly update the properties of the buffer input would be ideal for this application.

Lastly, the development of FF-CGF at the analytical scale would also allow further exploration for an improved understanding of this separation method. For example, faster heat dissipation and narrower chamber widths would enable observation of protein separations at higher G_x numbers. It would also act as a tool for optimizing experimental conditions for preparative scale applications while minimizing the use of costly proteins and other reagents. The wide range of fundamental studies and established fabrication techniques in microfluidics could also provide a strong foundation for developing FF-CGF further and exploring strategies for reducing dispersion.

Clearly, there are many useful applications for FFE at the analytical scale, and to leverage the advantages of FF-CGF, a device specifically designed for this scale is needed. In essence,

this chapter will expand upon the proof-of-concept FF-CGF device presented in Chapter 3 by providing a more comprehensive understanding of the design factors to consider when scaling down. Then, an analytical scale device will be constructed and a protein separation application will be demonstrated. Finally, a potential application for protein purification in tandem with mass spectroscopy will be proposed for future considerations.

7.2 Design Guidelines

The purpose of this section is to consider the requirements for analytical applications, and then propose a design with the help of numerical simulations and previously established guidelines. Hopefully, this will serve as a general framework for designing an analytical scale FF-CGF device.

7.2.1 Design Overview

A schematic of the proposed analytical scale device is presented in Fig. 7.1. Note that the length is 1 mm and the width is 2 mm, and these small dimensions have several benefits. For one, this will give the separation chamber a low hydrodynamic resistance, which helps produce a uniform counterflow gradient without constricting the height of the side channels, and therefore simplifies the fabrication and improves the voltage efficiency across the separation region. Second, the microscope is capable of viewing the entire chamber and no sagging was observed due to the poor structural integrity of PDMS. Third, these dimensions take up a small region of a standard glass slide, leaving room for additional analytical methods to be included on the same microfluidic chip for multidimensional analysis. Fourth, the narrow chamber enables protein separations at higher G_x numbers without challenging the limits of the syringe pumps and the voltage supply. Finally, the entire volume of the system is significantly reduced, and this can minimize sample consumption while also enabling fast separations and dynamic changes to the buffer properties.

7.2.2 Device Dimensions

The length and width of the separation chamber presented in Fig. 7.1 provide a general starting point, but other dimensions in the millimeter range are also acceptable depending on the application. The outlet channels have a width of 20 μm, and this value offers the potential to isolate closely spaced peaks. Ideally, this parameter could be reduced further, but this begins to challenge the fabrication quality. The side channels also have a width 20 μm, and these small dimensions help ensure a uniform counterflow gradient near the sidewalls. The length of the

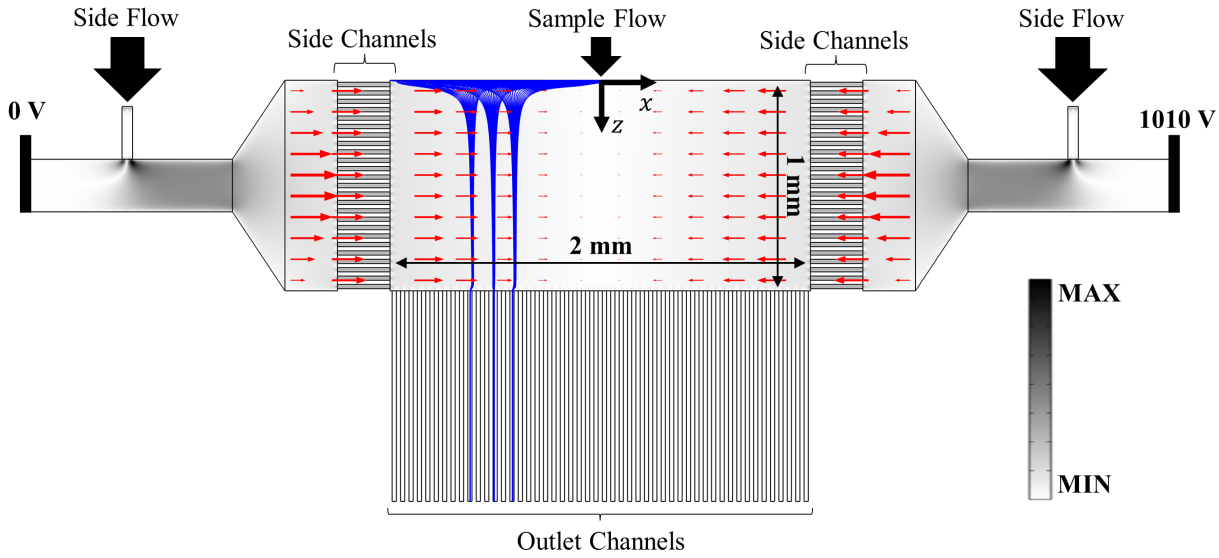


Figure 7.1: A schematic of a potential analytical scale device for FF-CGF. Numerical simulations show a surface plot for the x-velocity magnitude when the height is 50 µm, as well as the streamlines of several charged solutes with mobilities of 2, 2.5, and 3×10^{-4} cm^2/Vs.

side channels was chosen to be 250 µm, but there is potential to reduce this parameter further to improve the voltage efficiency. Finally, the height of the separation chamber can be chosen based on a number of factors that are presented in Table 7.1. Once again, it is preferable to have side channels with the same height as the separation chamber, and therefore the ratio between the hydrodynamic resistance of the side channels (R_{side}) and separation chamber (R_{cham}) are included in Table according to the equations provided in a previous chapter.

The parameters shown in Table 7.1 represent multiple scenarios where a protein can be focused in the large gradient regime ($G_x > 25$). Overall, note how the flow rates and applied voltage can be reduced at this scale. In addition, note the convenience of working with larger chamber heights due to the smaller electric fields and the increased counterflow gradient uniformity (see $R_{\text{side}}/R_{\text{cham}}$). Interestingly, the larger chamber height also provides a lower flow rate which is ideal for handling minute sample volumes. However, the low Pe_{EP}/G_x value at a height of 100 µm implies a lower peak capacity, and although this issue can be solved by increasing the width of the chamber, there may be a size limit imposed by the analytical scale application. Consequently, there is a benefit to reducing the height and pushing the limits of the electric field. Finally, it should be noted that a 25 µm chamber height becomes more manageable if the dimensions of the separation region are reduced, but this will reduce the peak capacity as well as the number of outlet channels available for sample collection.

Table 7.1: Experimental parameters for an FF-CGF chamber with $G_x = 50$, $L = 1$ mm, $2b = 2$ mm, $D = 5 \times 10^{-7}$ cm^2/s, and $u_{\text{EP}} = 2.5 \times 10^{-4}$ cm^2/Vs. The 25 parallel side channels have a length of 250 μm and a width of 20 μm.

Height ($2h$)	25 μm	50 μm	100 μm
Side Flow (Q_c)	24 μL/min	12 μL/min	6 μL/min
Sample Flow (Q_s)	0.24 μL/min	0.12 μL/min	0.06 μL/min
Electric Field (E)	3200 V/cm	800 V/cm	200 V/cm
Residence Time	0.33 s	1.33 s	5.30 s
Pe_{EP}/G_x	40	20	10
$R_{\text{side}}/R_{\text{cham}}$	3.01	8.21	27.49

7.2.3 Numerical Simulations

The design presented in Table 7.1 was simulated in COMSOL using the numerical methods outlined in a previous chapter. Fig. 7.1 shows the streamlines of various charged solutes, and the counterflow gradient appears to be uniform along the separation chamber. Additionally, the solutes have enough time to reach their focal point despite the short chamber length. Note that the applied voltage is 1010 V, and the simulations calculate an approximate voltage drop of 160 V across the separation region, indicating the voltage efficiency is around 15%. In a future iteration, the voltage efficiency could be improved by increasing the height of the side chambers, although this will complicate the fabrication.

One challenge associated with the design presented in Fig. 7.1 is that the solute streamlines smear along the top of the chamber due to the no slip boundary condition. This causes an issue at lower G_x values due to diffusion in the z-direction, and with the chamber length being so short, the solute may not have time to sufficiently focus. Furthermore, it is difficult to introduce a buffer flow along the top of the chamber to prevent this issue and create a cleaner sample entrance. For example, if microchannels that resemble the outlet channels are added to the top of the chamber to supply an initial buffer flow, there may be some backflow or stray current that affects the sample injection. Moreover, given the short length of the chamber, an initial buffer flow may prevent a solute from reaching its focal position.

7.3 Experimental Section

The purpose of this section is to outline the fabrication and experimental setup for the analytical FF-CGF device at high gradient numbers ($G_x > 25$).

7.3.1 Materials

All chemicals were purchased from Sigma-Aldrich. The electrode buffer consisted of 445 mM of Tris and 445 mM of boric acid, with the pH adjusted to 8.4 using an HCl solution. This was then diluted to 89 mM of Tris and 89 mM of boric acid to serve as the buffer counterflow pumped through the sides of the separation chamber. The protein solution was prepared in the separation buffer, and it contained 10 mg/mL of bovine serum albumin (BSA) labeled with a fluorescent dye known as fluorescein isothiocyanate conjugate (FITC).

7.3.2 Device Fabrication

The FF-CGF design seen in Fig. 7.1 was fabricated using standard soft lithography techniques outlined in Chapter 3.4.2. Briefly, the silicon master mold had a target height of 50 μm, and the PDMS was prepared with a 10:1 ratio of base to curing agent and then baked for 3 h at 95℃. Then, the PDMS was bonded to a standard glass slide using oxygen plasma with a power of 29.6 W at 500 mTorr for 1 min. Meanwhile, the construction of the electrode devices used the same procedure outlined in a previous section, and they included an ion exchange membrane (Nafion 117, FuelCellStore) and a PMMA housing (McMaster Carr). Once again, the buffer and current inlets were decoupled in order to separate the buffer inflow from the effects of ion concentration polarization (ICP) at the membrane. An image of the FF-CGF microfluidic chip connected to the electrode device can be seen in Fig. 7.2.

7.3.3 Experimental Setup

First, syringe pumps (Pump 11 and Pump33, Harvard Apparatus) were used for the sample and buffer flow. Note that another advantage of using the small chamber dimensions was that it was easy to remove bubbles from the separation region while loading the buffer. Second, a high voltage supply (HVS448-3000, LabSmith) was used to supply the electric field. A constant current mode was used to adjust for voltage changes that may arise in the electrode device due to ICP, Joule heating, and bubble formation. Third, an inverted epifluorescence microscope (ECLIPSE Ti, Nikon) and a high sensitivity CCD Camera (Retiga 2000R, QImaging) were used to view

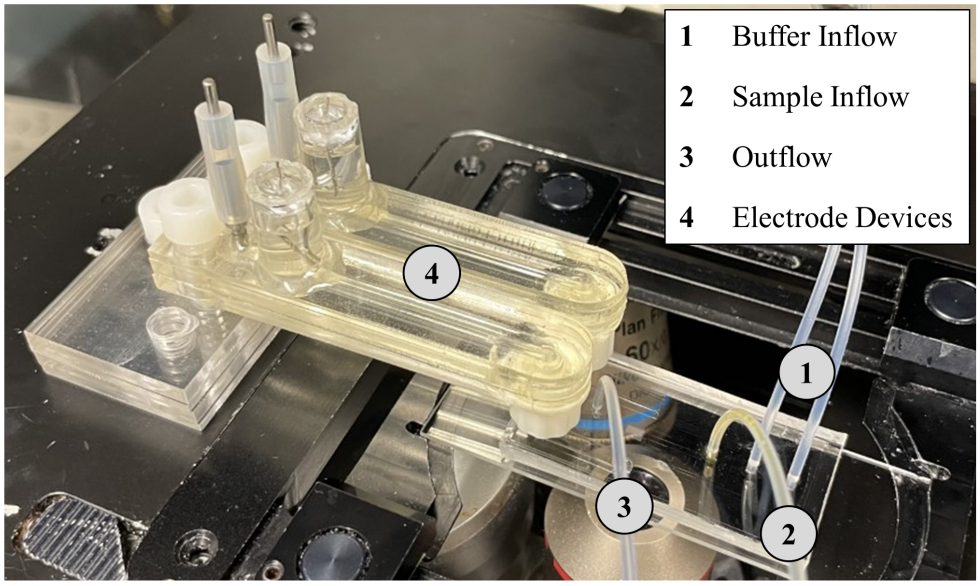


Figure 7.2: Image of the analytical scale FF-CGF device mounted on a fluorescence microscope.

the separation region. Illumination was supplied by a 100 W mercury halide lamp (Intensilight C-HGFIE, Nikon), and a filter cube (FITC, Nikon) was used to image the BSA-FITC stream. Finally, ImageJ software was used to acquire the fluorescence intensities across the lower half of the separation chamber, and then a custom MATLAB script was used to adjust the baseline and plot the peaks. Note that ImageJ was also used to merge fluorescent images at different applied currents in order to conveniently observe the focusing dynamics.

7.3.4 Experimental Parameters

The sample flow rates were 0.03, 0.04, and 0.08 µL/min, while buffer flow rates on each side were 7.5, 10, and 20 µL/min. The sample flow rates were chosen to enable peak visualization while also allowing for sufficient focusing. The flow rates of the buffer (Q) were used to approximate the side velocity inputs assuming $u_0 = Q/(2hL)$, with $2hL$ representing the cross-sectional area of the inflow. This was then used to approximate $G_x = \nabla\langle u\rangle h^2/D$, where $\nabla\langle u\rangle = u_0/b$ and it was assumed that $D = 6.15 \times 10^{-7}$ cm^2/s for BSA [187].

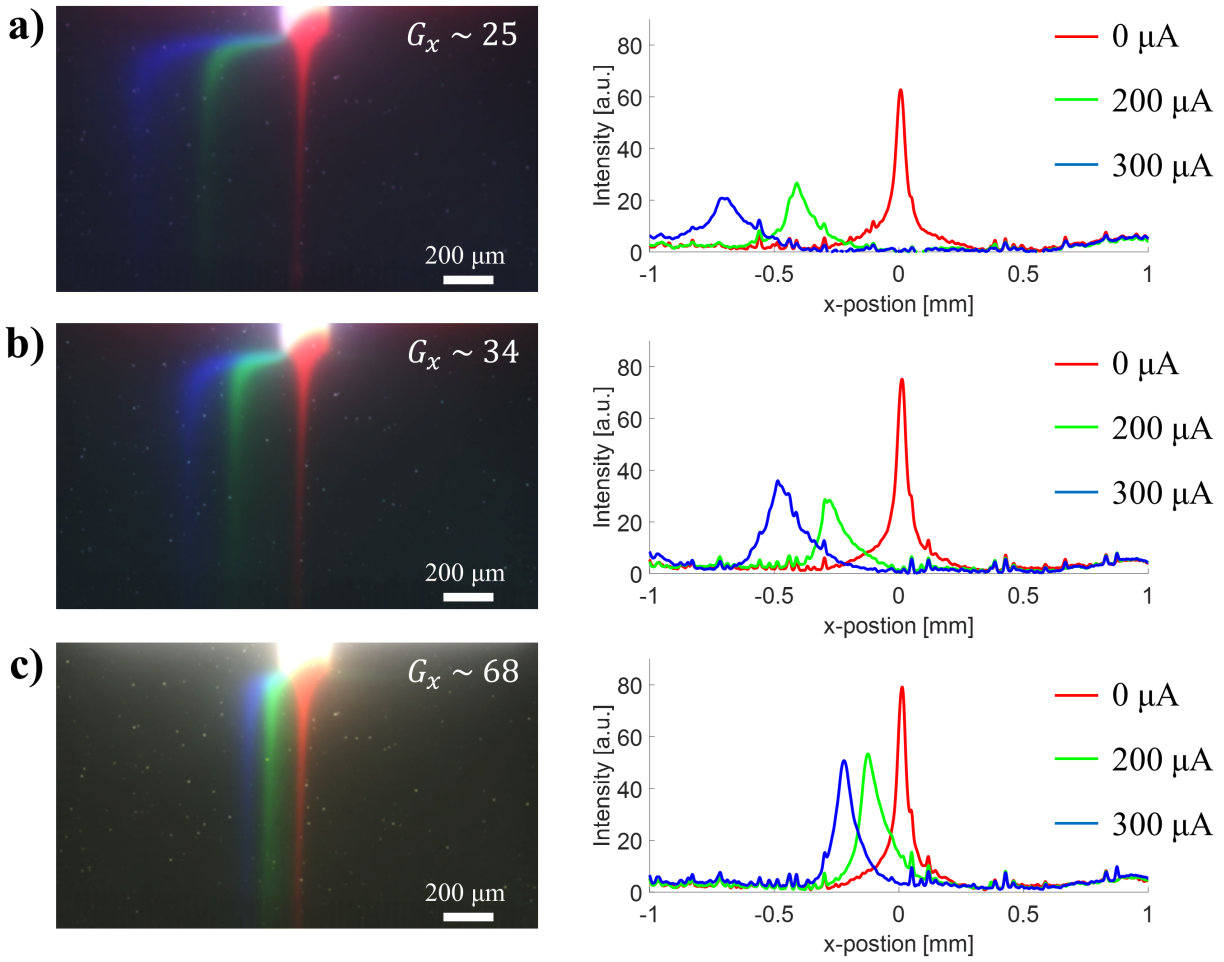


Figure 7.3: Fluorescent images of BSA-FITC at different applied currents and G_x numbers, and the corresponding peak measurements.

7.4 Results and Discussion

The focusing dynamics of a BSA-FITC sample in an FF-CGF chamber is studied in this section. Fig. 7.3 presents several images of BSA-FITC at different focal positions along the separation region for various G_x values, and the corresponding peak measurements are also shown. Overall, these results reveal some useful qualitative information about the device design and the solute dispersion.

7.4.1 Device Performance

For the counterflow gradient, it appears to be uniform along the length of the chamber, and this is most evident in Fig. 7.3a as the outer solute streams do not appear to deviate from their focal position. Consequently, this helps further validate the FF-CGF design guidelines experimentally, and demonstrates the ability to construct a successful FF-CGF device without restricting the height of the side channels. For the sample injection, there does not appear to be significant smearing along the top of the chamber, nor does there appear to be any significant diffusion along the z-direction. Moreover, the solute streams appear to approach their focal position quickly, and then reach an equilibrium width before exiting the chamber. Therefore, this device illustrates the potential to focus and separate proteins across a short chamber length that is ideal for many analytical scale applications. For the sample collection, the solute streams transition easily into the outlet channels located at the bottom of the separation region, and this highlights the ability to isolate several concentrated peaks with the potential for further analysis downstream. For the voltage efficiency, one drawback of this device was that bubbles began to appear due to Joule heating when the current exceeded 300 μA. This becomes an issue at the higher G_x numbers seen in Fig. 7.3, as this limits the effective width of the separation region. With that said, voltage efficiency and heat dissipation were not a priority for the current prototype, and future iterations could explore options for improving this aspect of the design.

7.4.2 Peak Dispersion

The peak measurements shown in Fig. 7.3 also provide a helpful comparison to the dispersion models presented in previous chapters at higher G_x numbers. For one, there appears to be a clear increase in the concentration and sharpness of the peaks as the G_x value increases. Second, both the images and the peaks appear to show a concentrated region followed by a tail region, and this is consistent with the modeling at higher G_x numbers. Third, the location of the tails on the right side of the peak indicates the presence of an EOF backflow that is overpowering the parabolic profile of the counterflow. Given that the electroosmotic mobility of a glass/PDMS chip is often greater than the magnitude of electrophoretic mobility of BSA, this result is expected. Finally, note how concentrated the peak is when there is no current, and this situation could be leveraged in future applications where the protein of interest is neutral. Overall, this FF-CGF device has shown the ability to measure peaks at higher G_x values, and could serve as a useful tool for future experimental validation of the dispersion models.

7.5 Future Considerations

At this point, it is difficult to determine how useful FF-CGF is at the analytical scale. In terms of real-time monitoring for biological assays or quality control, there are likely advantages over traditional FFE methods because the large gradient regime enables the continuous identification of many sharp peaks across a small separation region. However, this is an area that is yet to be fully explored for FFE. Furthermore, there will be significant peak overlap in this regime as seen in Fig. 7.3, and this contamination makes it less than ideal for applications involving protein purification and multidimensional analysis. With that said, there is some interesting potential for peaks focused around $Pe_{\mathrm{E}} = 0$ because they are highly concentrated and have limited peak tailing.

7.5.1 Protein Purification at the Isoelectric Point

In proteomics, capillary isoelectric focusing (cIEF) is a popular analytical technique that can provide high resolution separations with a low limit of detection [115]. However, there is often an interest in transferring the separated fractions to a mass spectrometer to gain additional information about the protein, and this can be challenging in cIEF when the peaks are closely spaced [106] [203]. For example, as the proteins exit the capillary, the resolution is reduced because the focusing mechanism is no longer counteracting molecular diffusion. On top of that, the pressure-driven flow used to extract the analytes will induce Taylor dispersion in the capillary, and this causes the resolution of the focused peaks to deteriorate further.

Therefore, the analytical scale FF-CGF device could serve as a useful intermediate step between cIEF and mass spectroscopy. In the first step, cIEF could be used to separate a sample and identify the pI of a target protein. In the second step, the sample could be transferred to the FF-CGF device where the pH of the buffer medium matches the pI of the target protein. This way, the target protein will have a neutral charge, and therefore focus in the middle of the chamber at $Pe_{\mathrm{E}} = 0$. Meanwhile, the other charged proteins, along with their peak tails, will be filtered away from this region. In the final step, an outlet channel could be used to transfer the highly concentrated target protein from the FF-CGF device to the mass spectrometer.

There are several additional features that can be considered for this system. For one, the EOF should be suppressed to ensure that the neutral protein is truly focused at $Pe_{\mathrm{E}} = 0$ because this will provide the highest purity. Ideally, a permanent wall coating will be used for this purpose because a dynamic coating may interfere with the mass spectroscopy signal. Second, it is possible to change the buffer medium in the FF-CGF chamber to dynamically vary the pH, and therefore run several target proteins through the mass spectrometer at $Pe_{\mathrm{E}} = 0$. Third, another FF-CGF device with different separation conditions could be added to this system to improve

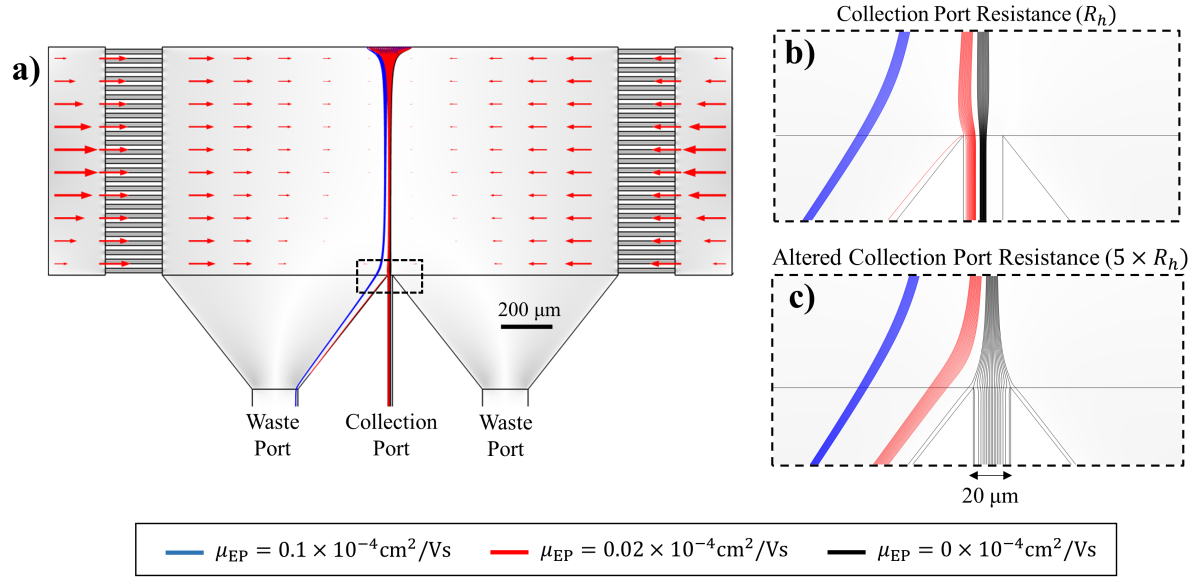


Figure 7.4: a) An alternative analytical FF-CGF device with the outlet channels replaced by a collection port and two waste ports. Numerical simulations show a surface plot of the x-velocity magnitude, as well as the streamlines of various charged solutes. The electric field is 800 V/cm, and $G_x = 50$ when the diffusion coefficient is $D = 5 \times 10^{-7}$ cm^2/s. A close-up view of two solutes that b) cannot be separated at the collection port and c) can be separated at the collection port when its hydrodynamic resistance (R_h) is increased.

the purity. For example, this step could be used to remove the carrier ampholytes and enhance the mass spectroscopy signal [106] [64]. Finally, if the electric field cannot fully resolve the proteins near $Pe_E = 0$, it is possible to increase the hydrodynamic resistance of the collection port for better resolution. As seen in Fig. 7.4, this is a convenient method for restricting the outflow and redirecting a portion of the solute streamlines to a waste port. At the collection port, this will increase the purity but reduce the throughput, and these variables can be tuned by simply changing the resistance of the outlet tubing.

7.6 Concluding Remarks

In this study, the potential of FFE at the analytical scale was discussed, with an emphasis on applications involving multidimensional analysis and real-time monitoring. Then, an FF-CGF device was designed and constructed based on some of the key requirements at this scale. Ex-

perimental results demonstrated its ability to generate a uniform gradient along the length of the chamber despite a simplified approach to the side channel fabrication. Furthermore, the device could separate proteins at higher gradient numbers ($G_x > 25$), and this provided a useful comparison to the previously derived dispersion models. Moving forward, this device could be useful for applications where peak identification is a priority, or for situations where a highly concentrated protein must be isolated for further analysis.

Chapter 8

Conclusions and Recommendations

8.1 Contributions of this Thesis

Free-flow electrophoresis (FFE) has the potential to be a powerful tool for protein separation and analysis, and this is mainly due to its ability to provide continuous separation and collection under gentle conditions. Furthermore, FFE can operate at the preparative scale to collect large quantities of protein, or it can operate at the analytical scale for real-time monitoring and direct interfacing with other technologies. However, FFE has yet to achieve widespread use despite several decades of development. One explanation for its lack of success is because it has many sources of dispersion that are detrimental to separation resolution. Another reason is due to the complex system design that is needed for successful operation. There have been significant efforts to address these challenges, and free-flow isoelectric focusing (FF-IEF) was introduced as an advanced separation mode that offers moderate improvement. With that said, practical problems related to the buffer composition and isoelectric point (pI) have limited the applicability of FF-IEF. Therefore, the purpose of this work was to introduce a counterflow gradient focusing (CGF) mode in FFE that has the potential for improved resolution and versatility.

In free-flow counterflow gradient focusing (FF-CGF), the goal is to supply a pressure-driven flow through the sidewalls of an FFE chamber. This will then produce a velocity gradient in the lateral direction to oppose electrophoretic migration. As a result, proteins and other charged solutes can focus at a position across the separation region where their electrophoretic velocity is counterbalanced by the fluid flow. In principle, the focusing mechanism is similar to FF-IEF, except no complex buffer compositions are required, and it avoids all of the practical concerns associated with the pI. Consequently, there was a strong interest in understanding FF-CGF further, and developing a device for experimental demonstration. In the first phase of this research, an analytical model was developed to calculate the fluid velocity in the chamber, and predict the

solute transit during operation. Then, 2D numerical simulations of the separation mechanism were provided for a more complete understanding. After the initial modeling, an FF-CGF prototype was constructed using standard soft lithography techniques, and it included high resistance side channels that help generate a uniform counterflow gradient along the length of the chamber. Overall, this technique demonstrated the separation of small molecules and proteins, and the performance was consistent with the model predictions.

In the second phase of this research, a model was developed to understand the dispersion that is present in FF-CGF. For this preliminary model, there was an emphasis on the interplay between molecular diffusion, the parabolic velocity profile of the counterflow, and the strength of the gradient. However, when the commonly used method of moments formulation was applied to the model, it was unable to yield a clean analytical solution, and it indicated a non-Gaussian solute distribution that gave the statistical moments less practical meaning. Therefore, the model was solved using numerical simulations, and analysis of the resulting solute distribution was aided by an asymmetric peak fitting method that is frequently used in chromatography. Results showed that FF-CGF can produce a wide variety of peak shapes depending on the strength of the gradient. For example, in a low gradient regime, diffusive transport tends to dominate, and this leads to a steady-state distribution that resembles a skewed Gaussian. On the other hand, when the gradient strength is high, convective transport dominates, and the focused peaks take on the shape of the parabolic velocity profile, with a long peak tail and a highly concentrated region at the centerline. In either case, it was determined that FF-CGF could provide high resolution separations, but there were trade-offs to consider, including throughput, cross-contamination, and Joule heating.

In the third phase of this research, the FF-CGF dispersion model was extended by also considering electroosmotic flow (EOF) in the system. In traditional FFE systems, EOF will produce a pressure-driven backflow due to blockage at the sidewalls, and the resulting parabolic velocity profile will contribute to solute dispersion. When studying the electroosmotic backflow in FF-CGF, the situation is slightly different due to the counterflow input from the sidewalls. This is true because the positive displacement pumps driving the counterflow will automatically adjust to account for the EOF in the system, and this leads to an inherent pressure-driven backflow. Interestingly, analytical equations derived to model this behaviour suggested that the focal position is not impacted by the presence of EOF. With that said, it can have a significant influence on solute dispersion due to the parabolic velocity profile of the pressure-driven backflow. Therefore, the 2D dispersion model was updated to account for EOF, and results showed that depending on its direction EOF can either enhance or suppress the hydrodynamic dispersion caused by the counterflow. Finally, experimental results from the initial FF-CGF prototype were investigated to provide a qualitative comparison to the dispersion model. It was found that the results were in agreement at low electric fields, but were much less so at higher electric fields. Notably, the

solute dispersion was better than anticipated at higher gradient strengths, and one possible explanation is due to the effects of Joule heating. However, further modeling and a more robust experimental setup are needed for complete experimental validation.

The fourth phase of this research involved the development of a new FF-CGF device with improved performance. This fabrication method transitioned away from soft lithography, and instead a robust acrylic-based device was made with the help of a laser cutter and double-sided tape. Along the way, the device design was guided by the possibility of scale-up for preparative applications. An essential feature of the device assembly was a porous membrane that was used to generate a uniform counterflow gradient along the length of the chamber. Moreover, the criteria for generating a uniform gradient was thoroughly investigated, and it can depend on a number of design parameters, including the resistance of the porous membranes, the separation chamber, the outlet channels, and the side chambers. Other aspects of the design were also studied, including the positioning of ion exchange membranes to mitigate the effects of electrolysis, and the influence of sample flow rates on throughput and resolution. Next, the device was developed, and experimental results demonstrated the potential for strong separation performance and high quality peaks measurements. Finally, an analysis for scaling up the device was provided, and showed that FF-CGF could rival the throughput of the traditional preparative scale FFE devices.

The fifth phase of this research presented an alternative FF-CGF device that was designed specifically for analytical scale applications, including real-time monitoring for dynamic bioassays, and direct interfacing with mass spectroscopy for protein sequencing. During this process, the design guidelines established in the previous chapter were used to help supply a uniform counterflow gradient while maximizing voltage efficiency. Interestingly, successful operation was achieved without the need for high resistance side channels, and the protein was able to focus almost immediately after entrance. Another unique feature of this design was its ability to operate at high gradient strengths, which was not possible with previous devices due to voltage limitations. Therefore, protein focusing could be observed in this gradient regime for the first time, and the resulting peak measurements appeared to resemble shapes that were predicted by the previously derived dispersion models. For example, the peak appeared to consist of a highly concentrated region, followed by a long peak tail. Furthermore, the location of the peak tail suggested the presence of EOF as predicted by the electrodynamic model.

8.2 Recommendations for Extension of Work

In the end, FF-CGF appears to be a promising separation mode, and will hopefully allow FFE to reach its potential as a powerful protein fractionation tool. However, FF-CGF has its own limitations which need to be addressed in future studies, and this includes physical modeling,

active cooling, detection, and device fabrication. In terms of physical modeling, there is likely to be Joule heating, and preliminary experimental results suggest that thermal effects are influencing solute dispersion in a complicated manner that is difficult to model. For example, many of the separation parameters depend on temperature, including mobility, diffusion, and viscosity. Moreover, the continuous supply of counterflow from the sidewalls will produce a nonuniform temperature distribution across the separation chamber, and this could make dispersion dependent on focal position. In terms of active cooling strategies, there is clearly a need due to the aforementioned Joule heating effects. Ideally, existing cooling methods could be leveraged, and it would be an added bonus to probe the temperature within the chamber. In terms of detection, a UV system would greatly expand the potential of FF-CGF at the analytical scale, as this could enable the separations to be continuously monitored without the need for fluorescent labels. This would require a device material that is UV transparent, which leads to the next point. In terms of device fabrication, while the methods used in this work were ideal for prototyping, a more robust approach is needed for high quality separations. For example, because this focusing method relies heavily on fluid dynamics, minor defects in the system can influence the performance. One option for analytical scale applications would be a device made from glass, and injection molding has demonstrated potential for larger scale applications. Ideally, this material will also be rigid and have stable surface properties.

With all that said, the biggest limitation in FF-CGF by far is the dispersion caused by the parabolic velocity profile of the counterflow. Even at moderate gradient strengths, this leads to significant solute dispersion that would appear to make this regime unusable. At higher gradient strengths, the influence of the parabolic profile continues to increase, although here at least there is the benefit of having a highly concentrated region. However, the peak tails are long, and this is undesirable for many protein purification applications due to cross-contamination and sample loss. Therefore, it is important to explore different options for reducing the influence of the parabolic profile. One option would be to carry out the separation in a porous media, as this will help flatten the velocity profile. Some capillary-based CGF techniques have adopted this strategy successfully [132], although it is important to be aware of the fabrication challenges, as well as the potential protein interactions with the porous media. Another promising option would be to incorporate an additional counterflow focusing mechanism along the height direction. As a result, proteins could focus in the middle of the chamber where the curvature of the parabola is lowest, and this would eliminate the peak tails for high resolution separations. On top of that, the flow from these regions can provide a source of cooling, and they can help counteract the harmful effects of density gradients at the preparative scale. Of course, this system would be more complicated to build, but the potential benefits are significant.

References

[1] Bruce Alberts, Alexander Johnson, Julian Lewis, Martin Raff, Keith Roberts, and Peter Walter. *Molecular Biology of the Cell*. Garland Science, 4th edition, 2002.

[2] Rob Phillips, Jane Kondev, Julie Theriot, and Hernan G. Garica. *Physical Biology of the Cell*. Garland Science, 2nd edition, 2013.

[3] Glen L. Hortin, Steven A. Carr, and N. Leigh Anderson. Introduction: Advances in protein analysis for the clinical laboratory. *Clinical Chemistry*, 56(2):149–151, 2010.

[4] Xiaohua Li, Shikun He, and Binyun Ma. Autophagy and autophagy-related proteins in cancer. *Molecular Cancer*, 19(1):1–16, 2020.

[5] Jianwei Zhu. Mammalian cell protein expression for biopharmaceutical production. *Biotechnology Advances*, 30(5):1158–1170, 2012.

[6] Bilal Aslam, Madiha Basit, Muhammad Atif Nisar, Mohsin Khurshid, and Muhammad Hidayat Rasool. Proteomics: Technologies and their applications. *Journal of Chromatographic Science*, 55(2):182–196, 2017.

[7] Paul R. Graves and Timothy A.J. Haystead. Molecular Biologist's Guide to Proteomics. *Microbiology and Molecular Biology Reviews*, 66(1):39–63, 2002.

[8] Laurent Maveyraud and Lionel Mourey. Protein X-ray crystallography and drug discovery. *Molecules*, 25(5):1–18, 2020.

[9] Walter Becker, Krishna Chaitanya Bhattiprolu, Nina Gubensäk, and Klaus Zangger. Investigating Protein–Ligand Interactions by Solution Nuclear Magnetic Resonance Spectroscopy. *ChemPhysChem*, 19(8):895–906, 2018.

[10] Marketa Bockova, Jiri Slaby, Tomas Springer, and Jiri Homola. Advances in Surface Plasmon Resonance Imaging and Microscopy and Their Biological Applications. *Annual Review of Analytical Chemistry*, 12(July):151–176, 2019.

[11] B. Owczarek, A. Gerszberg, and K. Hnatuszko-Konka. A Brief Reminder of Systems of Production and Chromatography-Based Recovery of Recombinant Protein Biopharmaceuticals. *BioMed Research International*, 2019:1–13, 2019.

[12] Irene Van Den Broek, Wilfried M A Niessen, and William D Van Dongen. Bioanalytical LC – MS / MS of protein-based biopharmaceuticals. *Journal of Chromatography B*, 929:161–179, 2013.

[13] Maria M. Papathanasiou and Cleo Kontoravdi. Engineering challenges in therapeutic protein product and process design. *Current Opinion in Chemical Engineering*, 27:81–88, 2020.

[14] Szabolcs Fekete, Davy Guillarme, Pat Sandra, and Koen Sandra. Chromatographic, Electrophoretic, and Mass Spectrometric Methods for the Analytical Characterization of Protein Biopharmaceuticals. *Analytical Chemistry*, 88(1):480–507, 2016.

[15] Geng Xindu and Wang Lili. Liquid chromatography of recombinant proteins and protein drugs. *Journal of Chromatography B*, 866(1-2):133–153, 2008.

[16] Pier Giorgio Righetti. Electrophoresis: The march of pennies, the march of dimes. *Journal of Chromatography A*, 1079:24–40, 2005.

[17] Jan-Christer Janson. *Protein Purification*. John Wiley Sons, Inc., 3rd edition, 2011.

[18] Huiming Yuan, Bo Jiang, Baofeng Zhao, Lihua Zhang, and Yukui Zhang. Recent Advances in Multidimensional Separation for Proteome Analysis. *Analytical Chemistry*, 91(1):264–276, 2019.

[19] Dietrich Kohlheyer, Jan C.T. Eijkel, Albert van den Berg, and Richard B.M. Schasfoort. Miniaturizing free-flow electrophoresis - A critical review. *Electrophoresis*, 29(5):977–993, 2008.

[20] Ou Yang, Maen Qadan, and Marianthi Ierapetritou. Economic Analysis of Batch and Continuous Biopharmaceutical Antibody Production: a Review. *Journal of Pharmaceutical Innovation*, 15(1):182–200, 2020.

[21] Pedro Novo and Dirk Janasek. Current advances and challenges in microfluidic free-flow electrophoresis—A critical review. *Analytica Chimica Acta*, 991:9–29, 2017.

[22] Ludmila Krivankova and Petr Boeek. Continuous free-flow electrophoresis. *Electrophoresis*, 19:1064–1074, 1998.

[23] Free flow electrophoresis service. https://www.ffeservice.com/products/. Accessed: 2022-04-29.

[24] Dietrich Kohlheyer, Jan C.T. Eijkel, Stefan Schlautmann, Albert Van Den Berg, and Richard B.M. Schasfoort. Bubble-free operation of a microfluidic free-flow electrophoresis chip with integrated pt electrodes. *Analytical Chemistry*, 80(11):4111–4118, 2008.

[25] Von Jean Barrollier, Eugen Watzke, and Heinz Gibian. Einfache Apparatur für die trägerfreie präparative Durchlauf-Elektrophorese. *Zeitschrift für Naturforschung B*, 13B:754–756, 1958.

[26] Kurt Hannig. Die träigerfreie kontinuierliche Elektrophorese und ihre Anwendung. *Z. Anal. Chem.*, 181(1):244–254, 1961.

[27] Robert S. Snyder, Percy H. Rhodes, and Teresa Y. Miller. Continuous flow electrophoresis system experiments on shuttle flights STS-6 and STS-7. *NASA Technical Memorandum*, 1:1–12, 1988.

[28] Gerhard Weber. Method and Apparatus for Carrier-Free Deflection Electrophoresis, US 2011/0174624 A1, 2011.

[29] Gerhard Weber and Petr Boček. Optimized continuous flow electrophoresis. *Electrophoresis*, 17(12):1906–1910, 1996.

[30] Daniel E. Raymond, Andreas Manz, and H. Michael Widmer. Continuous Sample Pretreatment Using a Free-Flow Electrophoresis Device Integrated onto a Silicon Chip. *Analytical Chemistry*, 66(18):2858–2865, 1994.

[31] Pedro Novo, Margherita Dell'Aica, Matthias Jender, Stefan Höving, René P. Zahedi, and Dirk Janasek. Integration of polycarbonate membranes in microfluidic free-flow electrophoresis. *The Analyst*, 142(22):4228–4239, 2017.

[32] Christian Benz, Michael Boomhoff, Johannes Appun, Christoph Schneider, and Detlev Belder. Chip-based free-flow electrophoresis with integrated nanospray mass-spectrometry. *Angewandte Chemie - International Edition*, 54(9):2766–2770, 2015.

[33] Matthew Geiger, Nicholas W. Frost, and Michael T. Bowser. Comprehensive multidimensional separations of peptides using nano-liquid chromatography coupled with micro free flow electrophoresis. *Analytical Chemistry*, 86(10):5136–5142, 2014.

[34] Ryan T Turgeon, Bryan R Fonslow, Meng Jing, and Michael T Bowser. Measuring Aptamer Equilbria Using Gradient Micro Free Flow Electrophoresis. *Anal. Chem.*, 82(9):3636–3641, 2010.

[35] Ryan T. Turgeon and Michael T. Bowser. Micro free-flow electrophoresis: Theory and applications. *Analytical and Bioanalytical Chemistry*, 394(1):187–198, 2009.

[36] Alexander C Johnson and Michael T Bowser. Micro free flow electrophoresis. *Lab on a Chip*, 18:27–40, 2018.

[37] Bryan R. Fonslow and Michael T. Bowser. Optimizing band width and resolution in micro-free flow electrophoresis. *Analytical Chemistry*, 78(24):8236–8244, 2006.

[38] Jean Louis Afonso and Michael J. Clifton. Optimization of protein separation by continuous-flow electrophoresis: Influence of the operating conditions and the chamber thickness. *Electrophoresis*, 20(14):2801–2809, 1999.

[39] Michael J Clifton, Nicolas Jouve, Helene de Balmann, and Victor Sanchez. Conditions for purification of proteins by free-flow zone electrophoresis. *Electrophoresis*, 11:913–919, 1990.

[40] Sabrina Hoffstetter-Kuhn, Reinhard Kuhn, and Horst Wagner. Free flow electrophoresis for the purification of proteins: I. Zone electrophoresis and isotachophoresis. *Electrophoresis*, 11:304–309, 1990.

[41] Reinhard Kuhn, Sabrina Hoffstetter-Kuhn, and Horst Wagner. Free-flow electrophoresis for the purification of proteins: 11. Isoelectric focusing and field step electrophoresis. *Electrophoresis*, 11(4):942–941, 1990.

[42] Gerhard Weber and Petr Boček. Recent developments in preparative free flow isoelectric focusing. *Electrophoresis*, 19(10):1649–1653, 1998.

[43] Debashis Dutta. Broadening of analyte streams due to a transverse pressure gradient in free-flow isoelectric focusing. *Journal of Chromatography A*, 1484:85–92, 2017.

[44] John S. Fawcett. Continuous-Flow Isoelectric Focusing and Isotachophoresis. *Annals of the New York Academy of Sciences*, 209(1):112–126, 1973.

[45] Milan Bier. Isoelectric Focusing Apparatus, US Patent 4,362,612, 1982.

[46] Milan Bier and Garland E. Twitty. Process and Apparatus for Recycling Isoelectric Focusing and Isotachophoresis, US Patent 4,897,169, 1990.

[47] Noah I. Tracy and Cornelius F. Ivory. Preparative isoelectric focusing of proteins using binary buffers in a vortex-stabilized, free-flow apparatus. *Electrophoresis*, 25(12):1748–1757, 2004.

[48] Jonathan G. Shackman and David Ross. Counter-flow gradient electrofocusing. *Electrophoresis*, 28(4):556–571, 2007.

[49] J Calvin Giddings and Karin Dahlgren. Resolution and Peak Capacity in Equilibrium-Gradient Methods of Separation. *Separation Science*, 6(3):345–356, 1971.

[50] Cornelius F. Ivory. Several new electrofocusing techniques. *Electrophoresis*, 28(1-2):15–25, 2007.

[51] Matthew Courtney and Carolyn L. Ren. Counterflow gradient electrophoresis for focusing and elution. *Electrophoresis*, 40(5):643–658, 2019.

[52] Todd M. Squires and Stephen R. Quake. Microfluidics: Fluid physics at the nanoliter scale. *REVIEWS OF MODERN PHYSICS*, 77:977–1026, 2005.

[53] Debashis Dutta. A method-of-moments formulation for describing hydrodynamic dispersion of analyte streams in free-flow zone electrophoresis. *Journal of Chromatography A*, 1340:134–138, 2014.

[54] Debashis Dutta. An analytic description of electrodynamic dispersion in free-flow zone electrophoresis. *Journal of Chromatography A*, 1404:124–130, 2015.

[55] Cornelius F. Ivory. Continuous Flow Electrophoresis: The Crescent Phenomena Revisited Part I. Isothermal Effects. *Journal of Chromatography*, 195:165–179, 1980.

[56] Xiangchun Xuan, David Sinton, and Dongqing Li. Thermal end effects on electroosmotic flow in a capillary. *International Journal of Heat and Mass Transfer*, 47(14-16):3145–3157, 2004.

[57] Debashis Dutta. Joule heating induced stream broadening in free-flow zone electrophoresis. *Electrophoresis*, 39(5-6):760–769, 2018.

[58] Cornelius F. Ivory. Continuous flow electrophoresis: The crescent phenomena revisited Part II: Nonisothermal effects. *Electrophoresis*, 2:31–39, 1981.

[59] Jean Louis Afonso and Michael J. Clifton. Coupling between transfer phenomena in continuous-flow electrophoresis: Effect on the steadiness of the carrier flow. *Chemical Engineering Science*, 56(10):3053–3064, 2001.

[60] Hideyuki Matsumoto, Nobuaki Komatsubara, Chiaki Kuroda, Nobuyoshi Tajima, Etsuo Shinohara, and Hirobumi Suzuki. Numerical simulation of temperature distribution inside microfabricated free flow electrophoresis module. *Chemical Engineering Journal*, 101(1-3):347–356, 2004.

[61] Percy H. Rhodes, Robert S. Snyder, and Glyn O. Roberts. Electrohydrodynamic distortion of sample streams in continuous flow electrophoresis. *Journal of Colloid And Interface Science*, 129(1):78–90, 1989.

[62] Reinhard Kuhn and Horst Wagner. Free flow electrophoresis as a method for the purification of enzymes from E. coli cell extract. *Electrophoresis*, 10:165–112, 1989.

[63] Debashis Dutta. Stream broadening due to fluid shear across the wider transverse dimension of a free-flow zone electrophoresis channel. *Physics of Fluids*, 31:073605, 2019.

[64] Tiemin Huang, Xing Zheng Wu, and Janusz Pawliszyn. Capillary isoelectric focusing without carrier ampholytes. *Analytical Chemistry*, 72(19):4758–4761, 2000.

[65] Milan Bier, Garland E. Twitty, and J.E. Sloan. Recycling isoelectric focusing and isotachophoresis. *Journal of Chromatography*, 470:369–376, 1989.

[66] Yi Xu, Chao Xuan Zhang, Dirk Janasek, and Andreas Manz. Sub-second isoelectric focusing in free flow using a microfluidic device. *Lab on a Chip*, 3(4):224–227, 2003.

[67] Dietrich Kohlheyer, Jan C.T. Eijkel, Stefan Schlautmann, Albert Van Den Berg, and Richard B.M. Schasfoort. Microfluidic high-resolution free-flow isoelectric focusing. *Analytical Chemistry*, 79(21):8190–8198, 2007.

[68] Jacob W. Albrecht, Jamil El-Ali, and Klavs F. Jensen. Cascaded free-flow isoelectric focusing for improved focusing speed and resolution. *Analytical Chemistry*, 79(24):9364–9371, 2007.

[69] Jian Wen, Erik W Wilker, Michael B Yaffe, and Klavs F Jensen. Microfluidic Preparative Free-Flow Isoelectric Focusing : System Optimization for Protein Complex Separation. *Anal. Chem.*, 82(4):1253–1260, 2010.

[70] Bin Han, Pingli Wang, Guijie Zhu, Lihua Zhang, Feng Qu, Yulin Deng, and Yukui Zhang. Microchip free flow isoelectric focusing for protein prefractionation using monolith with immobilized pH gradient. *Journal of Separation Science*, 32(8):1211–1215, 2009.

[71] Li Jing Cheng and Hsueh Chia Chang. Switchable pH actuators and 3D integrated salt bridges as new strategies for reconfigurable microfluidic free-flow electrophoretic separation. *Lab on a Chip*, 14(5):979–987, 2014.

[72] J. K. Park, C. D.M. Campos, P. Neužil, L. Abelmann, R. M. Guijt, and A. Manz. Direct coupling of a free-flow isotachophoresis (FFITP) device with electrospray ionization mass spectrometry (ESI-MS). *Lab on a Chip*, 15(17):3495–3502, 2015.

[73] Dirk Janasek, Michael Schilling, Joachim Franzke, and Andreas Manz. Isotachophoresis in free-flow using a miniaturized device. *Analytical Chemistry*, 78(11):3815–3819, 2006.

[74] Stefan Hoving, Dirk Janasek, and Pedro Novo. Flow rate independent gradient generator and application in microfluidic free-flow electrophoresis. *Analytica Chimica Acta*, 1044:77–85, 2018.

[75] Johann Bauer and Gerhard Weber. Interval carrier free electrophoresis for high resolution protein purification. *Journal of Dispersion Science and Technology*, 19(6-7):937–950, 1998.

[76] Peter Hoffmann, Horst Wagner, Gerhard Weber, Matthias Lanz, Jitka Caslavska, and Wolfgang Thormann. Separation and purification of methadone enantiomers by continuous-and interval-flow electrophoresis. *Analytical Chemistry*, 71(9):1840–1850, 1999.

[77] Bo Højen Justesen, Tomas Laursen, Gerhard Weber, Anja Thoe Fuglsang, Birger Lindberg Møller, and Thomas Günther Pomorski. Isolation of monodisperse nanodisc-reconstituted membrane proteins using free flow electrophoresis. *Analytical Chemistry*, 85(7):3497–3500, 2013.

[78] Marco Becker, Abraham Mansouri, Cornelia Beilein, and Dirk Janasek. Temperature gradient focusing in miniaturized free-flow electrophoresis devices. *Electrophoresis*, 30(24):4206–4212, 2009.

[79] Vasileios A. Papadimitriou, Loes I. Segerink, and Jan C. T. Eijkel. Free Flow Ion Concentration Polarization Focusing (FF-ICPF). *Analytical Chemistry*, 92(7):4866–4874, 2020.

[80] Bo Pang, Jing Shao, Jie Zhang, Jia Zhen Geng, Liu Yin Fan, Cheng Xi Cao, and Jing Li Hou. Enhancing separation of histidine from amino acids via free-flow affinity electrophoresis with gravity-induced uniform hydrodynamic flow. *Electrophoresis*, 33(5):856–865, 2012.

[81] Robert L. Moritz, Hong Ji, Frédéric Schütz, Lisa M. Connolly, Eugene A. Kapp, Terence P. Speed, and Richard J. Simpson. A proteome strategy for fractionating proteins and peptides using continuous free-flow electrophoresis coupled off-line to reversed-phase high-performance liquid chromatography. *Analytical Chemistry*, 76(16):4811–4824, 2004.

[82] Brigitta Bondy, Johann Bauer, Ingrid Seuffert, and Gerhard Weber. Sodium chloride in separation medium enhances cell compatibility of free flow electrophoresis. *Electrophoresis*, 16(1):92–97, 1995.

[83] Su Chen, James F. Palmer, Wei Zhang, Jing Shao, Si Li, Liu Yin Fan, Ren Sun, Yu Chao Dong, and Cheng Xi Cao. A simple preparative free-flow electrophoresis joined with gratis gravity: I. Gas cushion injector and self-balance collector instead of multiple channel pump. *Electrophoresis*, 30(11):1998–2007, 2009.

[84] Kadi L. Saar, Thomas Müller, Jérôme Charmet, Pavan Kumar Challa, and Tuomas P.J. Knowles. Enhancing the Resolution of Micro Free Flow Electrophoresis through Spatially Controlled Sample Injection. *Analytical Chemistry*, 90(15):8998–9005, 2018.

[85] Gerhard Weber. Stabilizing and Separation Media for Electrophoresis Applications, WO 2008/087218 A3, 2008.

[86] Cheng Zhang Yang, Jian Yan, Qiang Zhang, Chen Gang Guo, Fan Zhi Kong, Cheng Xi Cao, Liu Yin Fan, and Xin Qiao Jin. Negative-pressure-induced collector for a self-balance free-flow electrophoresis device. *Journal of Separation Science*, 37(11):1359–1363, 2014.

[87] Mark C Roman and Phyllis R Brown. Free-Flow Electrophoresis As a Preparative Separation Technique. *Analytical Chemistry*, 66(2):86–94, 1994.

[88] Matthias Jender, Pedro Novo, Dominic Maehler, Ute Münchberg, Dirk Janasek, and Erik Freier. Multiplexed Online Monitoring of Microfluidic Free-Flow Electrophoresis via Mass Spectrometry. *Analytical Chemistry*, 92(9):6764–6769, 2020.

[89] Gerhard Weber. Method and Apparatus for Continuous, Carrier-Free Deflection Electrophoresis, US Patent 5,275,706, 1994.

[90] Bryan R. Fonslow, Victor H. Barocas, and Michael T. Bowser. Using channel depth to isolate and control flow in a micro free-flow electrophoresis device. *Analytical Chemistry*, 78(15):5369–5374, 2006.

[91] Stefan Köhler, Claudia Weilbeer, Steffen Howitz, Holger Becker, Volker Beushausen, and Detlev Belder. PDMS free-flow electrophoresis chips with integrated partitioning bars for bubble segregation. *Lab on a Chip*, 11(2):309–314, 2011.

[92] Britta Walowski, Wilhelm Hüttner, and Hainer Wackerbarth. Generation of a miniaturized free-flow electrophoresis chip based on a multi-lamination technique — isoelectric focusing of proteins and a single-stranded DNA fragment. *Anal Bioanal Chem*, pages 2465–2471, 2011.

[93] Stefan Köhler, Christian Benz, Holger Becker, Erik Beckert, Volker Beushausen, and Detlev Belder. Micro free-flow electrophoresis with injection molded chips. *RSC Advances*, 2(2):520–525, 2012.

[94] Sarah K Anciaux and Michael T. Bowser. Reduced Surface Adsorption in 3D Printed Acrylonitrile Butadiene Styrene Micro Free-Flow Electrophoresis Devices. *Electrophoresis*, 41(3):225–234, 2020.

[95] Youngbok Lee and Jae-Sung Kwon. Microfluidic free-flow electrophoresis: A promising tool for protein purification and analysis in proteomics. *Journal of Industrial and Engineering Chemistry*, 109:79–99, 2022.

[96] Dietrich Kohlheyer, Geert A J Besselink, Stefan Schlautmann, and Richard B M Schasfoort. Free-flow zone electrophoresis and isoelectric focusing using a microfabricated glass device with ion permeable membranes. *Lab on a Chip*, 6:374–380, 2006.

[97] Ruedi Aebersold and Matthias Mann. Mass spectrometry-based proteomics. *Nature*, 422(6928):198–207, 2003.

[98] Ankit Sinha and Matthias Mann. A beginner's guide to mass spectrometry–based proteomics. *Biochem (Lond)*, 42(5):64–69, 2020.

[99] Cornelius F Ivory. The Prospects for Large-Scale Electrophoresis. *Separation Science and Technology*, 23:875–912, 1988.

[100] Robert Wildgruber, Gerhard Weber, Petra Wise, Daniela Grimm, and Johann Bauer. Free-flow electrophoresis in proteome sample preparation. *Proteomics*, 14(4-5):629–636, 2014.

[101] Markus Islinger, Robert Wildgruber, and Alfred Volkl. Preparative free-flow electrophoresis, a versatile technology complementing gradient centrifugation in the isolation of highly purified cell organelles. *Electrophoresis*, 39:2288–2299, 2018.

[102] Markus Islinger, Christoph Eckerskorn, and Alfred Völkl. Free-flow electrophoresis in the proteomic era: A technique in flux. *Electrophoresis*, 31(11):1754–1763, 2010.

[103] Johan Malmström, Hookeun Lee, Alesey I. Nesvizhskii, David Shteynberg, Sonali Mohanty, Erich Brunner, Mingliang Ye, Gerhard Weber, Christoph Eckerskorn, and Ruedi Aebersold. Optimized peptide separation and identification for mass spectrometry based proteomics via free-flow electrophoresis. *Journal of Proteome Research*, 5(9):2241–2249, 2006.

[104] Brian D. Hosken, Charlene Li, Berny Mullappally, Carl Co, and Boyan Zhang. Isolation and Characterization of Monoclonal Antibody Charge Variants by Free Flow Isoelectric Focusing. *Analytical Chemistry*, 88(11):5662–5669, 2016.

[105] Suli Liu, Seth Madren, Pamela Feng, and Zoran Sosic. Characterization of the acidic species of a monoclonal antibody using free flow electrophoresis fractionation and mass spectrometry. *Journal of Pharmaceutical and Biomedical Analysis*, 185:113217, 2020.

[106] Anne Chartogne, Ubbo R. Tjaden, and Jan Van Der Greef. A free-flow electrophoresis chip device for interfacing capillary isoelectric focusing on-line with electrospray mass spectrometry. *Rapid Communications in Mass Spectrometry*, 14(14):1269–1274, 2000.

[107] Tristan F. Kinde, Thomas D. Lopez, and Debashis Dutta. Electrophoretic extraction of low molecular weight cationic analytes from sodium dodecyl sulfate containing sample matrices for their direct electrospray ionization mass spectrometry. *Analytical Chemistry*, 87(5):2702–2709, 2015.

[108] Tristan F. Kinde, Natalie Hess, and Debashis Dutta. Enhancement in MS-based peptide detection by microfluidic free-flow zone electrophoresis. *Electrophoresis*, 41(7-8):545–553, 2020.

[109] Matthew Geiger and Michael T. Bowser. Effect of Fluorescent Labels on Peptide and Amino Acid Sample Dimensionality in Two Dimensional nLC × μFFE Separations. *Analytical Chemistry*, 88(4):2177–2187, 2016.

[110] Bryan R Fonslow and Michael T Bowser. Fast Electrophoretic Separation Optimization Using Gradient Micro Free-Flow Electrophoresis. *Analytical Chemistry*, 80(9):3182–3189, 2008.

[111] Debashis Dutta. Stream Broadening in Free Flow Affinity Electrophoresis. *Journal of Chromatography A*, 1671:463019, 2022.

[112] Alexander C. Johnson and Michael T. Bowser. High-Speed, Comprehensive, Two Dimensional Separations of Peptides and Small Molecule Biological Amines Using Capillary

Electrophoresis Coupled with Micro Free Flow Electrophoresis. *Analytical Chemistry*, 89(3):1665–1673, 2017.

[113] Francis S. Collins, Michael Morgan, and Aristides Patrinos. The Human Genome Project: Lessons from large-scale biology. *Science*, 300(5617):286–290, 2003.

[114] Rachel K. Harstad, Alexander C. Johnson, Megan M. Weisenberger, and Michael T. Bowser. Capillary Electrophoresis. *Analytical Chemistry*, 88(1):299–319, 2016.

[115] Roberto Rodriguez-Diaz, Tim Wehr, and Mingde Zhu. Capillary isoelectric focusing. *Electrophoresis*, 18:2134–2144, 1997.

[116] C. F. Ivory. A brief review of alternative electrofocusing techniques. *Separation Science and Technology*, 35(11):1777–1793, 2000.

[117] Patrick H O'Farrell. Separation Techniques Based on the Opposition of Two Counteracting Forces to Produce a Dynamic Equilibrium. *Science*, 227(4694):1586–1589, 1985.

[118] Cornelius F. Ivory. The development of recycle zone electrophoresis. *Electrophoresis*, 11(1):919–926, 1990.

[119] Joseph B. Culkin. Apparatus and Method for Separating Particles, US 5,080,770, 1992.

[120] Ned B. Egen, Garland E. Twitty, and David W. Sammons. Electrical Separator Apparatus and Method of Counterflow Gradient Focusing, US 5,336,387, 1994.

[121] Cornelius F. Ivory. Taylor dispersion in equilibrium gradient focusing at steady state. *Electrophoresis*, 36(5):662–667, 2015.

[122] Geoffrey Taylor. Dispersion of soluble matter in solvent flowing slowly through a tube. *Proceedings of the Royal Society of London. Series A. Mathematical and Physical Sciences*, 219(1137):186–203, 1953.

[123] R. Aris. On the dispersion of a solute in a fluid flowing through a tube. *Proceedings of the Royal Society of London. Series A, Mathematical and Physical Sciences*, 235(1200):67–77, 1956.

[124] J Calvin Giddings. Crossflow Gradients in Thin Channels for Separation by Hyperlayer FFF, SPLITT Cells, Eiutriation, and Related Methods. *Separation Science and Technology*, 21(8):831–843, 1986.

[125] Stacey J. Hoebel, Karin M. Balss, Barbara J. Jones, Constantin O. Malliaris, Matthew S. Munson, Wyatt N. Vreeland, and David Ross. Scanning temperature gradient focusing. *Analytical Chemistry*, 78(20):7186–7190, 2006.

[126] Jeffrey M Burke, Zheng Huang, and Cornelius F Ivory. Simultaneous Separation of Negatively and Positively Charged Species in Dynamic Field. *Anal. Chem.*, 81(19):8236–8243, 2009.

[127] Wendy S. Koegler and Cornelius F. Ivory. Field gradient focusing: A novel method for protein separation. *Biotechnology Progress*, 12(6):822–836, 1996.

[128] Paul H Humble, Ryan T Kelly, Adam T Woolley, H Dennis Tolley, and Milton L Lee. Electric Field Gradient Focusing of Proteins Based on Shaped Ionically Conductive Acrylic Polymer. *Analytical Chemistry*, 76(19):5641–5648, 2004.

[129] Ryan T. Kelly, Yi Li, and Adam T. Woolley. Phase-changing sacrificial materials for interfacing microfluidics with ion-permeable membranes to create on-chip preconcentrators and electric field gradient focusing microchips. *Analytical Chemistry*, 78(8):2565–2570, 2006.

[130] Paul H. Humble, John N. Harb, H. Dennis Tolley, Adam T. Woolley, Paul B. Farnsworth, and Milton L. Lee. Influence of transport properties in electric field gradient focusing. *Journal of Chromatography A*, 1160(1-2):311–319, 2007.

[131] Daniel Maynes, Joseph Tenny, Brent W. Webbd, and Milton L. Lee. Influence of varying electroosmotic flow on the effective diffusion in electric field gradient separations. *Electrophoresis*, 29(3):549–560, 2008.

[132] Xuefei Sun, Paul B. Farnsworth, Adam T. Woolley, H. Dennis Tolley, Karl F. Warnick, and Milton L. Lee. Poly(ethylene glycol)-functionalized devices for electric field gradient focusing. *Analytical Chemistry*, 80(2):451–460, 2008.

[133] Xuefei Sun, Paul B. Farnsworth, H. Dennis Tolley, Karl F. Warnick, Adam T. Woolley, and Milton L. Lee. Performance optimization in electric field gradient focusing. *Journal of Chromatography A*, 1216(1):159–164, 2009.

[134] Shu Ling Lin, Yuanyuan Li, Adam T. Woolley, Milton L. Lee, H. Dennis Tolley, and Karl F. Warnick. Programed elution and peak profiles in electric field gradient focusing. *Electrophoresis*, 29(5):1058–1066, 2008.

[135] Zheng Huang and Cornelius F. Ivory. Digitally controlled electrophoretic focusing. *Analytical Chemistry*, 71(8):1628–1632, 1999.

[136] Jeffrey M. Burke and Cornelius F. Ivory. Characterization of voltage degradation in dynamic field gradient focusing. *Electrophoresis*, 29(5):1013–1025, 2008.

[137] Jeffrey M. Burke and Cornelius F. Ivory. Influence of the semi-permeable membrane on the performance of dynamic field gradient focusing. *Electrophoresis*, 31(5):893–901, 2010.

[138] Pilar González Tuñón, Yating Wang, Peter Myers, Keith D. Bartle, Larry Bowhill, Cornelius F. Ivory, and Richard J. Ansell. Electrophoretic field gradient focusing: An investigation of the experimental parameters. *Electrophoresis*, 29(2):457–465, 2008.

[139] Jeffrey M Burke, Colin D Smith, and Cornelius F Ivory. Development of a membraneless dynamic field gradient focusing device for the separation of low-molecular-weight molecules. *Electrophoresis*, 31(5):902–909, 2010.

[140] P. Myers and K. D. Bartle. Towards a miniaturised system for dynamic field gradient focused separation of proteins. *Journal of Chromatography A*, 1044(1-2):253–258, 2004.

[141] Noah I. Tracy and Cornelius F. Ivory. Protein separation using preparative-scale dynamic field gradient focusing. *Electrophoresis*, 29(13):2820–2827, 2008.

[142] Noah I. Tracy and Cornelius F. Ivory. Assessing the scalability of dynamic field gradient focusing by linear modeling. *Journal of Separation Science*, 31(2):341–352, 2008.

[143] Robert D. Greenlee and Cornelius F. Ivory. Protein focusing in a conductivity gradient. *Biotechnology Progress*, 14(2):300–309, 1998.

[144] Qinggang Wang, Shu Ling Lin, Karl F. Warnick, H. Dennis Tolley, and Milton L. Lee. Voltage-controlled separation of proteins by electromobility focusing in a dialysis hollow fiber. *Journal of Chromatography A*, 985(1-2):455–462, 2003.

[145] S L Lin, H D Tolley, and M L Lee. Voltage-controlled electric field gradient focusing with online UV detection for analysis of proteins. *Chromatographia*, 62(5-6):277–281, 2005.

[146] Sung Jae Kim and Jongyoon Han. Self-Sealed Vertical Polymeric Nanoporous-Junctions for High- Throughput Nanofluidic Applications. *Analytical Chemistry*, 80(9):3507–3511, 2008.

[147] Lung Ming Fu, Hui Hsiung Hou, Ping Hsien Chiu, and Ruey Jen Yang. Sample preconcentration from dilute solutions on micro/nanofluidic platforms: A review. *Electrophoresis*, 39(2):289–310, 2018.

[148] Qinggang Wang, Bingfang Yue, and Milton L. Lee. Mobility-based selective on-line preconcentration of proteins in capillary electrophoresis by controlling electroosmotic flow. *Journal of Chromatography A*, 1025(1):139–146, 2004.

[149] David W. Inglis, Ewa M. Goldys, and Nils P. Calander. Simultaneous concentration and separation of proteins in a nanochannel. *Angewandte Chemie - International Edition*, 50(33):7546–7550, 2011.

[150] David Ross and Laurie E. Locascio. Microfluidic temperature gradient focusing. *Analytical Chemistry*, 74(11):2556–2564, 2002.

[151] Jonathan G. Shackman, Matthew S. Munson, Cheuk Wai Kan, and David Ross. Quantitative temperature gradient focusing performed using background electrolytes at various pH values. *Electrophoresis*, 27(17):3420–3427, 2006.

[152] Takuya Matsui, Joachim Franzke, Andreas Manz, and Dirk Janasek. Temperature gradient focusing in a PDMS/glass hybrid microfluidic chip. *Electrophoresis*, 28(24):4606–4611, 2007.

[153] Sun Min Kim, Greg J. Sommer, Mark A. Burns, and Ernest F. Hasselbrink. Low-power concentration and separation using temperature gradient focusing via Joule heating. *Analytical Chemistry*, 78(23):8028–8035, 2006.

[154] M. Akbari, M. Bahrami, and D. Sinton. Optothermal sample preconcentration and manipulation with temperature gradient focusing. *Microfluidics and Nanofluidics*, 12(1-4):221–228, 2012.

[155] David E. Huber and Juan G. Santiago. Taylor-Aris dispersion in temperature gradient focusing. *Electrophoresis*, 28(14):2333–2344, 2007.

[156] David E. Huber and Juan G. Santiago. Ballistic dispersion in temperature gradient focusing. *Proceedings of the Royal Society A*, 464:595–612, 2008.

[157] Hao Lin, Jonathan G Shackman, and David Ross. Finite sample effect in temperature gradient focusing. *Lab on a chip*, 8(6):969–978, 2008.

[158] Karin M. Balss, Wyatt N. Vreeland, Peter B. Howell, Alyssa C. Henry, and David Ross. Micellar Affinity Gradient Focusing: A New Method for Electrokinetic Focusing. *Journal of the American Chemical Society*, 126(7):1936–1937, 2004.

[159] Mary W. Kamande, David Ross, Laurie E. Locascio, Mark Lowry, and Isiah M. Warner. Simultaneous concentration and separation of coumarins using a molecular micelle in micellar affinity gradient focusing. *Analytical Chemistry*, 79(5):1791–1796, 2007.

[160] Seyed Mostafa Shameli, Tomasz Glawdel, Zhen Liu, and Carolyn L. Ren. Bilinear temperature gradient focusing in a hybrid PDMS/glass microfluidic chip integrated with planar heaters for generating temperature gradients. *Analytical Chemistry*, 84(6):2968–2973, 2012.

[161] Seyed Mostafa Shameli, Tomasz Glawdel, Vivian E. Fernand, and Carolyn L. Ren. Micellar affinity gradient focusing in a microfluidic chip with integrated bilinear temperature gradients. *Electrophoresis*, 33(17):2703–2710, 2012.

[162] Seyed Mostafa Shameli, Tomasz Glawdel, and Carolyn L. Ren. Model of separation performance of bilinear gradients in scanning format counter-flow gradient electrofocusing techniques. *Electrophoresis*, 36(5):668–674, 2015.

[163] Seyed Mostafa Shameli and Carolyn L. Ren. Microfluidic Two-Dimensional Separation of Proteins Combining Temperature Gradient Focusing and Sodium Dodecyl Sulfate-Polyacrylamide Gel Electrophoresis. *Analytical Chemistry*, 87(7):3593–3597, 2015.

[164] Matthew Courtney, Ethan Thompson, Tomasz Glawdel, and Carolyn L. Ren. Counter-flow Gradient Focusing in Free-Flow Electrophoresis for Protein Fractionation. *Analytical Chemistry*, 92(10):7317–7324, 2020.

[165] Percy H. Rhodes and Robert S. Snyder. Method for Eectrophoretic Focusing, US 6,660,146 B2, 2003.

[166] David W. Richman. System for Hydrodynamic Compensation for Electrophoresis Crescent Distortion, US 4,309,268, 1982.

[167] Kwang W Oh, Kangsun Lee, Byungwook Ahn, and Edward P Furlani. Design of pressure-driven microfluidic networks using electric circuit analogy. *Lab on a Chip*, 12:515–545, 2012.

[168] Schurie L M Harrison and Cornelius F Ivory. Prediction of the location of stationary steady-state zone positions in counterflow isotachophoresis performed under constant voltage in a vortex-stabilized annular column. *J Sep Sci.*, 30(18):3255–3261, 2007.

[169] Matthew Courtney, Tomasz Glawdel, and Carolyn L. Ren. Investigating peak dispersion in free-flow counterflow gradient focusing. *Electrophoresis*, 43(5-6):776–784, 2022.

[170] H. M. Gladney, B. F. Dowden, and J. D. Swalen. Computer-Assisted Gas-Liquid Chromatography. *Analytical Chemistry*, 41(7):883–888, 1969.

[171] Mindy L. Phillips and Robert L. White. Dependence of Chromatogram Peak Areas Obtained by Curve-Fitting on the Choice of Peak Shape Function. *Journal of Chromatographic Science*, 35(2):75–81, 1997.

[172] Athanasios Papouliss and Unnikrishna Pillai. *Probability, random variables, and stochastic processes*. McGraw-Hill, 2002.

[173] Gil A, Segura J, and Temme N. Fast and accurate computation of the weber parabolic cylinder function w(a, x). *IMA J. Numer. Anal*, 31:1194–1216, 2011.

[174] Abu M, Alderson T, and Hamdan M. Weber's inhomogeneous differential equation with initial and boundary conditions. *Int. J. Open Probl. Comput. Sci. Math*, 9:1–11, 2016.

[175] Grushka E, Myers M, Schettler P, and Giddings J. Computer characterization of chromatographic peaks by plate height and higher central moments. *Anal. Chem*, 41:30, 1969.

[176] Morton D and Young C. Analysis of peak profiles using statistical moments. *J. Chromatogr. Sci*, 33:514–524, 1995.

[177] Mark S. Jeansonne and Joe P. Foley. Review of the exponentially modified gaussian (EMG) function since 1983. *Journal of Chromatographic Science*, 29(6):258–266, 1991.

[178] Carmen Moret-Tatay, Daniel Gamermann, Esperanza Navarro-Pardo, and Pedro Fernández de Córdoba Castellá. ExGUtils: A python package for statistical analysis with the ex-Gaussian probability density. *Frontiers in Psychology*, 9:1–11, 2018.

[179] Eli Grushka. Characterization of Exponentially Modified Gaussian Peaks in Chromatography. *Analytical Chemistry*, 44(11):1733–1738, 1972.

[180] Rolf-Dieter Reiss and Michael Thomas. *Statistical Analysis of Extreme Values*. Birkhäuser, 3rd edition edition, 2007.

[181] Ying Yang, Fan Zhi Kong, Ji Liu, Jun Min Li, Xiao Ping Liu, Guo Qing Li, Ju Fang Wang, Hua Xiao, Liu Yin Fan, Cheng Xi Cao, and Shan Li. Enhancing resolution of free-flow zone electrophoresis via a simple sheath-flow sample injection. *Electrophoresis*, 37(14):1992–1997, 2016.

[182] Milan Bier. Recycling isoelectric focusing and isotachophoresis. *Electrophoresis*, 19(7):1057–1063, 1998.

[183] Sandip Ghosal. Fluid mechanics of electroosmotic flow and its effect on band broadening in capillary electrophoresis. *Electrophoresis*, 25(2):214–228, 2004.

[184] Wei Wang, Fang Zhou, Liang Zhao, Jian Rong Zhang, and Jun Jie Zhu. Measurement of electroosmotic flow in capillary and microchip electrophoresis. *Journal of Chromatography A*, 1170(1-2):1–8, 2007.

[185] Marina Cretich, Marcella Chiari, Giovanna Pirri, and Alessandro Crippa. Electroosmotic flow suppression in capillary electrophoresis: Chemisorption of trimethoxy silane-modified polydimethylacrylamide. *Electrophoresis*, 26(10):1913–1919, 2005.

[186] Roberto Venditti, Xiangchun Xuan, and Dongqing Li. Experimental characterization of the temperature dependence of zeta potential and its effect on electroosmotic flow velocity in microchannels. *Microfluidics and Nanofluidics*, 2(6):493–499, 2006.

[187] Lonnie D. Shea, Donald L. Feke, and Uziel Landau. Counteracting Flow Electrophoresis: A Technique for Separating Biochemicals or Charged Macromolecules. *Biotechnology Progress*, 10(3):246–252, 1994.

[188] A. K. Kontturi, K. Kontturi, P. Niinikoski, A. Savonen, and M. Vuoristo. The effective charge number and diffusion coefficient of cationic cytochrome c in aqueous solution. *Acta chemica Scandinavica*, 46(4):348–353, 1992.

[189] Denitsa Milanova, Robert D. Chambers, Supreet S. Bahga, and Juan G. Santiago. Electrophoretic mobility measurements of fluorescent dyes using on-chip capillary electrophoresis. *Electrophoresis*, 32(22):3286–3294, 2011.

[190] Minsub Chung, Dohyun Kim, and Amy E. Herr. Polymer sieving matrices in microanalytical electrophoresis. *Analyst*, 139(22):5635–5654, 2014.

[191] Pavel Glukhovskiy and Qyula Vigh. Analytical- and preparative-scale isoelectric focusing separation of enantiomers. *Analytical Chemistry*, 71(17):3814–3820, 1999.

[192] Rajendrani Mukhopadhyay. When isn't the PDMS best. *Analytical Chemistry*, pages 3248–3253, 2007.

[193] Shahab Karimifard, Xu Li, Christian Elowsky, and Yusong Li. Modeling the impact of evolving biofilms on flow in porous media inside a microfluidic channel. *Water Research*, 188:116536, 2021.

[194] Christopher T. Culbertson, Stephen C. Jacobson, and J. Michael Ramsey. Diffusion coefficient measurements in microfluidic devices. *Talanta*, 56(2):365–373, 2002.

[195] David Ross and Laurie E. Locascio. Effect of caged fluorescent dye on the electroosmotic mobility in microchannels. *Analytical Chemistry*, 75(5):1218–1220, 2003.

[196] Pavel Glukhovskiy and Gyula Vigh. Improved preparative-scale, continuous, free-flow electrophoretic separation of the enantiomers of terbutaline utilizing equal-but-opposite enantiomer mobilities. *Electrophoresis*, 22(13):2639–2645, 2001.

[197] Miao Yu, Tiago Castanheira Silva, Andries van Opstal, Stefan Romeijn, Hayley A. Every, Wim Jiskoot, Geert Jan Witkamp, and Marcel Ottens. The Investigation of Protein Diffusion via H-Cell Microfluidics. *Biophysical Journal*, 116(4):595–609, 2019.

[198] Vladislav Dolník and William A. Gurske. Size separation of proteins by capillary zone electrophoresis with cationic hitchhiking (CZECH). *Electrophoresis*, 32(1):2884–2892, 2011.

[199] Miroslava Šťastná, Sergey P. Radko, and Andreas Chrambach. Separation efficiency in protein zone electrophoresis performed in capillaries of different diameters. *Electrophoresis*, 21(5):985–992, 2000.

[200] J. McGrath, M. Jimenez, and H. Bridle. Deterministic lateral displacement for particle separation: A review. *Lab on a Chip*, 14(21):4139–4158, 2014.

[201] Taehong Kwon, Sung Hee Ko, Jean Francois P. Hamel, and Jongyoon Han. Continuous Online Protein Quality Monitoring during Perfusion Culture Production Using an Integrated Micro/Nanofluidic System. *Analytical Chemistry*, 92(7):5267–5275, 2020.

[202] Vratislav Kostal, Bryan R. Fonslow, Edgar A. Arriaga, and Michael T. Bowser. Fast determination of mitochondria electrophoretic mobility using micro free-flow electrophoresis. *Analytical Chemistry*, 81(22):9267–9273, 2009.

[203] Qing Tang, A Kamel Narrate, and Cheng S Lee. Capillary Isoelectric Focusing-Electrospray Mass Spectrometry for Protein Analysis. *Analytical Chemistry*, 67(19):3515–3519, 1995.

APPENDICES

Appendix A

Supporting Information of Peak Dispersion Investigation

A.1 Analytical Model

The area-averaged x-position of a mass particle in the chamber has been previously derived in Chapter 3.2. More generally, this can be derived as a function of the y-position:

$$\frac{\partial x}{\partial t} = u_{EP} - \frac{3}{2} \nabla \langle u \rangle x \left(1 - \frac{y^2}{h^2}\right) \tag{A.1}$$

Assuming $x = 0$ at $t = 0$, this differential equation can be used to find the x-position of the analytes as a function of t:

$$x(y,t) = \frac{2u_{EP}}{3\nabla \langle u \rangle} \left(1 - \frac{y^2}{h^2}\right)^{-1} \left[1 - e^{-\frac{3}{2}\nabla \langle u \rangle \left(1 - \frac{y^2}{h^2}\right) t}\right] \tag{A.2}$$

Notice that the term in front of the square brackets represent the focal point $x_f(y)$ along the y-direction. Similarly, the z-position can be derived from the following equation:

$$\frac{\partial z}{\partial t} = \frac{3}{2} \left(\nabla \langle u \rangle z + w_0\right) \left(1 - \frac{y^2}{h^2}\right) \tag{A.3}$$

Assuming $z = 0$ at $t = 0$, this differential equation can be used to find the z-position of the analytes as a function of t:

$$z = \frac{w_0}{\nabla \langle u \rangle} \left(e^{\frac{3}{2} \nabla \langle u \rangle \left(1 - \frac{y^2}{h^2}\right) t} - 1 \right) \tag{A.4}$$

Rearranging this equation for t gives the transit time in the FFE chamber as:

$$t = \frac{2}{3 \nabla \langle u \rangle} \left(1 - \frac{y^2}{h^2}\right)^{-1} \ln \left(1 + \frac{\nabla \langle u \rangle}{w_0} z\right) \tag{A.5}$$

Finally, substituting the above equation into Eq. A.2 gives the x-position as a function of y and z:

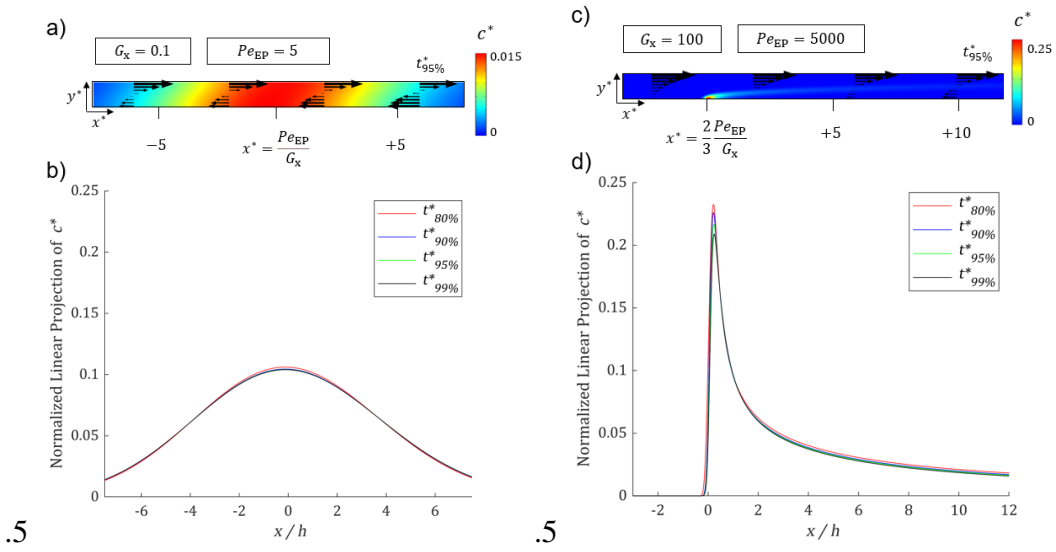
$$x(y,z) = \frac{2 u_{EP}}{3 \nabla \langle u \rangle} \left(1 - \frac{y^2}{h^2}\right)^{-1} \left(1 - \left(1 + \frac{\nabla \langle u \rangle}{w_0} z\right)^{-1}\right) \tag{A.6}$$

If the x-position is described relative to the theoretical focal point $x_f(y)$, the focusing percentage can then be defined as:

$$\frac{\%focused}{100} = 1 - \left(1 + \frac{\nabla \langle u \rangle}{w_0} z\right)^{-1} \tag{A.7}$$

A.2 Equilibrium Conditions

In reality, the time-dependence is more complicated because solute at the centreline will focus faster and have a shorter residence time than a solute near $y = \pm 1$. Nonetheless, the Eq. 4.12 and 4.15 are valid estimates at high focusing percentages, as the following figures show that the solute



distribution approaches an equilibrium position. Interestingly, for both $G_x = 0.1$ and $G_x = 100$, the peak shape remains relatively unchanged between 80% and 99% focusing. Therefore, it can be worth it to settle for 80% focusing and reduce the chamber length significantly. It should be noted that a shifted coordinate makes the transit time predicted by Eq. 4.12 and 4.15 less representative, but they remain useful approximations for equilibrium conditions.

A.3 Sample Dilution

A disadvantage with using a 2D model is that it does not account for the dilution of the focused peaks due to the addition of flow from the sidewalls. It can be difficult to predict this dilution because it is not a constant process. At first, as the solute flows towards the outlets, its peak will become more concentrated due to the focusing process, before eventually being diluted by the constant addition of counterflow as well as the smearing effect. Moreover, the final concentration of the solute peak will also depend in the width of both the sample inlet and its corresponding outlet. With that said, the time-dependent 2D COMSOL model can be used to estimate the dilution process. For example, the width of the sample inlet and all of the relevant outlets can be predefined as discussed previously. Furthermore, each time step can be related to the z^*-position of the solute in the chamber. Therefore, the dilution factor can be derived as follows:

$$C_0 Q_0 = C_{z^*} Q_{z^*} \tag{A.8}$$

where C_0 and Q_0 represent the concentration and volumetric flow rate, respectively, at the inlet, while C_{z^*} and Q_{z^*} represent the concentration and volumetric flow rate, respectively, position z^*. Given that the volumetric flow rate is the average fluid velocity multiplied by the cross-sectional area of the chamber, and rearranging for C_{z^*}/C_0, the following dilution factor can be derived:

$$\frac{C_{z^*}}{C_0} = \frac{Pe_Z}{G_x z^* + Pe_Z} \tag{A.9}$$

In its current form, the above equation cannot be used in COMSOL due to its dependence on z^*. Therefore, rearranging Eq.4.12 for z^*, this can be substituted into Eq. A.9 to give:

$$\frac{C_{t^*}}{C_0} = e^{-G_x t^*} \tag{A.10}$$

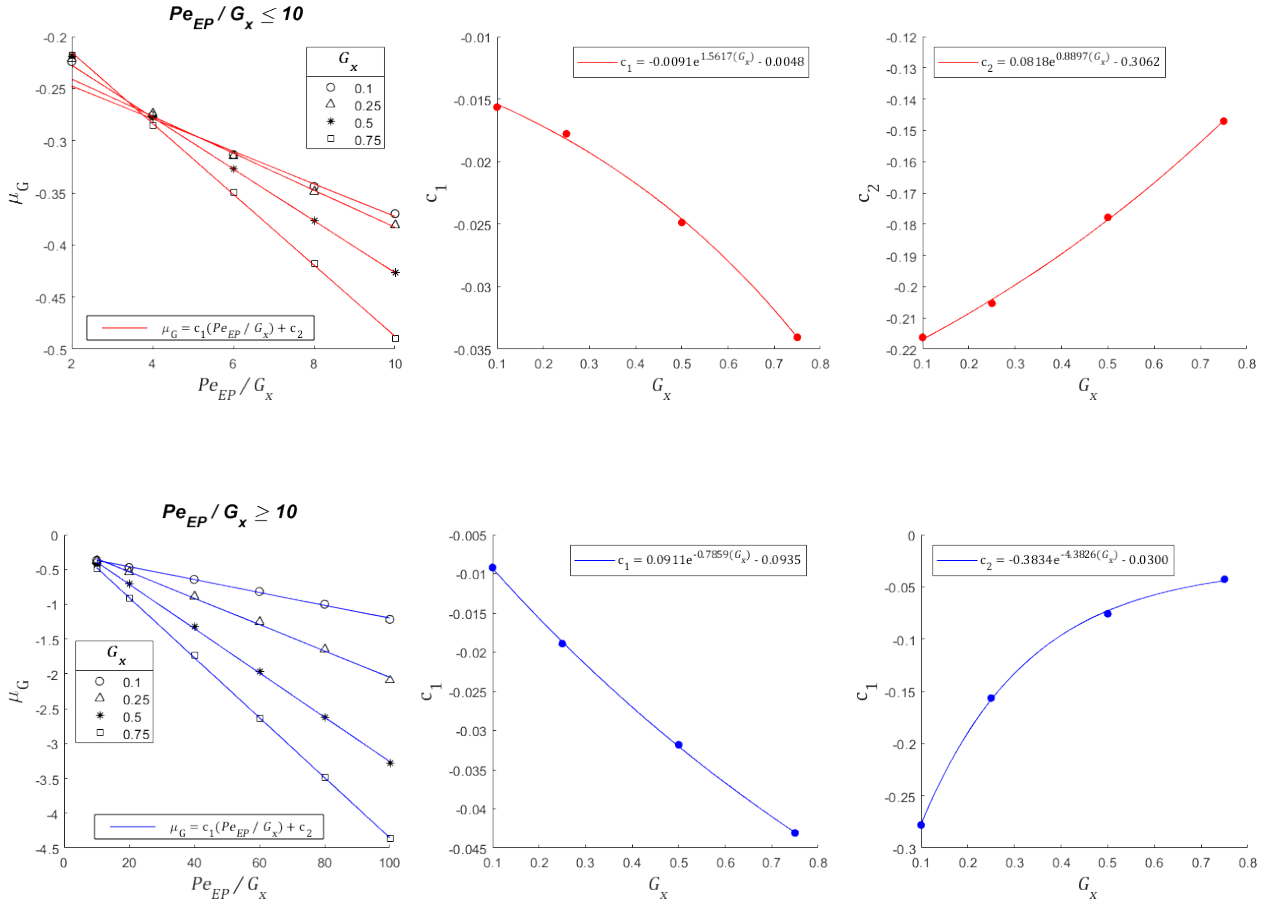
It is interesting to note that the above equation is an exponential decay in concentration, where an increasing G_x will increase the rate of decay. If Eq.4.15 is substituted into this equation, then the dilution factor can be written as

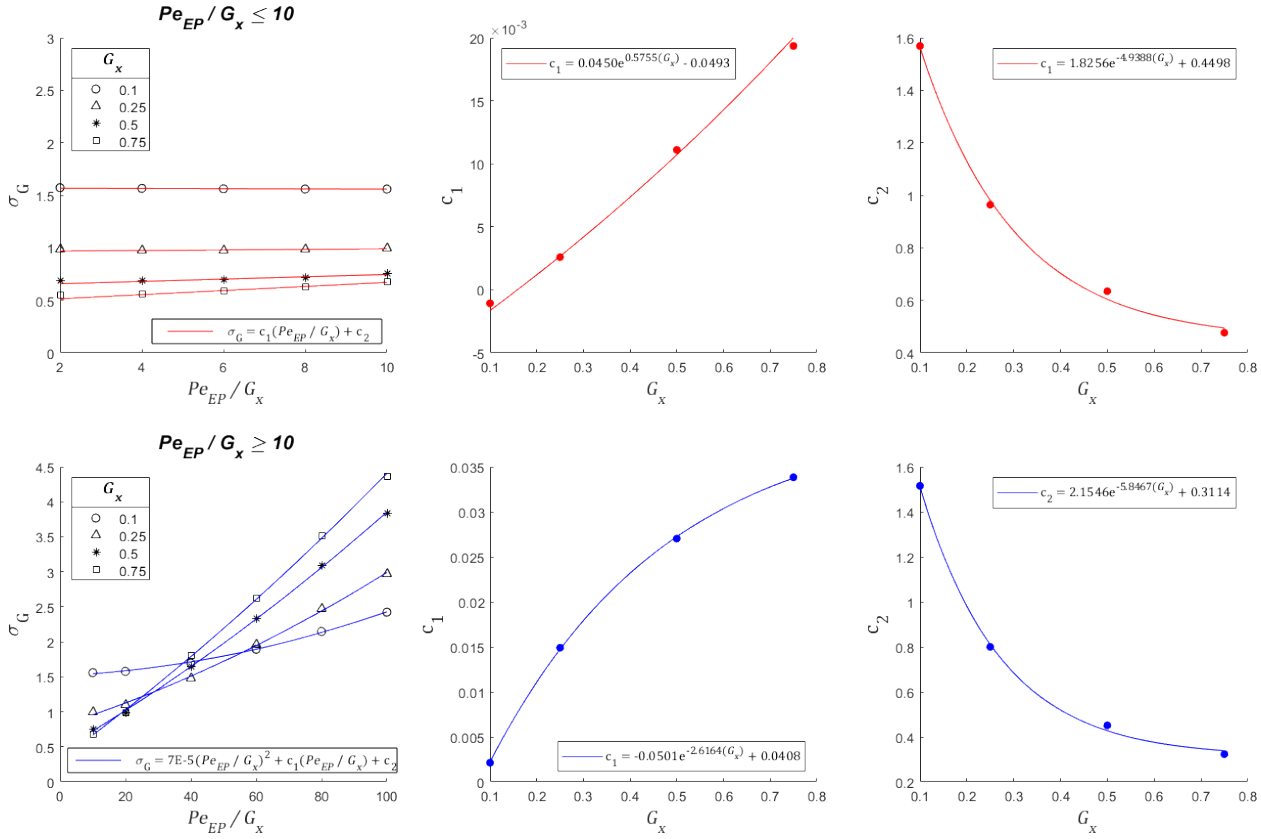
$$\frac{C_{t^*}}{C_0} = 1 - \frac{\%focused}{100} \tag{A.11}$$

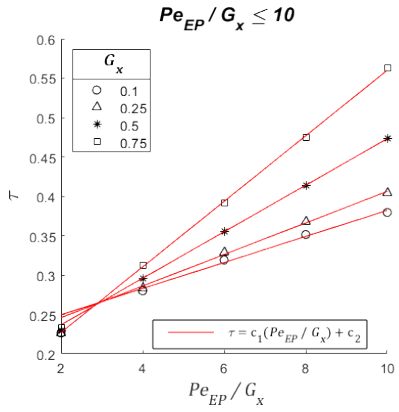
Notice that it is now independent of the dimensionless parameters, and determined entirely by the level of focusing in the system.

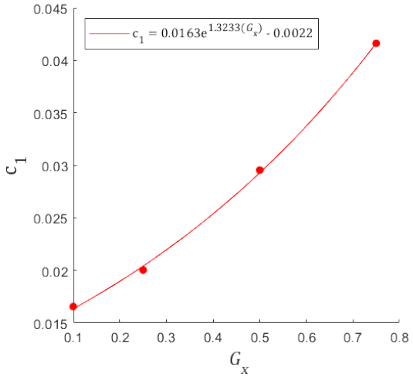
A.4 Trendlines for Fitting Parameters

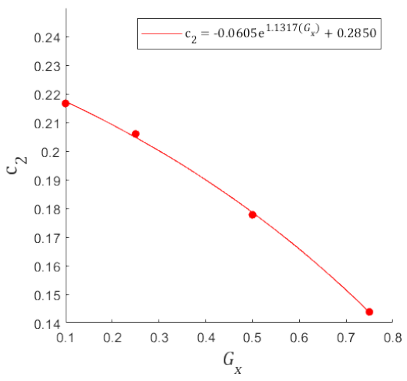
Preliminary curve-fitting identified the following regimes that can be fit with either an EMG function or a combination of the EMG and EV functions. To identify a trend in peak behaviour, several G_x values can be simulated and fitted over a wide range of Pe_{EP}/G_x values, and then their fitting parameters can be plotted. As discussed previously, the peaks exhibit different behaviour for $Pe_{EP}/G_x \geq 10$, and therefore the fitting parameters above and below this threshold will be plotted separately for an improved accuracy.

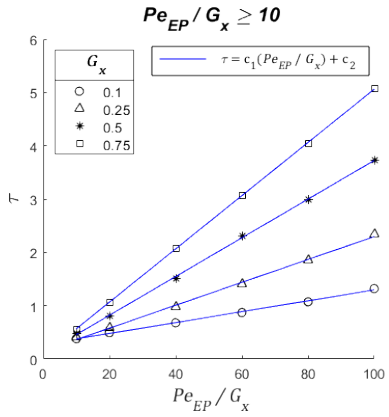

$Pe_{EP}/G_x \leq 10$
G_x
0.1
0.25
0.5
0.75
$\mu_G = c_1(Pe_{EP}/G_x) + c_2$
μ_G
Pe_{EP}/G_x
$c_1 = -0.0091e^{1.5617(G_x)} - 0.0048$
c_1
G_x
$c_2 = 0.0818e^{0.8897(G_x)} - 0.3062$
c_2
G_x
$Pe_{EP}/G_x \geq 10$
G_x
0.1
0.25
0.5
0.75
$\mu_G = c_1(Pe_{EP}/G_x) + c_2$
μ_G
Pe_{EP}/G_x
$c_1 = 0.0911e^{-0.7859(G_x)} - 0.0935$
c_1
G_x
$c_2 = -0.3834e^{-4.3826(G_x)} - 0.0300$
c_1
G_x

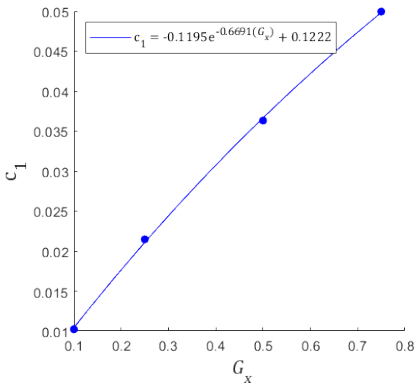

$Pe_{EP}/G_x \leq 10$
G_x
0.1
0.25
0.5
0.75
$\sigma_G = c_1(Pe_{EP}/G_x) + c_2$
σ_G
Pe_{EP}/G_x
$c_1 = 0.0450e^{0.5755(G_x)} - 0.0493$
$\times 10^{-3}$
c_1
G_x
$c_1 = 1.8256e^{-4.9388(G_x)} + 0.4498$
c_2
G_x
$Pe_{EP}/G_x \geq 10$
G_x
0.1
0.25
0.5
0.75
$\sigma_G = 7E\text{-}5(Pe_{EP}/G_x)^2 + c_1(Pe_{EP}/G_x) + c_2$
σ_G
Pe_{EP}/G_x
$c_1 = -0.0501e^{-2.6164(G_x)} + 0.0408$
c_1
G_x
$c_2 = 2.1546e^{-5.8467(G_x)} + 0.3114$
c_2
G_x

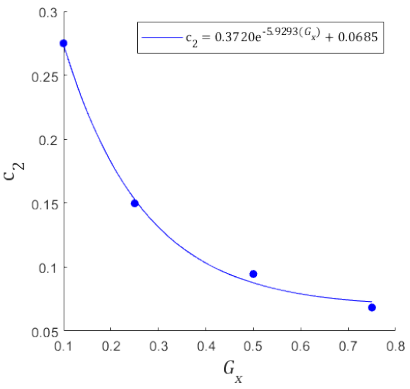

$Pe_{EP}/G_x \leq 10$
G_x
0.1
0.25
0.5
0.75
$\tau = c_1(Pe_{EP}/G_x) + c_2$
τ
Pe_{EP}/G_x

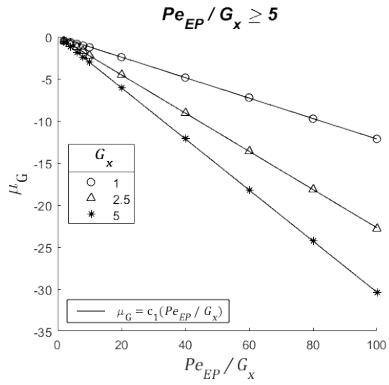

$c_1 = 0.0163e^{1.3233(G_x)} - 0.0022$
c_1
G_x

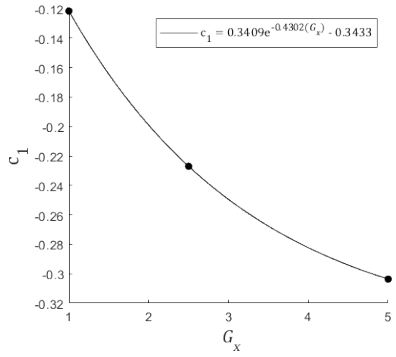

$c_2 = -0.0605e^{1.1317(G_x)} + 0.2850$
c_2
G_x

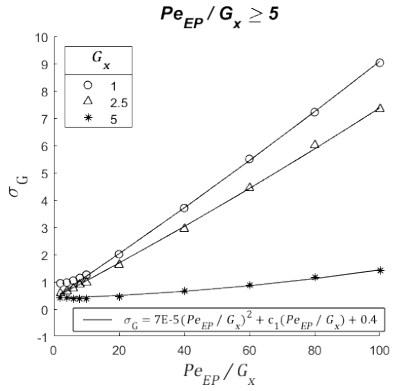

$Pe_{EP}/G_x \geq 10$
G_x
0.1
0.25
0.5
0.75
$\tau = c_1(Pe_{EP}/G_x) + c_2$
τ
Pe_{EP}/G_x

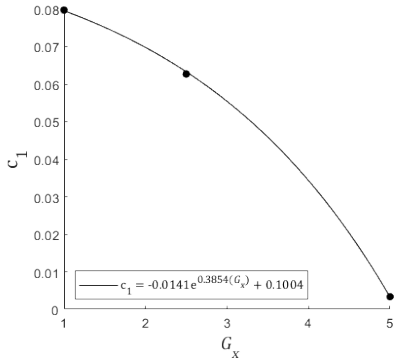

$c_1 = -0.1195e^{-0.6691(G_x)} + 0.1222$
c_1
G_x

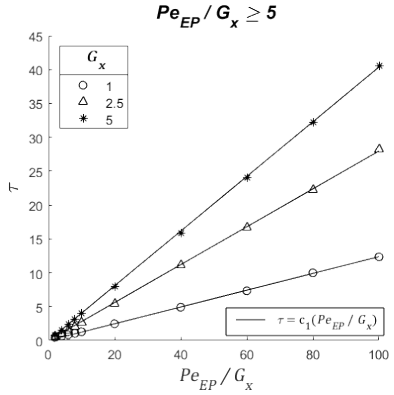

$c_2 = 0.3720e^{-5.9293(G_x)} + 0.0685$
c_2
G_x

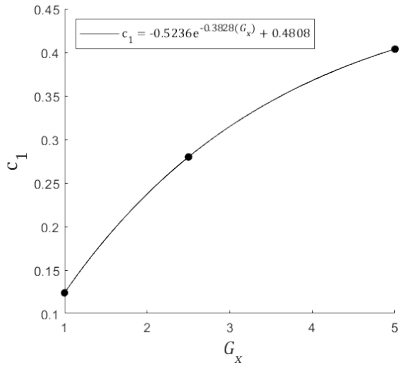

$Pe_{EP}/G_x \geq 5$
G_x
1
2.5
5
$\mu_G = c_1(Pe_{EP}/G_x)$
μ_G
Pe_{EP}/G_x

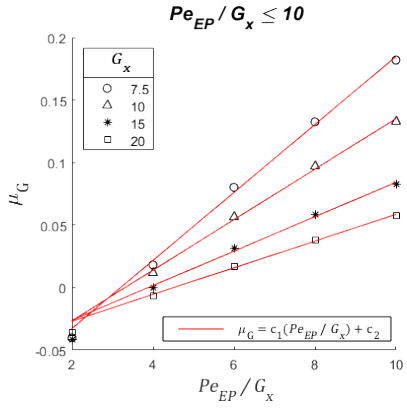

$c_1 = 0.3409e^{-0.4302(G_x)} - 0.3433$
c_1
G_x

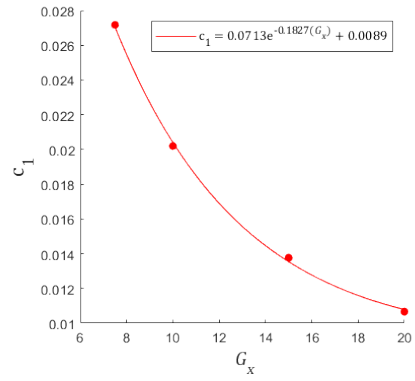

$Pe_{EP} / G_x \geq 5$
G_x
1
2.5
5
σ_G
$\sigma_G = 7E\text{-}5(Pe_{EP} / G_x)^2 + c_1(Pe_{EP} / G_x) + 0.4$
Pe_{EP} / G_x

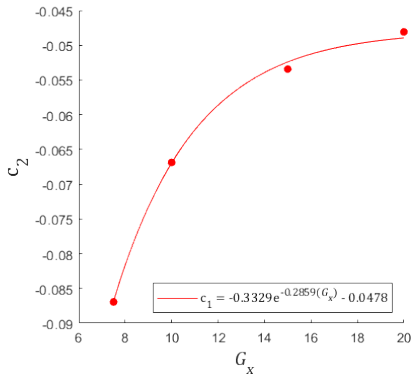

c_1
$c_1 = -0.0141e^{0.3854(G_x)} + 0.1004$
G_x

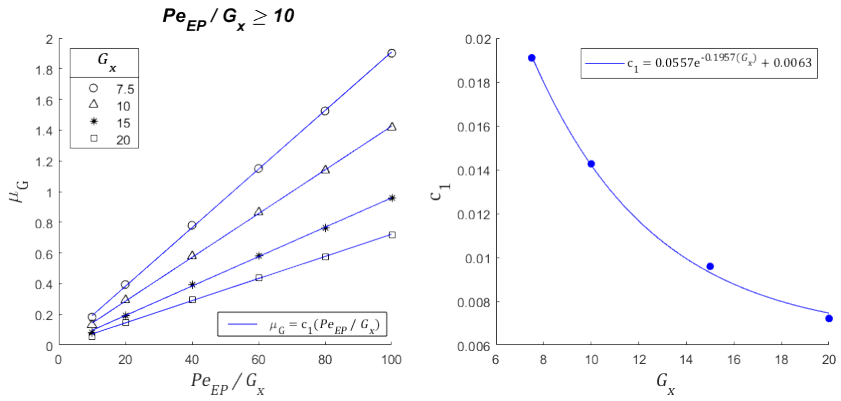

$Pe_{EP} / G_x \geq 5$
G_x
1
2.5
5
τ
$\tau = c_1(Pe_{EP} / G_x)$
Pe_{EP} / G_x

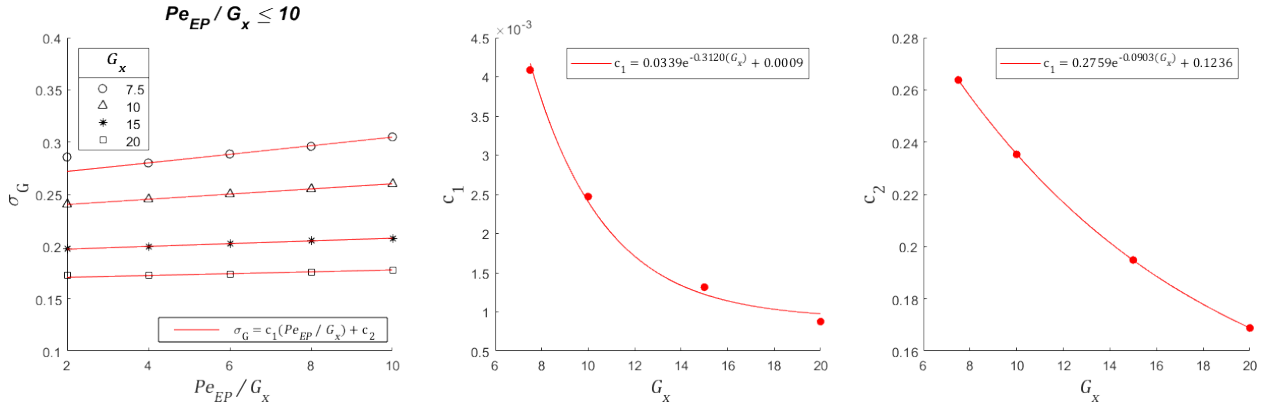

$c_1 = -0.5236e^{-0.3828(G_x)} + 0.4808$
c_1
G_x

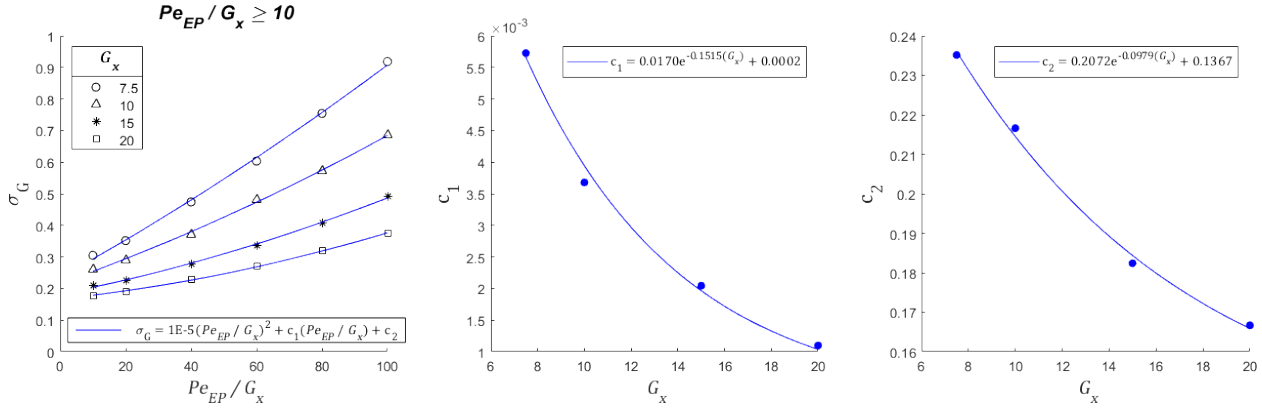

$Pe_{EP} / G_x \leq 10$
G_x
7.5
10
15
20
μ_G
$\mu_G = c_1(Pe_{EP} / G_x) + c_2$
Pe_{EP} / G_x

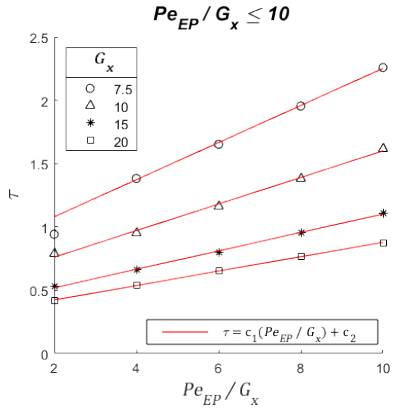

$c_1 = 0.0713e^{-0.1827(G_x)} + 0.0089$
c_1
G_x

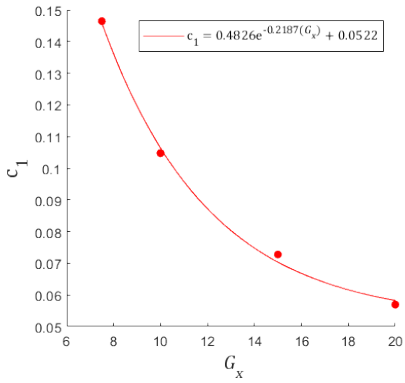

$c_1 = -0.3329e^{-0.2859(G_x)} - 0.0478$
c_2
G_x

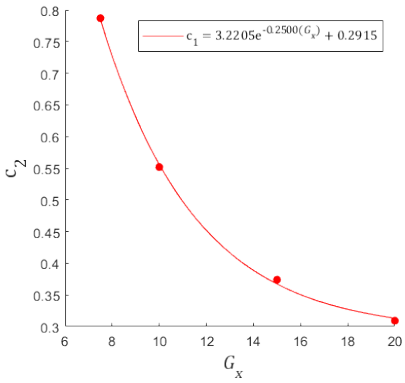

$Pe_{EP}/G_x \geq 10$
G_x
7.5
10
15
20
$\mu_G = c_1(Pe_{EP}/G_x)$
μ_G
Pe_{EP}/G_x
$c_1 = 0.0557e^{-0.1957(G_x)} + 0.0063$
c_1
G_x

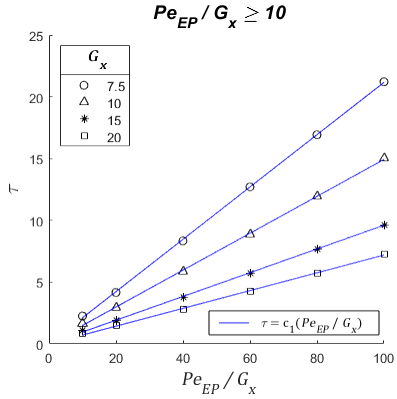

$Pe_{EP}/G_x \leq 10$
G_x
7.5
10
15
20
$\sigma_G = c_1(Pe_{EP}/G_x) + c_2$
σ_G
Pe_{EP}/G_x
$c_1 = 0.0339e^{-0.3120(G_x)} + 0.0009$
c_1
G_x
$c_2 = 0.2759e^{-0.0903(G_x)} + 0.1236$
c_2
G_x

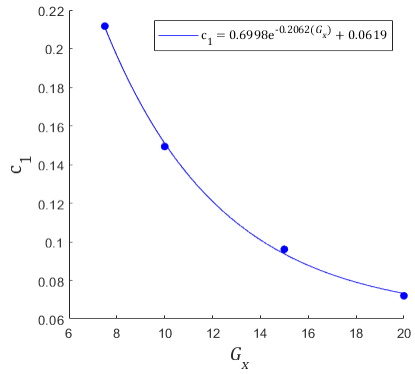

$Pe_{EP}/G_x \geq 10$
G_x
7.5
10
15
20
$\sigma_G = 1E\text{-}5(Pe_{EP}/G_x)^2 + c_1(Pe_{EP}/G_x) + c_2$
σ_G
Pe_{EP}/G_x
$c_1 = 0.0170e^{-0.1515(G_x)} + 0.0002$
c_1
G_x
$c_2 = 0.2072e^{-0.0979(G_x)} + 0.1367$
c_2
G_x

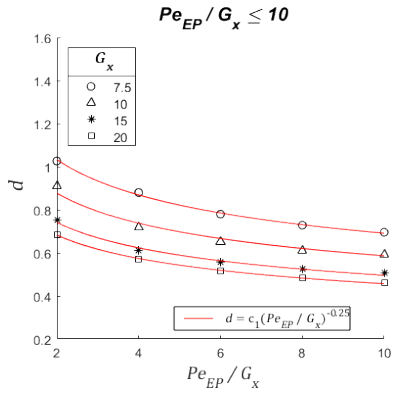

$Pe_{EP}/G_x \leq 10$
G_x
7.5
10
15
20
$\tau = c_1(Pe_{EP}/G_x) + c_2$
τ
Pe_{EP}/G_x

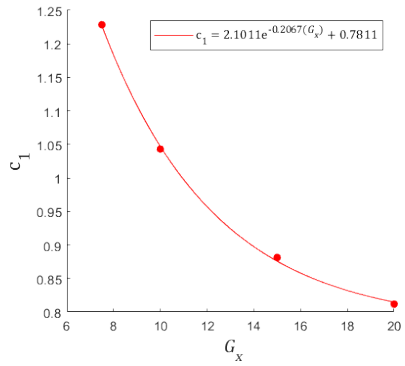

$c_1 = 0.4826e^{-0.2187(G_x)} + 0.0522$
c_1
G_x

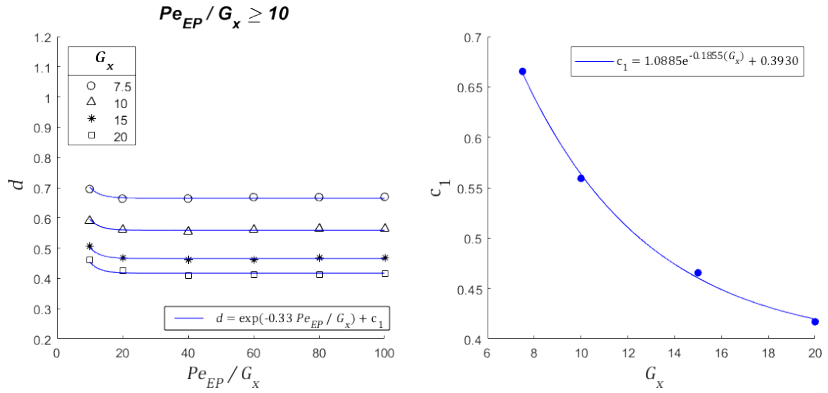

$c_1 = 3.2205e^{-0.2500(G_x)} + 0.2915$
c_2
G_x

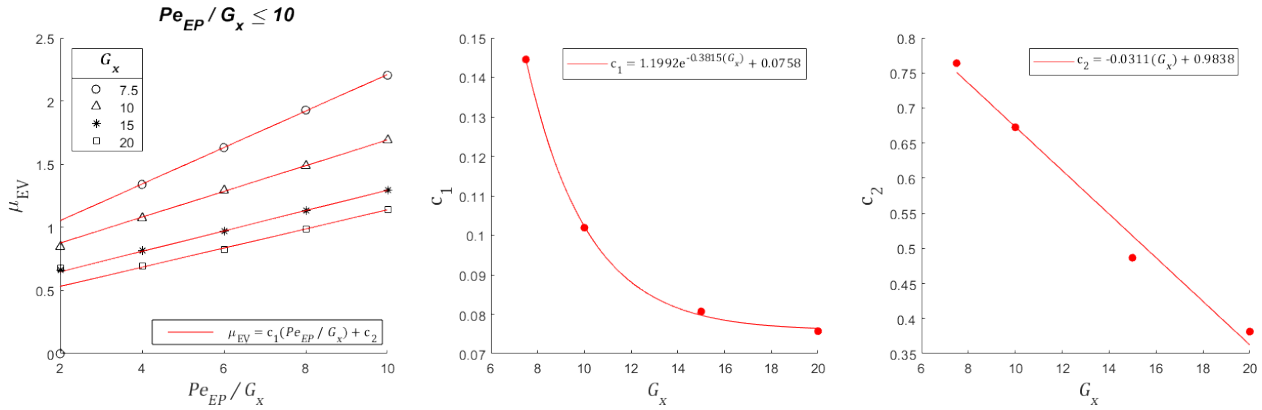

$Pe_{EP}/G_x \geq 10$
G_x
7.5
10
15
20
$\tau = c_1(Pe_{EP}/G_x)$
τ
Pe_{EP}/G_x

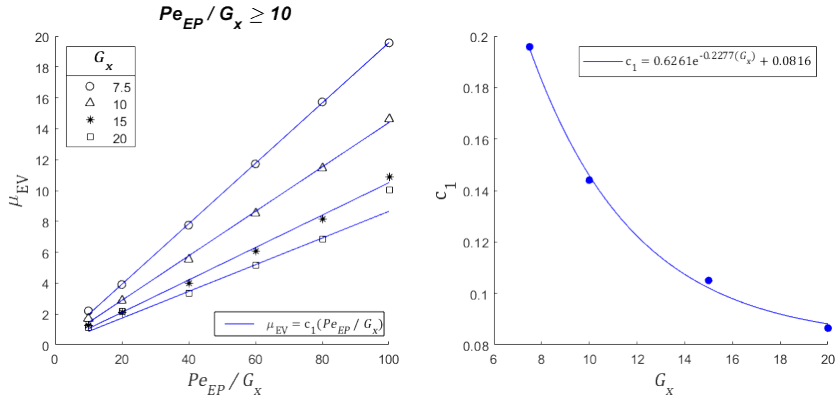

$c_1 = 0.6998e^{-0.2062(G_x)} + 0.0619$
c_1
G_x

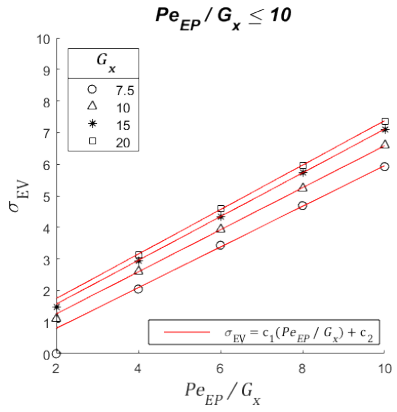

$Pe_{EP}/G_x \leq 10$
G_x
7.5
10
15
20
$d = c_1(Pe_{EP}/G_x)^{-0.25}$
d
Pe_{EP}/G_x

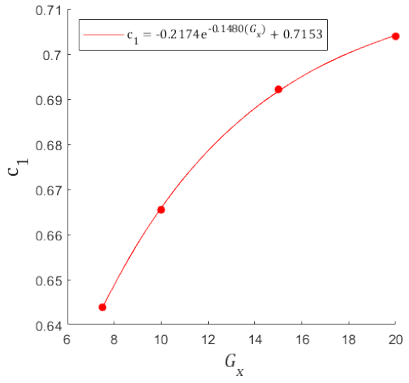

$c_1 = 2.1011e^{-0.2067(G_x)} + 0.7811$
c_1
G_x

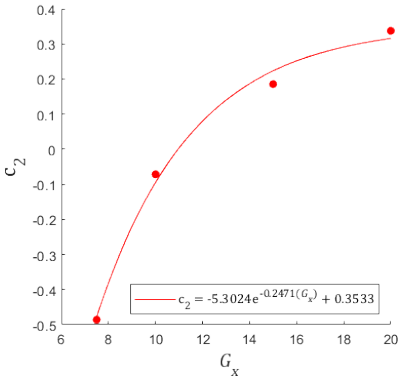

$Pe_{EP} / G_x \geq 10$
G_x
7.5
10
15
20
$d = \exp(-0.33\ Pe_{EP} / G_x) + c_1$
d
Pe_{EP} / G_x
$c_1 = 1.0885e^{-0.1855(G_x)} + 0.3930$
c_1
G_x

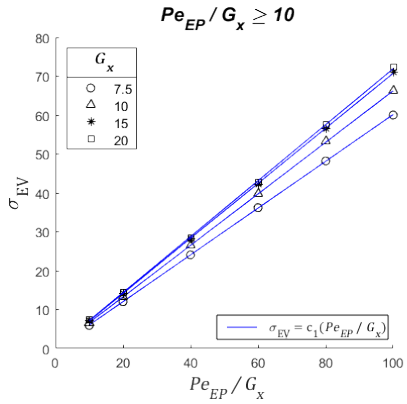

$Pe_{EP} / G_x \leq 10$
G_x
7.5
10
15
20
$\mu_{EV} = c_1(Pe_{EP} / G_x) + c_2$
μ_{EV}
Pe_{EP} / G_x
$c_1 = 1.1992e^{-0.3815(G_x)} + 0.0758$
c_1
G_x
$c_2 = -0.0311(G_x) + 0.9838$
c_2
G_x

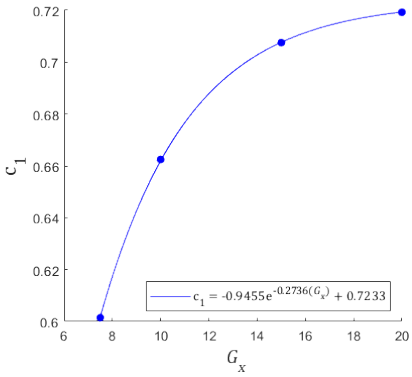

$Pe_{EP} / G_x \geq 10$
G_x
7.5
10
15
20
$\mu_{EV} = c_1(Pe_{EP} / G_x)$
μ_{EV}
Pe_{EP} / G_x
$c_1 = 0.6261e^{-0.2277(G_x)} + 0.0816$
c_1
G_x

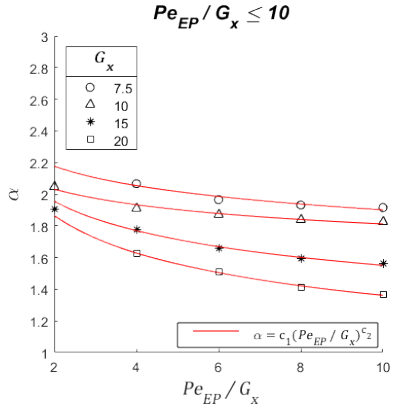

$Pe_{EP}/G_x \leq 10$
G_x
7.5
10
15
20
$\sigma_{EV} = c_1(Pe_{EP}/G_x) + c_2$
σ_{EV}
Pe_{EP}/G_x

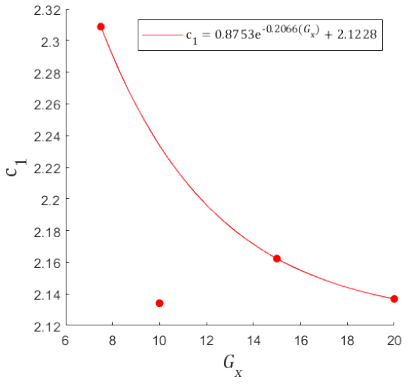

$c_1 = -0.2174e^{-0.1480(G_x)} + 0.7153$
c_1
G_x

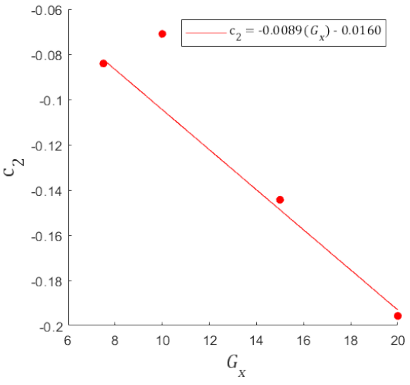

$c_2 = -5.3024e^{-0.2471(G_x)} + 0.3533$
c_2
G_x

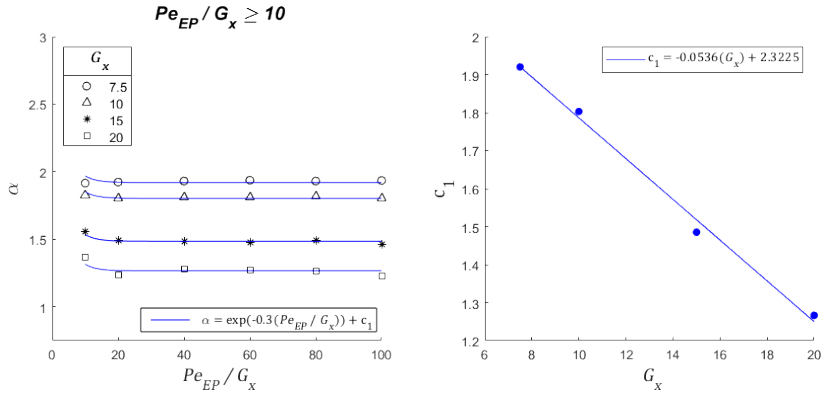

$Pe_{EP}/G_x \geq 10$
G_x
7.5
10
15
20
$\sigma_{EV} = c_1(Pe_{EP}/G_x)$
σ_{EV}
Pe_{EP}/G_x

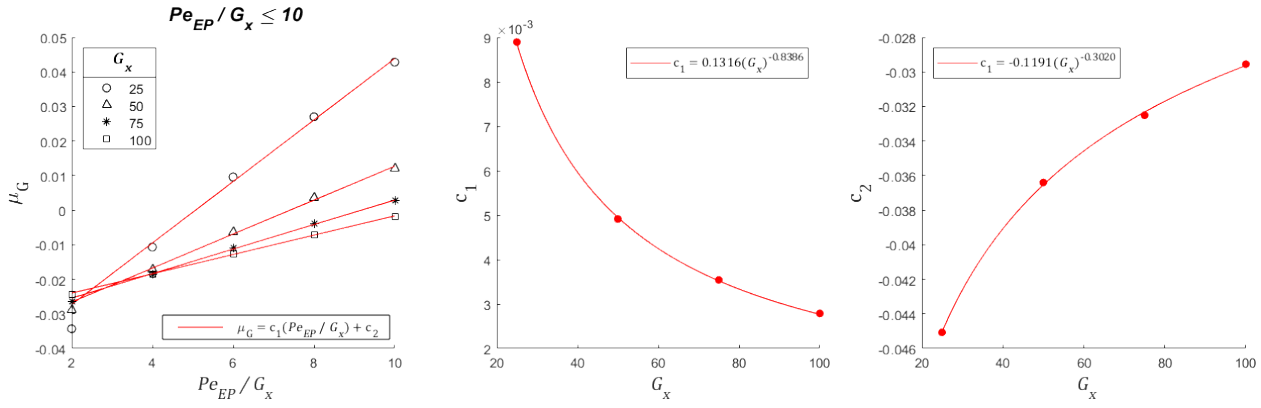

$c_1 = -0.9455e^{-0.2736(G_x)} + 0.7233$
c_1
G_x

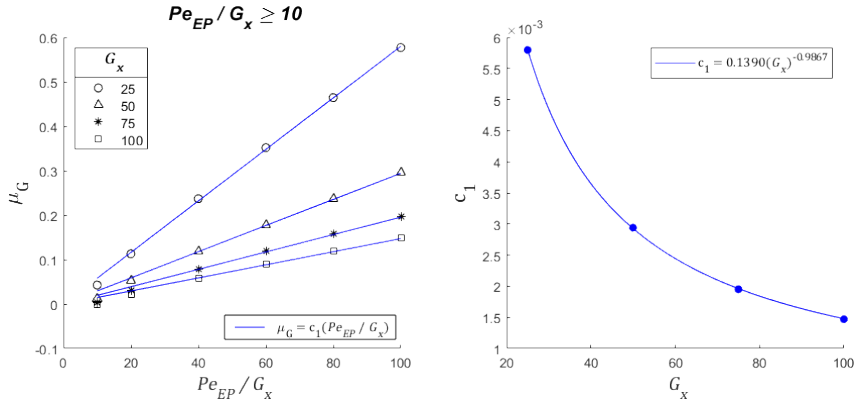

$Pe_{EP}/G_x \leq 10$
G_x
7.5
10
15
20
$\alpha = c_1(Pe_{EP}/G_x)^{c_2}$
α
Pe_{EP}/G_x

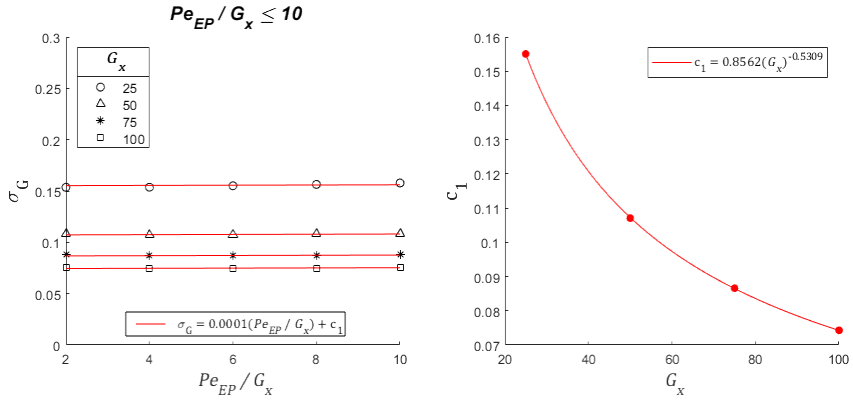

$c_1 = 0.8753e^{-0.2066(G_x)} + 2.1228$
c_1
G_x

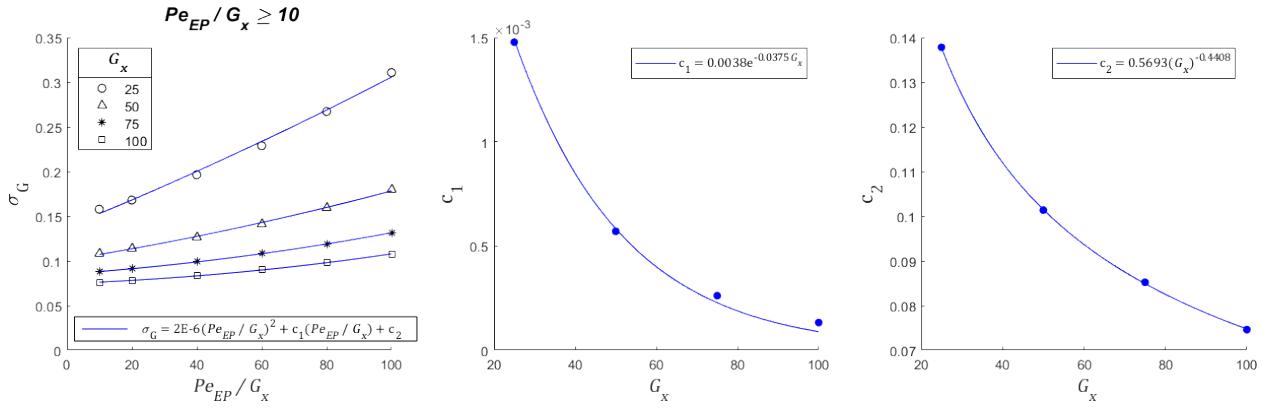

$c_2 = -0.0089(G_x) - 0.0160$
c_2
G_x

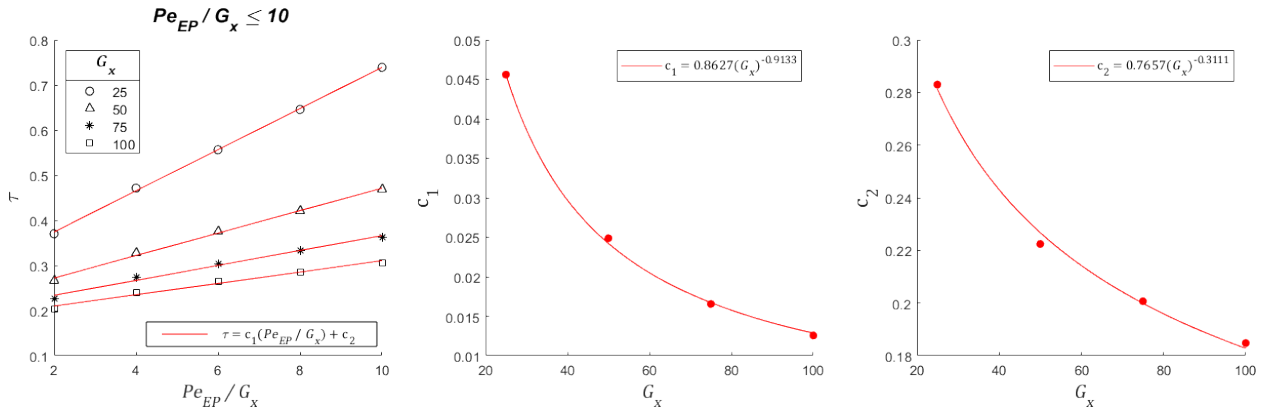

$Pe_{EP} / G_x \geq 10$
G_x
7.5
10
15
20
$\alpha = \exp(-0.3(Pe_{EP} / G_x)) + c_1$
α
Pe_{EP} / G_x
$c_1 = -0.0536(G_x) + 2.3225$
c_1
G_x

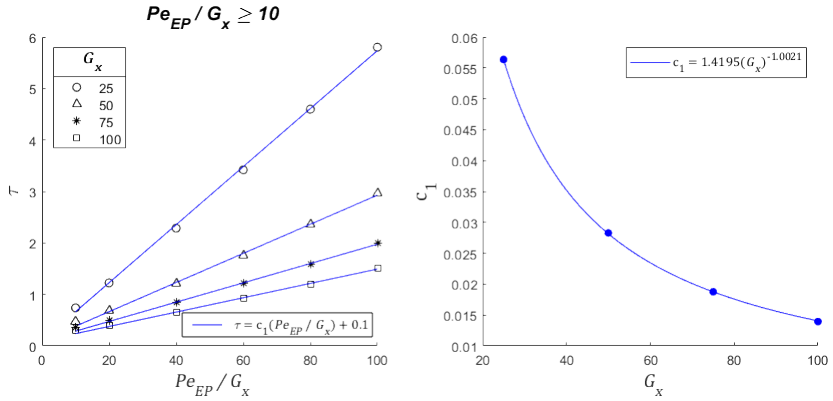

$Pe_{EP} / G_x \leq 10$
G_x
25
50
75
100
$\mu_G = c_1(Pe_{EP} / G_x) + c_2$
μ_G
Pe_{EP} / G_x
$c_1 = 0.1316(G_x)^{-0.8386}$
c_1
G_x
$c_1 = -0.1191(G_x)^{-0.3020}$
c_2
G_x

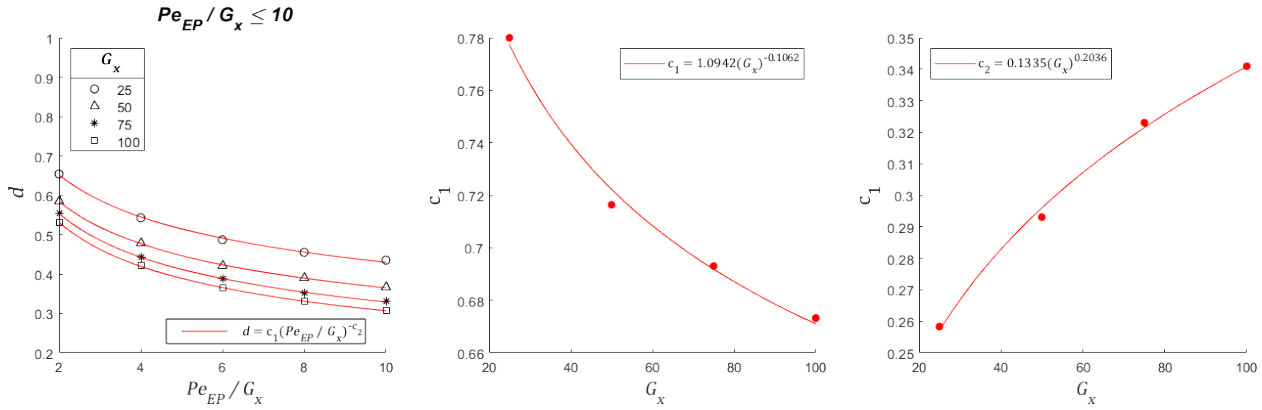

$Pe_{EP} / G_x \geq 10$
G_x
25
50
75
100
$\mu_G = c_1(Pe_{EP} / G_x)$
μ_G
Pe_{EP} / G_x
$c_1 = 0.1390(G_x)^{-0.9867}$
c_1
G_x

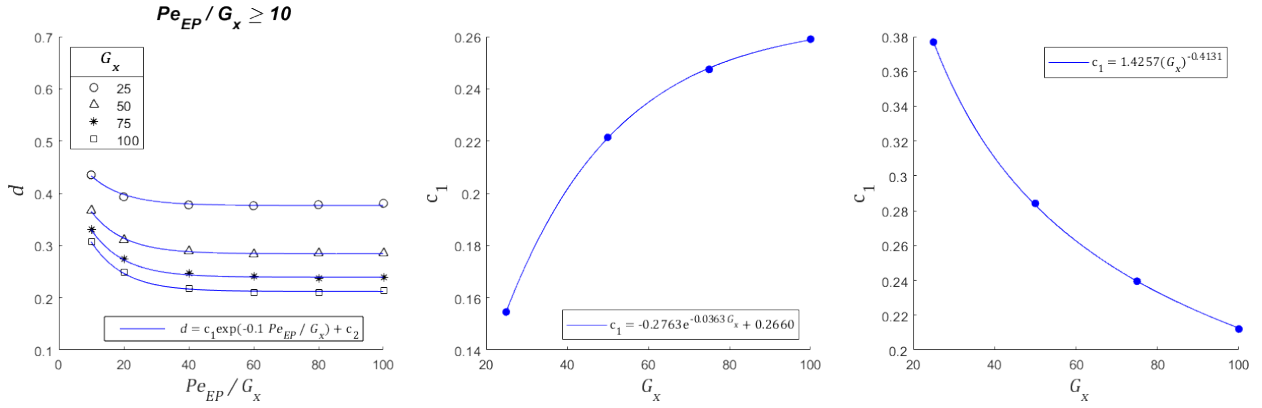

$Pe_{EP} / G_x \leq 10$
G_x
25
50
75
100
$\sigma_G = 0.0001(Pe_{EP} / G_x) + c_1$
σ_G
Pe_{EP} / G_x
$c_1 = 0.8562(G_x)^{-0.5309}$
c_1
G_x

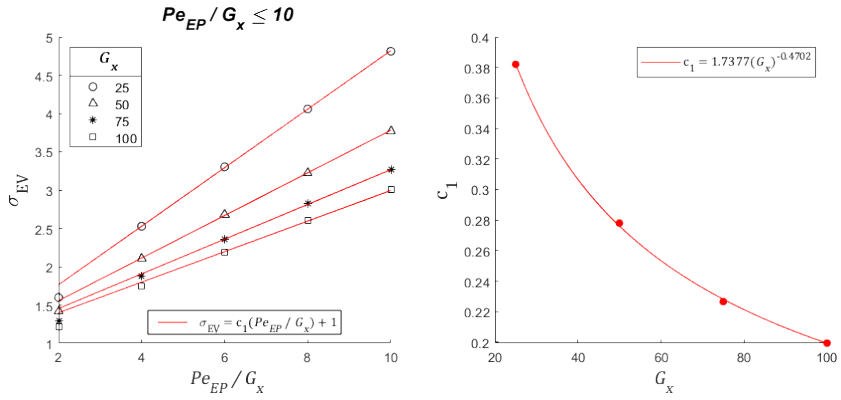

$Pe_{EP} / G_x \geq 10$
G_x
25
50
75
100
$\sigma_G = 2E\text{-}6(Pe_{EP} / G_x)^2 + c_1(Pe_{EP} / G_x) + c_2$
σ_G
Pe_{EP} / G_x
$\times 10^{-3}$
$c_1 = 0.0038e^{-0.0375 G_x}$
c_1
G_x
$c_2 = 0.5693(G_x)^{-0.4408}$
c_2
G_x

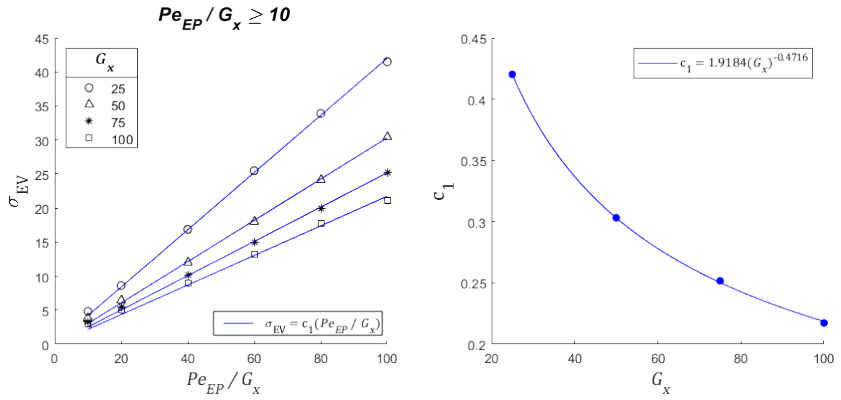

$Pe_{EP} / G_x \leq 10$
G_x
25
50
75
100
$\tau = c_1(Pe_{EP} / G_x) + c_2$
τ
Pe_{EP} / G_x
$c_1 = 0.8627(G_x)^{-0.9133}$
c_1
G_x
$c_2 = 0.7657(G_x)^{-0.3111}$
c_2
G_x

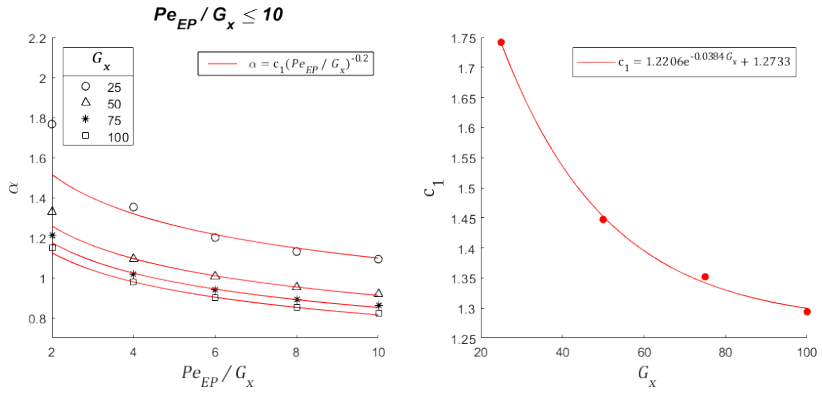

$Pe_{EP}/G_x \geq 10$
G_x
25
50
75
100
$\tau = c_1(Pe_{EP}/G_x) + 0.1$
τ
Pe_{EP}/G_x
$c_1 = 1.4195(G_x)^{-1.0021}$
c_1
G_x

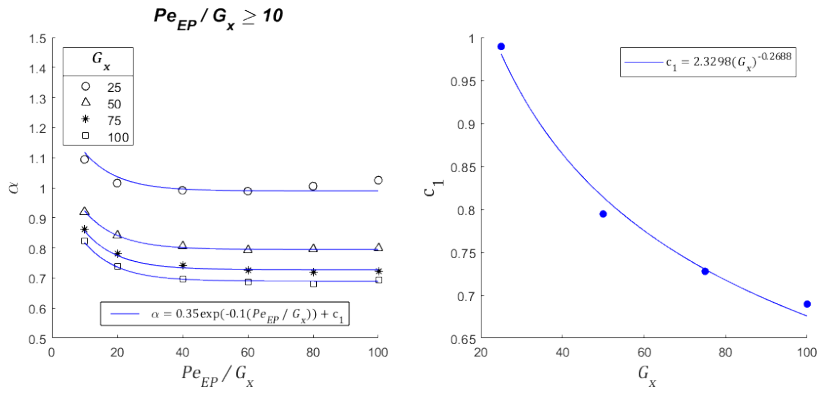

$Pe_{EP}/G_x \leq 10$
G_x
25
50
75
100
$d = c_1(Pe_{EP}/G_x)^{-c_2}$
d
Pe_{EP}/G_x
$c_1 = 1.0942(G_x)^{-0.1062}$
c_1
G_x
$c_2 = 0.1335(G_x)^{0.2036}$
c_1
G_x


$Pe_{EP}/G_x \geq 10$
G_x
25
50
75
100
$d = c_1\exp(-0.1\ Pe_{EP}/G_x) + c_2$
d
Pe_{EP}/G_x
$c_1 = -0.2763e^{-0.0363G_x} + 0.2660$
c_1
G_x
$c_1 = 1.4257(G_x)^{-0.4131}$
c_1
G_x


$Pe_{EP}/G_x \leq 10$
G_x
25
50
75
100
$\sigma_{EV} = c_1(Pe_{EP}/G_x) + 1$
σ_{EV}
Pe_{EP}/G_x
$c_1 = 1.7377(G_x)^{-0.4702}$
c_1
G_x


$Pe_{EP}/G_x \geq 10$
G_x
25
50
75
100
$\sigma_{EV} = c_1(Pe_{EP}/G_x)$
σ_{EV}
Pe_{EP}/G_x
$c_1 = 1.9184(G_x)^{-0.4716}$
c_1
G_x


$Pe_{EP}/G_x \leq 10$
G_x
25
50
75
100
$\alpha = c_1(Pe_{EP}/G_x)^{-0.2}$
α
Pe_{EP}/G_x
$c_1 = 1.2206e^{-0.0384G_x} + 1.2733$
c_1
G_x


$Pe_{EP} / G_x \geq 10$
G_x
25
50
75
100
$\alpha = 0.35\exp(-0.1(Pe_{EP} / G_x)) + c_1$
α
Pe_{EP} / G_x
$c_1 = 2.3298(G_x)^{-0.2688}$
c_1
G_x